Flow boiling of R245fa in vertical small metallic tubes

A thesis submitted for the degree of Doctor of Philosophy

By

Emily A. Pike-Wilson

Mechanical Engineering Department

School of Engineering and Design

Brunel University, London,

Uxbridge, UB8 3PH

September 2014

Abstract

The research presented is part of a larger study, dedicated to investigating flow boiling in small to microchannels. The test facility, originally designed by Huo (2005) and since used by Chen (2006) and Mahmoud (2011), has been used to investigate flow boiling of R134a across a range of channel diameters and both seamless cold drawn and welded channels. These previous studies concluded that one of the reasons for discrepancies in reported data is the result of surface characteristics. The objective of this current study is to further investigate the effect of channel characteristics and changing the refrigerant to R245fa. Surface characteristics are investigated with stainless steel, copper and brass channels, all seamless cold drawn and 1.1 mm internal diameter. Experiments using R245fa were initially conducted in the same stainless steel channel used with R134a by Mahmoud (2011). This allowed for the surface characteristics to be negated and the comparison to be based purely on the changes in the thermophysical properties between R134a and R245fa. Experiments were conducted at inlet pressures of 1.85 and 2.45 bar, mass fluxes of 100 – 400 kg/m^{2}s, heat fluxes from 1 – 60 kW/m^2 and vapour qualities from 0 – 0.95.

The test section surfaces were evaluated based on scanning electron microscopy (SEM) and confocal laser microscopy (CFLSM). SEM allowed for a visual inspection of the channel surface, with clear differences in the surface stricter evident. The surfaces were then compared based on two CFLSM profilers. The values of the surface parameters differed between the two profilers but the same trend was seen, brass being the roughest surface and copper the smoothest. Changes in the surface parameter values were found to be a function of the scan area, scan resolution and cut-off value.

A borosilicate glass tube, at the test section exit, allowed for flow visualisation. Mahmoud (2011) reported bubbly, slug, churn and annular flow for R134a, with no effect of hysteresis. Churn and annular flow were present for R245fa with an increasing heat flux. This was a result of a higher surface tension for R245fa which facilitates annular flow. Hysteresis was evident for R245fa, with bubbly, slug, churn and annular flow seen with a decreasing heat flux. The hysteresis effect is a result of nucleation sites activating during the increase in heat flux and remaining activated as the heat flux is decreased. The activation of nucleation sites depends on the size, which was constant due to the same channel being used, and the wall superheat. The wall superheat is lower for R245fa which does not allow for the nucleation sites to be initially activated with an increasing heat flux. The same effect of hysteresis was evident for copper and brass. Differences in the exit vapour quality and heat flux at which flow patterns occurred were seen between the three materials.

The heat transfer coefficient varied in both magnitude and trend between R134a and R245fa. Mahmoud (2011) reported an almost constant heat transfer coefficient with vapour quality at a higher magnitude than seen for R245fa. R245fa showed an increasing trend with vapour quality. Peaks in the heat transfer coefficient were seen to be a result of surface flaw, evident when plotting as a function of the axial location. The test section was reversed in orientation, moving the location of the peak from near the entry of the test section to near the exit. A similar heat transfer coefficient peak was

seen at the same axial location, near the exit of the test section, confirming that the peak was a result of a surface flaw and a result of the flow developing. The heat transfer coefficient changed in magnitude and trend for copper and brass. The magnitude of the recorded heat transfer coefficient did not follow the same trend as the surface parameters. The heat transfer correlations in literature did not predict the increase in the heat transfer with vapour quality, performing poorly compared with R134a. The best correlation for the prediction of both refrigerants was that of Mahmoud and Karayiannis I (2012).

The pressure drop for R245fa was over 300 % higher than that of R134a, with a steeper increase with heat flux. This is attributed to a higher liquid viscosity and lower vapour density for R245fa. The pressure drop was highest for the roughest channel, brass, but lowest for stainless steel which had the intermediate roughness. The smoothest channel, copper, showed the largest difference in the effect of inlet pressure on the measured pressure drop and the roughest surface, brass, the smallest difference. The effect of surface characteristics on pressure drop is greater than the effect of changes in the fluid properties with inlet pressure. Pressure drop correlations performed poorly for R245fa in comparison with R134a, with the majority under predicting the pressure drop. Only one pressure drop correlation included a function of the surface parameters, Del Col et al. (2013), but this correlation under predicted the effect of the surface parameters on pressure drop. There was no one correlation which gave satisfactory results for all three materials.

Acknowledgments

Foremost, I would like to express my sincere gratitude to my husband, Tom, who has supported me through all of my studies and who without, none of this would be possible. I am also thankful for the support of my parents who have guided and encouraged me though my education in many ways. I will always be grateful for the support, moral and financial, which you provided.

I am extremely thankful to the support of Beatriz Lopez, Lesh 'Bob' Gowreesunker, Ruth MacKay and especially, Giovanna Cossali for the amazing support and friendship which helped me survive my PhD.

I am especially thankful to the funding of the Thomas Gerald Gray charitable trust for my scholarship.

Lastly, I would like to thank my supervisor, Tassos Karayiannis for his guidance and John Lewis for passing on his valuable knowledge. I would also like to thank Mohamed Mahmoud for teaching me the experimental facility and Costas Xanthos for helping me with my experiments and keeping me company in the lab.

Research outputs

Conferences

- Flow boiling of R134a and R245fa in a 1.1 mm diameter tube. Presented at The Eleventh International Conference on Nanochannels, Microchannels and Minichannels. ICNMM13 June 16 – 19, 2013, Sapporo, Japan.
- Flow boiling of R245fa in 1.1 mm diameter stainless steel and brass tubes. 8th World Conference on Experimental Heat Transfer, Fluid Mechanics, and Thermodynamics (ExHFT-8), June 16 – 20, 2013, Lisbon, Portugal.
- Flow boiling patterns in a 1.1 mm diameter tube with different refrigerants. 13th UK Heat Transfer Conference, UKHTC2013, 2 – 3 September 2013, Imperial College, London.
- Flow Patterns and Comparison with Correlations for Vertical Flow Boiling of R245fa in Small to Micro Tubes, 4th Micro and Nano Flows Conference, MNF, 7 – 10 September 2014, UCL, London, UK.

Invited presentations

- A Comparison of Heat Transfer and Pressure Drop Correlations for Flow Boiling in Microchannels. 9th UK – Japan Seminar on Multi-Phase Flows 2013, 16th – 18th September 2013, Brunel University London, UK.
- Flow Boiling of R245fa in 1.1 mm Diameter Tubes of Different Materials, 9th UK – Japan Seminar on Multi-Phase Flows 2013, 16th – 18th September 2013, Brunel University London, UK.

Journals

- Flow Boiling of R245fa in 1.1 mm Diameter Stainless Steel, Brass and Copper Tubes, Experimental Thermal and Fluid Science, In Press, 2014.

Declaration

This research was conducted at Brunel University London, under the supervision of Prof. T. G. Karayiannis. All research presented, unless otherwise stated or referenced, is the work of the author.

The work has not been submitted for another degree or award to any other institution.

Contents

Figure numbers

Table numbers

Nomenclature

Latin

A	Area	m^2
Bd	Bond number	-
Bo	Boiling number, q/Gh_{fg}	-
C_L	Loss coefficient	$W K^{-1}$
Co	Confinement number	-
Cp	Specific heat	$J kg^{-1} K^{-1}$
D	Diameter	m
E	Enhancement factor	-
Eö	Eötvos number, $4\pi^2\sigma/D^2\Delta\rho g$	-
F	Enhancement factor	-
f	Friction factor	-
f_b	Bubble frequency	Hz
Fr	Froude number	-
g	gravity	ms^{-1}
G	Mass flux	$kgm^{-2}s^{-1}$
Gz	Graetz number	-
h	Heat transfer coefficient	$Wm^{-2}K^{-1}$
hf	Liquid enthalpy	$kJ kg^{-1}$
hfg	Enthalpy of evaporation	$kJ kg^{-1}$
hg	Total enthalpy	$kJ kg^{-1}$
I	Current	Amps
j	Liquid slug velocity	$m s^{-1}$
j_G	Superficial gas velocity	$m s^{-1}$
k	Thermal conductivity	$W m^{-1}K^{-1}$
L	Length	m
La	Laplace constant	m

Lh	Heated length	m
L_p	Pressure drop length	m
$\dot{m}$	Mass flow rate	kg s^{-1}
M	Molecular weight	kg $kmol^{-1}$
N	Number of samples	-
Na	Number of active nucleation sites	-
N_{conf}	Confinement number	-
Nu	Nusselt number	-
P	Pressure	bar
P_m	measured pressure drop	Pa
Pr	Prandtl number	-
P_R	Reduced pressure	-
q	Heat flux	Wm^{-2}
Q_{loss}	Heat loss	W
Ra	Average surface roughness	µm
r_b	Bubble radius	m
Re	Reynolds number	-
Rp	Maximum profile peak height	µm
Rq	Root mean square deviation	µm
Rsm	Mean spacing of profile irregularities	µm
Rt	Maximum height	µm
Rv	Maximum profile valley depth	µm
Rz	Average maximum height	µm
S	Suppression factor	-
Su	Suratman number, $\rho_g \sigma D/\mu_g^2$	-
t	time	s
t_{95}	95 % confidence limit	-
T	Temperature	˚ C

U_{gs}	Superficial gas velocity	m s^{-1}
U_{ls}	Superficial liquid velocity	m s^{-1}
U_{sys}	Systematic error	-
U_p	Pair velocity	m s^{-1}
V	Voltage	V
W	Weight	kg
We	Weber number	-
x	Vapour quality	-
X	Martinelli parameter	-
Y	Muller-Steinhagen and Heck Parameter	-
z	Axial location	m

Greek letters

α	Heat transfer coefficient	W m^{-2} K^{-1}
β	Percentage of data within ±30%	-
δ	liquid film thickness	m
ε	Volumetric void fraction	-
λ	Thermal conductivity	W m^{-1} K^{-1}
μ	Viscosity	N s m^{-2}
ρ	Density	kg m^{-3}
σ	Surface tension	N m^{-1}
τ	Shear stress	N m^{-2}
τ_b	Bubble generation period	s
τ_i	Interfacial shear stress	N m^{-2}
τ^*	non-dimensional bubble generation period	-
υ	Specific volume	m^3 kg^{-1}
φ	Two phase frictional multiplier	-
ψ	Lee and Lee (2001) parameter, $\mu_f j/\sigma$	-

Subscripts

acc	acceleration
cb	Confined bubble
crit	Critical
cv	Convective
e	Exit
f	Fluid
fb	Fluid bulk
fric	Frictional
g	Gas
GC	Gas core
go	Gas only
Go	Gas only
grav	Gravitational
h	heated
ins	insulation
l	Liquid
lam	Laminar
lo	Liquid only
lo	Liquid only
nb	Nucleate boiling
ref	Reference
sat	Saturated
sp	Single phase
sub	Subcooled
tot	Total
tp	Two phase
turb	Turbulent

v	Vapour
w	Wall
wi	Inside wall
wo	Outside wall

Chapter 1

1. Introduction

1.1 Cooling techniques

Thermal management of new and developing technologies has been the subject of research for many years. There are multiple techniques available for cooling, each with their own merits but also limitations. The motivation behind the research into flow boiling in microchannels is to expand the current knowledge in this field, in order to reduce the number of limitations to the application of this technology. Firstly, we must consider the current cooling techniques available.

1.1.1 Spray and micro jet cooling

Spray cooling is based on liquid passing through a nozzle at high pressure, resulting in droplets being propelled onto the heated surface. Depending on the conditions, there are multiple possible outcomes for the droplets generated. The droplets may evaporate or form together to form a film, with options of both single phase convection or two phase evaporation or boiling (Ebadian et al. 2011). Spray cooling can also utilise enhanced surfaces to increase the rate of heat flux removal, similarly to flow boiling. Piezoelectric droplets, i.e. droplets are formed through piezoelectric vibrations rather than passing through high pressure nozzles, have been used to enhance spray and jet impingement cooling. This method is unsteady and consequently the heat transfer behaviour differs from spray cooling. Amon et al. (2001) investigated the use of droplet impingement to remove heat fluxes in the range of 70 – 100 W/cm^2. The study was based on numerical simulations, concluding that the heat flux removal is a function of the micro-structure of the surface. As the interaction between the droplets affects the heat transfer mode, surface structures can be used to enhance and control these interactions. Ebadian et al. (2011) review noted work of Fabbri et al. (2003) who compared the heat flux removal of multiple microjets and spray cooling with water.

Based on the same pumping power and temperature difference, the multiple microjets removed up to 240 W/cm^2 but the spray only removed up to 93 W/cm^2. However, if not compared at the same conditions, the spray cooling had a higher rate of heat flux removal than any jet configuration. The review concluded that of the five cooling methods considered (microchannels, jet impingement, sprays, wettability effects and piezoelectric droplets), that although jet impingement was shown to have the highest heat flux removal, all the techniques are open to optimisation through changes in the geometry and working fluid. This is contrary to a study by Oliphant et al. (1998) which compared the heat transfer coefficients achieved from liquid spray and jet impingement. It was found that spray cooling equalled the heat transfer rates as jet impingement but at a lower mass flux. Ravikumar et al. (2014) conducted experiments using air-atomized spray with polymer additives. This method was given as an alternative to jet impingement, which can suffer adverse effects of film boiling. As the liquid is propelled onto the surface, nucleate boiling removes heat from the surface. If the heat flux is too high and the heat is not removed at a suitable rate, due to the jet impingement occurring at a low velocity, then a liquid film can form on the surface and film boiling can occur. This can result in high surface temperatures which is detrimental to electronics. The results showed potential in higher heat flux applications, with a high critical heat flux of 4.212 MW/m^2. Air atomized spray cooling uses compressed air to break down the vapour film on the surface, moving the partially evaporated droplets before further spraying the surface. Spray cooling is also suitable for high heat flux applications as a method of maintaining a constant surface temperature. Tan et al. (2013) used R134a in a closed loop system with multi-nozzle spray cooling to remove heat fluxes up to 165 W/cm^2 while keeping a constant surface temperature of 48˚C. Panão et al. (2012) investigated the use of intermittent multijet sprays as a means of intelligent electronics cooling for the application in electric vehicles, where power peaks occur in the converters and inverters of the powertrain, which require higher cooling rates during power peaks. The tests were conducted using methanol, with the aim to keep a stable surface temperature of below 125 ˚ C. The intermittent spraying showed an improved result from continuous spraying and showed potential for cooling in applications which show power variations. Tie et al. (2011) investigated jet impingement for the cooling of electronic chips, conducted experiments into the jet diameters and Reynolds numbers, with water as the working fluid. The inlet water temperature was taken to be 20 ˚C and the maximum surface heat flux was measured to be 270 W/cm^2, with an average surface temperature maintained at 75.73 ˚C.

1.1.2. Heat pipes

McGlen et al. (2004) presented the concept of a cooling technique which combined two phase heat transfer and heat pipe technology, with the application of cooling high pack density electronics which is currently limited by the forced air convection method. Heat pipes are a method of transferring heat from one location to an alternative location which can allow for easier dispersion of the heat. The inside of the heat pipe is kept under vacuum, with a working fluid vapourising at the hot end and moving adiabatically to the cooler end. Focusing on the cooling of Therma buses, which are used in the telecoms industry, an experiment was conducted on three different designs with the aim to keep a maximum component temperature of 70 ˚C with an air temperature of 55 ˚C. The materials used within the heat pipes becomes a dominating factor for high heat flux applications where surface imperfections can trap air, creating a layer of insulation. The study aimed to investigate micro heat exchangers, using both single and two phase flow, with the potential to combine with embedded heat pipes.

1.1.3 Phase change materials

An alternative method for thermal management of electronics was presented Kandasamy et al. (2007), phase change materials. Phase change materials are suggested as a transient cooling method for personal computers, as opposed to the conventional air cooling. Phase change materials store heat, which is removed from the heat source, during the melting phase and released during the freezing phase. The study concluded that a better understanding of phase change materials has resulted in smaller packages being produced which can be used for cooling applications. This is in agreement with a previous study by Tan et al. (2004) who conducted experiments using phase change materials to cool personal digital assistants, maintaining the chip temperature at 50 ˚ C for 2 hours of transient use. The work focused on the orientation of the phase change material package, which was shown to affect the temperature distribution. A larger quantity of phase change material was seen to increase the length of time that the chip temperature was stable, but this increased the size of the package which is limited for personal computing.

1.1.4. Comparison of various techniques

Ebadian et al. (2011) reviewed the current technologies which are being developed for heat removal of high heat flux applications, considering both single and two phase flow heat transfer. The techniques evaluated included jet impingement, sprays, wettability effects, piezoelectrically driven droplets and microchannels, with applications in both commercial and defence electronics cooling. Wettability effects refer to controlling the interaction between the surface and bubble formation, based on the surface tension dominating in the micro scale. This interaction, usually referring to the contact angle, can be used to control the heat transfer and pressure drop in pool boiling. This review categorised high heat fluxes to be those between 10^2-10^3 W/cm^2, with heat fluxes between 10^3-10^4 W/cm^2 being ultra-high heat fluxes and heat fluxes greater than 10^4 W/cm^2 to be extreme heat fluxes. A comparison of the five suggested cooling methods, from literature focused on the high and ultra-high heat flux range, see figure 1.1. There are large discrepancies between the highest heat fluxes achieved but jet impingement is seen to give the best cooling, followed by microchanels.

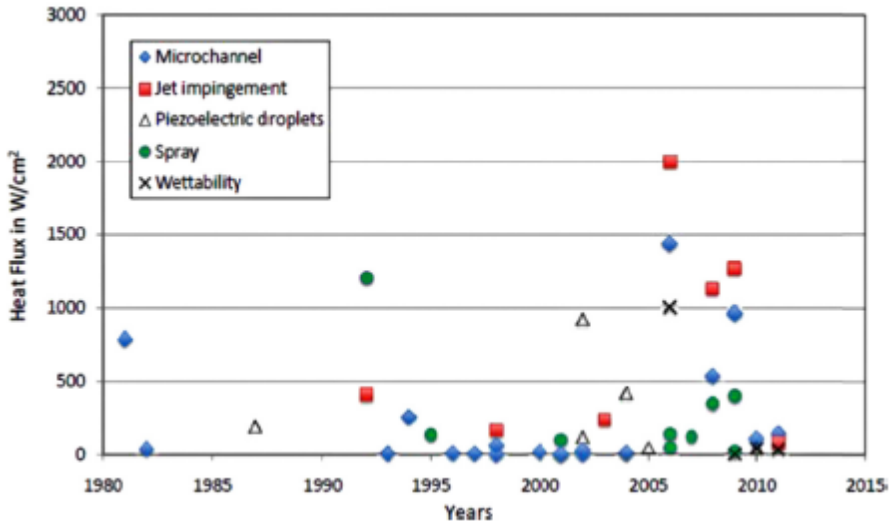

Figure 1.1. Maximum heat fluxes reported in literature across the years, Ebadian et al. (2011)

Although jet impingement is shows to have the highest rate of heat flux removal, this process is not necessarily suitable for electronics cooling. The high density jet array required to maintain very uniform surface temperatures may need large changes to the hardware which may be impractical. From this, the most practical cooling technique for high heat flux removal and ease of implementation, is microchannels.

1.2 Overview of microchannel heat exchangers

Two phase flow boiling has been under investigation in many industries as a method of cooling high heat flux devices. As the size of new technology components decreases and the applied heat fluxes increase, the thermal management of these systems is under question. The miniaturisation of these systems is environmentally beneficial, with a reduction in the materials, including refrigerants, and improved efficiency with higher coefficients of performance (COP). This consequently results in reduced weight and costs which is attractive for industrial applications. Reduced channel diameter provides a higher volume to surface area ratio which allows for larger heat and mass transfer rates (Kandlikar, 2012). A review by Kandlikar (2012) stated that research into flow boiling has developed since 1981, although mainly since 1991, from the fundamental issues of flow boiling into the study of flow patterns, difference in adiabatic and diabatic flow and modelling. Although there is a large amount of research in this field, there are still many unanswered questions and discrepancies. One of which is the stability of the flow, an issue which is widely reported in literature and a limitation on the industrial application of flow boiling (Balasubramanian et al. 2013). Other limitations into the application of flow boiling include gaps in the understanding, including why there are discrepancies in data between labs using the same working fluid and experimental conditions, which results in limited applicability of prediction methods. These issues are especially true for applications in electronics cooling where a constant chip temperature is preferred and temperature spikes and hot spots will damage the chip. Single phase flow can result in changing surface temperature along the flow direction which can be a problem. In two phase flow the resulting heat transfer coefficient and hence surface temperature will depend on flow patterns.

Flow boiling has long been used for cooling applications, for example, in nuclear and chemical reactors, in conventional sized channels but now the growing demand is for small diameter heat exchangers. Single phase flow is widely used in both large and small diameter tubes, without added complications from the reduction in the channel diameter, but the heat fluxes for which this can be used are considerably lower than that of two phase flow. Heat transfer and pressure drop in single phase flow can be more easily predicted, which is beneficial for heat exchanger design. The application of microchannels for two phase flow brings in new questions and uncertainties about flow behaviour and the consequent heat transfer coefficients and pressure drops. The

reduction in the channel diameter can result in the bubbles becoming confined within the channel, a phenomenon which was not previously seen with larger diameter two phase heat exchangers. Although there is a large amount of research into two phase flow in microchannels, both experimental and simulations (Szczukiewicz et al. 2014), there are still unknowns, namely that of the effect of changing thermophysical properties and surface characteristics.

The original working fluid which is still widely used is water. Refrigerants were then introduced to allow for a wider range of experimental conditions, for example, those above and below the boiling and freezing points. There are a large number of refrigerants which have been tailored to suit specific requirements, ranging from those used for cryogenics to those used for high temperature and pressure applications. Refrigerants can be categorised in many forms, from those which are based on the toxicity of the chemicals, to the pressure at a set temperature and to those based on the global warming potential (GWP) and ozone depletion potential (ODP). The Montreal Protocol was an international agreement which was put in place to stop the damage to the ozone layer. All EU member states are required to follow the EC ozone regulations. These regulations define which refrigerants are currently banned, including HCFC's, and which refrigerants are due to be phased out based on the ODP. These restrictions have resulted in the need for new generation refrigerants to replace those which are being removed. Due to this, research into replacement refrigerants is growing in popularity. This is seen for R134a which is widely used in industry and domestic appliances. The phase out of R134a within the automotive industry is already taking place, in favour or more environmentally friendly alternatives (Bobbo, et al. 2014.) There are two main types of refrigerants for consideration, natural and synthetic, although refrigerant blends can also be used. Natural refrigerants include CO_2, water, air, ammonia and hydrocarbons and are not harmful to the ozone but cannot be modified to suit experimental parameters. Synthetic refrigerants have higher GWP and ODP than natural refrigerants but can offer better thermal and system efficiencies.

Flow boiling in microchannels show differing dominant forces to those seen in conventional sized channels, namely that of surface tension (Yang et al. 2014). The ability to design a working fluid which has a favourable surface tension is desirable for two phase applications. It has been widely shown that changes in the fluid properties have an effect on the flow patterns, heat transfer rates and pressure drops. Correlations used for predicting the flow behaviour generally use dimensionless parameters which are based on the fluid properties, and hence should account for changes in the working

fluid. However, these correlations are generally based on a small experimental database and do not account for the true changes seen. Further work in new generation refrigerants is required to be able to accurately predict the flow behaviour and the effect of the property changes in the working fluid.

Surface characteristics are widely regarded to be important in pool boiling but can be overlooked in flow boiling. A nucleation site or surface flaw is required for the onset of nucleation to occur and so surface characteristics are an important consideration. The neglect of surface characteristics was noted to be a possible reason for discrepancies in published data (Karayiannis et al. 2012) and for differences seen in simulated and experimental work. The biggest obstacle in defining a heater surface is that there is no clear method of defining surface characteristics. There are multiple techniques available for scanning a surface, with a range of outputs, including 1D to 3D data profiles and a variety of surface parameters. Surface topography methodology includes both contact and contactless techniques, each with its own merits. The issue related to these surface parameter readings is that the same surface, measured using the same technique, can give various readings between laboratories. This is partly due to the many variables involved in surface scans and partly due to the vast number of post processing techniques which can be employed. Not only is there an issue with surface definition, the effect of surface characteristics is still in question. Research conducted by Mahmoud and Karayiannis (2012) into surface characteristics found that the heat transfer coefficients were dramatically different depending on how the test section had been manufactured, comparing welded and cold drawn seamless tubes. Experimental studies in literature rarely include details of the surface characteristics of the test sections which inhibit direct comparisons. The surface profile of a test section will be affected by both the manufacturing process and the material. A study by Zou and Jones (2013) concluded that difference in the heat transfer coefficient seen between different test sections was due to the different thermal conductivities of the materials. There is no conclusive result on the effect of the surface characteristics and the test section material. These are considerations which need to be evaluated for future correlations.

As discussed above, there are still many questions which are unanswered in flow boiling and require further research. The dominant heat transfer mechanisms in flow boiling are still being debated, with some researchers stating that convective boiling is dominant and other that nucleate boiling dominants. Flow instabilities have been widely reported in literature but the cause and method of prevention are still being investigated.

Instabilities are important for multichannel systems, where confined bubbles can block the channel and cause flow reversal and uneven flow distribution.

1.3 Applications of micro heat exchangers

Compact heat exchangers, which utilise microchannels, can be applied for both heating and cooling applications, with both applications suffering from similar limitations. One of the advantages to these systems is the increased heat transfer area density due to the small hydraulic diameter of the channels. Compact heat exchangers can use either serpentine single channels to increase the surface area or parallel channels. Flow maldistribution is an issue in parallel channels, where the amount of liquid flowing into the individual channels is not even. In the case of flow boiling, this is caused by the bubble diameter reaching that of the channel diameter, a phenomena which is not seen in large diameter systems, which results in reversed flow. As the flow is reversed and re-enters the inlet manifold, the flow is unevenly distributed, with this occurring periodically in the channels (Tuo et al. 2013). As a result of the channel flow being blocked, the heat is not removed from the channel surface which can cause dryout and surface hotspots which can be damaging. Compact microchannels used for cryogenic applications, commonly used for liquefied natural gas storage, also suffer from flow maldistrubtuion.

Compact heat exchangers have the potential for energy saving and improved efficiency for the acquisition of natural gas (Baek et al. 2011). The current process of pumping natural gas from offshore locations to an onshore processing plant requires large amounts of energy and resources, resulting in remote locations not necessarily being cost efficient. A compact heat exchanger which can be placed on a floating platform would allow for the natural gas to be liquefied at the location of the gas well and be directly transferred to a transfer ship. This process would reduce the energy and cost of natural gas production. Xu et al. (2014) noted that the liquefied natural gas is often converted back into gaseous form for use and therefore the heat exchangers used in both phases are of interest. The study included an experimental investigation into the heat transfer characteristics during flow boiling of liquefied natural gas for industrial applications. Other energy applications which can utilise microchannel heat exchangers include hydrogen fuel cells. Ahn et al. (2014) investigated micro reactors as an alternative to conventional reactors for the production of hydrogen from the processing of liquefied natural gas. The micro reactors are constructed from parallel microchannels

being etched onto the reactor surface. These micro reactors were seen to convert a higher percentage of liquefied natural gas at the same operating temperatures as the conventional reactors which are currently used. Kolb et al. (2013) conducted research into the use of microchannels for fuel processors which can be used as a source of hydrogen from fossil fuels. The proposed system of microchannel reactors is a compact design which would allow for the use of hydrogen production in mobile applications. Odabaee et al. (2013) conducted an experimental study into the use of metal foam heat exchangers as an alternative to the air-cooled fuel cell stacks which are currently used which reduces the pumping power required. The current system employ a microchannel heat exchanger which uses either air or water to cool each individual fuel cell to maintain the operational temperature.

The reduction in size of everyday technology has required more complex systems for thermal management. One example of this is the cooling of data centres, which is widely done with air cooling. Data centres are generally air cooled through multiple air conditioning units which is estimated to annually cost 3.6 million US dollars worldwide (Joshi et al. 2012). It is also estimated that between 40 and 45% of the electricity used for data centres is used for cooling devices, dissipating between 5 – 15 kW. Due to the large costs involved in maintaining data centres, there is interest in alternative thermal management systems which will be reliable, cheaper and greener. Joshi et al. (2012) identified four suitable technologies as alternatives for cooling data chips: microchannel single phase flow, porous media flow, jet impingement and microchannel two phase flow. The only one of which is not negatively rated due to the high pumping power requirements for the required temperature gradient is microchannel two phase flow. It is noted that this method is highly complex but has the potential for greener chip cooling. This study also considered the use of waste heat recovery using micro heat exchangers to further reduce the CO_2 consumption. Microchannels have many benefits for computer chip cooling, namely that the extremely small volume make for easy integration into the electronics systems but there are also challenges into the application of this technology. The large pressure drops reported in microchannels requires an increased pumping power and there are issues with nonuniform temperatures, coolant leaks and fluid maldistribution. Microchannels can be utilised in various formats to suit different needs. Wei et a. (2002) and Koo et al. (2002) investigated the use of 3D stacked architecture, where parallel channels are fabricated onto a surface which is then bonded to further layers of parallel channels, which can be attached to a chip. Koo et al. (2002) found that with a maximum temperature of 85 ˚C, a 3D stacked microchannel

array can remove heat flux densities of 135 W/cm^2, with single phase flow. Higher heat fluxes were removed by Hirshfield et al. (2006), with values up to 1500 W/cm^2 with single phase water, but with a large pressure drop of 3.75 bar which would result in a large pumping power requirement. Further research in this field suggests that the use of pin fins could increase the maximum heat flux removed. Lee and Mudawar (2009) conducted experiments for using two phase microchannel cooling for the thermal management of defence electronics. The study investigated both direct and indirect cooling systems. For direct cooling, the refrigerant is used to cool the electronics directly but for indirect cooling, the refrigerant is used in a secondary fluid loop to cool the primary fluid. For the direct system, R134a is used in a microchannel heat sink as an evaporator, HFE7100 is used for the indirect cooling of the heat sink. The indirect cooling was deemed to be better suited due to the higher critical heat flux values but a large heat transfer coefficient was achieved with the direct cooling using microchannels.

1.4 Research objectives

There are two main objectives to this research, (i) to investigate R245fa, a new generation refrigerant and (ii) to investigate the effect of surface characteristics. R245fa will be studied in a comparison with R134a data to evaluate the effects of changes in the thermophyscial properties. This data will be recorded using the same stainless steel test section, of 1.1 mm in internal diameter and length of 300 mm, used in the R134a study, to negate the effect of surface characteristics. R134a is a high pressure refrigerant which is widely used in both domestic and industrial applications. R245fa is a low pressure refrigerant which is also used in industrial chillers and organic Rankine cycles, as with R134a. Due to the differences in pressure, the refrigerants are compared based on the two saturation temperatures, over a range of mass and heat fluxes. Commonly used dimensional parameters, including superficial velocities and mass flux, and dimensionless parameters, including Weber number, which are used for predicting flow boiling results are property dependent and will therefore vary between the two refrigerants. Experiments with both refrigerants will allow for these parameters to be evaluated for flow boiling prediction.

The second part of this work is based on an investigation into the effect of surface characteristics with further test sections constructed of copper and brass. These materials were chosen as they are often used in the construction of heat exchangers and show different material properties, including thermal conductivity. The test sections are

all manufactured in the same process, seamless cold drawn, so that any differences seen are due to the material alone. In pool boiling, the average surface roughness, Ra, is often used to define the heating surface which was carried over into flow boiling. Although the suitability of this parameter has been bought into question as different surface structures can have the same average roughness value (Kandlikar and Speisman, 1997). There is no clear definition in literature, for either pool boiling or flow boiling, on what is a suitable surface parameter to define a heater surface.

The performance of the refrigerants and channel material are evaluated based on the heat transfer coefficient, pressure drop and flow patterns. The heat transfer coefficient is calculated based on the recorded wall temperatures and applied heat flux. The pressure drop is measured using pressure transducers at the inlet and the outlet of the test section. The flow patterns are recorded simultaneously at the exit of the test section to the heat transfer data so that comparisons can be drawn between the flow patterns and heat transfer trends.

A full background and literature review is presented in Chapter 2. Chapter 3 presents the experimental methodology and uncertainties for all of the data and demonstrates how the heat transfer coefficient and two phase pressure drop is determined. The three test sections were examined using two contactless techniques and those techniques are compared, with the results presented in Chapter 4. The flow patterns for the R245fa data and for the three materials are presented in Chapter 5, as well as a comparison of the experimental data with flow pattern maps from literature. Chapter 6 presents the heat transfer coefficient data for R245fa compared with R134a and for the three test sections. This comparison includes the effect of hysteresis on the heat transfer magnitude and trend. Chaper 7 presents the heat transfer correlations from literature were used for a comparison with the experimental data based on the mean absolute percentage error (MAE) and the amount of data which was predicted with ± 30%, β. Pressure drop correlations were evaluated based on the same parameters, which are presented in Chapter 8. Chapter 9 presents the conclusions of this work and recommendations for future research in this field.

Chapter 2

2. Literature review

2.1 Introduction

The application of microchannels spans multiple industries and applications, with new technology being developed on a continuous basis. These applications include automotive, aerospace, chemical reactors, heat pipes, cryosurgery, electronics cooling, and medicine among others (Ohadi et al. 2013). Offshore facilities benefit from miniaturisation due to the low available space and high energy demands. These applications include the improvement of systems which currently use conventional sized channels and new applications which have become apparent with the reduction in channel size. One application for this channel size reduction is in new generation chillers. The main design considerations are the size and cost of the units. Previous improvements in the system included improving the efficiency of individual units, such as the compressor, which would often increase both the size and cost. An alternative to this is to use micro heat exchangers which are commonly used in the automotive industry. The potential application for this is to use microscale technology for the condenser coil design within chillers. Multiple advantages were noted for the use of micro coil design as opposed to the tradition coil design, including thermal performance and a reduction in size. The production and use of chemicals often results in environmentally damaging by-products. Lerou et al. (2010) noted that this damaging effect can be reduced by process intensification with the use of microchannel technology. This allows for enhancement in the heat and mass transfer of chemical reactions. This study concluded that the use of microchannels process technology will be required in the future to meet the 'green' demands of chemical processing. A later study also evaluated the applications of micro channels for use in micro technologies for chemical processes (Bajus, 2012). Decreasing the size of these systems allows for a shorter response time due to the high surface to volume ratios. The reduced volume required is an advantage when using hazardous materials. Future plans for miniaturisation of technology for chemical processing include replacing large plants with smaller plants which allows for a more dynamic production which can respond to supply and demand as required, producing a more sustainable development. Further

development and research is required to fully understand the effects of reducing the diameter, with contradictions in literature the true extent of these effects. Some literature states that there are new phenomena which occur only in small diameter tubes or passages which cause large discrepancies between modelled flow and experimental results. A study by Kandlikar et al. (2003) investigated the evolution of microchannel technology and the thermohydraulic performance of this technology. This study concluded that the smaller channel dimensions allows for a higher heat transfer coefficient due to the larger surface area per volume flow. According to Kandlikar et al. (2003), this is only true for two phase flow with no improvement seen for single phase flow. The smaller diameter shows improvement in the heat transfer but other complications, including the surface roughness effects, are magnified. The effects of surface tension are also magnified, effecting the interaction between liquid and vapour phase. There are many advantages to the use of micro technology but these will only become applicable when the cost of this technology is comparable to that of larger systems. A large part of this is the fabrication of the new equipment and the associated manufacturing methods, which may be complicated and hence costly.

In summary, microchannel technology has the potential to improve the efficiency and environmental impact of current conventional systems. The technology can improve the two phase heat transfer coefficient of heat exchangers which can be used in a wide variety of industrial applications. However, there are limitations to these advancements, due to the conflicting results on the effect of miniaturization.

2.2 Macro to micro scale

The study of flow boiling is mostly focused on the flow patterns, heat transfer coefficient and pressure in the channels. These studies are further segregated based on the channel diameter, from macro to small and micro channels. As the channel size decreases, boiling behaviour changes as the magnitude of the dominant forces change. (Kandlikar, 2010). It is important to understand the transition at which these changes occur to understand the flow boiling process. There are multiple methods used to define the transition diameters, some based on the diameter alone and others using the fluid properties. Those based on the diameter alone benefit from simplicity and ease of use as they can be applied across a range of test fluids. The idea behind the use of fluid properties to define the transition diameters is based on effects which are only evident when the channel diameter is decreased. This includes bubble confinement, not evident in larger channel diameters. As bubble dynamics are fluid dependent, the fluid

properties can be considered to affect bubble confinement. An example of a diameter based system is that of Kandlikar and Gradne (2004), which also includes transitional diameters;

Conventional channels: Dh ≥ 3 mm

Minichannels: 200 μm ≤ Dh < 3 mm

Microchannels: 10 μm ≤ Dh < 200 μm

Transitional Channels: 0.1 μm < Dh < 10 μm

Transitional Microchannels: 1 μm < Dh ≤ 10 μm

Transitional Nanochannels: 0.1 μm < Dh ≤ 1 μm

Molecular Nanochannels: Dh ≤ 0.1 μm

An alternative method is to use non-dimensional parameters to define the size of the channel. The Eötvös number, Eö, was proposed by Brauner et al. (1992), defined below, after conducting an investigation into flow transitions for a single channel. The flow pattern transition for small diameter tubes was found to be when Eö < unity.

$$E\ddot{o} = \frac{g(\rho_L - \rho_G)d_i^2}{\sigma} \tag{2.1}$$

Other non-dimensional parameters have been used in the definition of channel size. The confinement number, Co, suggested by Kew and Cornwell (1997), can be used to calculate the transitional diameter between macro and micro scale based on the fluid properties, see equation 2.2. Note that this is the square root of the inverse Eötvös number. The heat transfer and flow characteristics were seen to change from that of macro channels to micro channels at Co = 0.5. A confinement number greater than 0.5 is considered micro scale. R245fa flowing in a 1.1 mm internal diameter tube at a saturated temperature of 31 ºC has a confinement number of 0.9, and R134a has a confinement number of 0.7 at the same conditions.

$$Co = \left(\frac{\sigma}{g(\rho_L - \rho_G)d_i^2}\right)^{0.5} \tag{2.2}$$

A study by Harirchian and Garimella (2010) concluded that the channel diameter and fluid properties were not enough to define the transition alone but the mass flux must also be considered. Experiments were conducted using FC-77 in twelve

rectangular microchannels of varying hydraulic diameters over a mass flux range of 225 to 1420 kg/m^{2}s. The bubble diameter, and hence the occurrence of confinement, was dependent on the mass flux. The occurrence of bubble confinement was plotted as a function of the Reynolds number and Bond number, see figure 2.1

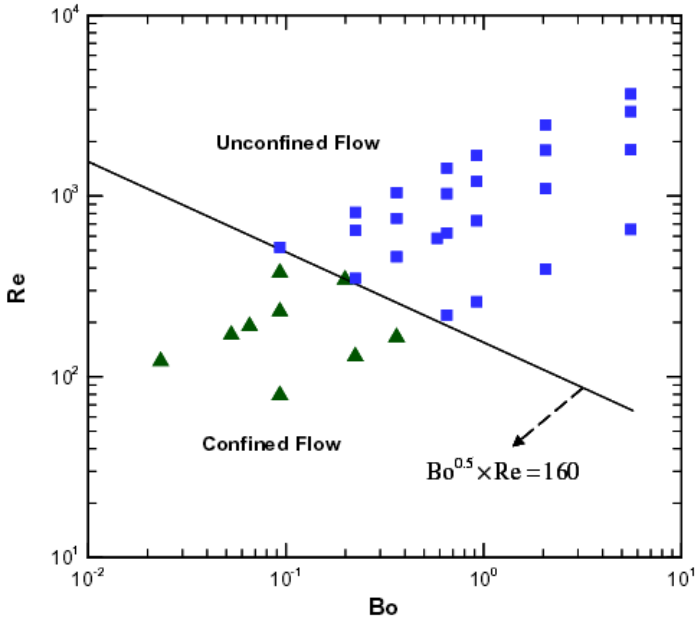

Figure 2.1. Transition from confined to unconfined flow as a function of Reynolds number and Bond number, (Harirchian and Garimella, 2010).

As figure 2.1 shows, there is a clear line at which the flow transitions from being confined to unconfined. The equation for this line is therefore based on the parameters of the Reynolds number and Bond number. From equation 2.3, it can be noted that these parameters include the channel diameter, fluid properties and the mass flux.

$$Bo^{0.5} x\ Re_L = \frac{1}{\mu_f}\left(\frac{g(\rho_f - \rho_g)}{\sigma}\right)^{0.5} GD^2 = 160 \qquad (2.3)$$

Harirchian and Garimella (2010) concluded that this criterion showed promise for flow pattern prediction, based on a comparison with data from literature for water, dielectric liquids, FC-72 and R134a, across a range of channel diameters and mass fluxes. Li and Wu (2010) also concluded that the Bond number and Reynolds number should be used for defining the transition from macro to micro channel. The transition value is higher than that of Harirchian and Garimella (2010), where values less than 200 are considered micro scale.

$$Bo\ x\ Re_L^{0.5} = 200 \qquad (2.4)$$

Many of these proposed criterions are limited to defining whether the flow is confined or unconfined but do not offer any further definition. There is currently no universal method for channel classification but varies from author to author and therefore there is no set definition for micro channels which can hinder comparisons between data.

2.3 Flow patterns

Flow patterns are an important factor in both the heat transfer and pressure drop within channels. They are an important part of heat exchanger design and the ability to predict them reduces the cost and time required for experiments. Good knowledge of flow patterns is needed to accurately design for system requirements. Flow patterns are a method of defining the interaction between the liquid and vapour phases in the flow. The method of applying these definitions is variable which reduces the ability to accurately compare between flow pattern data. The flow patterns will depend on many variables, including channel diameter and working fluid.

The definition and categorisation of flow patterns is open to interpretation, with a large range of flow pattern terminology used in literature. Chen et al. (2006) studied the effect of tube diameter on flow patterns using R134a in 1.1, 2.01, 2.88 and 4.26 mm diameter tubes. This study defined flow patterns of dispersed bubble, bubbly, confined bubble, slug, churn, annular and mist flow. The flow patterns evident were dependent on the channel diameter. The confined flow, only seen for smaller diameter channels, is a point of contention, with some researchers referring to this as slug flow. The difference between confined flow and slug flow is the shape of the bubble tail. Confined flow has a rounded end as opposed to slug flow which has a disturbed end and can have a trial of bubbles. Many of the flow patterns in literature use a variation of these definitions, although often less detailed. For example, Mishimi and Hibiki (1996) uses bubbly, slug, churn and annular flow. An alternative method of flow pattern categorisation was presented by Revellin and Thome (2007) who produced a flow pattern map based on the transitions from isolated bubble to confined bubble and confined bubble to annular flow. This model was updated to include further refrigerants with an additional flow regime of slug-plug (Ong and Thome, 2009). Harirchain et al. (2012) defined the flow regimes as confined slug, churn/confined annular, bubbly, churn/wispy-annular and churn/annular. The different flow pattern definitions seen in literature results in poor agreement between researchers which hinders the understanding of bubble dynamics.

2.3.1 Flow patterns in microchannels

Many studies have shown that flow patterns change with a reduction in channel diameter (Zhang et al. (2011), Saisorn et al. (2010)). Flow patterns, which were not evident in larger diameter channels, become apparent with smaller channel diameters. This is partly due to the bubble becoming confined, a phenomena which is only applicable in small diameters. As previously discussed, the diameter at which the bubble will become confined can be considered to be fluid dependent. The dominating forces within the channel are also seen to change with diameter. This can be shown by considering the forces acting on a bubble.

Surface tension is a complex variable, where the effects will depend on many other variables, including channel diameter. Surface tension is a force which acts on the surface of a liquid to repel external forces. The water molecules are attracted to each other, those molecules on the surface do not have water molecules to bond with, this forms a 'film' (Breithaupt, 2000). This surface 'film' resists the motion of an object in an opposing direction; in this case, the flow resists the surface of the channel. This force is balanced by inertia and buoyancy forces, figure 2.2. The buoyancy force is calculated from the gravity, density change and area. It is the ratio of these forces which contribute towards defining the flow patterns.

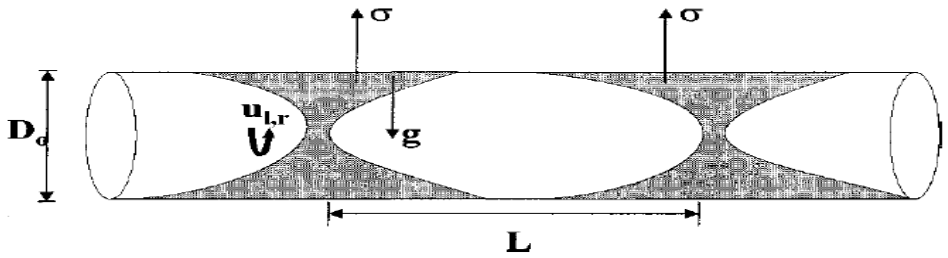

Figure 2.2. Balance of forces for a given length of flow, Tabatabai et al (2001)

In larger channels, the effects of surface tension is small as the surface 'film' is negligible in comparison to the bulk volume of the flow. Due to the buoyancy (gravity) forces, the balance of surface tension will not only differ for that of vertical over horizontal flow but also based on whether the flow is opposing gravity. The importance of surface tension is evident by its presence in many of the dimensionless groups, including the Bond number, Weber number, Eotvös number and capillary number. It has also been regarded that those flow models which neglect the effect of surface tension can not accurately predict flow transition boundaries (Biswas et al. 1985).

A bubble forms over a cavity or nucleation site, this gives the bubble radius (r_b). The growth of this bubble will depend on the pressure inside the bubble (P_v) and the pressure of the surrounding liquid (P_l). The relationship, given by Kandlikar (2006), shows that the excess pressure is a ratio of surface tension and bubble radius.

$$P_v - P_l = \frac{2\sigma}{r_b} \tag{2.5}$$

Equation 2.5 gives further weight to the argument that surface tension impacts the heat transfer mechanisms and flow patterns. Kandlikar (2004) investigated the heat transfer mechanisms in flow boiling for microchannels. Figure 2.3 shows how the bubble on the surface of a heated surface is acted upon by both the surface tension (F'_S) and the change in momentum caused by evapouration force per unit length (F'_M), presented in equations 2.6 and 2.7.

$$F'_S = \sigma \cos \vartheta \tag{2.6}$$

$$F'_M = \left(\frac{q}{h_{fg}}\right)^2 \frac{D}{\rho_g} \tag{2.7}$$

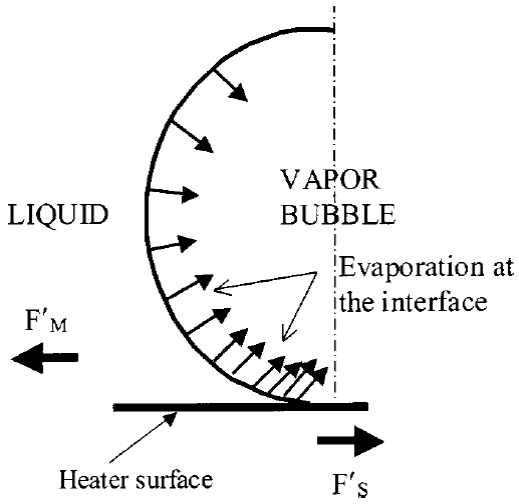

Figure 2.3. A symmetrical vapour bubble growing on a heater surface (Kandlikar, 2004**)**

The balance of these forces relate to whether the bubble departs from the heated surface and consequently how the heat is transferred. Kandlikar (2004) states that this force balance changes during evaporation which governs the two-phase structure during flow boiling and the heat transfer characteristics.

It was from this research that a new dimensionless group (equation 2.8) was presented which represents the ratio of the evaporation momentum force and the surface

tension force. The evaporation momentum force is evaluated using the heat flux (q), latent heat of vaporization (h_{fg}), characteristics dimension (D) and density (ρ).

$$K_2 = \frac{\left(\frac{q}{h_{fg}}\right)^2 \frac{D}{\rho_g}}{\sigma} = \left(\frac{q}{h_{fg}}\right)^2 \frac{D}{\rho_g \sigma} \qquad (2.8)$$

This dimensionless group is not suitable for a full evaulation as the contact angle is neglected. However it is suitable for less complex experiments. This ratio is based on the inertia at the contact point between the bubble and the heater surface. A high evaporation momentum force at the interface is required to overcome the surface tension and for the bubble to depart from the surface. This study did present an unexpected result as the viscous forces were shown to become more dominant than that of surface tension as the channel diameter decreased. This agrees with the work of Cho et al. (2011) who stated that the viscous and surface tension forces are more important compared to inertia forces in small channel diameters. Research by Mukherjee and Kandlikar (2006) into surface tension consisted of numerically studying the growth of vapour bubbles within microchannels, with a constant contact angle of 40˚ but varying the surface tension. This work concluded that the surface tension had little affect on bubble growth but did affect the bubble shape, with a lower surface tension resulting in longer and thinner bubbles. This work also commented on other research (Lee et al, 2004) which found that the departure radius of the bubble from the heater surface was largely influenced by the surface tension. This paper also highlighted the effects of the surface tension forcing the bubble to be spherical. In small diameter channels, this effect of surface tension causes the bubble to grow laterally once the bubble is confined, as the surface tension decreases, the bubble becomes slightly narrower and longer.

The common agreement from researchers (Biswas (1985), Tripelett et al (1999), Akbar et al (2003)) is that surface tension is dominant within microchannels resulting in a lack of smooth stratified flow . As stated by Barnea (1983) and Tripelett et al. (1999), the flow regime transitions from stratified to slug is due to the dominance of surface tension. This is often seen within microchannels where there is no smooth stratified flow and a very short, if any, stratified wavy region. Tabatabi et al. (2001) worked on producing a new flow map which fully compenstated for the effect that surface tension has on the flow regime transitions. This study commented on the work by Barnea et al. (1983) which concluded that the dominance of slug flow, and lack of stratified flow was due to the surface tension forces raising the liquid up the channel which reduces the liquid within a vicinity and encourages the slug formation. Akbar et al. (2003) stated

that the stratified flow region was not apparent due to the surface tension dominanting over the bouyancy effect. This research also went on to conclude that the surface tension played a significant role in the flow regimes and their transitions. Akbar et al. (2003) commented on the work of Zhao and Rezkallah (1993) who stated that the flow regime map can be divided into three zones:

1. Surface tension is dominant; Includes bubbly, slug and plug flow.
2. Inertia is signigficanlty larger than surface tension, annular flow.
3. Inertia and surface tension forces are comparable, this is the transition zones.

Using this three zone flow regime, correlations were produced for each of the three zones to predict the flow regime transitions based on the Weber number. The Weber number is a function of the surface tension which contributes to the arguement that surface tension is a factor in flow patterns. This conclusion was also made by Niño et al (2002) i.e. that surface tension was a defining factor in flow regime transitions, especially when referring to smaller diameter channels. This study analysed the pressure drop characteristics to see the effect of surface tension. For small diameter channels, the dominating surface tension promoted annular or intermittent flow. Intermittent flow includes elongated bubbly, slug and wavy annular flow. This was also found by Triplett et al. (1999) and (Kandlikar et al, 2004a), i.e. that churn and annular flow was present over an extensive range when using smaller diameter channels.

Surface tension is an unusual variable as there is not necessarily an optimum value; it is not possible to say whether all experiments would want high or low surface tension as it depends on so many other factors and the experimental parameters. The surface tension effects the formation and coalescence of bubbles which will in turn affect the heat transfer mechanisms. A lower surface tension reduces the coalescence of bubbles, with bubble coalescence having a negative impact within microchannels due to confinement and reversed flow. Therefore, for the use within microchannels, the surface tension should be low (Chen, 2006).

An experimental study by Yin et al. (2014) looked at bubble confinement and elongation in microchannels using di-ionised water in rectangular channels. Bubble confinement and elongation were investigated for a range of inlet sub-cooling, mass flux and heat flux conditions. The results showed that depending on the mass flux, there was a limit of heat flux beyond which bubbles would become confined. At heat fluxes lower than this limit, the bubbles would depart before becoming confined, i.e. bubbly flow. At heat fluxes above this limit, bubbles became confined, although there was also an upper limit at which annular flow occurred, thus reducing the occurrence of bubbly

flow, due to an increased number of nucleation sites and rapid bubble coalescence. As the inlet sub-cooling was increased, the heat flux limit increased and delayed the occurrence of bubble confinement. This was also seen with an increase in the mass flux.

Figure 2.4 presents the typical bubble confinement and elongation seen. As seen in the figure, as the bubble grows to the diameter of the channel, bubble becomes elongated longitudinally where it is not confined. The bubble elongates in the direction of flow. This study concluded that the heat transfer mechanism in microchannels is still unknown due to the lack of understanding of the bubble dynamics in confined channels. Yin et al. (2014) stated that the bubble confinement was also defined on the initial shape of the bubble formed. The shape of the bubble was dependent on where in the channel nucleation began, namely in the corner or the centre of the channel wall. This is attributed to the area of the microlayer under the bubble varying, a larger microlayer base area results in larger bubble growth.

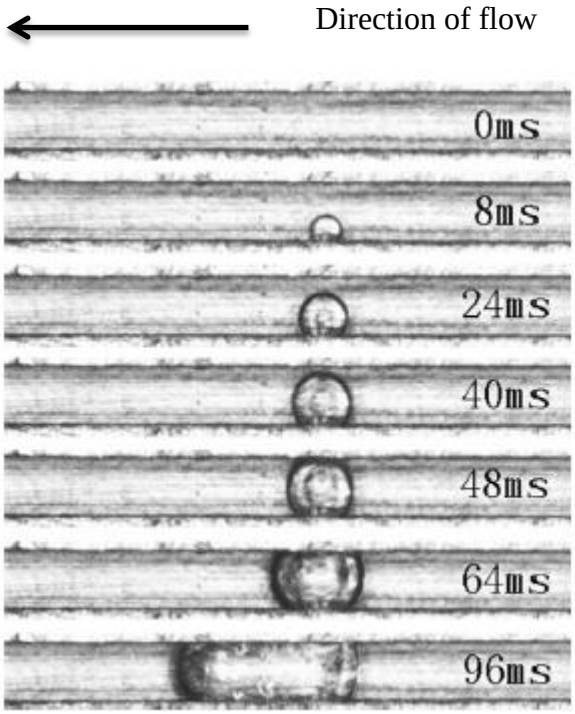

Figure 2.4. Bubble confinement and elongation, Yin et al. (2014).

2.3.2 Factors effecting flow patterns

Other factors, besides the channel diameter, must be considered when investigating flow patterns. One consideration is the working fluid which has an effect on the bubble dynamics. As previously discussed, surface tension is a dominating factor in bubble formation and flow patterns, which will vary between different fluids. Zhuan et al. (2012) numerically investigated flow patterns in microchannels, to evaluate the

important parameters related to bubble behaviour. A decrease in the saturated temperature results in an increase in the surface tension. This increase resulted in a faster expansion of bubbles and coalescence, and shift of the flow pattern transitions into lower vapour qualities. This is also true for changes in the liquid viscosity for certain flow regimes. During annular flow, the film thickness is a function of the liquid viscosity and a decrease in the film thickness results from increasing liquid viscosity (Kawahara et al. (2009)). This is of course important because a thinner liquid film, although beneficial for heat transfer, is more prone to dryout which can be detrimental to heat exchangers.

Mass flux effect

The experimental parameters which will influence flow patterns include the pressure, mass and heat flux. Revellin et al. (2006) investigated flow pattern transitions in microchannels, concluding that the increase in mass flux shifted the transitions to lower vapour qualities. The mass flux will have an effect on the momentum forces acting on the bubble during nucleation and a higher liquid velocity will encourage interactions and potential coalescence between bubbles. Harirchian et al. (2009a) found that an increase in the mass flux resulted in smaller and more elongated bubbles during the bubbly regime and a thinner liquid film during annular flow. The flow transitions were also seen to occur at higher heat fluxes with an increase in mass flux. Celeta et al. (2012) conducted experiments with FC-72 in a single channel of 0.48 mm internal diameter and found that flow transitions shift to the subcooled boiling region with a decrease in the channel diameter. There was little effect on the vapour quality with mass flux. Zhuan et al. (2012) found an increase in the mass flux was seen to reduce the diameter of the bubble as it detaches from the surface but the bubble diameter increased with heat flux at a constant mass flux. The surface tension is negligible after the bubble has detached from the surface but due to the small diameter of the channels and bubble confinement, surface tension was seen to be a dominant factor in bubble coalescence. Although this was only evident during the bubbly and slug regimes as convective boiling dominates in the annular region. The heat flux was seen to influence the location of the bubble departure, which shifted upstream at higher heat fluxes.

Geometry effects

Experimental configurations which were important for macroscale channels which are not a consideration for microchannels include the channel orientation. In larger scale channels, the flow patterns evident varied between vertical and horizontal flow (Gersey et al. 1995). Kandlikar and Balasubramanian (2004) found that as the channel diameter decreased, the effect of the channel orientation became negligible due to the dominance of surface tension over gravity. As the trend is shifting towards smaller diameter channels, channel orientation is no longer widely researched, but other experimental configurations are becoming more important. Further experimental considerations include the number of channels in question, with different flow patterns seen between single and multi-channel configurations. The differences seen between the two configurations are a result of the small channel diameter and bubble confinement. As the bubbles become confined, the vapour slug can grow in both the upstream and downstream directions, resulting in reversed flow into the inlet plenum (Balasubramanian et al. 2013). This flow reversal can cause malidistribution between the channels, resulting in different flow rates between the channels. As a uniform heat flux is applied across the channels, some channels can be showing signs of dryout while others are in the bubbly flow regime. The differences seen between the channels can prevent accurate flow pattern predictions.

Tran et al. (1996) conducted experiments with R12 in both a circular and a rectangular channel, with hydraulic diameter of 2.46 and 2.4 mm, respectively. The results showed very little difference between the heat transfer coefficients. Little effect in the flow pattern transitions, based on the superficial velocities, was reported by Triplett et al. (1998). This was based on flow patterns recorded in circular channels of 1.1 and 1.45 mm internal diameter and triangular channels of 1.09 and 1.49 mm hydraulic diameter.

Hysteresis effect

The effect of hysteresis is often ignored, in both conventional and microscale flow boiling. Bubble formation requires an active nucleation site, with an increasing heat flux, more of these sites can be activated which may remain active as the heat flux is decreased. This may result in changes in the flow pattern, and hence the heat transfer coefficient and pressure drop, of the channel. Microchannels have a smaller surface area

and therefore less potential nucleation sites to be activated. A study by Wang et al. (2012) investigated FC-72 in channels of 571, 762 and 1454 μm hydraulic diameter and aspect ratios of 20 and 10. The occurrence of a temperature overshoot, or incipient hysteresis, was more pronounced for the smaller diameter channels. The effect of hysteresis will only be seen at low heat fluxes, at the onset of nucleation. This is seen in Consolini et al. (2009) who found the majority of the data points were aligned for increasing and decreasing heat flux but a difference was seen for both R134a and R245fa at low heat fluxes. Mahmoud (2011) conducted experiments with R134a in channels of 0.52 and 1.1 mm diameter channels, concluding that the effect of hysteresis was only evident at low heat fluxes near the boiling incipience. Sitar et al (2012) conducted experiments with FC-72 in square parallel microchannels and found that the channel size and roughness influenced the magnitude of the hysteresis effect. Hysteresis was also deemed to be dependent on the working fluid and mass flux. Fu et al. (2013) concluded that the lack of hysteresis seen was due to the rough channel surface and the refrigerant used. Fu et al. (2013) tested multiple concentrations of a water-ethanol mix and found that hysteresis only occurred at certain mixtures. Piasecka et al. (2010) found that the heat transfer coefficient increased when decreasing the heat flux. The inlet pressure was found to have an effect on the surface temperature drop during hysteresis. Other researchers found that there was no effect of hysteresis (Bortolin et al. (2011), Ong et al. (2009)), with the same flow patterns and heat transfer trends occurring for both increasing and decreasing heat flux.

2.3.3 Flow pattern maps and prediction methods

As discussed, flow patterns differ between conventional and micro sized channels, resulting in different flow pattern prediction methods. Flow pattern maps are generally produced based on limited experimental data resulting in maps being specific to channel geometries and refrigerants. Harirchain et al. (2010) conducted experiments using 6 different channel diameters and found that a flow pattern map was required for each diameter in order to accurately predict the flow pattern transitions as flow pattern maps are often based on channel dimensions. This is contrary to the work of Oya (1971) who found that when using superficial velocities, the co-ordinates of flow pattern transitions were only slightly affected by the channel diameter for channels of 2, 3 and 6 mm. Recent work has focused on producing flow pattern maps which account for changes in both the channel dimensions and the refrigerant. The majority of flow maps

are based on non-dimensional numbers, which should account for the changes in thermophysical properties and channel diameter, but this depends on the numbers used. The dimensionless values applied may depend on what parameters are under consideration. Chen (2006) investigated flow patterns across a range of channel diameters and pressures using R134a. The channel diameters ranged from 4.26 to 1.1 mm internal diameter which spans normal to micro sized channels, allowing for an evaluation of both conventional and micro flow pattern maps. This investigation found large differences in flow pattern maps with the reduction in channel diameter. The flow patterns were originally plotted as a function of liquid and gas superficial velocities for the experimental range to investigate the effect of these on the transition boundaries. A comparison of these plots showed that the magnitude of the effect of pressure and channel diameter varied with the transition boundary in question. The transition boundaries from bubbly to slug and dispersed bubble to churn flow remained relatively constant. The remaining transition boundaries were seen to shift with both pressure and channel diameter. This experimental data was further plotted in different coordinate systems to evaluate other groups of parameters which can be used to predict these transition shifts. These other parameters included the widely used dimensionless liquid and gas Weber numbers and Reynolds numbers and the vapour quality and mass flux. Nineteen parameters were used for comparison with varying degrees of success. Some parameters were suitable for changes in channel diameter but not pressure and vice versa, concluding that new semi-empirical correlations could be developed based on this to include the changes for both pressure and channel diameter. The main cause for the discrepancies was thought to be the influence of surface tension being neglected, a parameter which is of more importance with a decreasing channel diameter. Further issues related to flow pattern maps being based on different working fluids, such as air-water, and the orientation of the channels. As previously discussed, there are flow patterns which occur only in horizontal channels, making flow patterns based on horizontal data less applicable for vertical flow. The evaluation of parameters which are important for transitions were used to produce a flow pattern map which would account for these factors. The effect of pressure for the transition of slug, churn and annular flow is predicted using the mass flux and the Lockhart-Martinelli Parameter. The churn to annular transition across the whole experimental range was predicted well using the parameters of liquid and gas Weber numbers and the gaseous Froude number. The Weber number alone was seen to predict the change in channel diameter between slug to churn and churn to annular flow well. The Weber number was also used by Akbar et

al. (2003) for the prediction of flow patterns in channels with less than 1 mm hydraulic diameter.

There are many advantages to using non-dimensional parameters, mainly that the influence of multiple variables can be included. This allows for a range of experimental conditions to be encompassed, including channel diameter and pressures. An alternative to this is to use dimensional parameters which include superficial velocities. The superficial velocity is the most commonly used co-ordinate system for flow pattern maps in literature, being favoured by Hassan et al. (2005), Chen (2006) and Yang and Shieh (2001).

Alternatively, the mass flux and vapour quality are used to define the flow pattern transitions in the work by Revellin and Thome (2007) and Ong and Thome (2009). The flow pattern map produced by Harirchian et al. (2010) uses a combination of boiling number, bond number and Reynolds number. The flow patterns are based on experimental results of 390 data points for FC-77 with channel cross sectional areas from 0.009-2.201 mm^2, a heat flux of 25-380 kW/m^2 and a mass flux range of 225-1420 kg/m^2s. The flow map consists of four main flow patterns; bubbly, confined slug, churn/confined annular and churn/annular wispy-annular. Experimental data from literature, for water and fluorocarbon, also showed good agreement with this proposed map. The parameters used include functions of heat flux, mass flux, enthalpy, channel diameter, density, viscosity and surface tension.

2.3.4 Microchannels and heat transfer

A reduction in channel diameter changes the flow patterns and dominant forces within the flow which in turn has an effect on the heat transfer. A study by Dupont et al. (2005) investigated flow boiling in reducing diameter channels based on a three zone model. This model predicts an increase in heat transfer coefficient with a reduction in channel diameter at low vapour qualities but a decrease in the heat transfer coefficient at higher vapour qualities. The influence of liquid film thickness was thought to be the cause of this effect during slug flow. This model is based on the evaporation of the liquid film surrounding the vapour bubbles dominating the heat transfer at low vapour qualities. The results of this model were compared with experimental data from nine sources in literature, covering a range of refrigerants and channel diameter. This model predicted 67% of the data points within a ± 30% range. An intensive study by Kandlikar et al. (2013) investigated the status and research needs for heat transfer in

microchannels. This study included an in depth look at both the single and two phase flow in microchannels. The two main points of consideration for two phase flow were identified to be the limitations in the lower heat transfer coefficients and critical heat flux. This study reviewed work on flow boiling instabilities and fins, concluding that future research is required in both of these areas for heat transfer enhancement. The advancements in electronics cooling with microchannels were analysed for past and future developments. The research needs in this area were deemed to be in the materials and structures to improve thermal management. Modelling techniques must also be improved to aid in future developments. The main obstacle in these advances is noted to be the manufacture of these devices at a competitive cost. Further limitations include the contradictions in literature of heat transfer behaviour for both laminar and turbulent flow.

2.3.5 Heat transfer mechanisms

There are conflicting conclusions in literature regarding the dominance of nucleate or convective boiling. Wang et al. (2012) conducted an investigation into the effect of channel diameter using FC-72 in channels of 571, 762 and 1454 μm. These experiments were conducted over a range of mass fluxes and heat fluxes. This study showed that the influence of channel diameter was higher at higher mass fluxes. The heat transfer coefficient increased with reducing channel diameter. The dominant heat transfer mechanism was deemed to be convective boiling. Peng a nd Wang (1998) conducted an experimental study of methanol and water, concluding that nucleate boiling is nearly impossible in microchannels. Harirchian and Garimella (2009) concluded that in confined channels, the convective flow is dominant due to the evaporation of the thin liquid film. This is contrary to the work by Bao et al. (2000), Wambsganss et al. (1993) and Lazark and Black (1982) who concluded that nucleate boiling dominates the heat transfer. Similarly, Yu et al. (2002) concluded that nucleate boiling dominates, but only at large mass fluxes and vapour qualities. Lin et al. (1999) found that nucleate boiling dominated in the region of low vapour qualities and convective boiling dominated at higher vapour qualities. This is similar to the Lee et al. (2005) conclusion that nucleate boiling initially dominates, which was seen experimentally to be at vapour qualities less than 0.05, after which convective boiling is the dominant heat transfer mechanism. The contradictory conclusions on the dominant heat transfer mechanism are reflected in the differences seen between the prediction

methods. Chen (1963) proposed a correlation to calculate the total heat transfer as a sum of the single phase and nucleate boiling parameters, with suppression and enhancement factors. This method has been adapted in literature across the years but Sun et al. (2009) concluded that the Chen type correlation was not suitable for microchannels. This study also concluded that the best correlations for microchannels were that of Kew and Cornwell (1997) and Lazark-Black (1982), with a modified Lazark-Black (1982) correlation being presented. The Lazark-Black (1982) correlation is a simple correlation which is based on the experimental conditions and fluid properties, which was adapted by Kew and Cornwell (1997) to include a function of the vapour quality. The Lazarek-Black (1982) correlation does not show a dependence on the vapour quality, suggesting a dominace of nucleate boiling. Shah (1987) presented a correlation where the Boiling number represented the nucleate boiling component and the convective number the convection component. Both these methods have been used in future correlations to represent the convective and nucleate boiling components to various extents. Correlations in literature are also seen to vary in what experimental conditions are seen to be dominant factors, such as the mass flux or heat flux. Tran et al. (1996) conducted experiments with R12 and R113 in brass channels, both circular and rectangular, and found the heat transfer coefficient was independent of vapour quality at $x > 0.2$ and mass flux. The independence of the heat transfer with mass flux and vapour quality was agreed with by Bao et al. (2000), who found the heat transfer to increase with heat flux. Huh and Kim (2007) also concluded that the heat transfer is independent of the mass flux and vapour quality based on experiments with water. Qu and Mudawar (2003) conducted experiments with water in a rectangular channel, finding that the heat transfer coefficient increases with vapour quality. The difference seen between the dominant forces maybe a result of the different experimental parameters used, including channel size, geometry and material and the different working fluids, which is why a greater understanding of these parameters is required.

There is no conclusion in literature of the trend of the heat transfer coefficient with vapour quality or the dominating variables which need to be considered. However, there is a general agreement that the channel diameter does have an effect on the heat transfer coefficient. This is due to the changes in the flow patterns which are directly related to the heat transfer coefficient. There are still gaps in the knowledge, including which heat transfer mechanism is dominant and which experimental variables are functions of the heat transfer rate. These unknowns are a limitation in the development of future technology and miniaturisation.

2.3.6 Microchannels and pressure drop

Wang et al. (2014) investigated degassed FC-72 in rectangular channels with hydraulic diameters of 571, 762 and 1454 μm. The results showed that the total measured pressure drop increased with a decreasing channel diameter. A comparison of the pressure drop fluctuations over a range of mass fluxes showed that the effect of channel diameter was more evident at higher mass fluxes. The pressure drop consists of three main components- gravitational, acceleration and frictional- of which the frictional component was deemed to be the highest for smaller diameter channels (Coleman and Krause 2004, Saitoh et al. 2005). Contrary to this, Kureta et al. (1998) found that the frictional pressure drop is equivalent to the acceleration losses under certain conditions in small diameter channels. This conclusion was based on a comparison of experimental data for water in channels of 2 and 6 mm and prediction methods in literature. With friction being the largest contributor, some research is focused on the evaluation of this parameter alone. Xu et al. (2012) evaluated 29 frictional pressure drop correlations based on 3480 experimental data points covering channel diameters of 0.0695 to 14 mm. The comparison showed varying degrees of success for predicting the pressure drop. It was noted that certain correlations performed well under different experimental conditions but further work was required to adapt these correlations to provide accurate pressure drop predictions across the entire range. Both homogenous and separated flow models were evaluated. Homogenous models assume that the velocity of the flow is equal for both the liquid and vapour phases, as opposed to the separated flow model which treats the liquid and vapour phases as different entities. The two models which were best for the entire range, Muller-Steinhagen and Heck (1986) and Sun and Mishima (2009), are both based on the separated flow model. Zhang et al. (2010) concluded that models based on the separated flow model showed good agreement across the entire data range used. This study focused on both the friction pressure drop and the void fraction correlations for mini channels. An artificial neural network was applied to identify the dominant parameters which influence the correlations. For the application of mini channels, the Laplace constant is a main parameter for the Chisholm constant, C. Alternative correlations, based on this study of parameters, were suggested to improve the accuracy of the frictional pressure drop predictions. These conflicting conclusions regarding the homogenous model and the separated flow model were addressed in Saisorn et al. (2012) who stated that a wider range of experimental

conditions need to be considered to fully evaluate the best prediction method. This is in agreement with the previous work of Huo et al. (2007) who investigated the pressure drop in channels of 4.26 and 2.01 mm using R134a over a range of mass and heat fluxes. The total measured pressure drop was seen to be three times higher for the 2.01 mm tube compared with the 4.26 mm tube. Prediction methods from literature were evaluated, mostly with poor agreement. This is thought to be due to the limited experimental conditions which these pressure drop correlations are based on. Pressure drop correlations are often adapted to include new parameters which are deemed important for pressure drop predictions. The Chisholm constant, C, was adapted by Youguang et al. (2010) to include the influence of aspect ratio and surface tension. Experiments were conducted in rectangular channels of 4 different aspect ratios, with the results showing a one-fold increase in aspect ratio resulted in a pressure drop nearly three times larger for the same conditions. This newly adapted C parameter allowed for improved prediction over the range of channel aspect ratios and working fluids to less than ± 20 %.

The pressure drop increases with a decrease in channel diameter (Wang et al., 2014) and fluid properties, including surface tension, are also a consideration. There are a large number of pressure drop correlations in literature, but these are often based on a small experimental range. This results in contradictions on which correlation is most suitable. For a large experimental range, models based on the separated flow model seem more appropriate for pressure drop prediction but the homogenous model is more accurate for smaller ranges. Therefore, choosing a correlation for pressure drop prediction will depend on the application.

2.4 Refrigerants

2.4.1 Introduction

Refrigerants have been widely used for decades, with the refrigerant composition evolving over time due to the increasing thermodynamic demands and environmental controls. Refrigerants are currently used in heat exchangers of all sizes across a range of industries, including defence and energy sectors. Due to the large number of refrigerant applications, there is a corresponding large range of refrigerants. These refrigerants are designed to work over a range of operating conditions, including very high or very low temperatures and pressures. Further considerations include material compatibility, especially with plastic and rubber seals. The importance of the

refrigerant composition will depend on the application, for example, extremely high pressure and temperature applications will require refrigerants with could not degrade of burn, which will damage the system. This is also true for low temperature applications, such as cryogenics. Although water is widely used for heat transfer applications, it is only suitable for a narrow temperature and pressure range compared with that of refrigerants. Refrigerants have evolved across the years to accommodate new chemical blends and heat transfer demands.

2.4.2 New generation refrigerants

Due to the wide variety available, there are many factors to consider when choosing a suitable refrigerant. The main consideration, which must be known before choosing a refrigerant, is the application. This includes the longevity of the product and the thermodynamic performance required. There are many refrigerants which are due to be phased out in the near future with tightening environmental restrictions. Therefore applications which have a large longevity may need to consider which refrigerants will be available in the future for further system production or repairs. This can be based on the ozone depletion potential (ODP) and the global warming potential (GWP). R11 is used as the base refrigerant, having an ODP value of 1. Carbon dioxide is used as the base for GWP, having a reference value of 1. The lower the values of ODP and GWP, the less harmful the refrigerant is to the environment. CFC's were phased out in 1996 due to their high ODP values (Kirkwood, 1994). Hydrochlorofluorocarbon's (HCFC), such as R22, are on schedule to be phased out from the same Montreal protocol. Although some refrigerants have acceptable ODP and GWP, there are alternatives which lower values and are therefore favoured. Hydrofluorocarbon's (HFC), such as R134a, R152a and R245fa, are currently widely accepted with ODP values of zero and GWP values of less than 1500. These are not currently subject to being phased out but are under consideration for alternatives with lower GWP values. Other alternatives include ammonia and carbon dioxide, which have zero ODP and a GWP of 1, but come with their own safety risks, namely that of toxicity (Da-Wen Sun, 2011). Both R134a and R245fa are HFC's, with GWP's of 1400 and 950 respectively. As of January 2011, refrigerants with a GWP > 150 are prohibited by the EU's mobile air conditioning directive (Minor and Spatz, 2008).There is no one refrigerant which has currently been put forward to replace R134a in all applications. This is partly due to the wide variety of applications which currently use R134a. The process of evaluating the most effective replacement is ongoing and can be country and company dependent. There are currently

three proposed alternatives, R1234yf, R152a and CO_2 for automotive air conditioning (Minjares (2011)). A study by Mohanraj et al. (2008) investigated the most suitable replacement for R134a in domestic refrigeration based on operating conditions required, including the pressure ratio, coefficient of performance and compressor discharge temperatures. This theoretical study concluded that pure hydrocarbons are not suitable alternatives for R134a due to large difference in the volumetric cooling capacity. One of the considerations for a theoretical comparison is the pressure of the refrigerants. R245fa is categorised as a low pressure refrigerant as opposed to R134a which is a high pressure refrigerant. The classification of low, medium and high pressure refrigerants is based on the saturated pressure of the refrigerant at 40 °C. The code of federal regulations (2008) states that a refrigerant is considered to be low pressure if the liquid phase saturation pressure is below 3.1 bar at 40 °C. One of the applications for R134a is centrifugal chillers, which also employ R123. R123 is a low pressure refrigerant which has already been phased out, with R134a being widely used as a replacement. Although R134a is technically a suitable replacement for R123, there are thermodynamic efficiency penalties. Due to this, a low pressure refrigerant is needed to replace low pressure applications which currently use R134a, with R245fa being the suggested substitute by Honeywell. R245fa is also deemed to be suitable for organic rankine cycles which currently use R134a. The pressure classification of the refrigerants will have an effect on the pressure drop in channels, especially in microchannels which already have a higher pressure drop compared with larger diameter channels. The increase in pressure drop results in a larger pumping power requirement. The extent of this pressure drop needs to be taken in to consideration when using a low pressure refrigerant to replace a medium or high pressure refrigerant. The thermophysical properties of the refrigerant must also be evaluated in terms of the heat transfer coefficient. Although less of a system requirement than the pressure drop, wall and fluid temperatures may not be suitable with some materials. Replacement refrigerants should have equal or improved heat transfer for the transition to be more readily implemented.

Improved heat transfer and pressure drop characteristics can be found in blended refrigerants, which are widely used for cooling applications. Blends can also be employed as a way of reducing the safety restrictions associated with some refrigerants, such as CO_2. Fatouh et al. (2006) conducted simulations to evaluate possible propane and butane blends as a replacement for R134a in domestic refrigerators. This study found that although pure propane or butane was not suitable to replace R134, a blend of butane and 60 % propane mass concentration yielded similar values for pressure and

temperature across the system which would make it a suitable drop in replacement across the full range tested. Brown et al. (2014) investigated the heat transfer and pressure drop performance of new generation refrigerants, both pure and blended. This study confirmed that by knowing only the refrigerants normal boiling point and molecular structure, good estimates can be made of the heat transfer and pressure drop characteristics for flow boiling. This study found that many of the refrigerants which are intended to replace R134a, have worse heat transfer and pressure drop performance than R134a, including blends. Brown (2014) conducted simulations of R1234yf and blends for the application of automotive refrigeration with low GWP. Although R1234yf is widely considered for as a replacement for R134a, one perceived drawback is the flammability. The study concluded that although there are many advantages and disadvantages to the new generation refrigerants, blending refrigerants allows for a fluid to be designed that will match the desired performance while still maintaining a low GWP. The number of blends available will depend on what performance sacrifices are deemed suitable for the application. There are many advantages to using blends but one consideration is the refrigerant glide, which can be both beneficial and detrimental. As the individual refrigerants will boil at different temperatures, the refrigerant glide refers to the saturated temperature range. Although as a result of the refrigerant glide, complications occur in maintaining a well-mixed blend throughout the system. A consistent mixture is also a consideration with refrigerant leakage, where one refrigerant can leak before the other.

2.4.3. Effect of different refrigerants on flow patterns and heat transfer

As discussed in Chapter 2.3.2, the forces which dictate bubble formation and bubble coalescence are properties of the working fluid. The most important is that of surface tension, which dominate in microchannels. As the surface tension changes between refrigerants, the flow patterns and consequent heat transfer coefficients will be affected. Consolini et al. (2009) conducted experiments with three refrigerants, with the distinguishing property stated to be surface tension. R134a has the lowest surface tension, with R236fa being 23 % higher and R245fa 83% higher. This is compared to the vapour density which only increases by 18 % between the refrigerants, and thermal conductivity by 13 %. It was predicted that the bubble departure frequency would reduce and the bubble departure diameter would increase with surface tension. The experimental investigation of R134a, R245fa and R236fa yielded differences in the flow

patterns evident and the controlling variables of the flow pattern transitions. Bubbly and slug flow were not evident with R245fa, with only churn and annular flow recorded. This is contrary to R134a where the full flow pattern range was seen. The changes between the flow patterns and refrigerants were evident in the heat transfer coefficient, with R245fa once again showing different trends to R134a and R236fa. The effect of heat flux was only evident at intermediate heat fluxes before the heat transfer coefficients converged for different heat flux values. The independence of the heat transfer coefficient on heat flux resulted in poor agreement with heat transfer coefficient prediction methods, which under-predicted the data. Bortolin et al. (2011) agreed with this conclusion for the heat transfer coefficient prediction of R245fa. Agostini et al. (2008) conducted experiments using R245fa and R236fa, concluding that the inlet saturated pressure had little effect on the heat transfer coefficient for R245fa but did have an effect on R236fa. Four characteristic trends were identified for R245fa: (i) The heat transfer coefficient increased with mass velocity and decreased with increasing heat flux and vapour quality at very high heat fluxes. No relationship could be found for the transition heat flux where this occurred; (ii) A constant or slightly increasing heat transfer coefficient with vapour quality and increasing with heat flux for medium heat fluxes. The heat transfer coefficient was found to increase as $q_w^{0.67}$, where q_w is the wall heat flux. Note that this is the same as the Rohsenow's pool boiling correlation; (iii) The heat transfer coefficient increased with vapour quality and was independent of heat flux and mass velocity at low vapour quality, heat flux and low to medium mass velocities (iv) The heat transfer coefficient versus vapour quality curve has a U shape, decreasing with increasing heat flux and independent of mass velocity at low vapour quality and heat flux and high mass velocities, see figure 2.5.

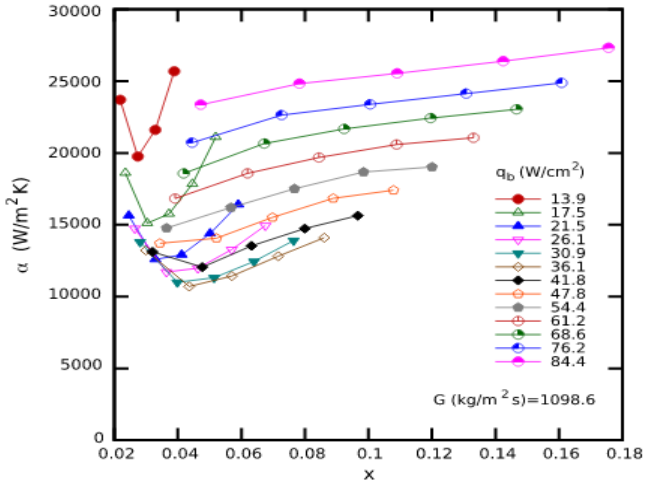

Figure 2.5. Heat transfer coefficient as a function of axial quality for R245fa, (Agostini et al. (2008)).

The difference in heat transfer coefficients between R245fa and R236fa was measured to be 11% but the Thome three-zone model (2004), which was deemed to be the best correlation, predicted the difference to be 25%. The thermophysical properties of the two refrigerants were compared, including non-dimensional numbers important for flow boiling. The boiling number, Weber number and Bond number were lower for R245fa, which suggested there may be a difference in bubble dynamics (Agostini et al. (2008)). Ong et al. (2009) conducted experiments with R245fa, R236fa and R134a, finding that R2454fa had the smallest vapour quality range for the isolated bubble regime. A comparison with the Revellin and Thome (2006) model showed poor agreement for R245fa and therefore was modified to account for the changing reduced pressures of R245fa and R236fa. A comparison of the heat transfer coefficient trends agreed with Consolini et al. (2009), with R245fa showing a convergence at higher vapour qualities. R245fa had the lowest heat transfer coefficient at low vapour qualities but rose to the same magnitude as R134a at higher vapour qualities, showing the fluid properties to be important for both the trend and magnitude of the heat transfer coefficient. Contrary to this, Ali et al. (2012) found there to be only a small difference between the heat transfer coefficient magnitude of R134a and R245fa, which followed the same trend. R245fa was slightly higher in magnitude at high vapour qualities. It was hypothesised that heat transfer correlations were not able to predict R245fa results due to the differences in surface tension, liquid viscosity and latent heat of vaporisation. They examine four correlations, namely Lazarek and Black (1982), Tran et al. (1996), Cooper (1984) and Owhaib (2007) and their comparisons resulted in a varying degree of success. Owhaib (2007) did not predict any R134a data within ±30% while Tran et al. (1996) and Cooper (1984) under predicted the heat transfer but with the majority of the data within ±30%. Lazarek and Black (1982) showed good results for R134a with all but one data point within the range. No correlation was able to predict data for R245fa within ±30%. This study concluded that no one correlation could accurately predict the heat transfer for both refrigerants. A similar conclusion was presented by Vakili-Farahani et al. (2013) who experimentally studied the heat transfer of R245fa and R1234ze(E) in 7 parallel channels. Heat transfer correlations from literature were compared with a 1117 point database of saturated flow boiling, excluding subcooled or post-dryout points. Dryout conditions were based on the deterioration of the heat transfer coefficient. The majority of the correlations were unable to predict across the entire experimental range, with the Thome et al. (2004) three zone model prediciting

77% of the experimental range to within ± 30%. The two refrigerants followed similar trends, with the heat transfer coefficient increasing with mass flux.

There is agreement in literature that the heat transfer coefficient changes with refrigerant, but the extent of this change is in question. Different trends were noted between refrigerants, with the effect of vapour quality, heat flux and inlet pressure all considerations. However, there is little agreement on the heat transfer coefficient trend with vapour quality, with differences reported for the same refrigerant. This in turn resulted in discrepancies in the accuracy of heat transfer correlations. The effect of fluid properties was seen to be over predicted by the Thome three zone model (2004) and no correlation was reported to be accurate across a range of refrigerants.

2.4.4. Effect of different refrigerants on pressure drop

An experimental study by Ali et al. (2011) investigated the effect of fluid properties on two phase pressure drop using R134a and R245fa. A fused silica tube of 781 μm internal diameter was used to test the two refrigerants at pressures of 1.8, 2.1 and 2.5 bar and 7.7, 8.9 and 10.2 bar, for R245fa and R134a respectively, which correspond to saturated temperatures of 30, 35 and 40 °C. The single phase pressure drop results showed R245fa to be higher than R134a, which was attributed to R245fa having a considerably higher viscosity. The higher two phase frictional pressure drop of R245fa was expected due to the lower vapour density resulting in an increased vapour shear at the liquid-vapour boundary as well as the higher liquid viscosity. The two phase frictional pressure drop for R245fa was not affected by the system pressure. Both macro and micro scale correlations were assessed and unlike R134a, there was no suitable macro-scale correlation for R245fa. This study found that the micro-scale pressure drop correlations were suitable for R245fa to within ±50%, although all of the correlations over predicted within this range. Xu et al. (2012) evaluated two phase frictional pressure drop correlations from literature, noting that there are contradictions in literature due to the limited available experimental data. This evaluation was conducted based on 29 correlations and 3480 experimental data points, covering a range of mass flux from 8 to 6000 kg/m^2s, hydraulic diameters 0.0695 to 14 mm and 14 working fluids. The diameters cover a range from micro to macro scale, based on the transition criteria of 3 mm. The thermophysical properties of the working fluids was deemed to be an important consideration for two phase frictional pressure drop. A higher liquid to vapour density ratio was seen to lean to a higher vapour velocity and

consequently a higher frictional pressure drop. The Muller-Steinhagen and Heck (1986) and Sun and Mishima (2009) correlation was deemed best for the full experimental range and recommended for two phase flow prediction. Costa-Patry et al. (2011) concluded that a lower vapour density resulted in a higher pressure drop, based on an experimental study of R245fa and R236fa. Li et al. (2012) conducted experiments using mixtures HFO1234yf and R32, for the application of residential air-conditioners, in a horizontal tube of 2 mm internal diameter. The two pure refrigerants were compared with two mixtures by mass percentage of HFO1234yf of 80/20 and 50/50. The measured pressure drops were compared with the Lockhart-Martinelli correlation (1949). The Lockhart-Martinelli (1949) correlation predicted the mixtures well but was not accurate for R32 which was generally lower than predicted, this is also true for HFO1234yf but to less of an extent.

Both the single and two phase pressure drop were seen to be a function of the refrigerant properties, namely that of the density. A lower vapour density was seen to result in a higher pressure drop, as was a higher liquid and vapour density ratio. The differences seen in the pressure drop between the refrigerants was not represented in the pressure drop correlations.

2.5 Surfaces

2.5.1. Surface measurements

The study of surface topography has been a focus of research for many years, with numerous advantages in technology allowing for further in-depth investigation into surface structure. The importance of surface topography is well known in manufacturing, from the large scale to small scale problems. The surface structures of large scale components are measured to ensure manufacture tolerances and reduce component wear. This is evident in the automotive industry where there is a large amount of scrap metal, up to 50%, which is costly and inefficient. This is partly due to the requirements of producing and testing new tool sets to ensure correct surface profiles and clearances (Benati, 2003). Kubiak et al. (2011) investigated the effect of surface roughness on the wettability, which is important for lubrication and reducing friction, for a range of materials commonly used in manufacturing. This investigation included surfaces which were produced with average roughness ranging from 0.15 – 7.44 μm. Smooth surfaces were seen to have improved wettability which could lead to better lubrication and consequently lower wear. The same influence of roughness was

seen across the range of materials. This indicates that the surface finish is a factor for consideration in manufacturing to improve the lifespan of components which suffer from excessive wear. Evans et al. (1999) noted that structured and engineered surfaces are an important development for new technologies, currently being used in industries ranging from reflective road signs to dental fillings. Jiang et al. (2012) presented a paper on the changes and developments in surface metrology. The paper presented three surface classifications, (a) Structured surfaces, (b) Engineered surfaces, (c) Non-engineered surfaces. For use in large scale manufacturing, these surfaces must be reproducible and measureable. Structured surfaces often have a high slope, referring to the gradient changes between the surface structures, which is not easily measured with current surface techniques. Smaller scale surface structure is also a consideration in automotive production for the application of paint, where the surface structure will affect how the paint bonds to components. Although there is a big difference in the magnitudes which are considered for large scale and small scale surface structures, the method of measuring and evaluating the surfaces is the same. There are two methods for measuring surfaces, contact and non-contact, the most suitable method will depend on the measurement sample, mainly the sample geometry and material. Contact methods use a stylus, most commonly a diamond tip with diameters down to 20 nanometres (Schaeffer, 2012). The tip is connected to a cantilever beam, as the tip moves along the surface; the movement of the beam is used to plot the surface structure. As the stylus tip has a minimum diameter of 20 nm, this may not be suitable for complex and restricting geometries, such as microchannels, where the tip is unable to reach the surface. This is compared to SEM, where surface details can be visualised that are less than 1 nm. The tip diameter also limits the amount that the tip can enter into cavities which results in a smoother measured profile, see figure 2.6. Bejan et al. (2003) states the approximate nucleation site diameter, for water at normal boiling point, to be 0.1 nm.

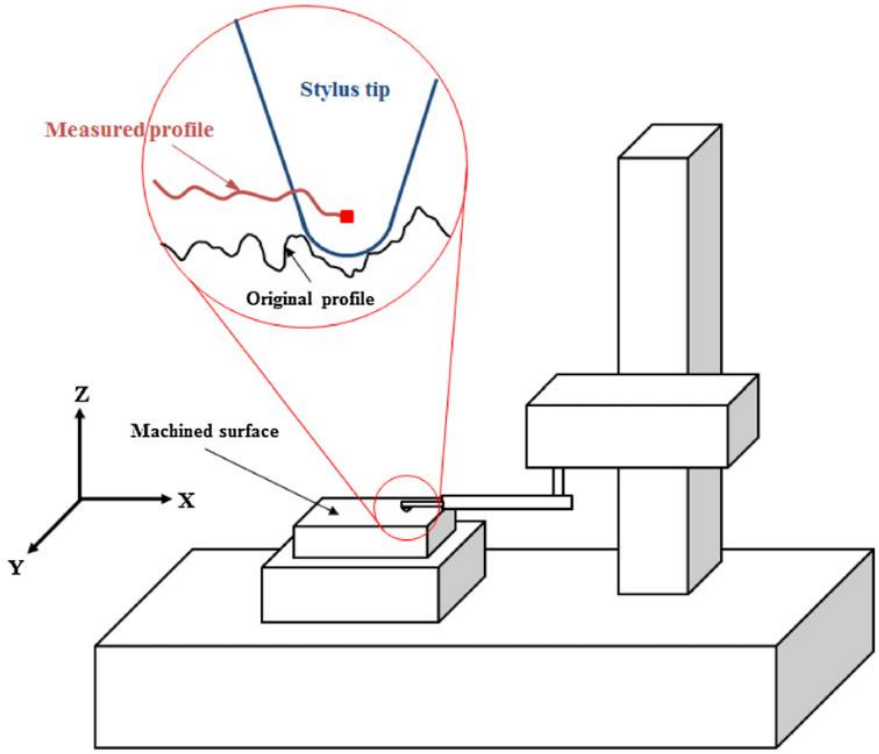

Figure 2.6. Surface profile measured by stylus-type profilometer, (Lee et al. 2012).

Depending on the softness of the material sample, the tip can damage the surface and therefore alter the surface finish. The shape of the tip is also a consideration, with the most common being a conical tip but cylindrical tips are also available. Figure 2.7 presents the profile differences seen from using a different tip shape.

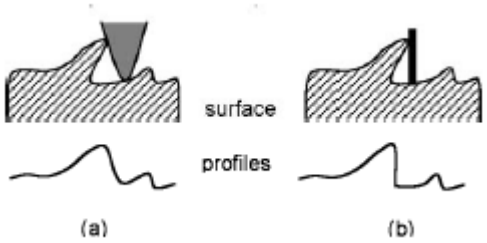

Figure 2.7. Example of profiles from a surface with re-entrance with a (a) conical tip and (b) cylindrical tip, Lonardo et al. (2002).

The main disadvantage to this method is that the line trace method can only give a 3D representation of the surface though time consuming methods (Simmonds et al. 1995). Contact methodology is the preferred methodology for certain conditions due to the advantages of the direct methodology. As the stylus is in direct contact with the

surface, there are fewer limitations on the material of the sample. Dirty environments and materials which are highly reflective or transparent can give misleading results when using non-contact techniques. Contact techniques are direct and require less data manipulation which can be an advantage. Mathia et al. (2011) also noted that although there have been large developments in optical process; the contact profilometer is the most commonly used method in industry. There is also greater uniformity from contact methodology due to standards including the calibration and measurement for contact techniques, including ISO 25178, which is not currently available for non-contact techniques. Non-contact techniques include a number of possible methods, depending on the desired surface structure output information. Methods including scanning electron microscopy (SEM), do not produce numerical data on the surface but can be used to produce a magnified image of the surface which can indicate the surface structure. These images can be analysed to identify possible surface imperfections and flaws. Confocal laser microscopy and interferometry are examples of non-contact optical techniques which can be used to produce 3D maps of the surface. Interferometry uses a light source, such as white light, to reproduce a map of the surface based on the interaction of light waves from the source and reflecting from the surface. Confocal laser microscopy uses a laser source which passes through a pin hole, to increase the resolution, and the returning light waves are used to form a 3D picture of the surface. Non-contact techniques give a larger range of surface parameters but the data is subject to manipulation which can lead to discrepancies between laboratories. The confocal laser is not suitable for surfaces with large slopes, above 90˚, due to the limitation of the laser beam (Mathia et al. 2011). Atomic force microscopy (AFM) is a contact technique which also uses a laser diode for improved resolution over the simple stylus method. As the tip is moved across the sample surface, the deflection of the cantilever beam is measured based on the reflection of the laser beam. All of the measuring techniques have limitations from the surrounding environment, including vibrations and thermal changes. Mathia et al. (2011) stated that optical methods are most likely to be used in the future, namely that of white light interferometry and confocal laser, but with the contact stylus method being used as a reference. A similar conclusion was presented by Lonardo et al. (2002), that contact stylus methodology can be used as a reference for other sampling methodologies. A reference point for surface measurements are important due to the differences seen between surface readings for the same sample but using difference sampling techniques. Poon et al. (1995) compared a contact method, surface profilemetery, AFM and a non-contact optical profiler for measuring the surface

roughness of a glass-ceramic disk. The same terminology is used for both contact and non-contact techniques, but to refer to different things. For example, the spatial resolution for contact methodologies refers to the stylus size but to the magnification of the objective lens for non-contact methods. This is a consideration when comparing results between the two methodologies. There are several variables, applied to both contact and non-contact methodologies, which need to be considered for surface scanning. The spatial resolution wants to be as high as possible, referring to the ability of the process to accurately follow the sample surface. A smaller tip will allow for a better trace of the surface and therefore a higher spatial resolution. Poon et al. (1995) found the spatial resolution to greatly affect the surface scan results, with a lower spatial resolution resulting in inflated surface readings. Another important parameter is the scan size, which is known to affect the magnitude of the surface parameters due to the filtering and data manipulation applied. As the scan size is increased, the surface parameters tend towards a constant value (Poon et al. 1995). The selection of a suitable scan size will depend on the surface structure and the measurements in question. Poon et al. (1995) concluded that the method of surface scanning will depend on the material of the sample, with AFM deemed most suitable for glass-ceramic substrate. Lonardo et al. (2002) noted that how the surface is defined, will depend on both the purpose of the surface and the measuring technique employed. Figure 2.8 presents the process which is recommended for choosing the suitable measurement technique.

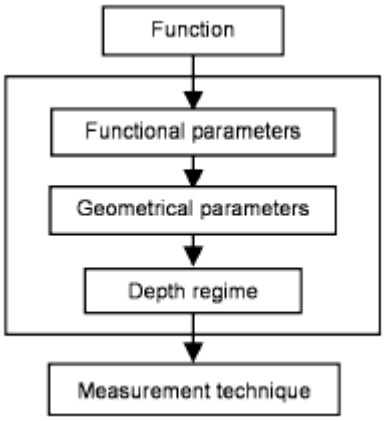

Figure 2.8. Recommended process for choosing the measurement technique, Lonardo et al. (2002).

The purpose of the surface is based on whether the region of the surface which is important for the function, i.e. the top upper layer of the surface or deeper regions of the surface. A new measurement strategy is proposed which requires a complete database of

function and geometric parameters and corresponding measurement systems which are suitable for each application.

2.5.2. Surface parameters

For all of the surface scanning methodologies discussed, the output data is represented in the same format, with surface parameters. The output is considered to be in a spectrum of wavelengths, with the shortest being the sampling interval and the longest is the length of the measurement. These wavelengths are separated into the profile (or form), waviness and roughness. The profile wavelength is the longest wavelength and refers to surface defects that are a result of misalignment or errors in machine components. The waviness is the result of manufacturing errors, including wear on manufacturing tools. The roughness is the small scale defects which are often due to the manufacturing process, including stretch marks from rolling metal sheets. These wavelengths are separated with filtering, with a number of filtering methods available. Filtering is based on the transverse length, assessment (evaluation) length and sampling length (cut-off length), see figure 2.9. The cut-off is the length used for filtering and for identifying the irregularities characterizing the surface (Griffiths, 2001) and is based on the measurements and the nature of the surface, not its geometrical properties (Salek, 2012). It should also be based on the profile wavelength and not the evaluation length (see figure 2.9). The cut-off and the sampling length are not necessarily always the same (Whitehouse, 2011), However, for roughness evaluation, see figure 2.9, these two parameters have the same value and are treated the same for the rest of this work. The evaluation length should be approximately 5 times the cut-off (Bewoor, 2009).

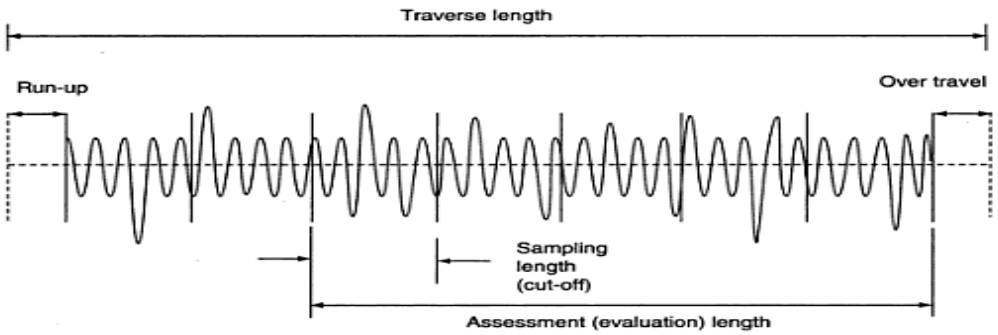

Figure 2.9. Length definitions for surface measurements, (Bewoor, 2009).

One or two sampling lengths are removed from either end of the transverse length, depending on the surface scanning method used (Bewoor, 2009). Nielsen (2000)

presented the rule of thumb for the transverse length to be 6-7 times greater than the cut-off length. The wavelengths available for surface analysis are limited by the technique employed. As previously stated, the traverse and evaluation lengths, seen in figure 2.9, are a multiple of the cut-off but they are also in turn limited by the capability of the machine. For both contact and non-contact techniques, there is a maximum and a minimum distance that can be travelled as well as a limitation due to the actual physical length of the sample placed on the instrument. For example, a traverse length of 10 mm results in an appropriate cut-off of 1.4 mm. In the study of microchannel roughness, this is a large cut-off, which would not give an accurate representation of the finer surface characteristics. Muralikrishnan et al. (2008) stated that the Ra values can be artificially inflated by increasing the cut-off filter as this allows for a larger bandwidth to be classed as roughness instead of waviness. This was also presented by Oberg et al. (1996) who found the Ra values to change with cut-off values, see figure 2.10, where Ra is the arithmetic mean of the absolute ordinance across the sampling length (integral of roughness profile divided by length). As seen in the figure, the roughness values for the same surface decrease with the cut-off value. When the cut-off value is increased, more data is considered to be part of the roughness that may have previously been considered to be waviness. This will inflate the surface roughness values. On the other hand, a low cut-off can result in surface features being lost as only a small range of data is considered to be roughness.

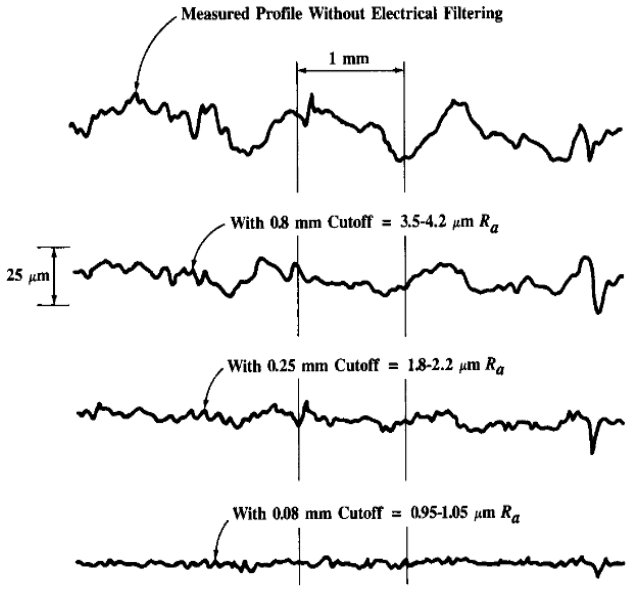

Figure 2.10. The effect of various cut off values on average roughness, Ra, (Oberg et al, 1996).

Kandlikar et al. (2005) reported that filtering is applied when processing the data, but the settings of the instrument when scanning will also affect the readings. The resolution and scan size, the latter being the width along the scan, will have an impact on the readings. The surface is divided into a grid, with the measurements based on the average of each grid co-ordinate. The higher the number of grid co-ordinates set, the higher the resolution of the results. If the scan size is too large, then the grids will also be large and the resolution will be lower. Due to the large differences seen with changes in the cut-off length and scan resolution, comparison of surface parameter data from different labs is difficult.

The cut-off length used to define the surface parameters is variable and will depend on the application of the sample. For example, large scale components, such as boat propellers, will have a considerable larger scale wavelength for roughness than a micro heat exchanger pin fin. For the purpose of this study, it is assumed that only roughness is of interest, and therefore the profile and waviness wavelengths are removed and only the shorter wavelength data is considered. The roughness values can then be further segregated into categories of amplitude, spatial or hybrid. Each wavelength, profile (P), waviness (W) and roughness (R), can be further sub-divided into these categories. For the purpose of flow boiling, we are only considering these parameters as a function of roughness, R. There are many surface parameters defined in literature and in the ISO standards. Mathia et al. (2011) identified that although there are many well defined and used surface parameters, as structures surfaces become more widely used in manufacturing, new special parameters may be considered. Table 2.1 presents the surface parameter which are included in these sub-categories (Davim, 2010). For the given equations, L refers to the sample length where applicable. Spatial parameters refer to the spacing between surface structures, such as peaks. The spatial paraemeters are used to access peak density and can be used to define between a highly textured surface or random surface structures (Blunt et al. 2003). Amplitude parameters are a function of the height deviation, consisting of six parameters which are either based on the average value or the extreme peak to valley values. Hybrid parameters are those which are based on both the lateral and the vertical components. These parameters are primarily used in research rather than industry (Bruce, 2012).

Table 2.1. Surface parameters based on the sub-categories, (Davim, 2010).

Spatial parameters		
Rsm	Mean width of profile elements in sampling length	$Rsm = \frac{1}{m}\sum_{i=1}^{m} Xsi$
Hybrid parameters		
$R_{\Delta}q$	Root mean square of ordinate slopes in sampling length	$R\Delta q = \sqrt{\frac{1}{L}\int_{0}^{L}\left(\frac{d}{dx}Z(x)\right)^{2} dx}$
Amplitude parameters (peaks and valleys)		
Rp	Maximum profile peak height	Measured
Rt	Total height for evaluation length	Rp + Rv
Rv	Maximum profile valley depth	Measured
Rc	Mean height of profile peaks	$Rc = \frac{1}{m}\sum_{L=1}^{m} Zti$
Rz	Total height for sampling length	Rp + Rv
Rz_{10}	Ten point height (sum of mean 5 highest peaks and 5 lowest valleys in sampling length)	$Rz_{10} = \frac{1}{5}\sum_{j=1}^{5}(Rp + Rv)$
Amplitude parameters (average)		
Ra	Arithmetic mean	$Ra = \frac{1}{L}\int_{0}^{L} \lvert Z(x)\rvert \, dx$
Rq	Root mean square	$Rq = \sqrt{\frac{1}{L}\int_{0}^{L} Z^{2}(x)dx}$
Ra_{75}	Centre line average	$Ra_{75} = \frac{1}{ln}\int_{0}^{ln} \lvert Z(x)\rvert \, dx$

Based on a survey conducted by the CIRP (The international academy for Production Engineering) of 284 industrial companies, the most commonly used roughness parameters are Ra, Rt, Rz and the ten point height Rz_{10}, which was removed from the ISO standards in 1997. Ra was by far the most used, with 92% of the companies using this parameter and with 13% only using this parameter. Interestingly,

the waviness and profile parameters were rarely used (De Chiffre et al. 2000). Although Ra is widely used, this parameter is also widely regarded as flawed as two surfaces can vary greatly in structure but have the same Ra value, see figure 2.11.

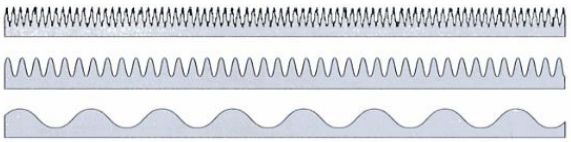

Figure 2.11. Three distinctly different surfaces with the same average roughness value (Kandlikar et al, 1997).

It is important to consider more than one surface parameter as surfaces can have the same amplitude parameters but vary in spatial parameters. The true surface structure which is important in cavitation and consequently flow boiling, can't be evaluated from one surface parameter alone.

Taylor et al. (2006) presented a review into the effect of surface roughness and texture on fluid flow in literature, stating that the true effect of surface roughness on fluid flow is still unknown. As technology shifts towards the use of microchannels, the relative roughness (roughness height to diameter) becomes less suitable, being limited to 14% relative roughness. This review concluded that the continuing trend of miniaturization for fluid based systems will require a greater understanding of the surface roughness, including the ability to manipulate surfaces in 3D. Improved understanding will allow for surfaces to be designed to specification for fluid systems.

2.5.3. Surfaces and pressure drop

Kandlikar and Schmitt (2005) conducted an experimental study of the effect of surface roughness in minichannels with single phase flow. The pressure drop was noted to be effected by the surface roughness due to roughness effect acting as a flow area constriction and increasing the wall shear stress. The roughness parameters proposed to define the roughness effects were Rp and Rsm (as previously defined) and a new parameter, Fp (the floor to distance mean line). The equivalent roughness is then defined as Rp + Fpm, see figure 2.12. They found that many surfaces which had similar roughness values, varied with the newly proposed equivalent roughness. Experiments were conducted over a range of laminar and turbulent flow, with the laminar to turbulent transition shifting to lower Reynolds numbers with an increase in the relative roughness.

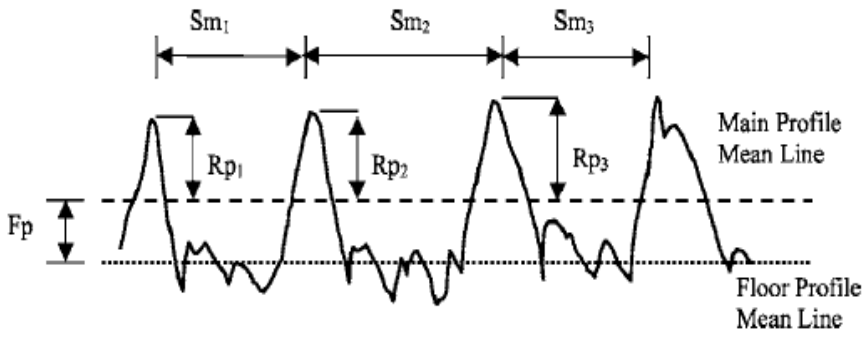

Figure 2.12. Maximum profile peak height (Rp), spacing between irregularities (Sm) and floor distance to mean line (Fp), (Kandlikar and Schmitt, 2005).

The investigation into the shift of the turbulent transition to lower Reynolds number was continued by Brackbill and Kandlikar (2007). Rectangular channels with varying surface element heights and pitches were used, with pressure measurements taken at 16 points along the channel length. This study concluded that although the shift correlated well with the previous results, further work was required to include other working fluids. During laminar flow, the friction factor was predicted well using the hydraulic diameter based on the constricted flow area. Croce and D'Agaro (2005) conducted simulations into the effect of surface roughness in microchannels during laminar flow. The surface roughness was modelled as randomly generated peaks along a smooth surface, with difference peak shapes and distributions modelled. The study found that the frictional pressure losses increased with roughness, which agreed with experimental data. The shape of the surface characteristic had an effect on the pressure losses, with a triangular peak showing significantly lower increments in pressure losses due to the less abrupt variation in the channels cross sectional area. Cavalinni et al. (2009) evaluated the frictional pressure drop of two phase flow in mini channels, through both modelling and experimentation. The experiments were conducted in channels with a range of surface roughness values and compared with previous results which were conducted in channels with roughness values of Ra = 0.08 and Rz = 0.43 µm, which were considered negligible. The liquid frictional factor was modified to include Ra in order to account for the changes in two phase frictional pressure gradient with surface roughness. Del col et al. (2013) concluded that surface roughness will have an effect on the two phase frictional pressure drop. Experimental data for horizontal channels, both circular and non-circular, with channel diameters from 0.96 to 2 mm was used to evaluate pressure drop correlations in literature. The data bank used covered a range of refrigerants, covering both high and low pressure refrigerants and relative

roughness's ranging from 0.0017 to 0.003. Relative roughness refers to the average height of the roughness divided by the average internal diameter. An updated model for prediction was presented which included the effect of the surface roughness as a function of the liquid only friction factor. Single phase analysis showed the surface roughness to only affect the frictional pressure drop during transitional and turbulent regions, with no effect in laminar flow. For the correlation to be applicable across a range of experimental conditions, a further parameter, X, is multiplied by the roughness parameter, RR, which is equal to 2*Ra/D. At low values of liquid only Reynolds number, X is equal to zero, thus negating the effect of surface roughness. At liquid Reynolds numbers greater than 3500, X is equal to 1. Intermediate values of the liquid only Reynolds number, the effect of surface roughness is higher, reflected in an X value greater than 1. This new correlation was verified in tubes of different geometries and diameters to good agreement.

Surface characteristics are a consideration for both single phase and two phase pressure drop, although there is no agreement on which surface parameter should be considered. Kandlikar and Schmitt (2005) concluded that Rp, Rsm and a new parameter, Fp, were important but Del Col et al. (2013) and Croce and D'Argaro (2005) concluded that Ra was the important parameter. The only correlation to directly include a function of the surface characteristics is that of Del Col et al. (2013), where the extent to which Ra influences the frictional pressure drop is a function of the Reynolds number. In general, it is noted that a higher surface roughness equates to a higher frictional pressure drop, but with the shape of the surface peaks affecting the extent of the increase.

2.5.4. Surfaces and heat transfer

The effect of surface characteristics is widely reported to influence the heat transfer for pool boiling (Jones et al. (2009)). In general, the effect of surface characteristics has been negated in flow boiling, with the majority of surface work reporting the average surface roughness, Ra, alone (Del Col et al. (2013a), Alam et al. (2012)). It is widely accepted that surface cavities and nucleation sites play a vital role in the onset of nucleation, as does the fluid properties, and therefore surface characteristics should not be ignored. Kandlikar (1991) produced a correlation to predict the fully developed boiling region which included the fluid-surface parameter, fl, noting that different combinations of fluids and surfaces would change the nucleation

characteristics. The correlation is limited by the fluid-surface value being available for a limited number of combinations only. This is especially true for microchannels which are growing in popularity and hence fluid-surface variations. Kandlikar and Spiesman (1998) conducted an experimental study into the effect of surface finish on heat transfer, using water over surfaces of different roughnesses. The surfaces are imaged and processed to analyse the cavity size distribution, to attain a relationship between this and the heat transfer. The results showed that there was no clear trend between the surface roughness and the heat transfer, although the roughest surface did perform best. The four roughened surfaces showed no significant differences between cavity size distribution and exhibited no signs of hysteresis. This is contrary to a commercially prepared sintered surface which showed signs of hysteresis and outperformed the other surfaces. Although the higher performance of the sintered surface is not necessarily better for industrial use due to the higher costs and degradation. The heat transfer showed a higher dependence on the number and cavity size of cavities rather than the average roughness.

A study by Karayiannis et al. (2012) investigated discrepancies between flow boiling data in literature. This study concluded that the heated length, surface characteristics and, in agreement with Consolini et al. (2009), flow instabilities contributed to the reported differences. Experiments were conducted on two stainless steel test sections of 1.1 mm internal diameter, one of which was welded and the other a seamless cold drawn tube. Scanning electron microscopy showed differences between the surfaces which resulted in differing heat transfer coefficient trends. This study noted that comparing heat transfer data in literature is limited due to the surface characteristics or manufacturing technique of the test section is not widely reported. This is in agreement with a previous study by Guo et al. (2003) who concluded that the reasons for discrepancies between conventional and microchannels included axial conduction, measurement errors and surface roughness, where surface roughness results in an early transition from laminar to turbulent flow. Morini et al. (2010) noted there are contradictions in literature over the effect of the roughness on the Nusselt numbers for single phase flow. Some authors concluded that relative roughness lower than 1 % affected the heat transfer coefficient while other authors found no effect of heat transfer at up to 4% relative roughness. For commercially produced stainless steel microchannels, the relative roughness can be up to 10%. Morini et al. (2010) concluded that in the laminar region, the Nusselt number was not influenced by relative roughnesses up to 4%. Wu et al. (2003) conducted an experimental study of the effect of

surface conditions on the heat transfer of water in silicon microchannels. The Nusselt number was seen to greatly depend on the geometric properties, increasing with surface roughness, especially at higher Reynolds numbers. This is in agreement with an earlier study by Qu et al. (2000) who conducted both an experimental and numerical study of the Nusselt number of water in silicon microchannels. They found that the experimentally determined Nusselt number was lower than that numerically predicted, thought to be a result of the effect of the surface roughness. A modified equation to calculate the Nusselt number was proposed, based on the roughness-viscosity model. Gamrat et al. (2009) modelled surface roughness as periodically distributed parallelepipedic elements in microchannels to investigate the effect of surface roughness on heat transfer in the laminar region. The model showed that in the laminar region, the Nusselt number increased with relative roughness and was almost independent of the Reynolds number. The roughness was seen to increase the friction factor more than the heat transfer coefficient. The study concluded that the relative roughness, as a result of microsystem fabrication, should be avoided. This is only true for the 'random' roughness as a result of manufacture, as pin fins were seen to enhance the heat transfer coefficient. This study was limited by the periodic nature of the surface structure tested, with manufactured surfaces having inhomogeneous surface texture.

Surface characteristics evidently have an effect on both the single and two phase heat transfer coefficient. However, this is not represented in correlations due to a lack of understanding as to which surface parameter is important. Larger databases of heat transfer data with equivalent surface parameter data is needed for this to be fully evaluated. There are many heat transfer correlations which utilise the Cooper (1984) correlation which includes the parameter Rp (Liu and Winterton (1991), Bertsch et al. (2009), Mikielewicz (2010), Mahmoud and Karayiannis (2012)). Due to Rp often being unknown, the equation has been adapted to no longer include this parameter (Li et al. (2013). The Rp value presented by Cooper (1984) is based on DIN 4762 has since been updated by Gorenflo (1993). Bertch et al. (2009) proposed a correlation which utilised the Copper (1984) correlation, where the Rp value is set to be equal to one if the value is unknown.

2.6 Summary

There is a growing trend towards miniaturisation of refrigerant systems, for both environmental and cost efficiency benefits. The move towards the use of small systems is currently hindered by a lack of understanding and contradictions in literature for the true effect of reducing the channel diameter. It is widely accepted that there are differences seen in the flow patterns with a reduction in the channel diameter due to bubble confinement and the dominance of surface tension. Other factors are seen to change the flow patterns, including the experimental conditions and working fluid, with a limited available data base resulting in specific flow pattern maps. A generic flow pattern map and comparison of data is also hindered by changes in terminology used when defining and describing flow patterns and transitions. The changes in flow patterns with changes in the channel diameter are reflected in a change in the heat transfer coefficient, with further understanding of the bubble dynamics required to develop accurate correlations. Tightening environmental regulations and increased thermal management demands has resulted in the need to introduce new generation refrigerants. The challenge with implementing these new refrigerants lies in the lack of available data and correlations available, with contradictions in literature over the trend and magnitude of the heat transfer coefficients and pressure drop.

There are many ways in which the surface parameters and structure can be analysed and measured, with visual inspection using SEM or 2D and 3D surface scans. These scans can be produced from either contact or non-contact methods, each with their own advantages. The method used for surface measurements will depend on the application of the surface and what surface parameters are of greatest importance. Although there is no clear conclusion on the effect of surface roughness on flow boiling, the investigation is hampered by the inability to accurately compare surface between laboratories. Surface parameter data are open to interpretation and so can vary greatly, even with the same surface, partly due to a lack of standardisation.

There are still many unanswered questions in literature about flow boiling in microchannels, especially relating to the effect that changes in refrigerant properties and surface structure have on the heat transfer coefficient and pressure drop. Further research and experimentation is required in these areas for accurate prediction methods to be produced. The inability to accurately predict the flow behaviour will limit the implementation of smaller heat exchangers and development of new technologies.

Chapter 3

3. Experimental methodology and uncertainty

3.1 Introduction

The previous experimental studies on this facility have used R134a as the working fluid, with experiments based on varying test section diameters, pressures and heated lengths, as well as detailed flow visualisation, with the aim of investigating flow boiling in microchannels. This test facility was designed and constructed by Huo (2005) who investigated the flow boiling heat transfer and pressure drop in two stainless steel test sections, with inside diameters of 4.26 and 2.01mm. The work was continued by Chen (2006) who investigated the flow patterns in stainless steel tubes having inside diameters of 4.26, 2.88, 2.01 and 1.1mm with the aim of developing flow maps. The investigation of pressure drops and flow boiling heat transfer in a further three stainless steel test sections, having inside diameters of 2.88, 1.1 and 0.52 mm was completed by Shiferaw (2008). The final investigation using R134a was completed by Mahmoud (2011) in flow boiling heat transfer and pressure drop for stainless steel tubes of 1.1 mm and heated lengths of 150, 300 and 450mm as well as the study of surface characteristics with 1.1 mm stainless steel test sections which were manufactured in two different processes, welded and seamless cold drawn. This study also included the use of a 0.52 mm test section.

For the current experimental studies, the working fluid has been replaced with new generation refrigerant, R245fa. Experiments with this refrigerant have focused on differences in the refrigerant properties and test section material, as well as flow visualisation.

The experimental facility consists of a R22 cooling loop and R245fa heating loop.

3.2 R22 cooling loop

The auxiliary R22 cooling loop is used to control the pressures and temperatures within the R245fa test loop. The cooling loop consists of a R22 storage tank (which doubles as an evaporator), a gear pump, compressor, oil separator, liquid receiver and condenser. A schematic diagram and photograph of the loop can be seen in figure 3.1 and 3.2 respectively. The cooling loop is integrated into the R245fa test loop through coils within the R245fa storage tank, condenser and sub-cooler. A gear pump is used to direct the cold R22 liquid into the R245fa system. The path and level of R22 flowing into the R245fa test loop is controlled with multiple needle valves.

The cooling loop contains a mixture of oil and R22, with the majority of the oil removed from the mixture when passed through an oil separator. The separated oil is returned to the compressor for lubrication. This high pressure gas flows to the roof top condenser which consists of six fans. The fans can be individually controlled to reduce the condensing power as required. The flow is passed through a liquid receiver before returning to the R22 storage tank via a sight glass, solenoid valve and thermostatic liquid level controller. A thermostatic liquid level controller is used to manage the level of R22 flowing into the tank. A bulb is fixed within the tank, when the liquid level falls below this point, the temperature inside the bulb increases. This temperature increase causes the gas inside to expand and open the valve to allow R22 to flow. The R22 will flow into the tank until the liquid level is greater than that of the bulb, decreasing the bulb temperature and reducing the gas pressure, consequently closing the valve. The solenoid valve and thermostatic liquid lever controller is used to reduce the pressure to the evaporator, with a liquid temperature of approximately – 40˚C. A hot gas bypass from the oil separator through a pressure regulator is used to allow the compressor to function with the continuous changes in load. The pressure regulator is set to 2 bar so that when the temperature inside the tank falls below approximately -25˚C, hot gas is allowed to flow into the tank. As the temperature inside the tank increases, the regulator stops the hot gas from entering the tank.

Although the oil separator removes the majority of the oil, any oil which enters the R22 storage tank will settle at the bottom of the tank. An oil return system is then utilised to replenish that with the oil in the compressor. This is used as alternative oil supply to the compressor, which is run continuously. The oil tank contains a heater

which allows for the separation of R22, which returns as vapour back into the loop, and oil which can be used to replenish the compressor as required.

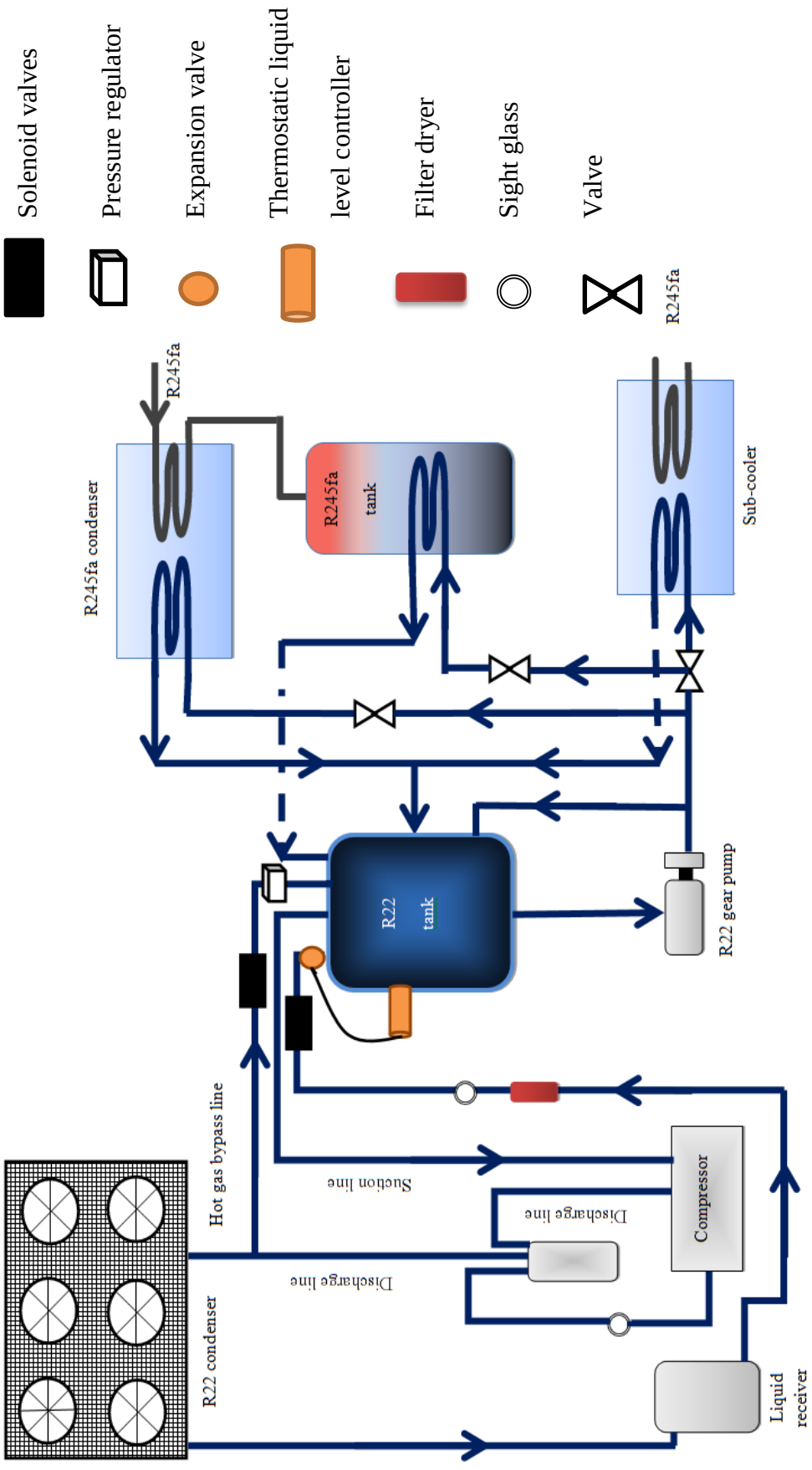

Figure 3.1. Schematic diagram of the R22 cooling loop.

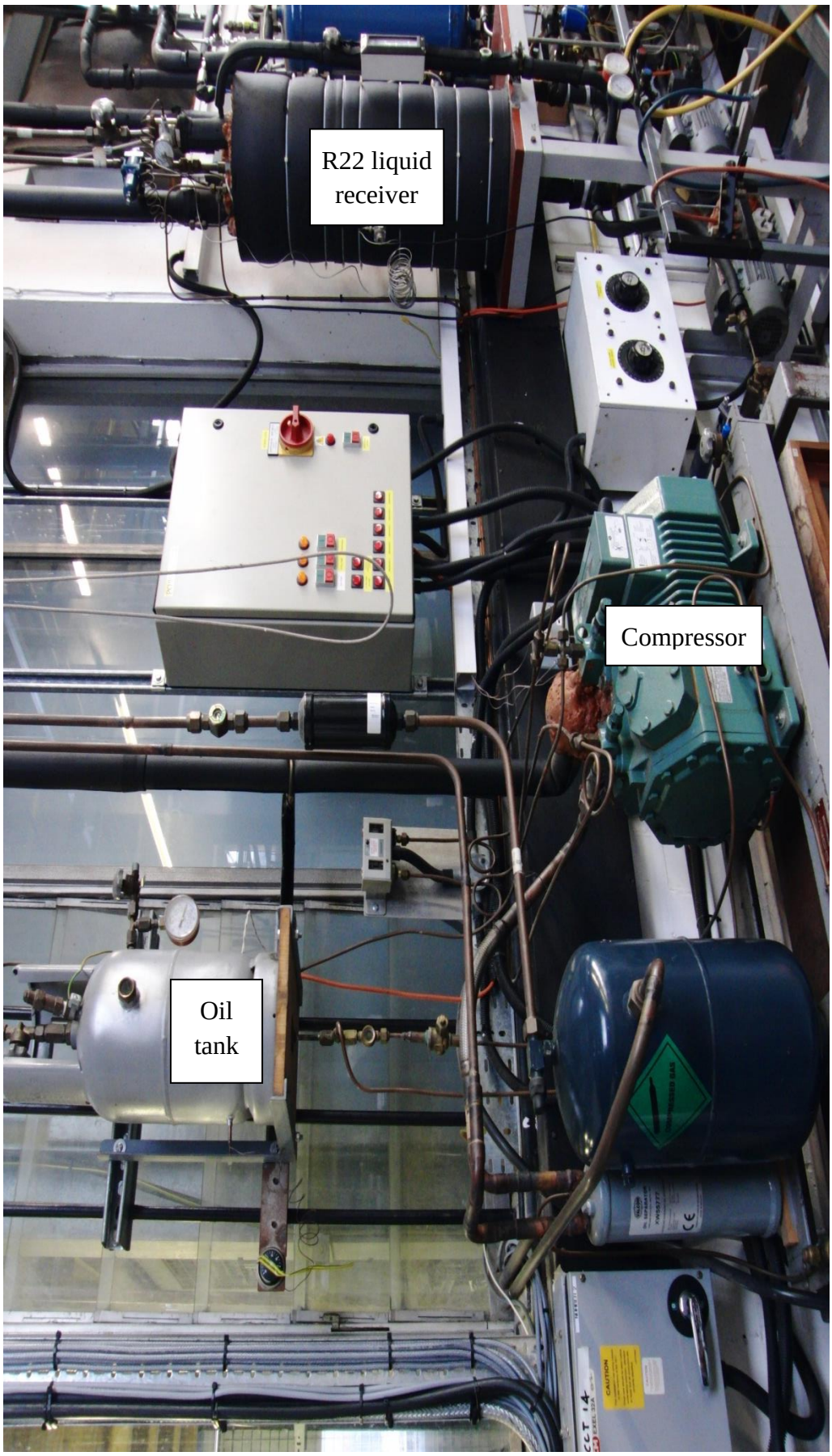

Figure 3.2. Photograph of the R22 cooling loop.

3.3 R245fa heating loop

A schematic diagram of the test loop can be seen in figure 3.3 and a photograph in figure 3.4. This loop consists of a R245fa storage tank, gear pump, coriolis flow meters, sub-cooler, pre-heater, liquid separator, condenser and the test section. All the tubes used are stainless steel which is highly resistant to corrosion. The test loop includes multiple sight glasses to ensure that there are no bubbles in the flow and filter dryers to remove any dirt particles throughout as well as valves which allows the test loop to be segmented for maintenance and upgrades as required. The R245fa tank is a 40 Litre cylinder which holds the majority of the refrigerant. The cylinder is modified to include a circular core which holds the heater. The tank pressure is regulated with the heater and a cooling coil, which has a cooling capacity of 500 W. Both the heater and the fluid temperature entering the cooling coils are controlled with variacs. A pressure gauge and thermocouple are inserted into the tank with a safety valve. The cooling coil in the tank is used as a small condenser when using low heating loads to prevent instabilities that can occur from using the main condenser. A Tuthill Pump 1010/028 with a 5 bar pressure head and a flow rate of 6 litres/minute is used to pump the R245fa. A bypass line is fitted after the pump which returns excess fluid to the storage tank and helps regulate the pressure to reduce the risk of over pressure from the increased flow resistance found with small diameter tubes. A pressure gauge and thermocouple are used to monitor the state of the liquid before entering a flow meter. There are two coriolis flow meters within this loop, with a valve used to direct the flow to the appropriate meter. Both coriolis meters were supplied by Micro Motion Ltd, a CFM010 with a flow range of 0-25 kg/hr and a CFM025 with a flow meter of 0-500 kg/hr. Each of the flow meter branches has a needle valve which is used to control the flow rate. A tube-in-tube heat exchanger is used as a sub-cooler with a maximum cooling capacity of 3.1 kW using R22. The inlet temperature is controlled, using a variac, with a 400 W rope heater acting as a pre-heater. The test section includes an initial calming section, to ensure that the flow is fully developed, a heated section and an observation section. The temperature and pressure of the refrigerant is recorded at the inlet and outlet of the heated section and the outlet of the observation section. The heated section wall temperature is recorded at 14 equidistance locations. Large pressure drops in the condenser are prevented by passing the two phase flow through a liquid separator. The vapour enters the condenser and the liquid is bypassed directly back to the R245fa storage tank. The main condenser uses R22 in a tube-in-tube heat exchanger with a cooling capacity of 11.6 kW.

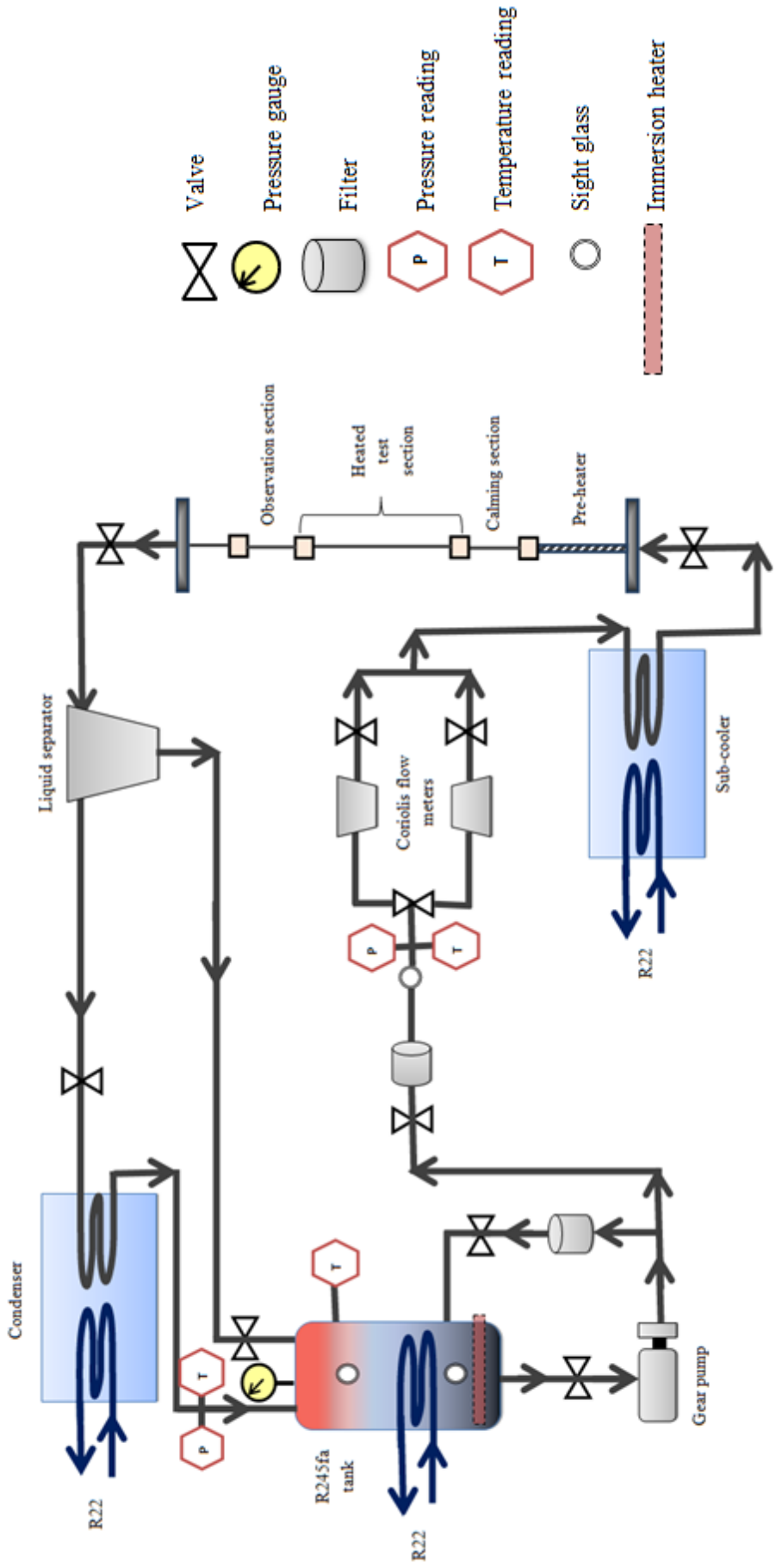

Figure 3.3. Schematic of the R245fa heating loop.

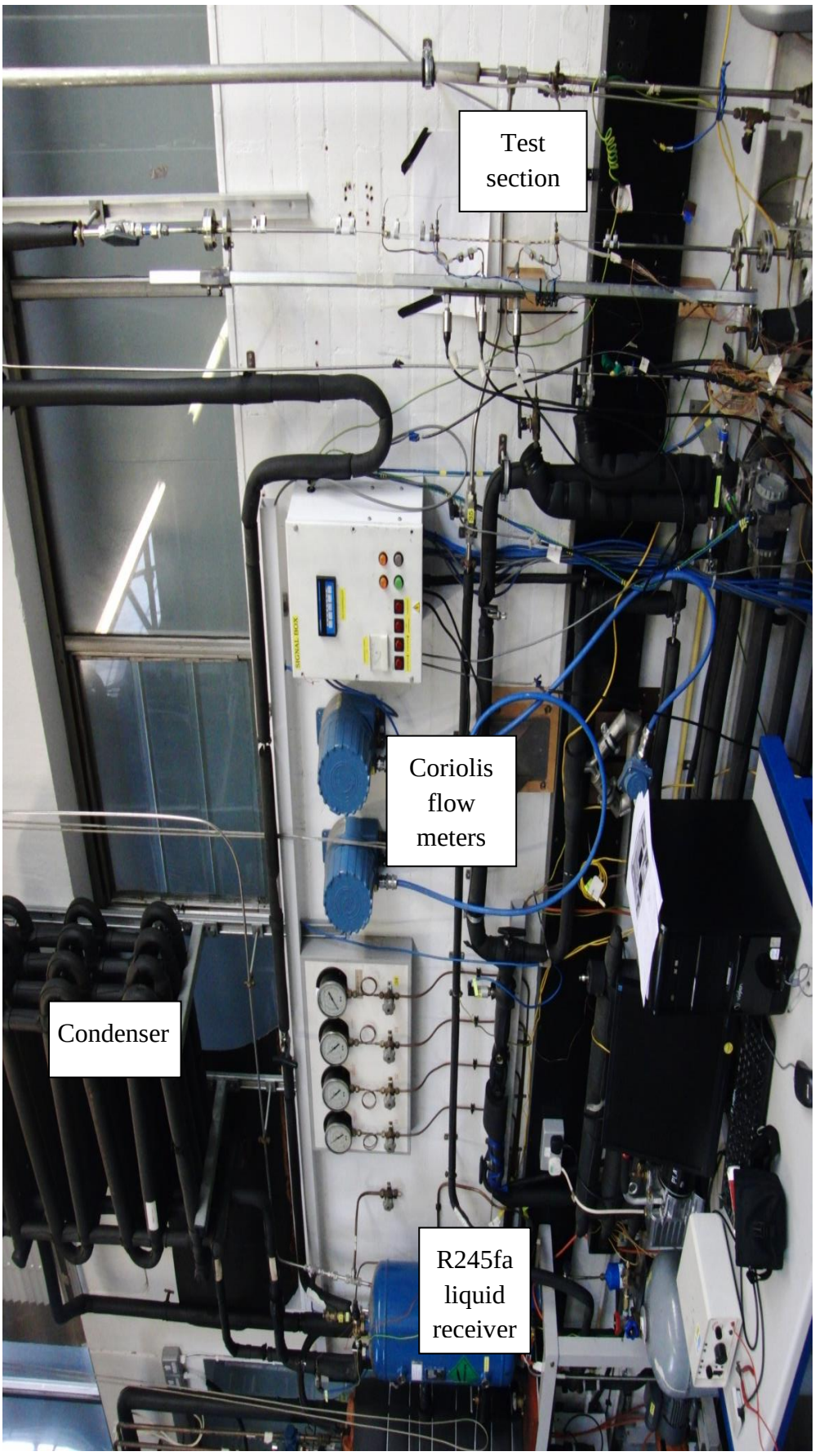

Figure 3.4. Photograph of the R245fa heating loop.

3.4 Upgrading of the experimental facility

One of the objectives of this research is to investigate a new refrigerant which required the R134a to be removed from the facility. The test facility had to be completely emptied and purged to ensure that all of the R134a was removed and would not contaminate the R245fa. Once the R134a had been removed, nitrogen was used to purge the system. Due to the size of the facility and large number of pipes, the valves were used to split the facility into four parts, with each segment individually vacuumed and cleaned with nitrogen. The change to a new refrigerant requires the experimental facility to be adapted to account for the changes in properties, namely that R245fa is a low pressure refrigerant. The pressure drop between the refrigerant storage tank and the test section is larger than with R134a, therefore requiring a larger pressure in the storage tank for testing. The pressure in the storage tank is controlled with a heater, with the previous heater having a rating of 1.5 kW. Due to the higher pressures required, this heater was replaced with a 3 kW heater. This upgrade required changing the heater variac to account for the increased power and allow greater control.

The increase in heating potential required an increase in the cooling capacity. The amount of R22 coolant entering the system is controlled with valves but the temperature of the R22 could not previously be controlled. An inverter was fitted to the compressor which controls the speed of the compressor and consequently the temperature of the R22.

The test section is heated directly with a DC current, with the applied current being controlled from the power supply. The current is applied through connecting wires to the test section. The original set up was based on stainless steel test sections but the resistivity of copper and brass is considerably lower than that of stainless steel, requiring a much higher current to be applied. This required the system of applying the DC current to be upgraded. The connecting wires were upgraded to take account of the higher current and the connections changed to reduce losses with the now higher current.

3.5 Methodology

The experimental facility is initially allowed time to stabilise, based on the fluctuations of temperature, pressure and mass flux. Once the facility was deemed stable, based on the oscillations in the inlet conditions, the inlet pressure and mass flux are set with an inlet subcooling of 10 K to allow for an initial single phase test. The DC power supply is used to apply a small amount of heat to the test section, which is used

to estimate the thermal loss coefficient and heat losses. The pre-heater is then used to decrease the inlet subcooling to 5 K. The facility must once again be given time for the wall thermocouples to reach a steady state. The high speed camera is used to simultaneously record the flow patterns with the recorded heat transfer data. Data is recorded for 90 seconds at a frequency of 1 Hz. The heat flux is then further increased in equal increments and the process repeated until an exit quality of approximately 0.95 or dry out occurred, at which point the experiments were stopped to prevent damage to the test section. The heat flux was then decreased, in the same increments as previously used. This experimental procedure was repeated for the remaining mass fluxes at the set inlet pressure, after which a new inlet pressure was set. The experiments are based on varying the heat flux for a constant mass flux and inlet pressure. The results are analysed using engineering equation solver (EES) to calculate the local heat transfer coefficient along the tube.

3.6 Test section

The current study investigated three test sections of different materials, stainless steel, brass and copper. All of the test sections are seamless cold drawn with an internal diameter of 1.1 mm, see Chapter 4 for further details on the test sections. The test sections have a calming section of 150 mm and a heated length of 300 mm. The test sections are the same in design, with the schematic seen in figure 3.5. The test section is a vertical upwards flow channel which consists of a preheater, calming section, heated section and observation section. The test section is held between two flanges which allow for the section to be easily removed. The pre-heater section consists of a rope heater wrapped around a 6 mm diameter stainless steel tube. The calming section is 150 mm stainless steel tube of 1.1 mm diameter. The length of the calming section is calculated based on the hydrodynamic developing length required for the channel diameter. The required length differs depending on whether the flow is laminar or turbulent. As laminar flow can require the longest length, this is used for the calculation to ensure that the flow will be fully developed across the whole experimental range. The equation used is based on the Reynolds number and diameter, see equation 3.1 from Incropera (2007). The Reynolds number was taken to be 2000, corresponding to a mass flux of 650 kg/m^{2}s. The calming section length is actually larger, with a safety factor of 1.5 included.

$$\frac{L_{h,fd}}{D} = 0.05Re \tag{3.1}$$

The heated section is heated directly using DC current which is supplied with a 6 kW DELTA ELEKTRONIKA BV, Model SM30-300 power supply from TELONIC INSTRUMENTS LTD. The current is applied through wires which are soldered onto copper electrodes at the inlet and outlet of the heated section. PTFE tubing was used to electrically insulate the heated section from the rest of the test section. The first and last wall thermocouples are positioned away from the electrodes to avoid readings being affected by axial heat transfer, i.e, end heat losses. Fourteen K-type wall thermocouples which are equidistantly spaced along the heated section are attached using Omega electrically insulating epoxy. The first thermocouple is 15 mm from the electrode and the last thermocouple is 25 mm below the electrode. Prior to attaching the thermocouples the outside wall is coated with a thin layer of electrically insulating varnish. T-type hypodermic thermocouples, from Omega, are used to measure the fluid temperature at the inlet and outlet of the heated section and the outlet of the observation section. The pressure is also measured at these points with Druck pressure transducers PDCR4010 and PDCR910-0826. An Omega Model PX771A-025DI differential pressure transducer is fitted across the heated length. A borosilicate glass tube at the exit of the heated section allows for flow visualisation. The flow patterns are recorded using a high speed camera (Photo-Sonics, Model Phantom V4 B/W, 1000 frames/s and 512 × 512 pixels). An exit calming section is used to ensure that there is no influence from the upstream flow due to sudden area enlargement, which would affect the flow patterns and recorded data from the heated section.

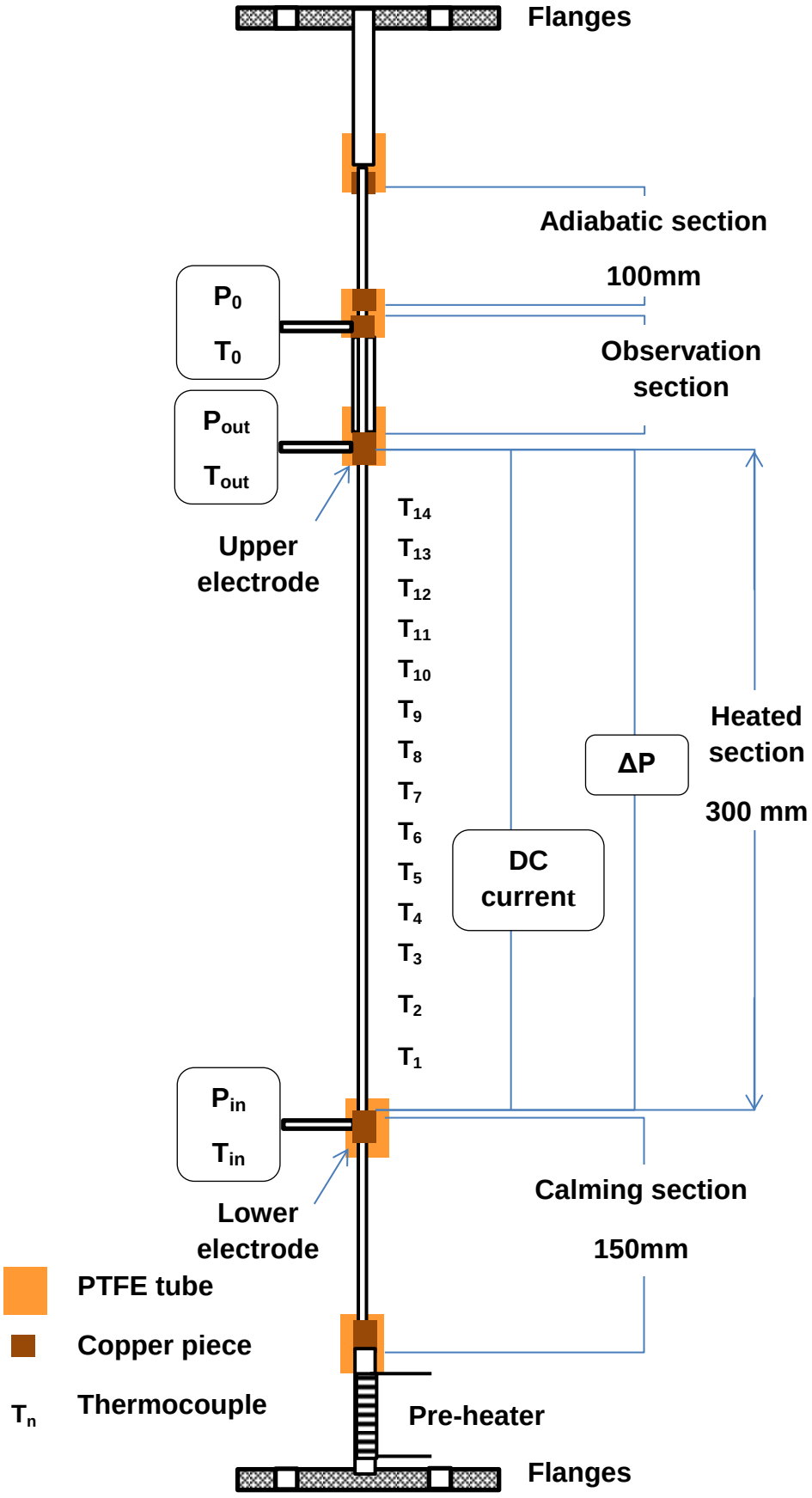

Figure 3.5. Schematic of the test section.

3.7 Data reduction

The heat transfer coefficient and two phase pressure drop is not directly measured but calculated from the measured parameters through data reduction. Both single phase and two phase parameters are investigated. Single phase parameters, including the friction factor and heat transfer coefficient, are used to validate the two phase experimental results. The data is recorded over 90 seconds, at a rate of 1 data point per second, and time averaged.

3.7.1 Single phase data

There are no restrictions at the inlet and outlet, and calming sections ensure that the flow is fully developed. Therefore standard equations for fully developed flow can be used. The single phase results are validated by a comparison of the experimental friction factor and the predicted friction factor which are plotted as a function of the Reynolds number, figure 3.6. The experimental friction factor is calculated from the liquid density (ρ_L), measured pressure drop (ΔP_m), inside channel diameter, mass flow rate and length, see equation 3.2. The friction factor is predicted for both laminar and turbulent flow from commonly used equations, equations 3.3 to 3.5.

$$f = \frac{\pi}{32}\frac{\rho_L \Delta P_m D_i^5}{\dot{m}^2 L} \tag{3.2}$$

Laminar flow theory: $f = \frac{16}{Re}$ for Re < 2000 (3.3)

Blasius (1913): $f = 0.079\, Re^{-0.25}$ for 2000 < Re > 100000 (3.4)

Choi et al. (1991): $f = 0.035\, Re^{-0.182}$ for 4000 < Re > 18000 (3.5)

Figure 3.6 represents the experimental single phase friction factor compared with the above equations. The error shown on the experimental data is based on the uncertainty which is discussed later in section 3.8.

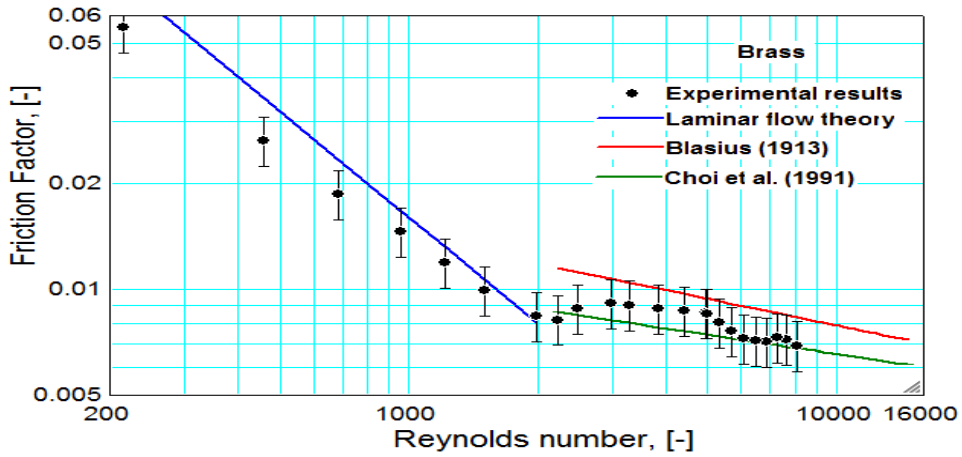

(a)

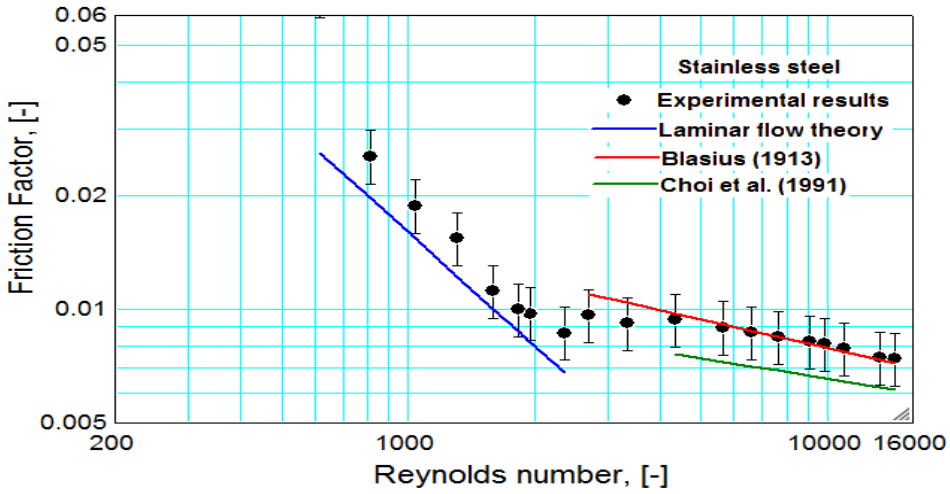

(b)

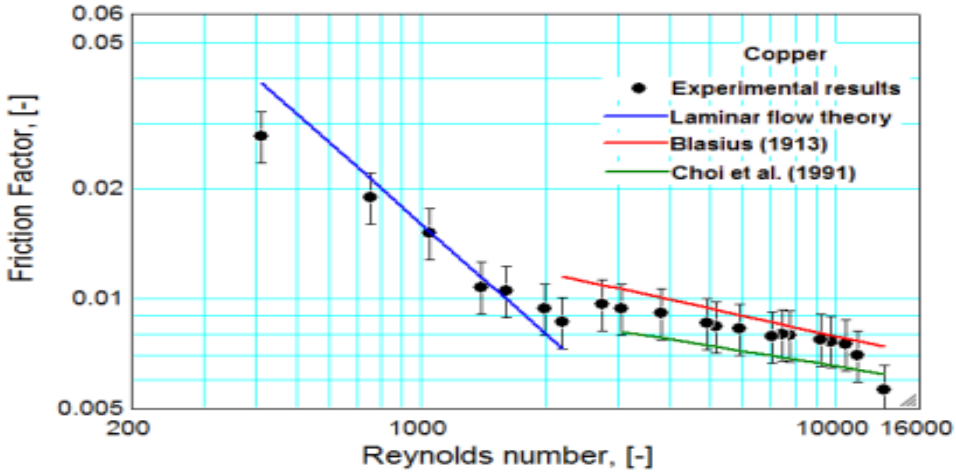

(c)

Figure 3.6. Single phase friction factor as a function of Reynolds number for (a) brass, (b) stainless steel and (c) copper.

The transition from laminar to turbulent flow can be clearly seen for all of the materials, within the region of Re=2000-3000. For both copper and brass, Reynolds

numbers of less than 500 were seen to have a lower friction factor than predicted with the laminar flow theory. For the turbulent region, Blasius (1913) performed well for stainless steel and copper, with the error being less than that of the laminar region. Choi et al. (1991) showed greater accuracy with brass, which has the lowest friction factor values in the turbulent region.

The single phase heat transfer coefficient is used to further validate the experimental results. The heat flux is not directly measured but calculated from the input power, heat loss and volume, see equation 3.6.

$$q = \frac{VI - Q_{loss}}{\pi D_i L_h} \tag{3.6}$$

The heat loss is calculated using a thermal loss coefficient (C_L), estimated during the single phase experiments and the average temperature difference across the insulation. The inside temperature ($T_{w,J}$) and outside temperature ($T_{ins,0}$) of the heated section insulation is measured using K type thermocouples.

$$\overline{\Delta T} = \frac{1}{N}\sum_{J=1}^{N} T_{w,J} - T_{ins,0} \tag{3.7}$$

$$C_L = \frac{VI - \dot{m}C_p(T_{out} - T_{in})}{\overline{\Delta T}} \tag{3.8}$$

$$Q_{loss} = C_L \overline{\Delta T} \tag{3.9}$$

The local single phase heat transfer coefficient is a function of the heat flux and the temperature between the inlet and the fluid bulk temperature, see equation 3.10.

$$h_{sp}(z) = \frac{q}{T_{wi}(z) - T_{fb}(z)} \tag{3.10}$$

Equation 3.11 represents the energy balance used to estimate the fluid bulk temperature, where z is the axial distance along the tube.

$$T_{fb}(z) = T_{in} + \frac{q\pi D_I}{GAC_p} z \tag{3.11}$$

The inside wall temperature is calculated based on one dimensional heat conduction with internal heat generation, see equation 3.12. The outside wall temperature is measured with fourteen K type thermocouples. The thermal conductivity of the wall, k_w, is taken from Engineering Equation Solver (EES).

$$T_{wi}(z) = T_{wo}(z) + \left[\frac{Q_v D_o^2}{16\, k_w}\right]\left[1 - \left(\frac{D_i}{D_o}\right)^2 + ln\left(\frac{D_i}{D_o}\right)^2\right] \tag{3.12}$$

The single phase heat transfer coefficient is then used to obtain the dimensionless Nusselt number, see equation 3.13.

$$Nu(z) = \frac{h_{sp}(z) D_i}{K_l} \tag{3.13}$$

Equation 3.14 is integrated to find the average Nusselt number for the heated section.

$$\overline{Nu} = \frac{1}{L_T}\int_0^{L_T} Nu(z)dz \tag{3.14}$$

This value is compared with Nusselt number values from literature for fully hydrodynamically developed flow, as a function of Reynolds number.

The Shah and London (1978) correlation is used for hydrodynamically developed flow but thermally developing flow. This can be applied to both laminar and turbulent flow, using the Graetz, Gz, number which is defined as:

$$Gz = \frac{RePr}{L/D} \tag{3.15}$$

For Shah and London (1978), the Graetz number must be evaluated first so that the appropriate Nusselt number correlations can be used:

$$Nu = \begin{cases} 1.953Gz^{1/3} & Gz \leq 33.3 \\ 4.364 + 0.0722Gz & Gz > 33.3 \end{cases} \tag{3.16}$$

An alternative correlation which can be applied to both laminar and turbulent flow is that of Choi et al. (1991) given in equation 3.17.

$$Nu = \begin{cases} 0.000972Re^{1.17}Pr^{1/3} & Re < 2000 \\ 3.82 \times 10^{-6}Re^{1.96}Pr^{1/3} & 2500 < Re < 20000 \end{cases} \tag{3.17}$$

Other correlations which have been considered are applicable only to the turbulent region, see equations 3.18 to 3.23.

Dittus-Boelter (1930): $Nu_{DB} = 0.023Re^{0.8}Pr^{0.4}$ (3.18)

Petukhov (1970): $$Nu_P = \frac{\left(f_p/_8\right)RePr}{1.07+12.7\left(f/_8\right)^{1/2}\left(Pr^{2/3}-1\right)}\left(\frac{\mu_{bulk}}{\mu_{wall}}\right)^{0.14} \tag{3.19}$$

Gnielinksi (1976): $$Nu_G = \frac{\left(f_p/_8\right)RePr}{1+12.7\left(f/_8\right)^{1/2}\left(Pr^{2/3}-1\right)}\left(\frac{\mu_{bulk}}{\mu_{wall}}\right)^{0.14} \tag{3.20}$$

where: $f_p = (1.82logRe - 1.64)^{-2}$ (3.21)

Adams et al. (1998): $Nu_A = Nu_G(1 + F_A)$ (3.22)

where: $F_A = 7.6 \times 10^{-6}Re\left(1 - \left[\frac{D_i}{1.164}\right]^2\right)$ (3.23)

Figure 3.7 represents a comparison of the single phase experimental Nusselt number and the above correlations. The average Nusseult number for the laminar flow was predicted well with Shah-London (1978). Overall, the Dittus-Boelter (1930) showed the best agreement with all three materials for the turbulent region. An example of the local wall temperature used to calculate the average Nusselt number is presented in figure 3.8.

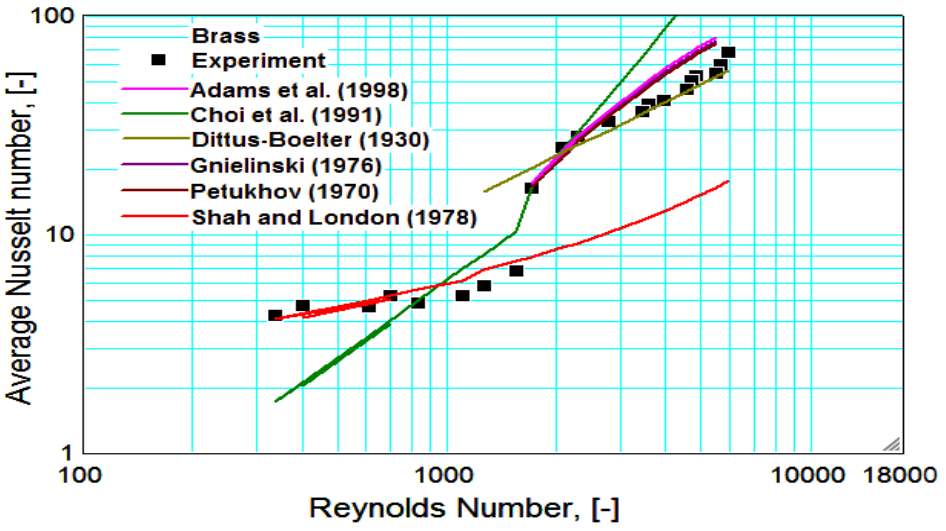

(a)

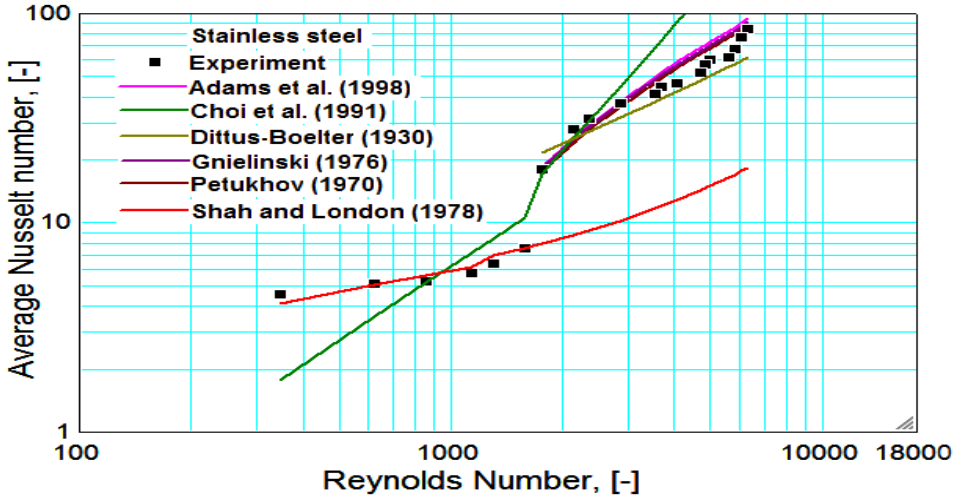

(b)

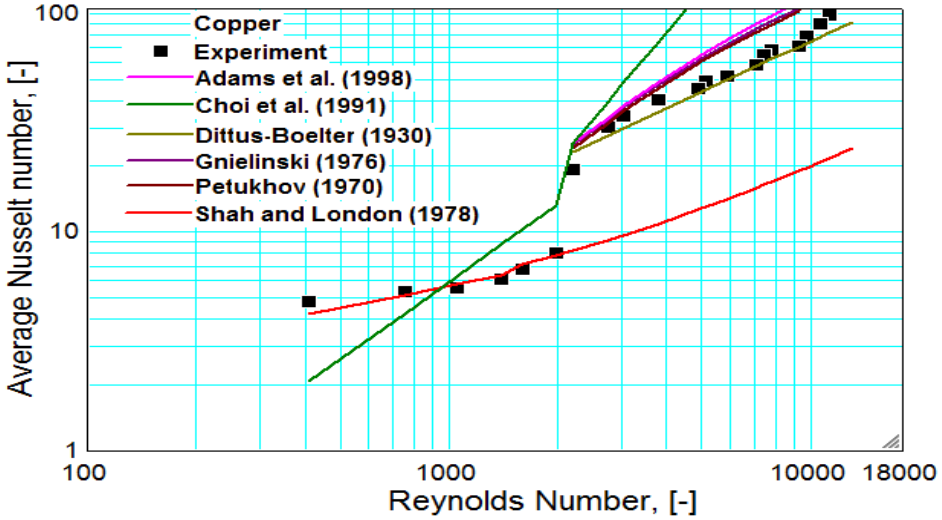

(c)

Figure 3.7. Average Nusselt number as a function of Reynolds number for (a) brass, (b) stainless steel and (c) copper.

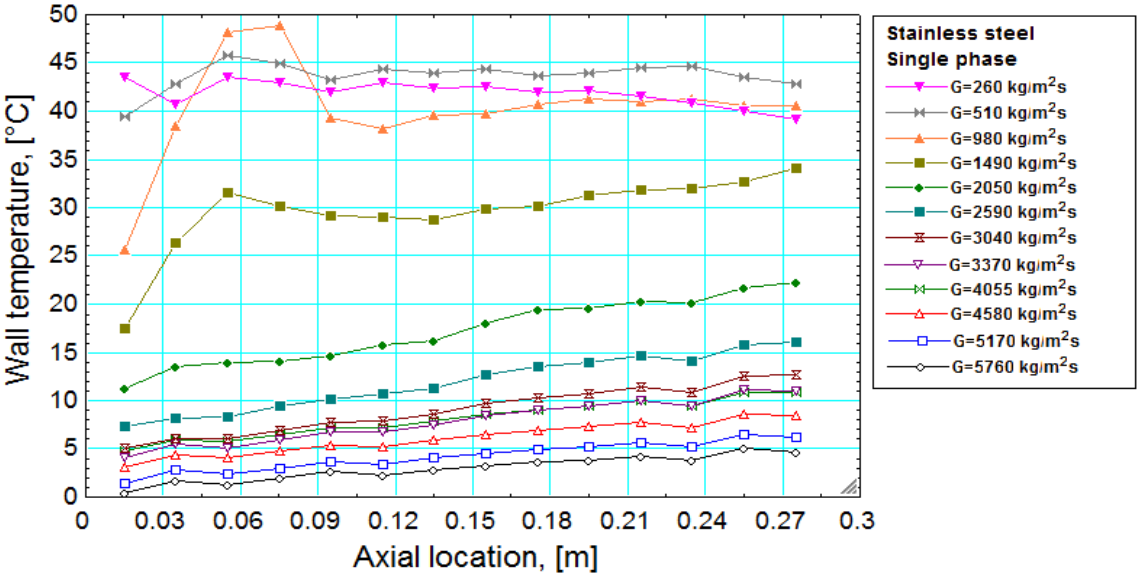

Figure 3.8. Local wall temperature readings for stainless steel single phase experiments.

3.7.2 Two phase data

Heat transfer coefficient

The two phase heat transfer is calculated from the heat flux, inside wall temperate and saturation temperature, see equation 3.24.

$$h_{tp}\,(z) = \frac{q}{T_{wi}\,(z) - T_{sat}(z)} \tag{3.24}$$

The average two phase heat transfer coefficient is calculated from:

$$\overline{h_{tp}} = \frac{1}{L_t}\int_0^{L_T} h_{tp}(z)dz \tag{3.25}$$

The local saturation temperature, $T_{sat}\,(z)$, is calculated from the local pressure, P (z). For this purpose, it is assumed that the two phase pressure drop is linear along the tube length. The length of the sub-cooled section is included and the sub-cooled length, Z_{sub}, is calculated from an energy balance, iterating between equation 3.26 and 3.28. The specific heat, Cp, used in Equation 3.26, is calculated based zero quality and local temperature. The friction factor, f, is calculated from Equations 3.3 and 3.4, depending on the Reynolds number. The saturation temperature ($T_{sat(Zsub)}$) and pressure ($P_{(Zsub)}$) are to be at the location of zero quality.

$$z_{sub} = \frac{GAC_p(T_{sat}(Z_{sub}) - T_{in})}{q\pi D_i} \tag{3.26}$$

$$\Delta P_{sp} = \frac{G^2 2f}{\rho_f D_i} Z_{sub} \tag{3.27}$$

$$P(Z_{sub}) = P_{in} - \Delta P_{sp} \quad (3.28)$$

$$\Delta P_{tp} = \Delta P_m - \Delta P_{sp} \quad (3.29)$$

$$P(z) = P(Z_{sub}) - \frac{Z - Z_{sub}}{L_h - Z_{sub}} \Delta P_{tp} \quad (3.30)$$

Local vapour quality

The local vapour quality can be found from the local enthalpy, which is calculated from equation 3.31. These are calculated from the local pressure, $P(z)$, and an energy balance.

$$h(z) = h_{in} + \frac{q\pi D_i z}{GA} \quad (3.31)$$

The local vapour quality can be found from;

$$x(z) = \frac{h(z) - h_f(z)}{h_{fg}(z)} \quad (3.32)$$

Two phase frictional pressure drop

The two phase frictional pressure drop is the measured pressure drop minus the pressure drop from other factors, including gravity and acceleration, as follows:

$$\Delta P_{tp} = \Delta P_m - \Delta P_{sp} - \Delta P_g - \Delta P_{acc} \quad (3.33)$$

The gravitational and acceleration pressure drop components can be calculated from a variety of methods. The method used for this experimental study depended on the correlation which was being considered for comparison. For example, the pressure drop results were compared with multiple pressure drop correlations, including the Lockhart-Martinelli (1949) correlation. Therefore, for this comparison, the gravitational and acceleration components were calculated from the Lockhart-Martinelli (1949) model, see equations 3.34 to 3.37. The same method is widely used in correlations from literature.

$$X_M = \left(\frac{1-x}{x}\right)^{0.64} \left(\frac{\rho_g}{\rho_f}\right)^{0.36} \left(\frac{\mu_f}{\mu_g}\right)^{0.07} \quad (3.34)$$

$$\alpha = \frac{1}{1 + 0.28 X_M} \quad (3.35)$$

$$\Delta P_{acc} = \frac{G^2}{\rho_f} \left[\frac{x_e^2}{\alpha_e} \frac{\rho_f}{\rho_g} + \frac{(1-x_e)^2}{(1-\alpha_e)} - 1\right] \quad (3.36)$$

$$\Delta P_g = g \frac{L_{tp}}{x_e} \int_0^{x_e} \left[\alpha \rho_g + (1-\alpha)\rho_f\right] dx \quad (3.37)$$

Equation 3.34 represents an example of a void fraction calculation for the Lock-hart Martinelli (1949) correlation. Although there are similarities, the void fraction equation can vary between correlations.

3.8 Uncertainties

The total experimental error is the sum of the systematic and random errors. Systematic errors are those which are repeatable and mainly due to instrumentation. These errors can be reduced by calibrating the instruments before use. Random errors result from unknown entities and can be reduced by increasing the number of readings taken (a larger sample size). Random errors, U_{random}, are accounted for by using a statistical analysis presented by Coleman and Steele (1999), adapted from Moffat (1988) . This method is based on the sample of N measurements following a normal or Gaussian distribution with a confidence level of 95%. The estimation is based on the mean value, $\bar{\bar{X}}$, standard deviation, S_x, and the value of the t distribution at the 95% confidence level, see equations 3.38 to 3.40 from Coleman and Steele (1999).

$$U_{random} = t_{95\%} S_X \tag{3.38}$$

$$S_X = \sqrt{\frac{1}{N-1}\sum_{i=1}^{N}(X_i - \bar{X})^2} \tag{3.39}$$

$$\bar{X} = \frac{1}{N}\sum_{i=1}^{N} X_i \tag{3.40}$$

The systematic uncertainty is calculated from the root sum square method which considers the bias, B_x, resulting from the component, k. This component can come from a variety of sources, including calibration which is often given by the manufacturer, equation 3.41. Coleman and Steele (1999) proposed the standard deviation of the systematic uncertainty, S_{Bx}, to be calculated from 3.42.

$$B_x = \sqrt{\sum_{k=1}^{M}(B_x)_k^2} \tag{3.41}$$

$$S_{Bx} = \frac{B_x}{2} \tag{3.42}$$

Coleman and Steele (1999) cite the ISO guide (1993) for the calculation of the total uncertainty, U, to be evaluated from the combined uncertainty of random and systematic errors,u_c:

$$u_c = \sqrt{S_{Bx}^2 + S_X^2} \tag{3.43}$$

$$U = t_{95\%} u_c \tag{3.44}$$

The error propagation of an experimental variable, r, is the function of the calculated uncertainty of variable, X:

$$r = r(X_1, X_2, X_3, \ldots\ldots\ldots X_j) \tag{3.45}$$

$$U_r^2 = \left(\frac{\delta r}{\delta X_1}\right)^2 U_{x_1}^2 + \left(\frac{\delta r}{\delta X_2}\right)^2 U_{x_2}^2 + \left(\frac{\delta r}{\delta X_3}\right)^2 U_{x_3}^2 + \cdots + \left(\frac{\delta r}{\delta X_j}\right)^2 U_{x_j}^2 \quad (3.46)$$

This can also be presented in the dimensionless form:

$$\frac{U_r^2}{r^2} = \left(\frac{X_1}{r}\frac{\delta r}{\delta X_1}\right)^2 \left(\frac{U_{x_1}}{X_1}\right)^2 + \left(\frac{X_2}{r}\frac{\delta r}{\delta X_2}\right)^2 \left(\frac{U_{x_2}}{X_2}\right)^2 + \cdots + \left(\frac{X_j}{r}\frac{\delta r}{\delta X_j}\right)^2 \left(\frac{U_{x_j}}{X_j}\right)^2 \quad (3.47)$$

This method was applied to the experimental parameters, the range of which is presented in Table 3.1. The uncertainty of the measured parameters is seen in Table 3.2. The uncertainty is presented as the percentage of the measuring range. These uncertainties are mostly given by the manufacturer or achieved through calibration. Calibration was conducted on pressure sensors using a deadweight tester, where calibrated weights are applied to generate a known pressure. Thermocouples were calibrated in a water bath, over a range of 10 – 90 ˚ C. The temperature of the water was increased in 5 ˚ C increments, with the corresponding thermocouple temperatures recorded on a data logger. Temperature and pressure calibrations were conducted three times. The actual and measured values were plotted on a graph and the best fit line used as the calibration equation. The actual temperature is determined with a temperature probe, with a manufacturing calibration of 0.01 %. The calibrated error refers to the largest difference between the measured value and the line of best fit.

Table 3.1. Range of experimental parameters

Parameter	Range
Inside Diameter, [mm]	1.1
System Pressure, [bar]	1.85, 2.45
Mass flux, [kg/m^{2}s]	100-400
Heat flux, [kW/m^2]	0.5-60
Exit quality, [-]	0.05-0.95
Inlet sub-cooling, [K]	-5

Table 3.2 Uncertainty in measured parameters

Parameter	Measuring method	Uncertainty
Outside diameter	Micrometer	±0.01mm
DC Voltage	Yokogawa power meter WT110	±0.29% (manufacturer)
DC Current		
Mass flow rate	Coriolis flow meter (CFM010)	±0.044% (manufacturer)
Inlet pressure	DRUCK PDCR4010	±0.42% (calibration)
Outlet Pressure	DRUCK PDCR910-826	±0.26% (calibration)
Observation section outlet pressure	DRUCK PDCR910-826	±0.26% (calibration)
Fluid temperature	T-type thermocouples	±0.18K
Wall temperature	K-type thermocouples	±0.23K
Differential Pressure	PX771A-025DI	±0.07% (calibration)

Inside diameter

The inside diameter of the test section and the glass observation tube is calculated from equation 3.48 and the error calculated from 3.49. An example is presented in Equations 3.50- 3.51, calculating the uncertainty in the inside diameter of the copper tube.

$$\frac{\pi}{4}(D_o^2 - D_i^2)L = \frac{M}{\rho} \tag{3.48}$$

$$U_{Di} = \left(D_o^2 - \frac{4M}{\pi\rho L}\right)^{-1/2} \cdot \sqrt{\left(D_o U_{D_o}\right)^2 + \left(\frac{-2}{\pi\rho L} U_M\right)^2 + \left(\frac{2M}{\pi\rho L^2} U_L\right)^2} \tag{3.49}$$

$$U_{Di} = \left(0.00159^2 - \frac{4 * 0.0003289}{\pi * 8948 * 0.3}\right)^{-\frac{1}{2}} \cdot \sqrt{(0.00159 * 0.00001)^2 + \left(\frac{-2}{\pi * 8948 * 0.3} * 0.00001\right)^2 + \left(\frac{2 * 0.0003289}{\pi * 8948 * 0.3^2} * 0.001\right)^2} \tag{3.50}$$

To calculate the percentage error;

$$\frac{U_{D_i}}{D_i} * 100 = \frac{1.050 * 10^{-5}}{0.00109} * 100 = 0.96\% \tag{3.51}$$

The outside diameter of the tube is measured at multiple locations along the length of the tube using vernier callipers, with an uncertainty of ± 0.01mm. A ruler,

with an uncertainty of ± 1mm, is used to measure the tube length. The tube mass is measured using a digital balance with a resolution of five decimal places, equating an uncertainty of ± 0.00001g. The density of the material is assumed to have no uncertainty. Table 3.3 shows the calculated uncertainty for inside diameters.

Table 3.3. Percentage uncertainty of test section inside diameters.

Inside Diameter, mm	Uncertainty, %
1.1 Stainless steel	±1.28
1.09 Brass	± 1.46
1.09 Copper	±0.89
Glass observation tube	±0.36

Mass Flux

The mass flux is a function of the mass flow rate, $\dot{m}$, and the inside diameter, see equation 3.50. The mass flow rate is measured through a coriolis flow meter which has a manufacturer's uncertainty of ±0.044%. The uncertainty is calculated from equation 3.53.

$$G = \frac{4\dot{m}}{\pi D_i^2} \tag{3.52}$$

$$\frac{U_G}{G} = \sqrt{\left(\frac{U_{\dot{m}}}{\dot{m}}\right)^2 + \left(2\frac{U_{D_i}}{D_i}\right)^2} \tag{3.53}$$

Table 3.4 presents the uncertainties in the mass flux calculations. The uncertainty varies between test sections due to the difference in value and uncertainty of the inside diameter.

Table 3.4. Percentage uncertainty of the mass flux for each heated section.

Test section, mm	Mass flux range, kg/m^{2}s	Uncertainty, %
Stainless Steel	100-400	2.56
Brass	100-400	2.92
Copper	100-400	1.78

Heat loss

The heat loss is required to calculate the heat flux and is based on the heat loss coefficient. The uncertainty in the heat loss coefficient is from the uncertainty in the voltage (V), current (I), mass flow rate and temperature.

$$C_L = \frac{VI - \dot{m}C_p(T_{out} - T_{in})}{\Delta T} = \frac{VI - \dot{m}C_p\Delta T_{fluid}}{\Delta T} \tag{3.54}$$

$$U_{C_L} = \sqrt{\left(\frac{I}{\Delta T}U_V\right)^2 + \left(\frac{V}{\Delta T}U_I\right)^2 + \left(-\frac{C_p\Delta T_{fluid}}{\Delta T}U_{\dot{m}}\right)^2 + \left(-\frac{\dot{m}C_p}{\Delta T}U_{\Delta T_{fluid}}\right)^2 + \left(-\frac{\dot{m}C_p\Delta T_{fl;uid}}{\Delta T^2}U_{\Delta T}\right)^2} \tag{3.55}$$

The above equation gives an uncertainty of ± 0.0169 W/K for the stainless steel, ± 0.09511 W/K for the brass and ± 0.082 W/K for the copper. The difference in the uncertainty between the materials is due to the changes in the actual values and uncertainty of the voltage, current and mass flow rate. The uncertainty in the heat loss can then be calculated, see equation 3.56.

$$U_{Q_{loss}} = \sqrt{\left(\Delta T U_{C_L}\right)^2 + (C_L U_{\Delta T})^2} \tag{3.56}$$

The heat loss uncertainty is calculated to be ± 0.21 W for stainless steel, ± 0.82 W for copper and ± 0.95 W for brass. The heat flux is a function of the voltage, current, heat loss and volume, see equation 3.57.

$$q = \frac{VI - Q_{loss}}{\pi D_i L_h} \tag{3.57}$$

$$U_q = \sqrt{\left(\frac{I}{\pi D_i L_h}U_v\right)^2 + \left(\frac{V}{\pi D_i L_h}U_I\right)^2 + \left(-\frac{U_{Q_{loss}}}{\pi D_i L_h}\right)^2 + \left(-\frac{q}{D_i}U_{D_i}\right)^2 + \left(-\frac{q}{D_i}U_{L_h}\right)^2} \tag{3.58}$$

The percentage uncertainty, see in Table 3.5, is greater for the brass heated section due to the higher resistance and therefore higher current.

Table 3.5. Percentage uncertainty of the heat flux for each heated section.

Test section, mm	Heat flux range, kW/m^2	Uncertainty, %
Stainless Steel	1-70	0.2 - 1.5
Brass	0.5-40	0.9 - 2.1
Copper	0.5-40	0.8 - 1.7

Heat transfer coefficient

The method used to calculate the uncertainty in both the single phase and two phase heat transfer coefficient is the same, equation 3.59.

$$U_h = \sqrt{\left(\frac{U_q}{\Delta T}\right)^2 + \left(-\frac{q}{\Delta T^2} U_{\Delta T}\right)^2} \tag{3.59}$$

The temperature difference used for calculation changes between single and two phase heat transfer coefficient, see equations 3.60 and 3.61.

$h_{tp}(z) = \frac{q}{T_{wi}(z) - T_{sat}(z)}$ for boiling (3.60)

$h_{sp}(z) = \frac{q}{T_{wi}(z) - T_{fb}(z)}$ for single phase (3.61)

This gives an uncertainty rang e of 0.038 – 1.8 % for the single phase heat transfer coefficient and 0.28 – 8.4 % for the two phase heat transfer coefficient.

Local quality

As previously discussed, the local vapour quality is evaluated in terms of the enthalpies and an energy balance. Combining these equations gives the local vapour quality equation to be:

$$x(z) = \frac{h_{in} - h_f}{h_{fg}} + \frac{q\pi D_i z}{\dot{m} h_{fg}} \tag{3.62}$$

Equation 3.63 shows the uncertainty to be a function of the energy balance, with the uncertainty in the enthalpies, obtained from EES, assumed to be negligible.

$$U_x = \sqrt{\left(\frac{\pi D_i z}{\dot{m} h_{fg}} U_q\right)^2 + \left(\frac{q\pi z}{\dot{m} h_{fg}} U_{D_i}\right)^2 + \left(\frac{q\pi D_i}{\dot{m} h_{fg}} U_z\right)^2 + \left(-\frac{q\pi D_i z}{\dot{m}^2 h_{fg}} U_{\dot{m}}\right)^2} \tag{3.63}$$

This gives the uncertainty in the local vapour quality to be from 1.1- 1.9% across the vapour quality range.

Single phase friction factor

Equation 3.64 represents the uncertainty in the friction factor. This is based on the measured pressure drop, inside diameter, mass flow rate and heated length. These vary with the experimental conditions, as does the liquid density, resulting in an average value of 15% being taken. The uncertainty ranges from 11 – 19 % across the Reynolds number range.

$$\square_f = \sqrt{\left(\frac{\pi^2 \rho_L D_i^5}{32\dot{m}^2 L} U_{\Delta P_m}\right)^2 + \left(\frac{5\pi^2 \rho_L \Delta P_m D_i^4}{32\dot{m}^2 L} U_{D_i}\right)^2 + \left(-\frac{\pi^2 \rho_L \Delta P_m D_i^5}{16\dot{m}^3 L} U_{\dot{m}}\right)^2 + \left(-\frac{\pi^2 \rho_L \Delta P_m D_i^5}{32\dot{m}^2 L^2} U_L\right)^2} \quad (3.64)$$

Single phase Nusselt number

The single phase Nusselt number is a function f the single phase heat transfer coefficient and diameter. The liquid thermal conductivity, taken from EES, is assumed to have no error. Equation 3.65 gives an error range of 1.8- 15.9 %.

$$U_{Nu_{sp}} = \sqrt{\left(\frac{D_i}{k_f} \square_{h_{sp}}\right)^2 + \left(\frac{h_{sp}}{k_f} U_{D_i}\right)^2} \quad (3.65)$$

The percentage uncertainties of the calculated parameters are presented in table 3.6.

Table 3.6. Percentage uncertainties of the calculated parameters.

Parameter	Range, %
Single phase heat transfer coefficient	0.038 – 1.8
Two phase heat transfer coefficient	0.28 – 8.4
Local quality	1.1 – 1.9
Single phase friction factor	11 - 19
Single phase Nusselt number	1.8 – 15.9

3.9 Summary

The experimental test facility used to investigate flow boiling heat transfer, pressure drop and flow patterns, originally designed by Huo(2005), is described. The test facility was originally designed to investigate stainless steel tubes of varying diameter and heated lengths. This test facility has now been updated to use R245fa, a new generation low pressure refrigerant. Upgrades to the facility, to account for the change in thermophysical properties of R245fa, include changes to the heating and cooling loop. Single phase experiments were conducted; both the friction factor and Nusselt number were compared with single phase correlations in good agreement. The measuring equipment was calibrated to reduce systematic errors and an uncertainty analysis completed.

Chapter 4

4. Surface Characteristics

4.1 Introduction

The effects of the change in refrigerant and the change of surface characteristics were investigated in the current study. The same stainless steel test section which had previously been investigated using R134a was used to negate the effect of surface characteristics for the refrigerant comparison. The investigation into the surface characteristics was based on this stainless steel (Grade 304) tube in addition to a copper (99% purity) and a brass (62% copper and 26% zinc) tube. The materials were chosen based on their common use in heat exchangers and the large difference in properties, including thermal conductivity and surface finish. The tubes are produced by seamless cold drawing and have an internal diameter of 1.1 mm.

The surface characteristics of each tube material were analysed and compared. A sample was cut from each end of the test sections (before the test section was used). These samples were carefully grinded in half to expose the inner surface of the tube. Both samples were examined for all the materials and further samples taken if there were inconsistencies between the two readings. The test sections were all analysed using scanning electron microscopy (SEM) and confocal laser scanning microscopy (CFLSM). Before undertaking any surface readings, the sections were cleaned in acetone to remove any dust or dirt which would skew the results. Both techniques were undertaken at Brunel University, the SEM at the Experimental Techniques Centre (ETC) and the CFLSM on loan from the EPSRC Engineering Instrument Pool (EIP). Further testing included the use of a CFLSM at Cranfield University. The aim of this further testing was to evaluate the difference in readings from different laboratories. The SEM results allowed for the surfaces to be visually compared for both material structure and potential cavities. SEM readings were taken at four scales, magnifying the sample image by 500 to 20000 times, which allows for an overview of the surface and further investigation of potential cavities and surfaces flaws. SEM analyse included determining the material composition which confirmed that any inconsistencies on the surface were not a foreign substance but an effect of the manufacturing process. The CFLSM was used to produce a 3D surface profile and obtain surface parameter data,

including Ra values. Readings were taken over a range of surface areas, resolutions and cut-off wavelengths.

All of the materials were seen to give uniform results for both sections with the SEM and the CFLSM. There was no evidence of surface flaws or imperfections which would skew the readings.

4.2. Manufacturing Process

There are many manufacturing methods used for producing small diameter tubes. Mahmoud (2012) investigated flow boiling in stainless steel tubes which had been welded and seamless cold drawn. This study found large discrepancies in the trend and magnitude of the heat transfer coefficient between the two tubes. In this study, all of the tubes were produced using the seamless cold drawn process to negate any differences in the surface due to the manufacturing process.

The surface finish of the tubes, even with the same manufacturing processes being used, is a function of the material. Manufacturing a seamless tube requires a solid bar to be passed between two rollers where a piercing point is used to produce a hollow tube. These tubes are then stretched to reduce the diameter. There is the option of hot or cold working the tube from this point, depending on the requirements. The cold drawn tubes have increased strength and tolerances compared with tubes made by hot rolling. Due to the small size and more uniform tolerances, cold drawn tubes were used for this investigation. The cooled tubes are further worked through a die or over a mandrel, reducing the size until the required dimensions. This process can change the grain structure and surface conditions [Okazaki, 2008]. The minimal amount of tube handling allows for an improved surface finish. These three materials have varying properties which will affect the surface finish.

4.3. Scanning Electron Microscopy (SEM)

Scanning electron microscopy uses an electron gun to accelerate electrons towards a specimen, forming a current over the surface. The interaction between the electron beam and the surface region is used to form the image (Khursheed, 2011). This process is conducted under a vacuum. In order to limit contamination to the surfaces, all of the samples were placed into the chamber and the readings taken during one session.

The surfaces were visually inspected with the use of SEM for potential nucleation sites and surface structures, which may aid in flow boiling. The initial scans, at a magnitude of 500, were used to give a large scale view of the internal tube

structure. The areas which are used for further magnification depend on any surface discrepancies seen at this point. At this magnification, it can be clearly seen that each material has a different surface structure, see figure 4.1 Stainless steel and brass, figure 4.1a and 4.1b, are similar in texture and appear uniform in structure. Copper, figure 4.1c, has a smoother texture but has deep ‘stretch marks’ which are not uniform across the surface.

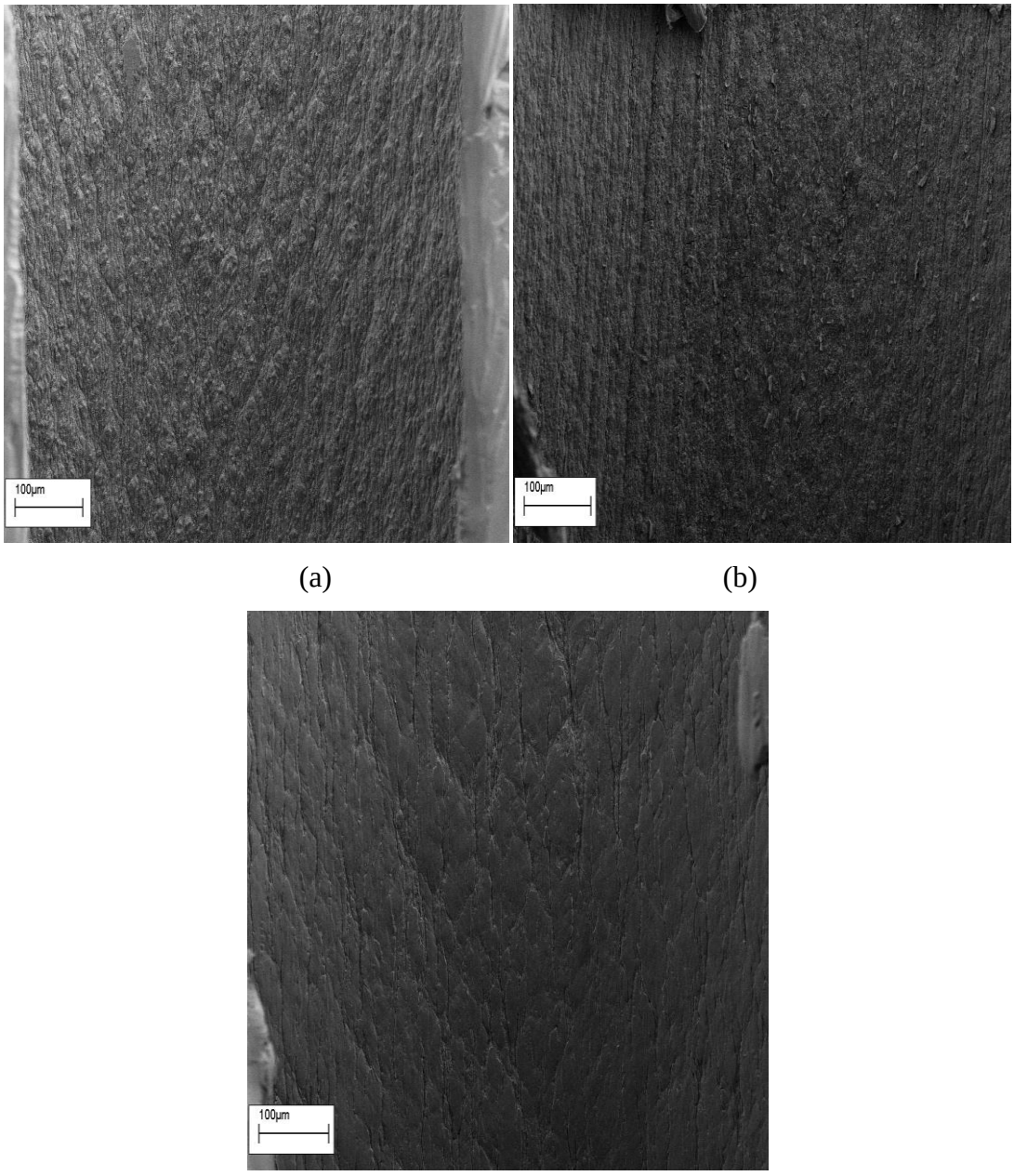

(a) (b)

(c)

Figure 4.1Topography images taken using the SEM at a magnitude of 500 for (a) Stainless steel, (b) Brass and (c) Copper.

Further magnification of the surfaces shows a large difference in the structure of the materials. A comparison of figures 4.2, 4.3 and 4.4 show a large variance in the

surface finish. The stainless steel tube, figure 4.2, shows a non uniform structure of grooves, along the length of the tube, and a deposit which has a splattering effect. The material composition analysis showed the deposit to be stainless steel and not a foreign substance, suggesting that this texture is a result of the manufacturing process. At the largest magnification, figure 4.2b, potential nucleation sites are evident due to cavities in the grooves and in the deposit. This non-uniform structure at both magnifications which suggests a vast number of potential nucleation sites which could aid in flow boiling.

Although the stainless steel and brass sections show similarities at the lowest magnification, figure 4.1, a higher magnification shows large differences in the surface structure. Figure 4.3 shows the brass surface to have a 'flaky' structure with horizontal cracks. These cracks vary in length and width across the length of the tube. At the highest magnification, figure 4.3b, all of the cracks appear to be in the horizontal direction, following the diameter of the channel, which adds some uniformity to the surface structure. Vertical creases, along the channel length, are evident which, similar to stainless steel, are curved along the length of the surface.

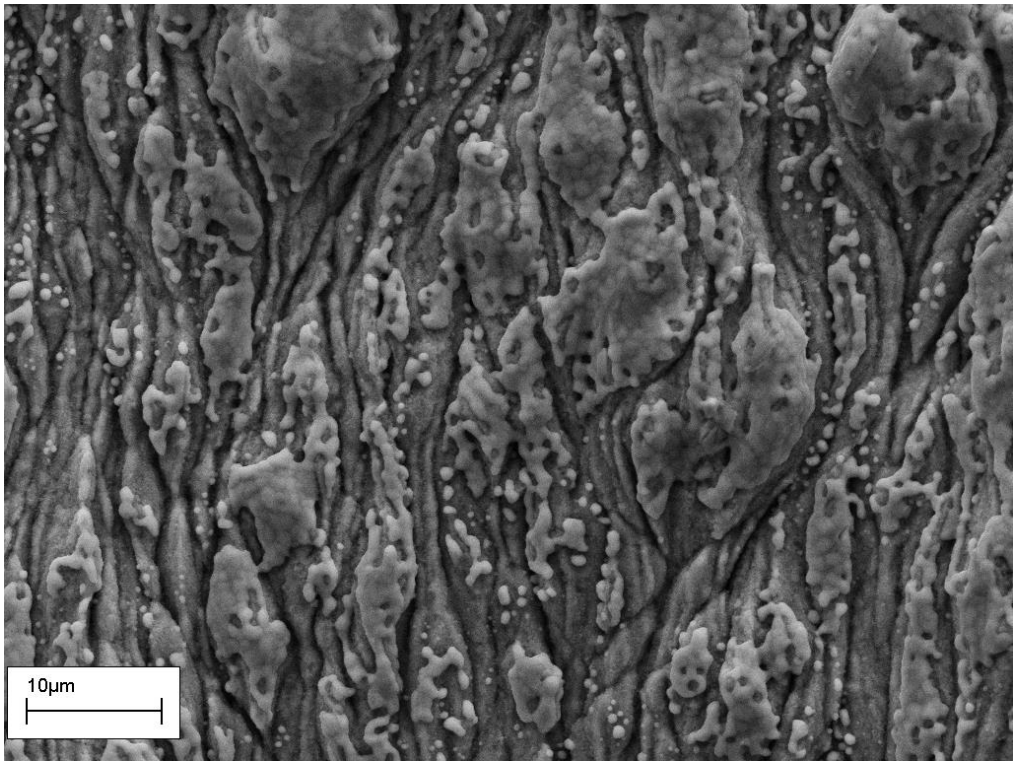

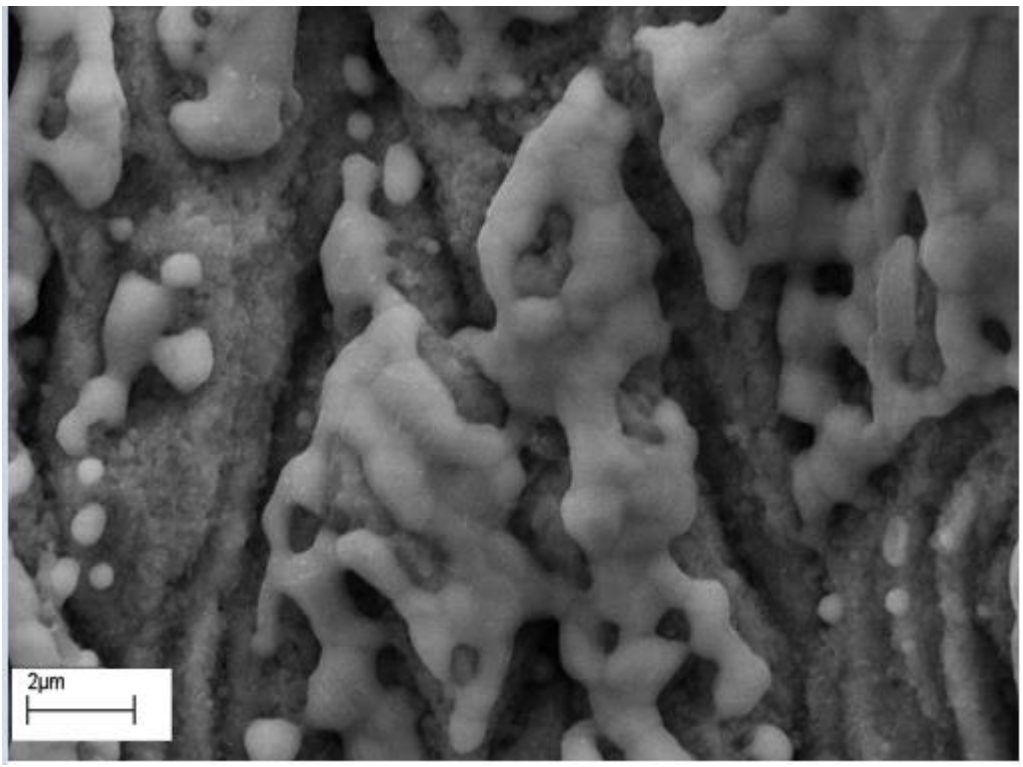

Figure 4.2 Topography images for stainless steel taken using the SEM at a magnitude of (a) 5000 and (b) 20000.

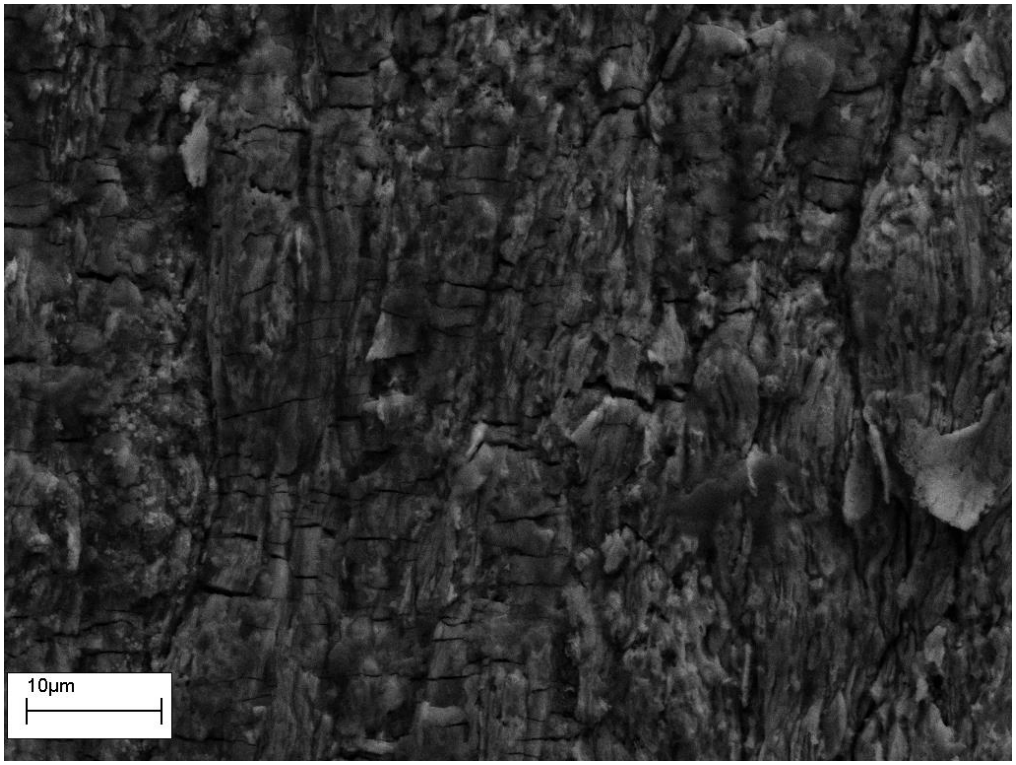

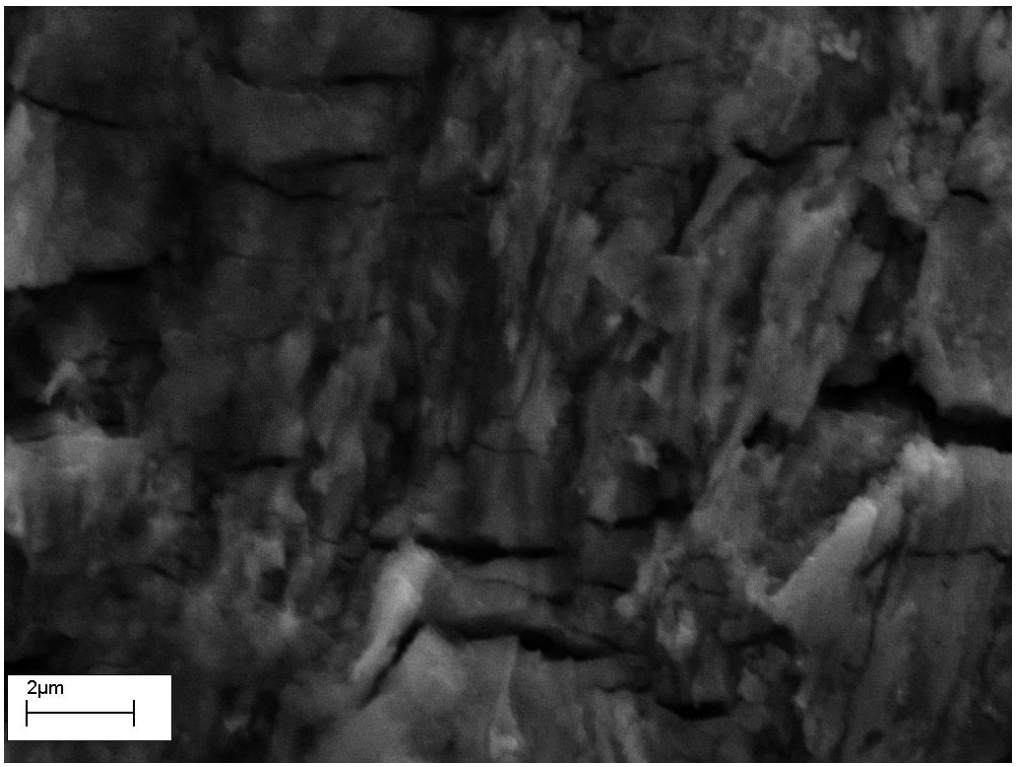

Figure 4.3. Topography images for brass taken using the SEM at a magnitude of (a) 5000 and (b) 20000.

Figure 4.4 represents the copper surface, which is the smoothest in appearance. The surface structure has grooves which follow the channel length, but straighter and shallower in comparison to the stainless steel, figure 4.2a. The copper surface does have some deeper grooved but the majority are shallow ‘stretch’ marks. It is likely that these are due to the rolling process during manufacture. Figure 4.4b shows that the surface to be smooth between these deep grooves.

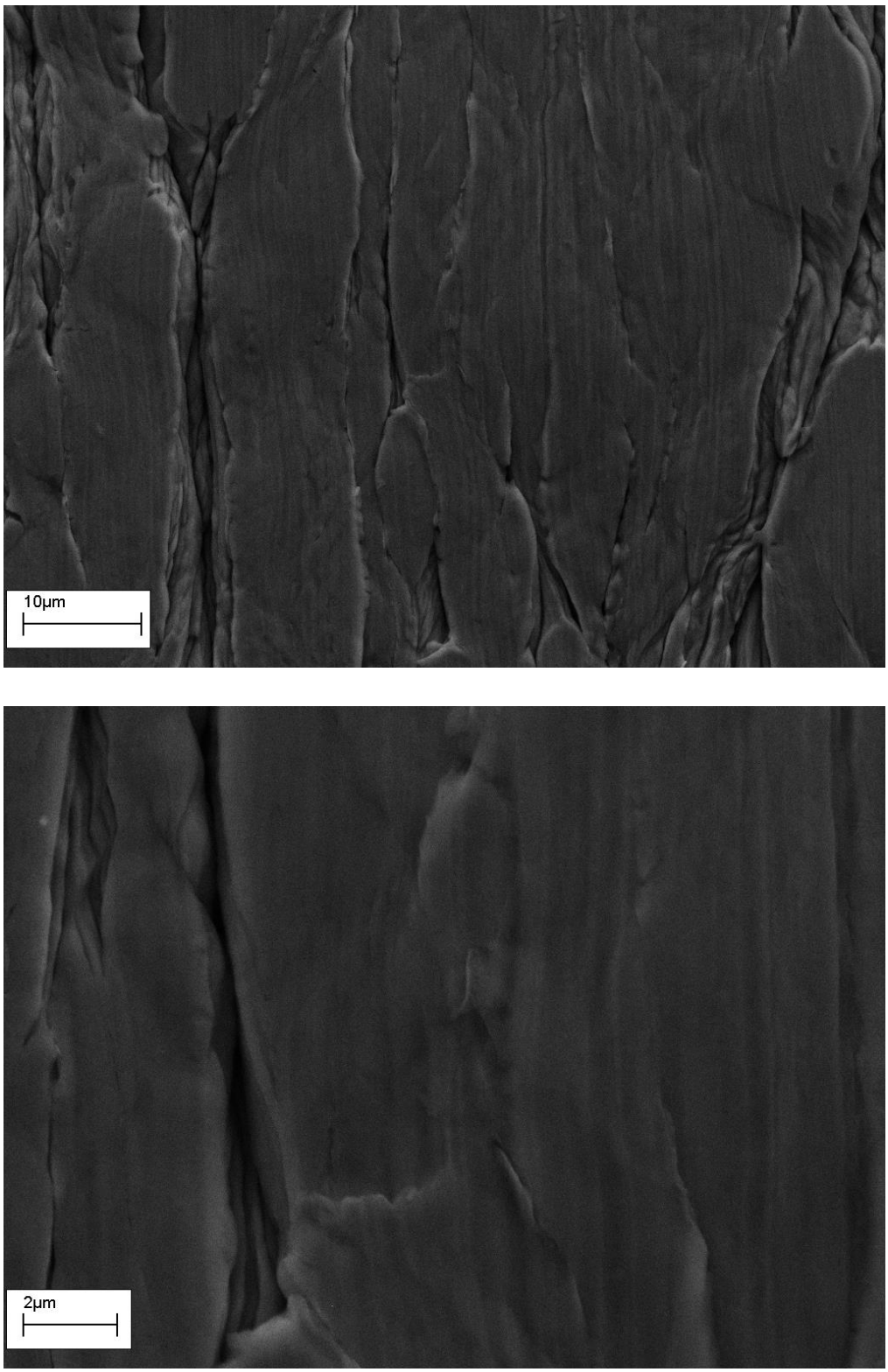

Figure 4.4. Topography images for copper taken using the SEM at a magnitude of (a) 5000 and (b) 20000**.**

All of the materials show grooves which follow the length of the channel, which is probably the result of stretching during manufacture. The severity, depth and uniformity of these grooves vary between the materials. The surface finish, besides the

grooves, also varies between the materials. The grooves for stainless steel and brass are less uniform, both curving as opposed to the copper grooves which are relatively straight.

4.4. Confocal Laser Scanning Microscopy (CFLSM)

Confocal laser scanning miscroscopy is a method of measuring 3D surface topography. This methodology is noted for having a high resolution and can be applied to multiple applications. A laser is focused on the surface and the intensity of the returning laser is used to determine the surface features. The laser scans across the given area, producing a 3D image of the surface (R. Leech, 2011). The outputs from this scan include a 3D image, a 2D profile along the surface length and the surface parameter data.

TaiCaan XYRIS 3D surface profiler

This TaiCaan model uses a 670 nm laser with a spot size of 2 µm to produce a 3D model of the surface. This 3D model is analysed for 2D data plots and surface parameter data. Each sample was scanned at multiple locations to give an accurate representation of the surface and prevent surface parameters being skewed by random surface defects. The initial 3D model was produced from a pre-set scan area and scan resolution. The scan area and the scan resolution are co-dependent; one characteristic cannot be changed without affecting the other. The resolution is the number of points in the x and y axis that the laser scans, forming a grid on the surface. The surface data is averaged across each cell. Therefore, a higher resolution means a larger number of cells which reduces the averaging required. This should give a more accurate view of the microstructure but does increase the scan time. A surface which is twice the size and twice the resolution will result to the same amount of data averaging as a smaller sample with a lower resolution. The initial scan was subject to filtering for skew and tilt; this was done within the software automatically. The surface parameter data is subject to interpretation and is processed post scan. After which, the 2D data profile and surface parameter data can be evaluated based on the cut-off filter applied. The cut-off filters available include; 0.0008, 0.0025, 0.008, 0.025, 0.08, 0.25, 0.8, 2.5 and 8mm. The application of these cut-off filters will depend on the surface scan area and the surface parameters, see Chapter 2 for further detail. The surface areas investigated included a combination of length and widths, these were:

4.2768 mm x 0.8118 mm

4.276 mm x 0.0798 mm

2.0988 mm x 0.8118 mm

2.0988 mm x 0.0798 mm

0.64 mm x 0.48mm

The Gaussian filter or cut-off changes with the surface scan length. Cut-offs of 0.8 mm, 0.25 m and 0.08 mm were applied to the scan lengths of 4.2768, 2.0988 and 0.64 mm respectively. A cut-off higher than appropriate will amplify the roughness parameters but a smaller cut-off will reduce roughness parameters as finer details are lost. Although this is not the only consideration when evaluating the effect of the cut-off. As discussed in Chapter 2, a cut-off is removed from each end of the scan. As the cut-off increases, the amount of data being included in the evaluation reduces. If surface flaws are located near the end of the scan length, these can be neglected with an increasing cut-off value. Figure 4.5 shows the 2D data line for copper at a scan length of 2.0988 mm with varying wavelengths. The appropriate cut-off value for this reading is 0.25 mm, see figure 4.5b, which gives an average roughness value of 1.506 μm. An increase in cut-off to 0.8 mm reduces the average surface roughness to 1.235 μm as the large surface flaws at both ends of the tube are removed from the data analysis, figure 4.5c. The lower cut-off of 0.08 mm gives a smaller average surface roughness of 0.888 μm, figure 4.5a. Although more of the surface data is included in the analysis, a smaller range of data is considered to be roughness and more is considered to be waviness. Table 4.1 presents all of the surface parameter data for copper across the three cut-offs. It can be seen that the highest value for all of the surface parameters is with a cut-off of 0.25 mm. As a cut-off length is removed from each end of the sample before analysis, a large surface peak which is evident in 4.5 a and b, is removed at the largest cut-off value of 0.8 mm. This results in lower surface parameter values for the higher cut-off. The lowest values for the Rp and Rt occur with the highest cut-off of 0.8 mm but the lowest Ra, Rq and Rv occur with the lowest cut-off of 0.08 mm. The Rp value refers to the highest point from the mean line and Rv to the lowest with Rt being the difference between Rp and Rv. A comparison of these values further shows the difference in magnitude, which is considerable for Rp and Rt.

(a)

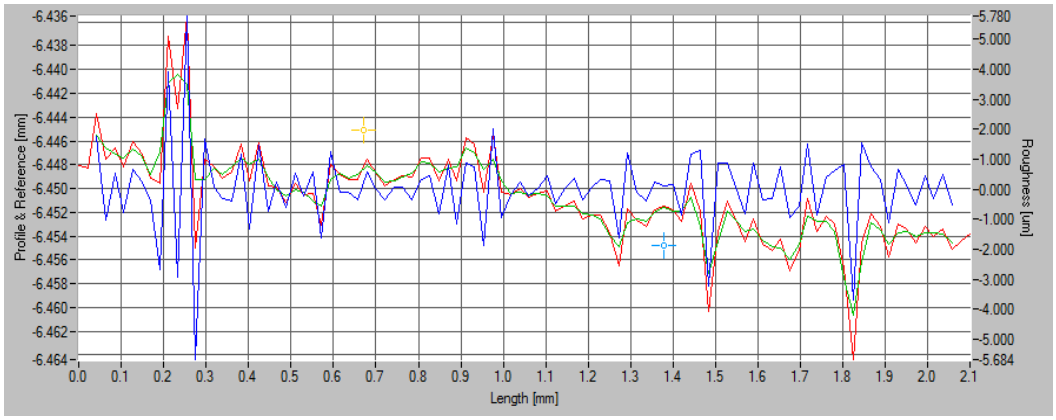

(b)

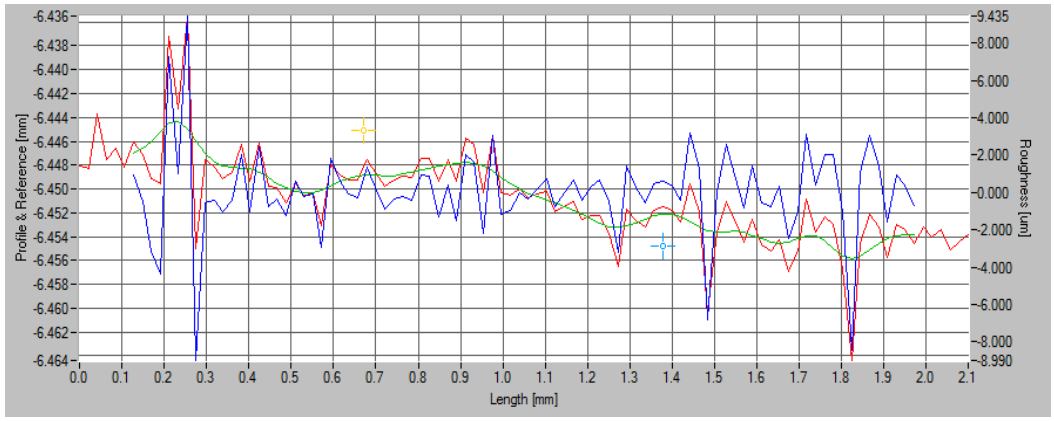

(c)

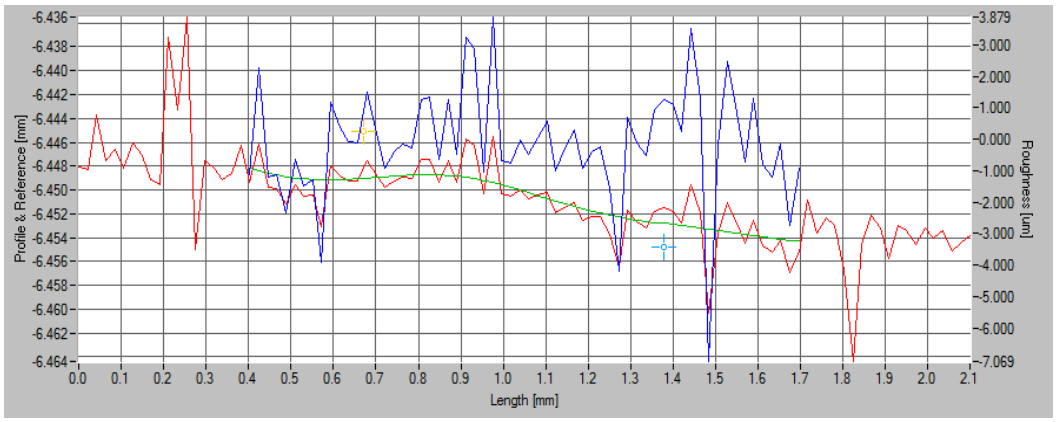

Figure 4.5. 2D data plots for copper with a scan size of 2.0988 mm x 0.8118 mm and an applied cut-off value of (a) 0.08, (b) 0.25 and (c) 0.8 mm. (Red line: profile, green line: waviness and blue line: roughness).

Table 4.1 Surface parameter data for copper with a scan size of 2.0988 mm x 0.8118 mm.

Cut-off, mm	Ra, µm	Rp, µm	Rt, µm	Rq, µm	Rv, µm
0.08	0.888	5.780	11.464	1.364	5.684
0.25	1.506	9.435	18.425	2.417	8.990
0.8	1.235	3.879	10.949	1.761	7.069

The difference in the roughness and the waviness profiles with changing cut-offs can clearly be seen from figure 4.5. The profile (red line) is constant across the cut-off range but the roughness (blue line) and the waviness (green line) change in magnitude. For example, the valley seen at a location of 1.5 mm is evident for all cut-offs but grows in magnitude with increasing cut-off values. The increasing difference between the roughness and profile lines is based on the nominal values, which are used for the graph axis of profile and reference. Note that these values are not used for analysis. This increasing difference is related to the change in magnitude of the values.

Although the cut-off is an important factor for surface characterisation, the scan area is also a consideration. Multiple scan areas were examined to allow for the surface scan to include the curve of the tube wall or the narrow tube area which is 'flat' to the laser. Figure 4.6 represents two of the scan widths investigated. These scans were conducted consecutively, without the sample moving. Therefore the surface parameter data compared for both areas is taken at the same location of the tube, at a resolution of 100 x 100. The same cut-off value is applied to both scans, 0.25 mm, as the scan length is kept the same. Although the scan resolution is kept constant, the change in scan width will change the size of the grid. This leads to the larger scan width having an effectively lower resolution. This change has an influence on all the surface readings. A comparison of the 2D data plots, seen in figure 4.7, shows a change in all of the surface readings, roughness, waviness and the profile. The overall trend and magnitude for the profile and waviness is similar across the length of the reading but the smaller details and peaks differ. The smaller surface area has a larger number of peaks with less extreme peaks and valleys. This is further seen in the surface parameter data, Table 4.2. The highest peak value, Rp is larger for the wider scan area, as is the Rt value which represents the distance between the highest peak and lowest valley. The values which are averaged, Ra and Rq, are similar between the two scan areas. The effect of the scan area will therefore depend on what surface parameters are of the most interest. This variation in Rp, Rt and Rv values can be addressed by conducting more surface scans.

(a)

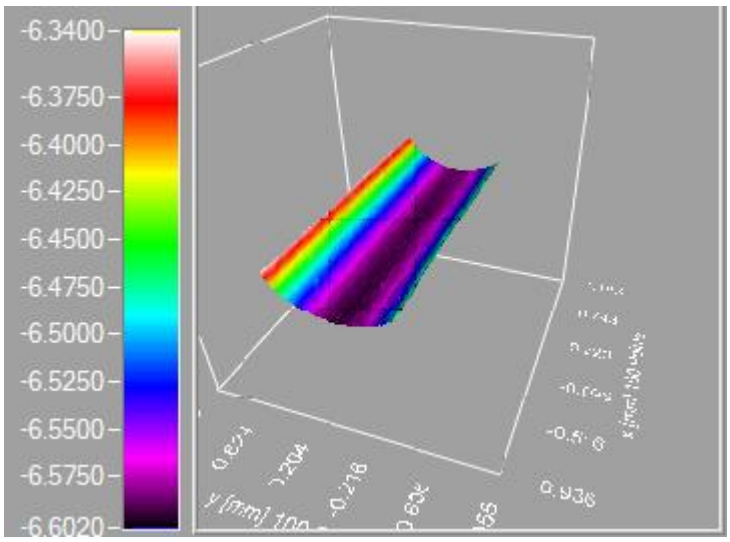

(b)

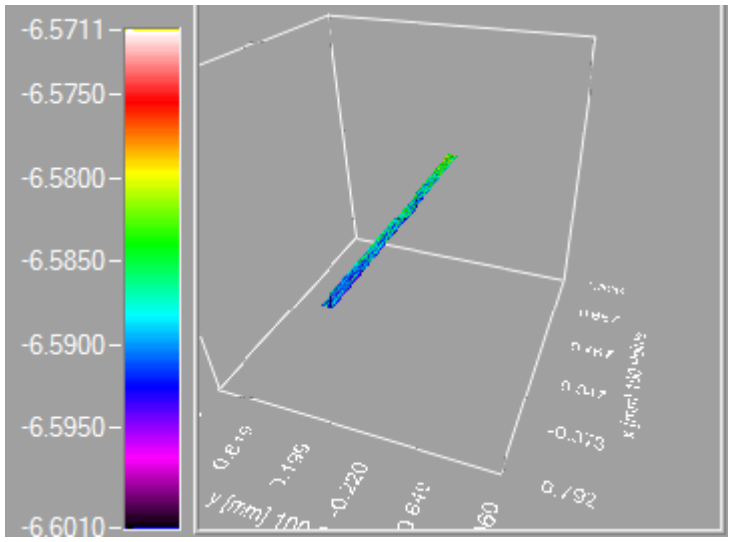

Figure 4.6. A 3D representation of the brass test section with a scan size of (a) 2.0988 mm x 0.8118 mm and (b) 2.0988 mm x 0.0798 mm.

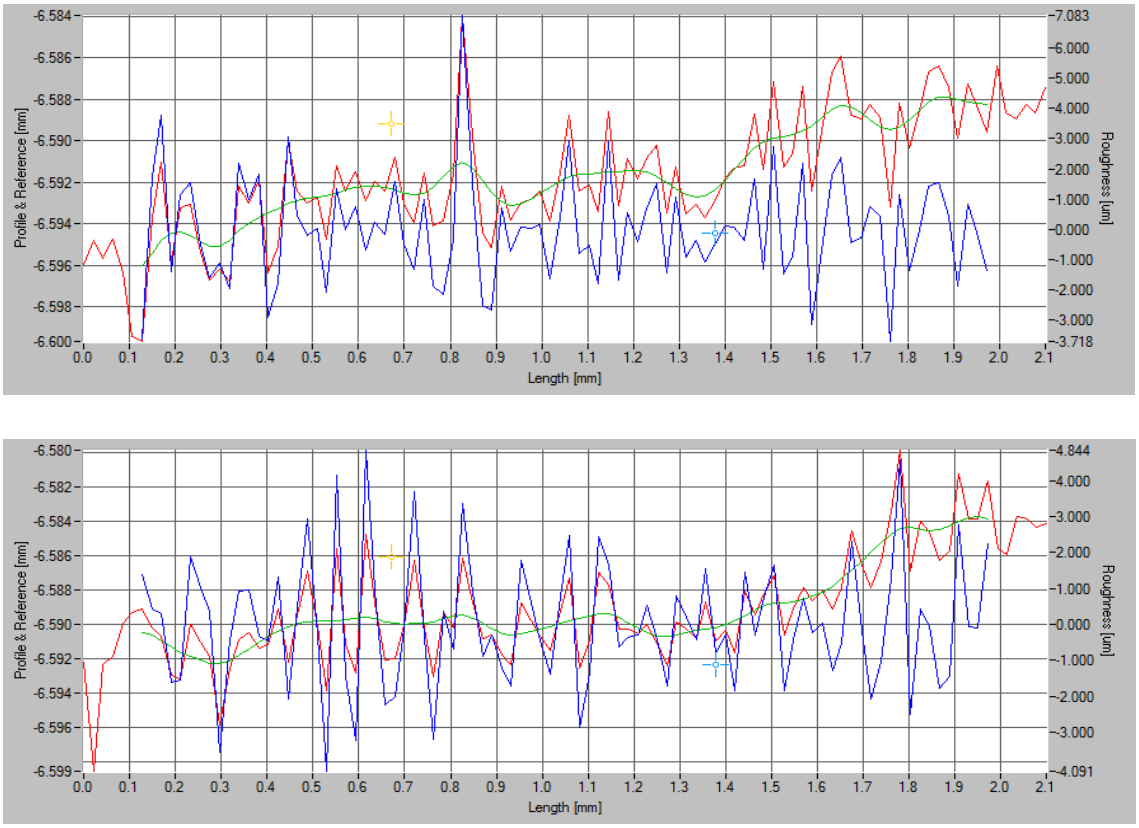

Figure 4.7. 2D data plot for the brass test section with a scan size of (a) 2.0988 mm x 0.8118 mm and (b) 2.0988 mm x 0.0798 mm. (Red line: profile, green line: waviness and blue line: roughness).

Table 4.2. Surface parameter data for the brass test section with a scan size of scan length of 2.0988 mm and widths of 0.8118 mm and 0.0798 mm.

Scan width	Ra, µm	Rp, µm	Rt, µm	Rq, µm	Rv, µm
0.8118	1.332	7.083	10.807	1.739	3.718
0.0798	1.363	4.844	8.935	1.771	4.091

The effect of the surface resolution was investigated by keeping the surface scan area constant but changing the scan resolution from 50 x 50 to 100 x 100. Figure 4.8 shows the 3D colour map for the two scans, with the colours corresponding to changes in surface height. As the tube curves, the colour changes from purple to dark blue and light blue. The transitions between these colours are more defined with the higher resolution with the dark blue transition being wider. Surface imperfections are evident within the purple region, in the way of dark blue spots, which are more evident with the higher resolution. As previously seen, the 2D data profile shows changes in the profile, waviness and roughness, but a similarity in the trend, see figure 4.9. The higher resolution produces a more detailed roughness line, with considerably more peaks and

valleys evident. Once again, the differences in surface parameters are seen more in the absolute values and not the averaged values. Table 4.3 shows that the Rp, Rv and Rt are larger with the higher resolution.

(a) 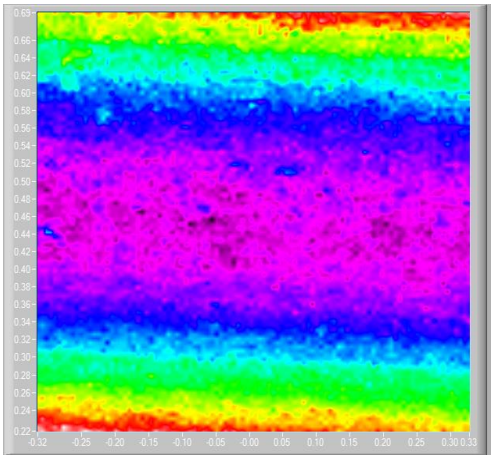 (b) 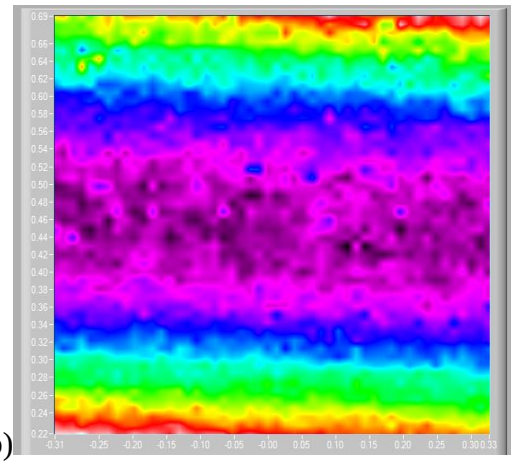

Figure 4.8. 3D colour map for brass with scan resolution of (a) 50x50 points and (b) 100x100 points.

(a)

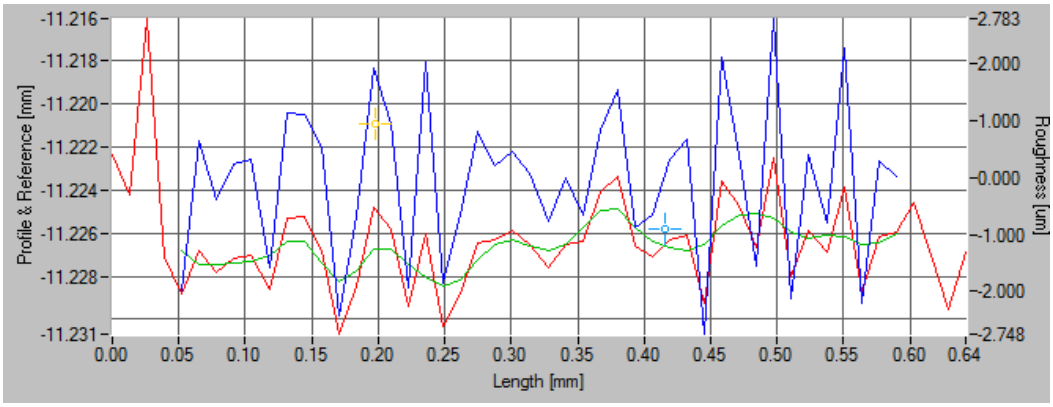

(b)

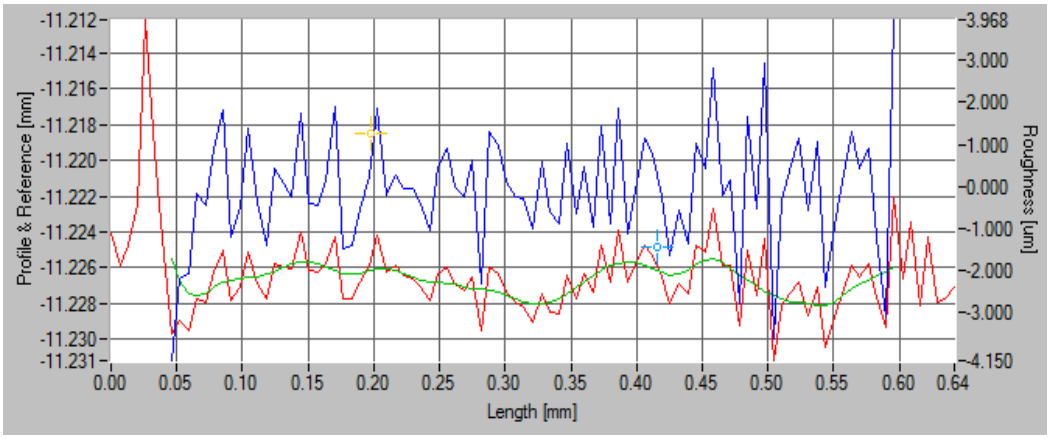

Figure 4.9. Scans for brass with (a) scan resolution of 50x50 points and (b) scan resolution of 100x100 points where red represents the surface profile and blue the roughness based on a cut-off of 0.08 μm. (Red line: profile, green line: waviness and blue line: roughness).

Table 4.3. Surface parameter data for brass with scan resolutions of 50x50 and 100x100 with a cut-off of 0.08 μm.

Resolution	Ra, μm	Rp, μm	Rt, μm	Rq, μm	Rv, μm
50x50	1.094	2.783	5.531	1.355	2.748
100x100	1.041	3.968	8.118	1.386	4.150

Although the scan area and the scan resolution are important parameters to consider for surface analysis, the importance of them is seen to be a function of the surface application. If the averaged values, such as Ra and Rq, are more important parameters then the scan resolution and scan area are less significant. Contrary to this, the Rt, Rp and Rv values remained similar but the averaged values changed with a changing surface scan length. Three scans were conducted with a width of 0.08 mm and lengths of 0.15, 0.48 and 1.5 mm. The applied cut-off increases with the scan length, as seen in Table 4.4. The values for Rp, Rt and Rv are similar for all three lengths but the Ra value increases with surface length. The Rq value also increases but not to the same extent. The Rq value is an indication of the uniformity of the surface structure, it is therefore expected that this value remains similar for the same surface. The values of Rp, Rq and Rt do have slight variations but there is no trend to the changes. If these values increased, it would suggest that the larger peaks or valleys are located in the new increased length. The changes are mostly likely due to the changes in the cut-off. As the cut-off increases, the amount of data which is considered to be roughness increases. This results in an increase in the average roughness value and potential changes in magnitude of the peaks and valleys. This is verified when comparing the 2D data plots for the three surface lengths, seen in figure 4.10. There is no clear trend which can be seen between the three plots, although this is not a function of the cut-off alone. A change in the cut-off alone would not have an effect on the profile line. A change in the profile, waviness and roughness may be due to the change in resolution caused by the increase in surface scan area.

Table 4.4. Surface parameter data for stainless steel with increasing scan lengths.

Scan length, mm	Cut-off, mm	Ra, μm	Rp, μm	Rt, μm	Rq, μm	Rv, μm
0.15	0.025	1.235	6.157	13.973	1.781	7.816
0.48	0.08	1.557	4.193	11.358	2.090	7.165
1.5	0.25	1.745	6.217	12.226	2.232	6.049

(a)

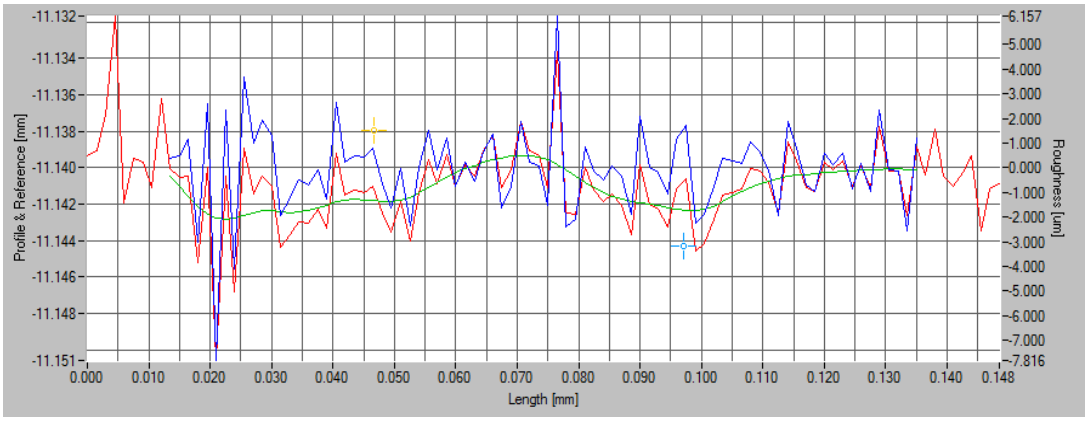

(b)

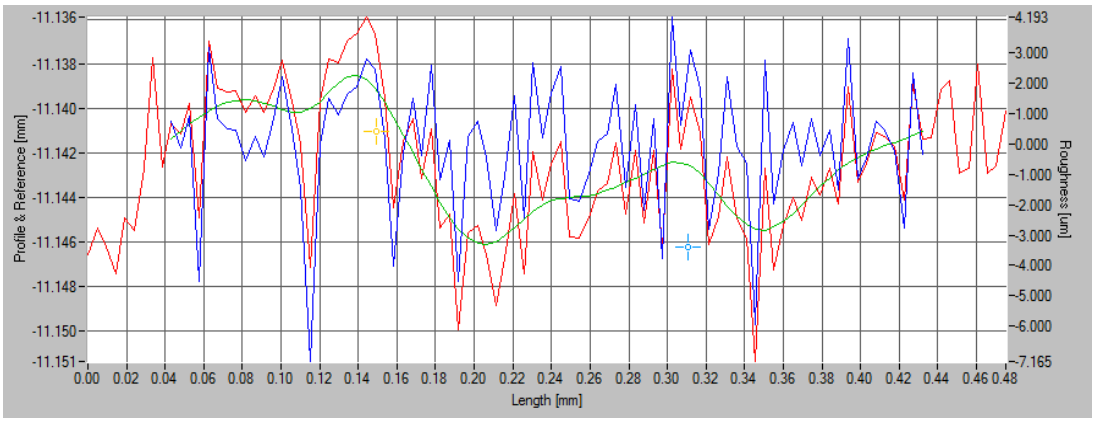

(c)

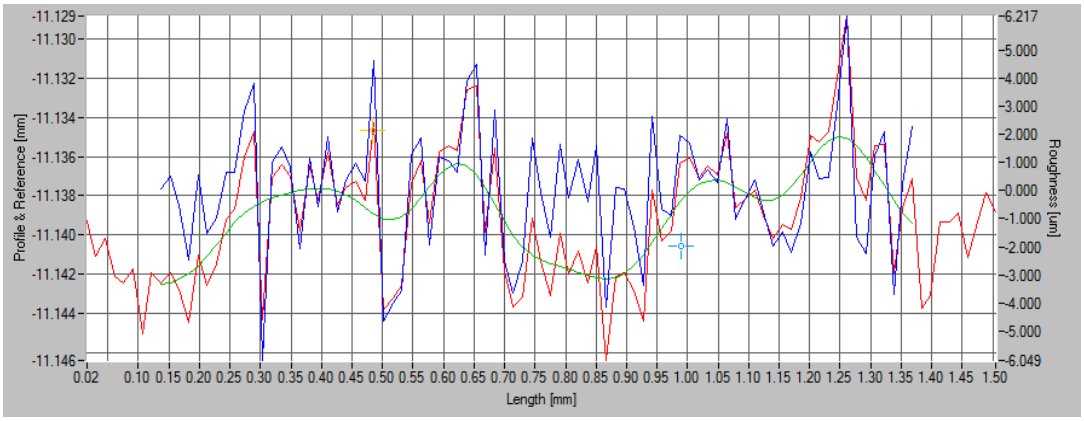

Figure 4.10. 2D data plots for stainless steel with a width of 0.08 mm and lengths of (a) 0.15, (b) 0.48 and (c) 1.5 mm. (Red line: profile, green line: waviness and blue line: roughness).

The effect of microscope configuration has been investigated, including taking readings over a range of scan sizes and resolutions. As the aim of this study is to compare the finer details of each material section, the higher resolution is deemed to be more suitable. As shown, the scan area does have an influence on the surface parameter data but there is no firm guidance on which area is most suitable. Scans were taken at multiple locations, with numerous readings taken per scan, and averaged for each

material. The final scan size, with the best consistency in readings, was taken to be 0.64 x 0.48 mm. This scan was used for the comparison between the three materials. Figure 4.11 presents the 2D profiles for each material taken with a cut-off of 0.08 mm. A comparison of these plots show a considerable difference in trends. The plots for brass, figure 4.11a, and copper, figure 4.11c, show a more uniform roughness with less frequent but severe peaks and valleys as opposed to the stainless steel. The 2D plot of copper corresponds to the SEM images, figure 4.4c, which appears to have smoother areas between 'stretch' marks. The 2D plot shows a relatively smooth area, 0.18 mm from the start of the scan, with large peaks and valleys either side. The brass SEM scan, figure 4.3a, shows a flaky surface with vertical grooves. This could also explain the large peaks and valleys seen with a smoother section in between for the 2D plot. The stainless steel 2D plot has the most uniform structure in terms of the peaks and valleys.

(a)

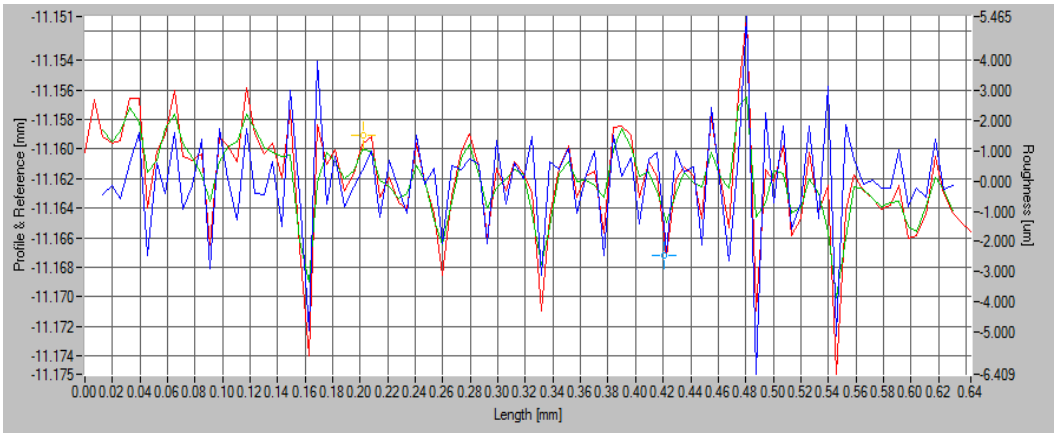

(b)

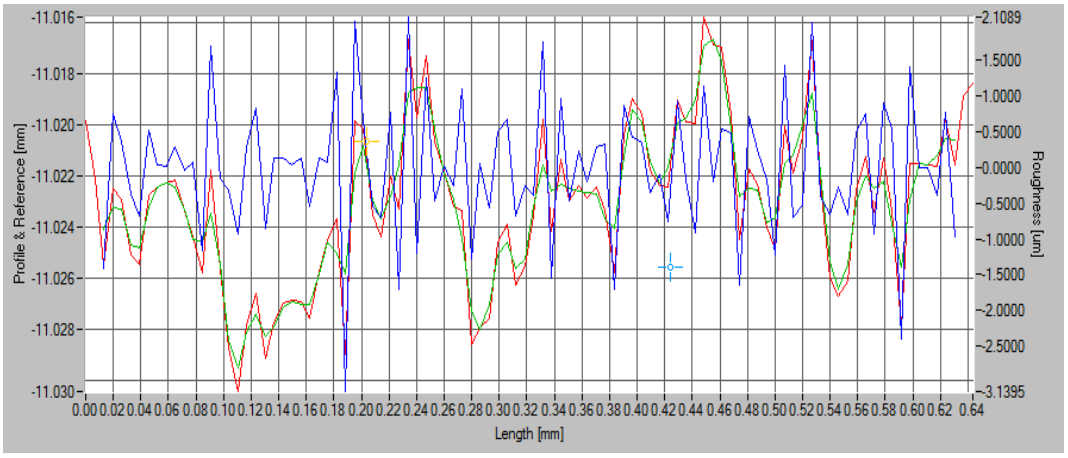

(c)

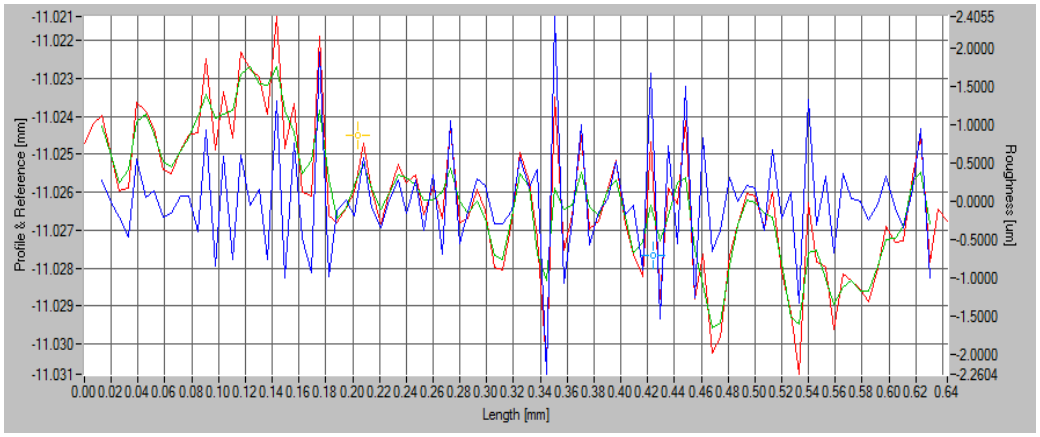

Figure 4.11. 2D profile of (a) brass, (b) stainless steel and (c) copper surface with a 0.08 mm cut-off. (Red line: profile, green line: waviness and blue line: roughness)

The severity of the peaks and valleys seen in the 2D plots can be further verified with the surface parameter data seen in Table 4.5. Brass has a much higher Rq and Rv values, and consequently Rt values, which are more than double that of stainless steel or copper. Brass also has the highest Ra and Rq values from the three materials. This is in agreement with the SEM images which show brass to have the roughest

appearance. The smoothest surface is copper, which also has the lowest Rv and Rt values but not the lowest Rp value. In comparison with stainless steel, copper has a higher maximum peak but a shallower maximum valley. This is not evident with the 2D plots alone as the nominal axis varies between scans.

Table 4.5. Surface profile data for brass, stainless steel and copper with a surface area of 0.64 x 0.48 mm and a cut-off of 0.08 mm.

Instrumentation	Material	Ra, µm	Rp, µm	Rt, µm	Rq, µm	Rv,µm
TaiCaan Surface Profiler	Brass	1.249	5.465	11.874	1.743	6.409
	Copper	0.524	2.406	4.666	0.722	2.260
	Stainless steel	0.716	2.109	5.248	0.928	2.992

As previously discussed, there are many variables to consider when using confocal laser microcopy. These include scattering from the laser, surface areas and cut-offs, which can be a function of the microscope used. With the use of different microscopes, changes in set up can change the readings. This was investigated by using an alternative microcscope to scan the same samples and compare the results.

Olympus Lext 3100 confocal laser scanning microscope

The Olympus Lext 3100 has multiple objective lenses, with a maximum magnification of 14400 x and a 408 nm laser. This system does limit the resolution to 50 points in the x and 50 points in the y axis with a surface scan area of 0.64 x 0.48 mm. The scans were taken at three locations for each material. The output data from this consisted of a 3D height maps, a 2D data profile and surface parameter data. The outputs do differ from the alternative confocal microscope. The Taicaan allows for the surface to be scanned and the measurements, taken post processing at a chosen location, in either the x or y axis. For the Lext 3100, the location and axis for the data output is chosen pre scanning. Three x axis locations and a y axis location was measured for each scan location, see figure 4.12.

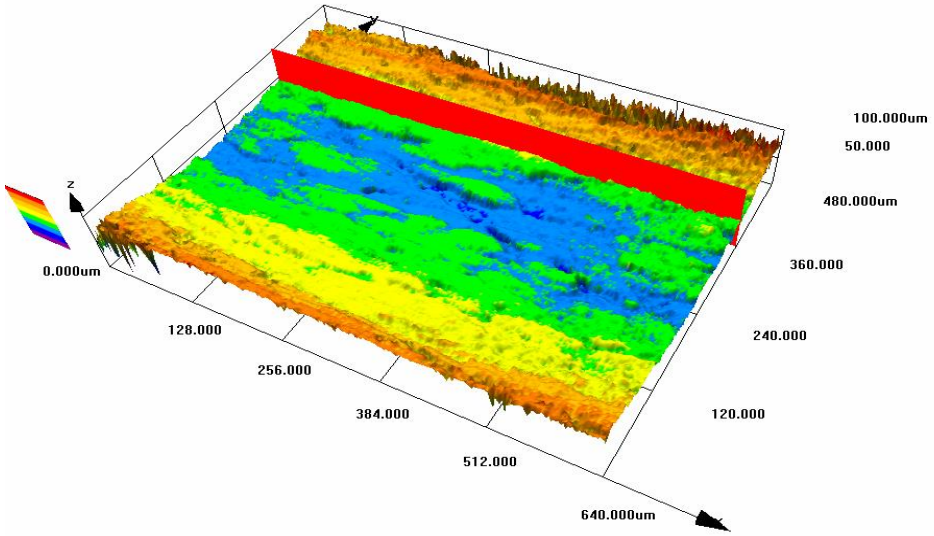
z
0.000um
100.000um
50.000
480.000um
360.000
240.000
120.000
128.000
256.000
384.000
512.000
640.000um

(a)

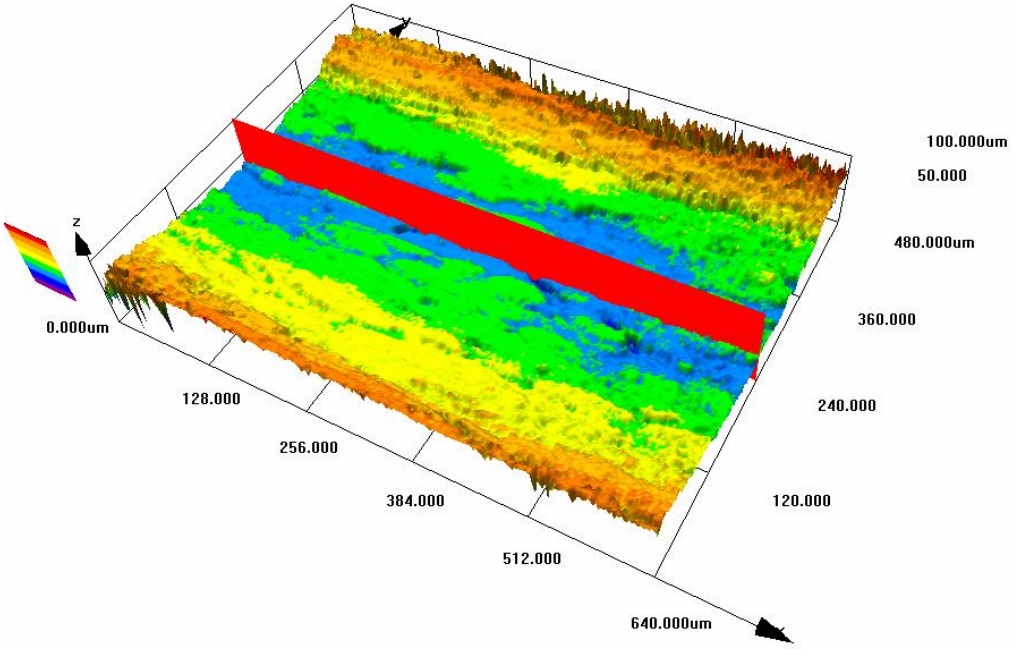
z
0.000um
100.000um
50.000
480.000um
360.000
240.000
120.000
128.000
256.000
384.000
512.000
640.000um

(b)

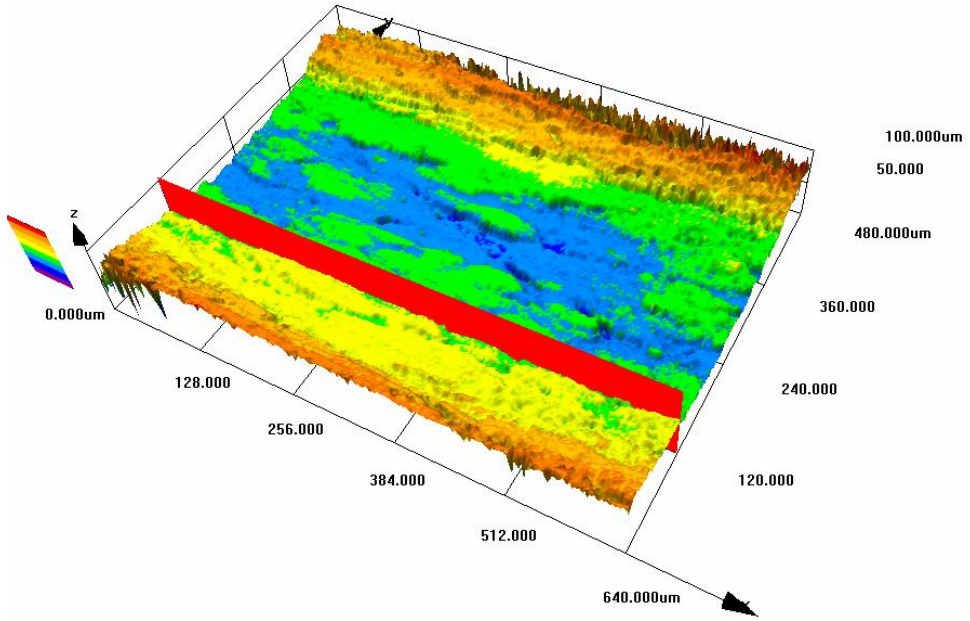

(c)

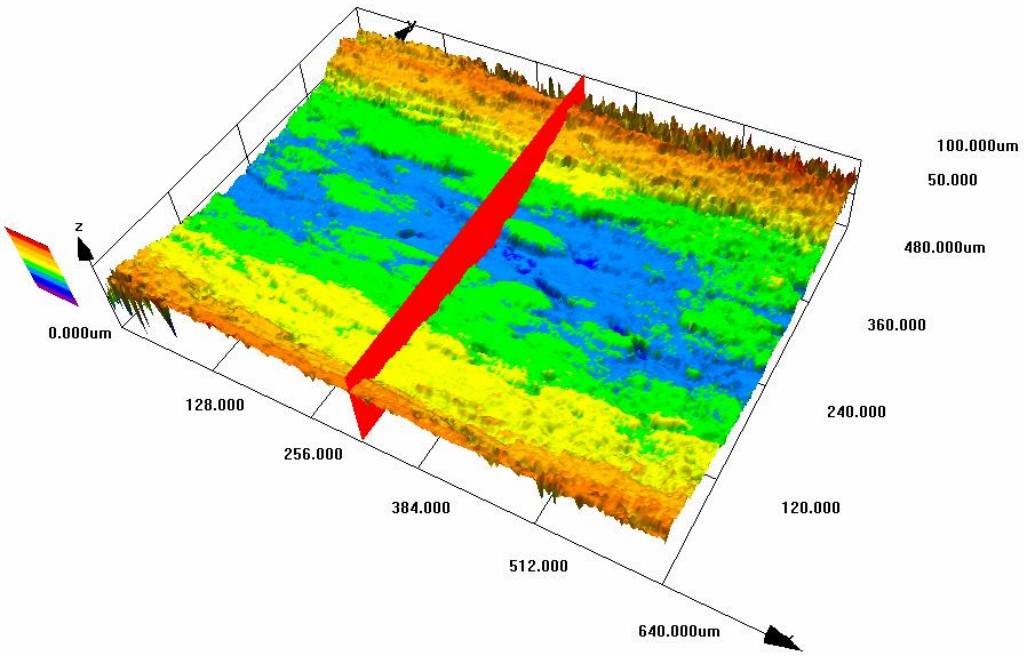

(d)

Figure 4.12. 3D height maps showing the location at which the readings are taken for (a) top X axis, (b) middle X axis, (c) bottom X axis and (d) Y axis.

Figure 4.12 represents the 3D height maps, with the red line indicating the locations of data acquisition. The colour of the map relates to the height of the surface from the laser. Due to the tube curvature, this is not an accurate representation of changes in the surface characteristics. The large scale of the readings, due to the changes in the height from the tube curvature, result in the smaller surface structure being lost. The surface is assumed to be flat, with the readings based on the distance from the laser. As the surface

curves, the distance from the laser decreases and the accuracy of the readings are reduced. This is also true of the readings taken at the edges of the curve, figures 4.12a and 4.12c, as the laser is at an angle to the surface which changes the surface readings. As the surface data is based on the intensity of the returning laser, the laser intensity can be affected by scattering from the curve which may affect the accuracy of the readings. A cut-off of 0.08 mm was applied to all of the readings. Only one cut-off was used for the Lext 3100 data as only one surface scan area was used.

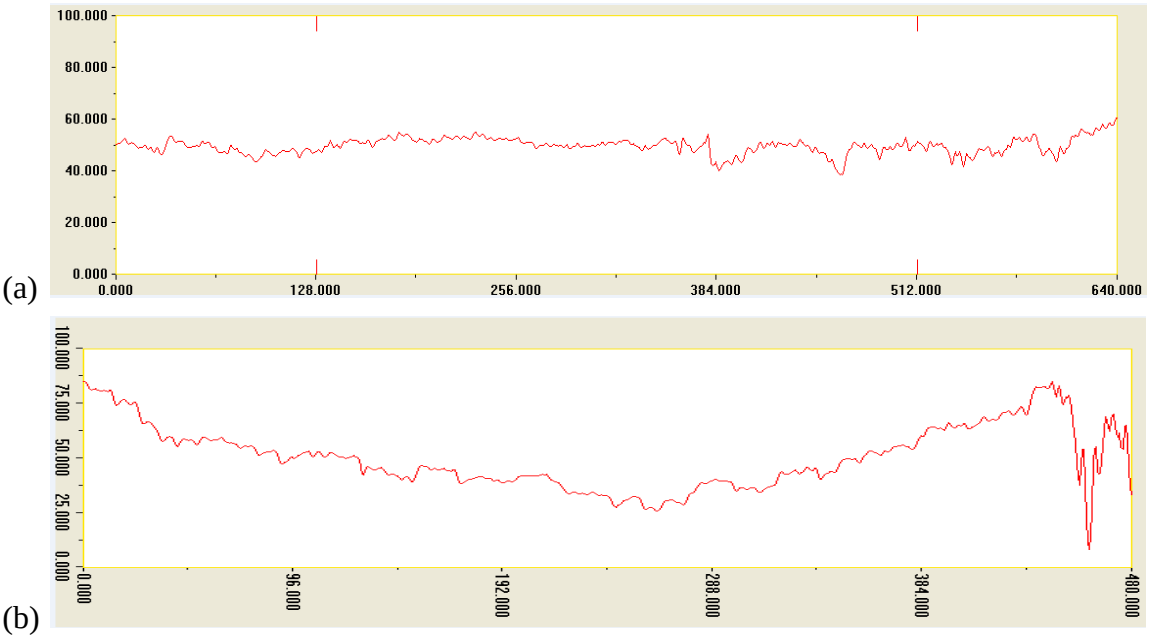

Figure 4.13. 2D data profile for the stainless steel in (a) the x axis and (b) the y axis.

Figure 4.13 shows the 2D data profile in both the x and y axis. The data profile in the y axis, figure 4.13b, shows the curvature of the channel and gives an indication of surface imperfections across the diameter of the channel. The data in the x axis, figure 4.13a, shows surface imperfections at one location along the length of the channel. The surface does appear to be smoother when compared with the Taicaan data profiles for the same surface scan area and resolution but this is due to the large scale used for these readings. A comparison for the three materials in the middle x axis location, see in figure 4.14, shows copper to have the smoothest appearance. Brass has a uniform surface structure with multiple peaks and valley on a smaller scale to that of stainless steel which has larger wavelength peaks and valleys. The waviness seen in the stainless steel is removed when the results are processed so that this deformation does not skew with the surface parameter readings. With this waviness removed from the stainless steel, the brass section once again has the roughest appearance which is validated by the surface parameter data seen in Table 4.6. The values for Rv and Rp are similar for the

stainless steel, representing an equal fluctuation in the peaks and valleys of the surface. Both brass and copper have higher Rv value. This could be a result of the stretch marks seen in the SEM images which would give a larger Rv value to the Rp value. The Rq values are proportionally all larger than the Ra value, which shows a good uniformity across the scan length.

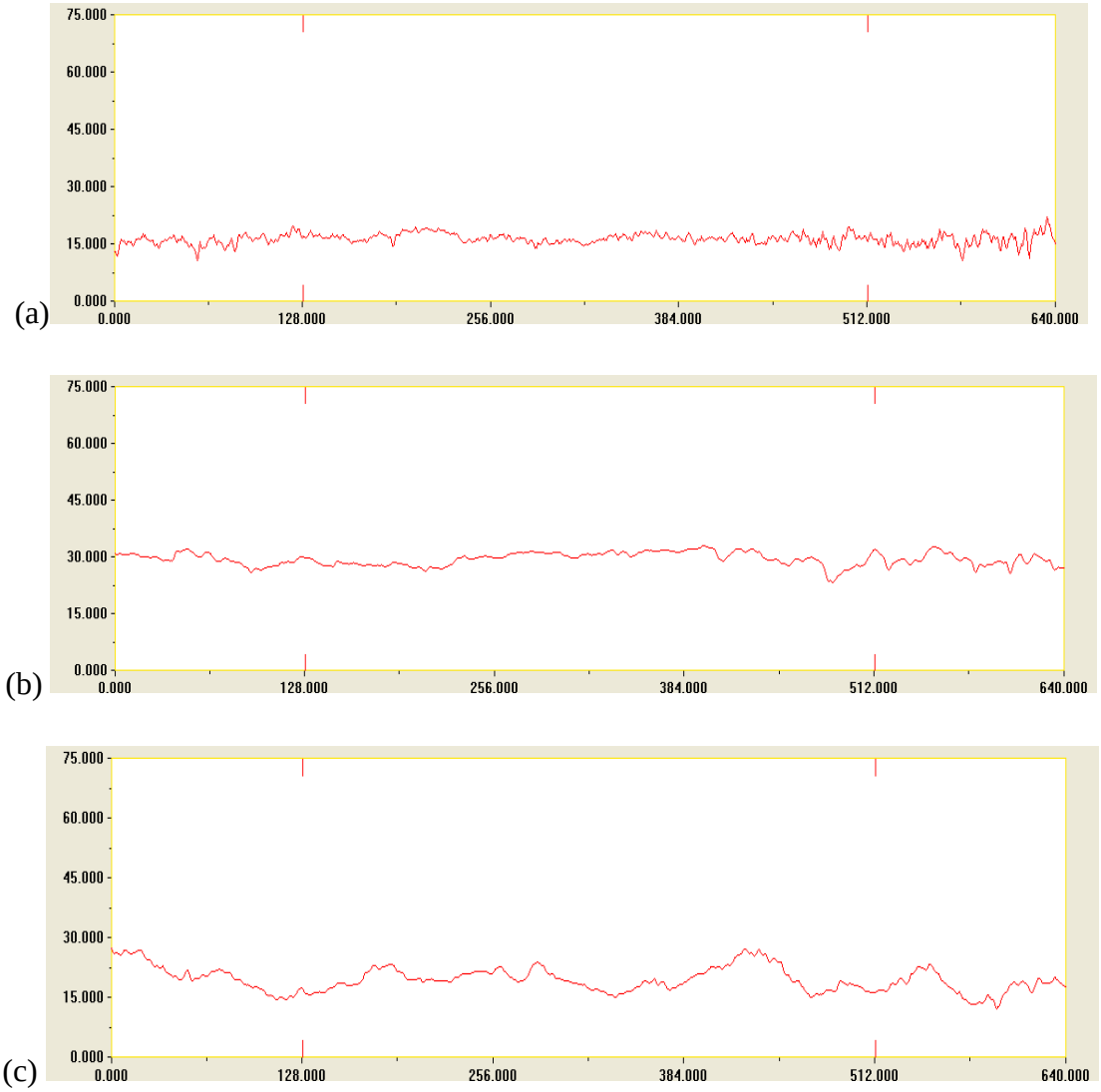

Figure 4.14. 2D data profiles for (a) brass, (b) copper and (c) stainless steel.

Table 4.6. Surface parameter data from the Olympus Lext 3100 at the central x axis location with a cut-off 0.08 mm.

Instrumentation	Material	Ra, µm	Rp, µm	Rt, µm	Rq, µm	Rv,µm
Olympus Lext 3100 CFLSM	Brass	1.0197	4.6753	11.5654	1.4016	6.8901
	Copper	0.3756	1.854	4.6396	0.5408	2.7856
	Stainless steel	0.5458	3.04	6.6532	0.7729	3.6132

4.5. Comparison of techniques

The 3D surface and 2D data plot outputs are vastly different between the two machines which limits the ability for comparison. A comparison of the surface parameter data, table 4.5 and 4.6, taken at the same surface scan area and cut-off, shows a difference in the magnitude but generally the same trend. The average surface roughness shows the roughest to be brass and copper to be the smoothest on both accounts, but the magnitude between the values differs. The average roughness values from the Taicaan are approximately 20% higher than those from the Lext 3100. This is also true for the Rq values which are of the same trend but with a magnitude of approximately 20% less. The results for Rp, Rv and Rt show varying degrees of correlation. The Rp trend differs between the two readings, with brass having the highest for both accounts but stainless steel being the lowest for the Taicaan and copper for the Lext 3100. The biggest difference is seen with the stainless steel readings, which are up to 40% higher with the Lext 3100 results. The results are very similar for brass and copper in terms of the Rt value but it is 25% higher for stainless steel with the Lext 3100. Besides that of Rp, the trends are the same for both machines across all surface parameters, with the difference being in the magnitude of the readings. The Rp and Rv values are similar for the Taicaan readings which is not seen with the Lext 3100 readings in which only stainless steel shows a similarity in these values.

The magnitude of the readings can be a function of many variables, although the scan size, resolution and cut-off are kept constant. The distance between the sample and the laser can have an effect on the readings, as can laser scattering. The averaged values are the same in trend and similar in value suggesting that the difference is due to the post processing and machine configuration which is fixed. Although it is not possible to say which readings are more accurate, the Taicaan results showed greater consistency in readings and so these are taken to be the true readings which will be used for surface analysis.

4.6. Summary

Three channels of copper, stainless steel and brass were ground open to allow for analyse of the inner surface. The surface analysis consisted of both visual inspection through SEM and surface structure analysis through CFLSM. The images captured using SEM showed differences in the surface structure between the three materials. SEM does not give any tangible surface data but does allow for a simple comparison of the surfaces and locations of potential nucleation sites which would be conducive to

flow boiling. CFLSM gives numerical values of the surface parameters and 3D images of the surface, but the results are easily influenced by the scan configuration. There are many variables which need to be considered for CFLSM, including the cut-off length and scan size. Due to the complex nature of the surface scanning variables, it is not possible to investigate each variable independently. For example, changing the scan size will also change the scan resolution. Changes in the scan size and resolution were seen to change the surface parameter values, more so for parameters which are not averaged. Parameters which are averaged, Ra and Rq, were less affected by these changes. Those parameters which are set values, increased with an increase in the scan resolution. Changes in the cut-off length have a more convoluted relationship with changes in the surface parameter values. In theory, the surface parameter values increase with cut-off length but this is not seen in practice due to the removal of cut-off lengths from each end of the evaluation length. A larger cut-off length results in a longer length of evaluation length being removed from the data being processed. This can result in large surface flaws being removed from the data and therefore a reduction in the surface parameter values. Due to this, multiple surface scans should be conducted at different locations along the channel to reduce the random errors which occur.

There are advantages and disadvantages to both SEM and CFLSM, but CFLSM is favourable for the application of surface analyse for heat transfer. The surface parameters recorded using CFLSM allow for an easier and more tangible comparison of the surfaces. Regardless of the surface analysis methodology used, the results are limited for defining a heat transfer surface. Both SEM and CFLSM image the top of the surface structure, with neither capable of detecting deeper and more complex surface structures, like re-entrant cavities. These more complex and deep structures are important parameters in flow boiling and heat transfer. The CFLSM surface readings were seen to be variable between the Taicaan and the Lext 3100, although the trends between the materials were similar. The difference between the two readings was less for averaged parameters, Ra and Rq. These differences show that comparison between laboratories can be difficult, with the values being open to interpretation. Although the actual surface parameter values do vary, the values can be used to compare different materials, based on the differential between the readings. As averaged parameters are less influenced by scan configuration, these are more easily compared between laboratories. For this study, the final surface data profile and parameter values were taken at a scan size of 0.64 x 0.48 mm with a cut-off value of 0.08mm, acquired from the Taicaan microscope, presented in Table 4.5.

Chapter 5

5. Flow patterns

5.1 Introduction

Flow visualisation occurred through a borosilicate glass tube at the exit of the heated test section, with flow patterns being recorded at 1000 fps with the high speed camera. The flow patterns are recorded across the entire experimental range, allowing for the effect of mass flux, inlet pressure and heat flux to be investigated. The flow patterns are categorised as bubbly, confined, slug, churn and annular flow, based on the work by Chen et al. (2006). The confined flow, only seen for smaller diameter channels, is a point of contention where some researchers refer to this as slug flow. The difference between confined flow and slug flow is the shape of the bubble tail. Confined flow has a rounded end as opposed to slug flow which has a disturbed end and can have a trail of bubbles. Chen et al. (2006) also reported flow patterns of dispersed and mist flow but these patterns were not present for any of the data presented in this chapter. The comparison of the experimental data with flow patterns in literature is based on bubbly, slug, churn and annular flows.

5.2 Effect of fluid properties

The effect of fluid properties is based on a comparison of the flow patterns for R245fa and R134a, with both flows occurring in the same stainless steel test section. The fluid properties are expected to have an effect on the flow pattern transitions, specifically that of surface tension, viscosity and vapour density. As discussed in Chapter 2, the surface tension plays an important part in the formation and coalescence of bubbles. Chen (2006) stated that a higher surface tension will result in a thinner liquid film during churn flow and facilitate the transition to annular flow. A higher surface tension will improve bubble rigidity and reduce bubble coalescence which will inhibit flow transitions. However, once the flow has transitioned into churn flow, a

higher surface tension will enhance the liquid bridge in annular flow. The surface tension of R245fa is over 80% higher than for R134a, which would suggest a dominance of annular flow for R245fa. This is also true for the liquid viscosity and vapour density which are both lower for R245fa which would move the transitions of churn and annular flow to lower superficial gas velocities (Furukawa and Fukano, 2001). There are various methods for defining the confinement of flow, see Chapter 2.2, all of which have both R134a and R245fa being classed as microscale for a channel diameter of 1.1 mm. Figure 5.1 presents the flow patterns seen for R134a, recorded by Mahmoud (2011). This figure shows a clear transition from bubbly, slug, churn and annular flow with an increase in the heat flux. Bubbly flow only occurs at low heat flux values, with slug and churn flow occurring over a larger heat flux range. The dominant flow pattern was annular flow. The flow transitions for R245fa, seen in figure 5.2, vary greatly from those of R134a. Bubble, slug and churn flow are not present and annular flow dominated for R245fa. As previously stated, the flow patterns are recorded at the heated test section outlet, so the bubbly, slug and churn flow could be evident within the heated section but transitioning to annular flow at the channel exit for R245fa. The flow patterns along the channel length can be assumed based on the local heat transfer coefficient as a function of axial location which is discussed in Chapter 7.8.1.

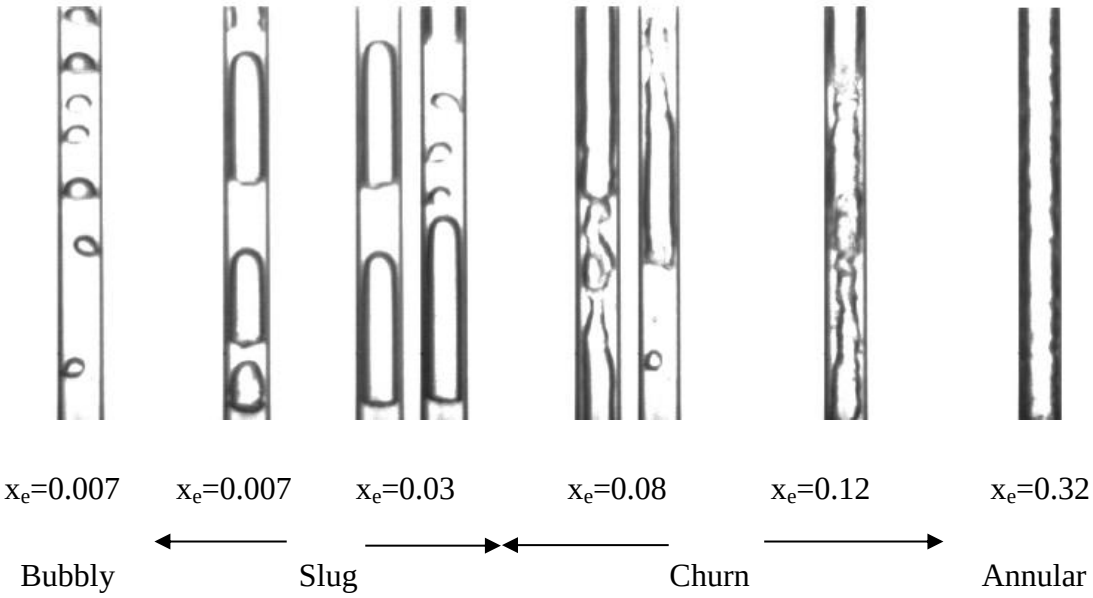

Figure 5.1. Flow patterns for R134a at G=300 kg/m^{2}s and Tsat=31 °C with increasing heat flux (Mahmoud (2011)).

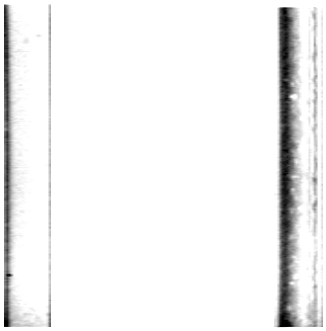

x_e=0.063 x_e=0.130

Single phase Annular

Figure 5.2. Flow patterns for R245fa at G=300 kg/m^{2}s and Tsat=31 °C, with increasing heat flux

Kandlikar et al. (2006) found that a higher wall superheat related to a smaller radius nucleation sites being activated. The wall temperature at which the onset of nucleation occurred was predicted from equation 5.1. The higher surface tension and lower vapour density resulted in a higher wall superheat for R245fa under the same operating conditions. For example, at a saturation temperature of 31°C and heat flux of 10 kW/m^2, R245fa has a calculated wall superheat of 1.51 K as opposed to 0.6 K for R134a. From this, it can be considered that the higher wall superheat resulted in the activation of more nucleation sites for R245fa which may explain the differences seen between figure 5.1 and 5.2. Assuming that more nucleation sites were activated for R245fa, bubbly flow may have quickly progressed into confined, slug and churn flow across the channel length. This would explain why only annular flow is seen at the channel exit for R245fa but further flow patterns are evident for R134a.

$$T_{wall} - T_{sat} = \sqrt{\frac{8.8\,\sigma\,T_{sat}q}{\rho_g h_{fg} k_f}} \tag{5.1}$$

5.2.1 Hysteresis

The experiments were conducted with both increasing and decreasing heat fluxes to investigate the effect of hysteresis on both the flow patterns and consequent heat transfer rates, see Chapter 7.8.2. No effect of hysteresis was seen for R134a and

this is contrary to the findings of R245fa. The heat flux was initially increased until a vapour quality of approximately 0.85, to avoid the effect of dryout, and then decreased in the same steps. Figure 5.3 shows the flow patterns recorded with decreasing heat flux were similar to those of R134a, with a transition from annular, churn, slug and bubbly flow. The occurrence of hysteresis is attributed to nucleation sites activating at higher heat fluxes which remain active when the heat flux is decreased. Cornwell and Brown (1978) found that the active nucleation sites were approximately equal to the wall superheat to a power of 4.5 for pool boiling. As the same stainless steel test section was used for both R134a and R245fa, the difference seen in the flow patterns and hence nucleation site activation must relate to the changes in wall superheat between the two fluids.

The wall superheat is considerably higher for R134a, with the onset of nucleate boiling occurring at a heat flux of 7 kW/m^2 and a wall superheat of 13.9 K. The onset of nucleate boiling for R245fa was seen to be at 4 kW/m^2 and a lower wall superheat of 9 K, for a saturation temperature of 31 ˚ C and mass flux of 200 kg/m^2s. Although as previously stated, the wall superheat is higher for R245fa at a given heat flux, the wall superheat value at the heat flux comparable to the start of nucleation, is higher for R134a.

The higher wall superheat of R134a at the onset of nucleate boiling would allow for the activation of more nucleation sites during increasing heat flux and would account for the difference in flow patterns seen. The same nucleation sites are not activated with R245fa until higher heat fluxes are reached, when decreasing the heat flux, these sites remain active and result in the flow patterns seen in figure 5.3. Annular flow is still the dominant flow pattern, occurring at vapour qualities and heat fluxes lower than seen when increasing the heat flux. The heat flux and vapour quality range at which churn, slug and bubbly flow are present, is smaller than seen for R134a. Bubbly and slug flow occurred at the same heat flux value of 2.2 kw/m^2 which is lower than that of R134a.

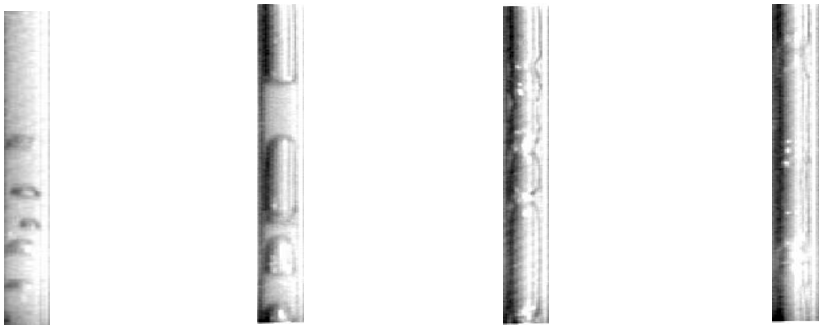

q=2.2094	q=2.2094	q=3.715	q=5.736 kW/m^2
X_e=0.0114	X_e=0.0114	X_e=0.01341	X_e=0.0559
Bubbly	Slug	Churn	Annular

Figure 5.3. Flow patterns for R245fa at G=300 kg/m^{2}s and 1.85 bar, with decreasing heat flux.

5.2.2. Effect of inlet pressure

Flow patterns are affected by the inlet pressure due to the changes in the thermophysical properties, with the degree of these changes being fluid dependent. The surface tension decreases with increasing temperature which, as a consequence, affects bubble dynamics and flow patterns. The percentage change in surface tension between the two pressures is double for R134a at 16% as opposed to 8% for R245fa. Chen et al. (2006) reported that the inlet pressure shifts some flow pattern boundaries to higher superficial gas velocities. Superficial velocities are commonly used in flow pattern maps, including the effect of mass flux, vapour quality and density, which are important parameters in flow patterns. The superficial velocities refer the relative velocity of the liquid and vapour stages separately which relates to the flow patterns present. For example, annular flow will occur at higher superficial vapour velocities and lower superficial liquid velocities as the gaseous core will flow at a higher velocity than the liquid film. Figure 5.4 presents a comparison of the superficial velocities for both R245fa and R134a at inlet pressures relative to saturation temperatures of 31 and 39 ˚C. The difference seen between the two fluids is due to changes in both the density and the vapour quality. The vapour density is 72% higher for R134a than R245fa at the lower pressure which equates to a smaller superficial vapour velocity, see figure 5.4. The difference in the liquid density between the two fluids is considerably smaller, with R245fa being 12% higher, which is reflected in the superficial liquid velocity being

slightly lower for R245fa. The R134a data agrees with the work of Chen et al. (2006), with a shift to higher superficial vapour velocities but this is not seen for R245fa. This results in the effect of inlet pressure on flow transitions being greater for R134a than R245fa.

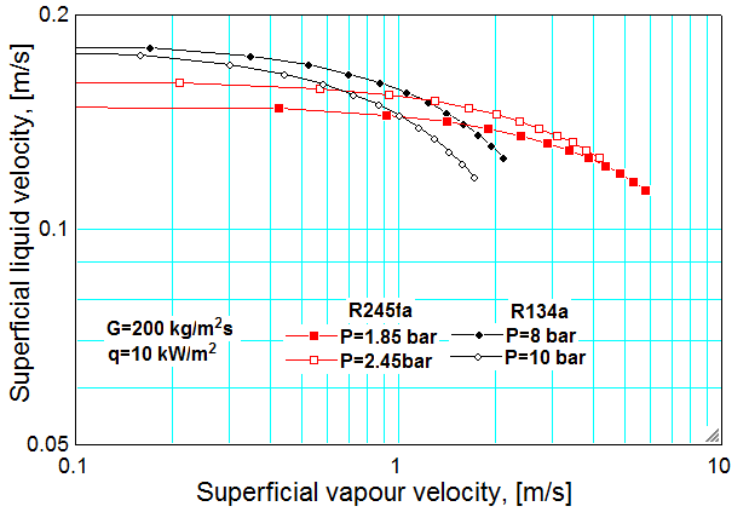

Figure 5.4. A comparison of the superficial velocities for R134a and R245fa at saturation temperatures of 31 and 39 ˚C.

5.3. Effect of surface characteristics

The effect of surface characteristics on flow patterns was investigated using R245fa in stainless steel, brass and copper test sections. The flow patterns were recorded across the same range of inlet pressures, mass fluxes and heat fluxes for comparison. The flow patterns were recorded for two inlet pressures, 1.85 and 2.45 bar, with differences in the flow transitions seen for stainless steel which showed no bubbly flow at the higher inlet pressure, hence comparisons are made based on an inlet pressure of 1.85 bar. A comparison of the three materials is conducted based on the liquid and vapour Weber numbers, suggested by Chen et al. (2006) who concluded that the Weber number was useful for incorporating the effects of surface tension and inertia forces. Figure 5.5 a presents the Weber number plot from Chen et al. (2006), using R134a, where the flow transitions are clearly visible. Due to the changes in surface tension, liquid density and vapour density for R245fa, figure 5.5 b is plotted with different axes. A comparison of figure 5.5 a and 5.5 b show a large difference in the trend and magnitude of the data between the two refrigerants. The clear distinction between the flow patterns is not seen

with R245fa. The lower liquid Weber numbers of R245fa shifts the data into the slug, churn and annular region, presented in figure 5.5a, and away from the dispersed bubble region. This is conducive with the experimental results which only showed churn and annular flow. Figure 5.5 b presents the Weber number, calculated from the experimental data, shows the same trend for all three materials, with similar liquid Weber numbers. The R245fa data was observed across the same experimental range with the same channel diameter and therefore the Weber numbers should be the same. Figure 5.5b shows that the liquid Weber number is very similar for all but there are slight variations in the vapour Weber number, due to the changes in the vapour quality. As brass showed the largest range of vapour qualities and heat fluxes, these results are used to evaluate flow pattern maps.

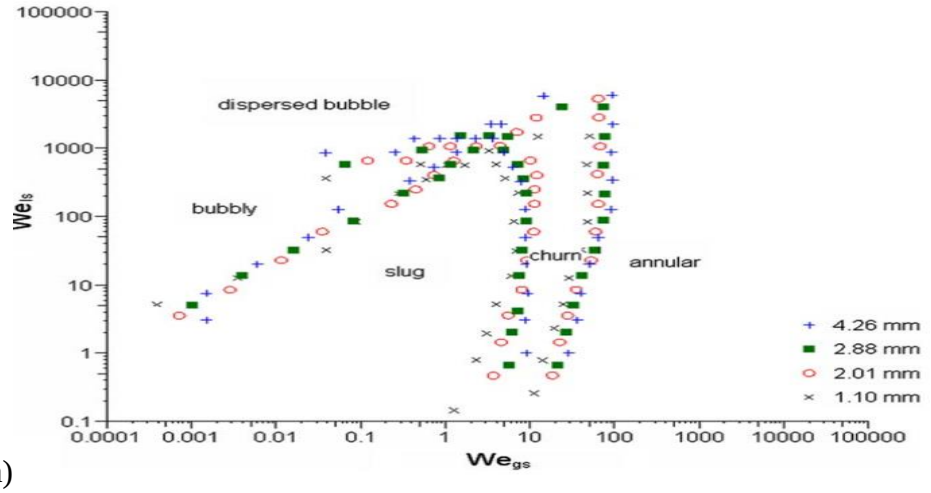

(a)

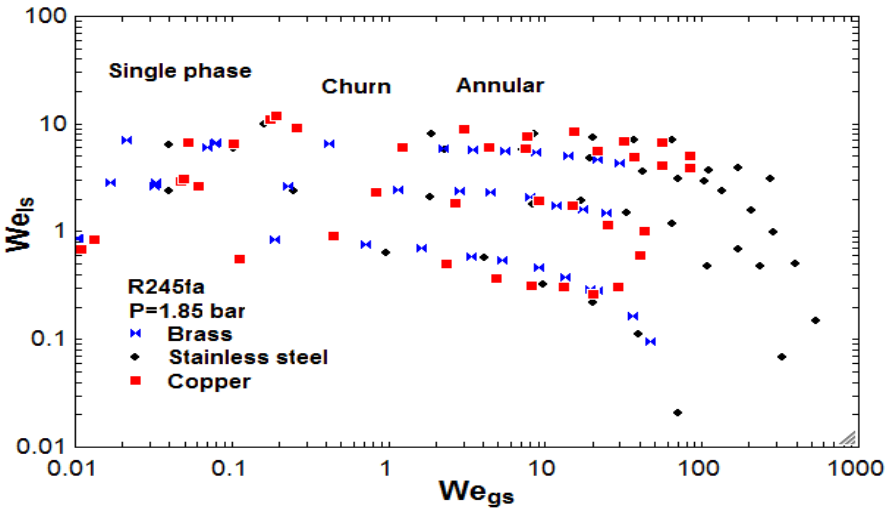

(b)

Figure 5.5. Experimental transitions for (a) R134a from Chen et al. (2006) (b) R245fa a 1.1 mm diameter stainless steel channel with decreasing heat flux.

Stainless steel has the lowest wall superheat, ranging from 5 K at low heat fluxes, for G=200 kg/m^{2}s, which suggest fewer active nucleation sites. This in turn may result in a reduced range of bubbly flow and slug flow. Copper has a slightly higher wall superheat of 7 K and brass the highest at 10 K. Based on the observations of Cornwell and Brown (1978), brass will have the highest number of active nucleation sites which will aid in bubbly, confined and slug flow. The wall superheat is higher with the increasing heat flux, with peaks of 24 K for brass in comparison with peaks of 11 K for decreasing heat flux. This high wall superheat should allow for small nucleation sites to be activated with increasing heat flux. For all cases, annular flow was the dominant flow pattern, with alternative flows only seen at lower heat fluxes.

5.3.1 Effect of hysteresis

As with R245fa in the stainless steel channel, the flow patterns were limited to single and annular flow with increasing heat flux.

Bubbly	Confined bubble	Slug	Churn	Annular
x_e= 0.01	x_e= 0.04	x_e= 0.07	x_e= 0.09	x_e= 0.14

Figure 5.6. Flow patterns for copper at G=300 kg/m^{2}s and P=1.85 bar with a decreasing heat flux.

Bubbly	Confined bubble	Slug	Churn	Annular
x_e=0.01	x_e=0.02	x_e=0.05	x_e=0.08	x_e=0.11

Figure 5.7. Flow patterns for brass at G=300 kg/m^{2}s and P=1.85 bar with a decreasing heat flux.

A comparison of figures 5.3, 5.6 and 5.7 show the same exit vapour quality for all three materials for the bubbly flow regime. This suggests that there is a similar bubble frequency, assuming that the bubble sizes are equivalent. Based on the value of the superheat, it suggests that the brass channel would have a higher number of active nucleation sites which should relate to a higher bubble frequency. However, the heat flux at which bubbly flow is seen differs between the materials, with the brass at the lowest heat flux of 1.5 kW/m^2 and highest for copper at 2.9 kW/m^2. The lower heat flux seen for brass may relate to a higher bubble frequency, from more active nucleation sites, resulting in a larger number of bubbles which coalesce or become confined at the higher heat fluxes. As stainless steel and copper, potentially, have a smaller number of active nucleation sites, there are fewer bubbles to become confined or coalesce and therefore bubbly flow is evident before that of brass. Confined flow was not evident for stainless steel and occurred at a heat flux and vapour quality in copper than is double that of brass. The higher vapour quality suggests that there is more vapour, which could be due to longer confined bubbles or more bubbles. A comparison of figure 5.6 and 5.7 shows copper to have longer confined bubbles than those of brass. This could be a result of a higher bubble departure frequency in brass, from more nucleation sites, resulting in smaller bubbles or due to the higher heat flux of copper. Higher heat fluxes and exit vapour qualities are again seen for the copper channel during the slug flow regime. The exit vapour qualities are similar between copper and brass for churn and annular flow, although slightly higher for copper, which suggests a similarity in the flow patterns due to

similar vapour content. The exit vapour qualities and heat fluxes are considerably lower for stainless steel, with annular flow dominating over a larger range. This is contrary to what is expected based on the wall superheats, and consequent nucleation site activation, and the surface characteristics. Brass has the highest wall superheat and is the roughest surface, which should ideally equate to more bubbles and higher exit vapour qualities. However copper has the higher vapour qualities but is the smoothest surface and has the median wall superheat. These results show that the surface characteritistics do have an effect on the flow patterns. Although the same flow patterns were evident, for both increasing and decreasing heat flux, across all three materials, the conditions at which these flow patterns occurred changed. The differences seen in the heat fluxes should relate to the wall superheat, with the changes in the heat flux directly affecting the wall temperature and hence superheat. The differences in the exit vapour qualities refer to differences in the number of bubbles or composition of the flow pattern, which should relate to the surface characteristics. There is no clear trend on which surface characteristic can be used to define the occurrence of the flow patterns.

5.3.2 Effect of mass flux

The effect of mass flux is seen to vary with material, with flow transitions shifting to higher vapour qualities with increasing mass flux for all materials but to different extends. Although, as stated in Chapter 3, the experiments were halted for copper and brass at mass fluxes of 400 kg/m^{2}s, due to instabilities, this was after the occurrence of annular flow. As seen from figure 5.3, 5.6 and 5.7, the vapour quality at which the flow transitions occur differs for the three materials. Figure 5.8 presents the experimental flow pattern transitions for the three materials as a function of the mass fluxes. It can be clearly seen that not only the vapour quality at which the transition occurs varies, but the relationship with mass flux also varies. Figure 5.8 a presents a comparison of the flow transition from single to bubbly flow, clearly showing a variation in both the trend and magnitude of the mass flux with vapour quality between the materials. Stainless steel and brass show the same relationship between the vapour quality and mass flux at the transition into bubbly flow, but the vapour quality for brass is double that of stainless steel. A higher vapour quality suggests that at the occurrence of bubbly flow, there are more bubbles present and a higher bubble departure frequency than for stainless steel. This may be due to a higher number of active nucleation sites on

the rougher surface, brass. Although copper has the highest vapour quality at the onset of bubbly flow, besides for mass fluxes over 400 kg/m^{2}s, but is the smoothest surface. The effect of mass flux is also seen to be considerably greater for copper than for stainless steel or brass. An increase in the mass flux will increase the turbulence within the channel which will improve the chances of bubble coalescence. Therefore, it is expected that the flow pattern transitions will change with mass flux, with annular flow occurring at low vapour qualities at higher mass fluxes. The differences seen in the flow transitions, in the relationship of mass flux and vapour quality, reflects on the differences seen in the flow patterns. The vapour quality was seen to be higher for copper than the other materials, suggesting a greater number of bubbles or larger bubbles. As the mass flux is increased, the chance of these bubbles coalescing is increased which would transition the flow into the succeeding flow pattern. The flow pattern transitions in relation to mass flux and vapour quality do not follow the same trend as seen with the superheat values at the onset of nucleate boiling. Stainless steel has the lowest superheat, followed by copper, but these show vastly different trends in the flow transitions. As the superheat is related to the number and size of the active nucleation sites, it is expected that this would relate to the flow transitions, especially for bubbly flow. Figures 5.8b to 5.8d depicts the flow transitions for slug, churn and annular flow, based on the recorded flow patterns with a decreasing heat flux and the corresponding vapour quality. It can be seen that the effect of mass flux for copper is evident across the whole flow range but the magnitude in vapour quality between stainless steel and brass increases. This increase in magnitude is evident in figures 5.3 and 5.7, where there is a larger vapour quality region for churn and annular flow with brass. The higher vapour quality of the flow transitions for brass could be a consequence of the higher vapour quality at the onset of bubbly flow due to a higher number of bubbles.

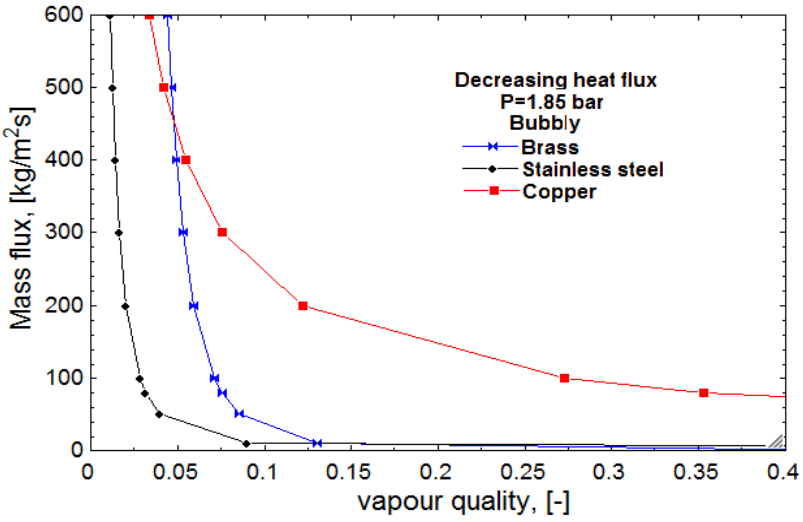
Decreasing heat flux
P=1.85 bar
Bubbly
Brass
Stainless steel
Copper
Mass flux, [kg/m2s]
vapour quality, [-]
0
100
200
300
400
500
600
0
0.05
0.1
0.15
0.2
0.25
0.3
0.35
0.4

(a)

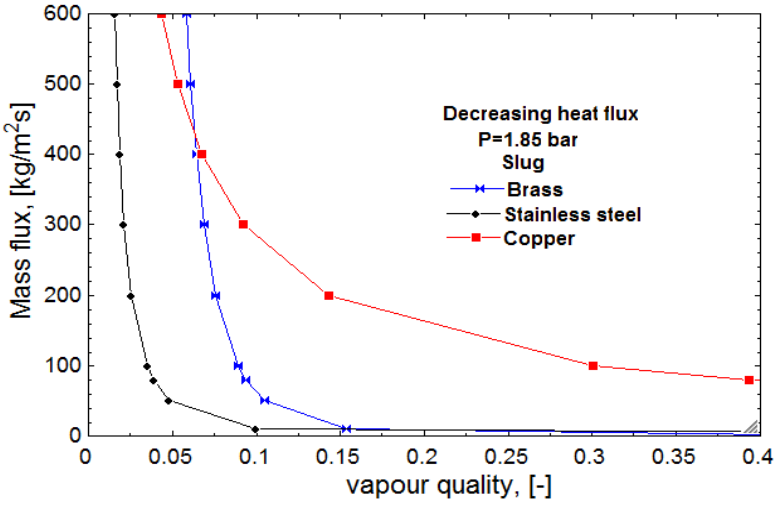
Decreasing heat flux
P=1.85 bar
Slug
Brass
Stainless steel
Copper
Mass flux, [kg/m2s]
vapour quality, [-]
0
100
200
300
400
500
600
0
0.05
0.1
0.15
0.2
0.25
0.3
0.35
0.4

(b)

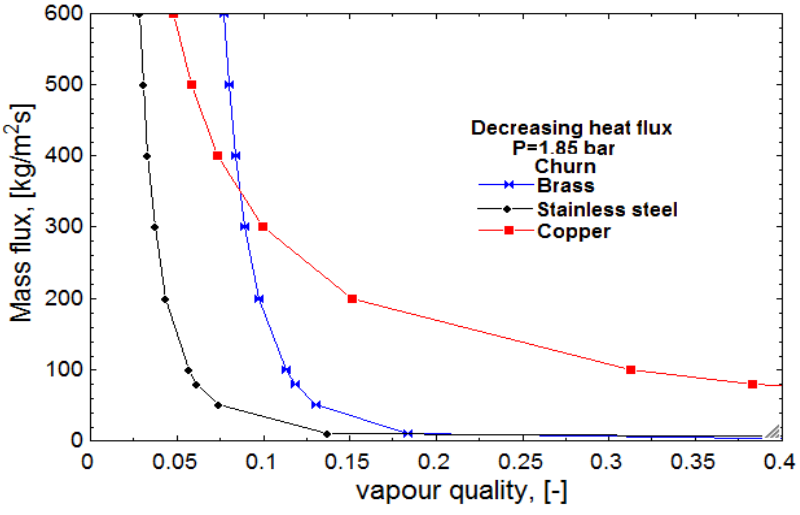
Decreasing heat flux
P=1.85 bar
Churn
Brass
Stainless steel
Copper
Mass flux, [kg/m2s]
vapour quality, [-]
0
100
200
300
400
500
600
0
0.05
0.1
0.15
0.2
0.25
0.3
0.35
0.4

(c)

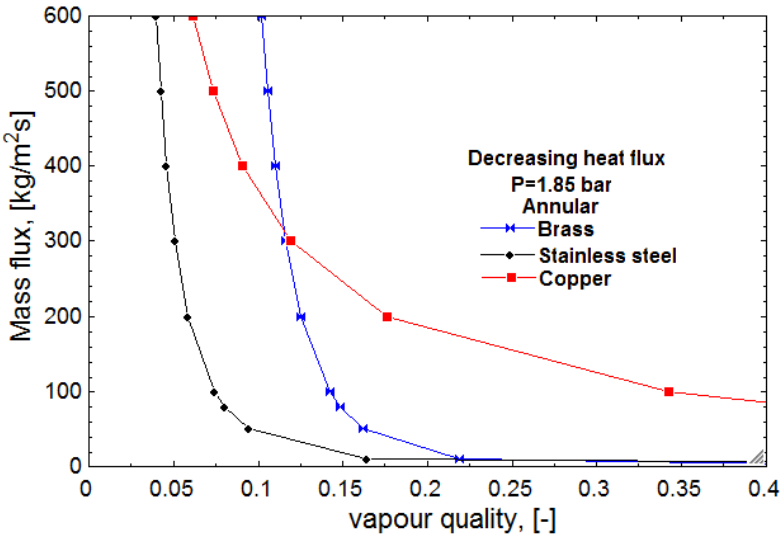

(d)

Figure 5.8. Experimental flow pattern transition lines for (a) bubbly, (b) slug, (c) churn and (d) annular, as a function of vapour quality and mass flux.

5.3.3 Effect of inlet pressure

The effect of inlet pressure was investigated at 1.85 and 2.45 bar for all three materials. Figure 5.9 presents the experimental superficial liquid and vapour velocities at both inlet pressures for the three materials, based on a comparison of the recorded flow patterns and corresponding calculated superficial velocities. From this, it can be seen that there is a clear difference between the effect of inlet pressure, with the extent of this being material dependent. The effect of inlet pressure is larger for copper and brass, with differences seen for both liquid and vapour superficial velocities. For stainless steel, the effect of inlet pressure is reduced as the superficial gas velocity increases. For all of the materials, the liquid superficial velocity decreases with an increasing superficial vapour velocity. This is expected due to the annular flow exhibiting a faster flowing vapour core and a slower liquid film. The liquid film is likely to vary between the materials, due to the effect of the surface roughness. For example, a large number of surface peaks and imperfections could disrupt the liquid film, and slow the liquid film due to the increasing friction. This would become more apparent as the liquid film thins with the increase in the heat flux. This could explain why the stainless steel results shows a greater decrease in the superficial liquid velocity with the increase in pressure compared to the other materials.

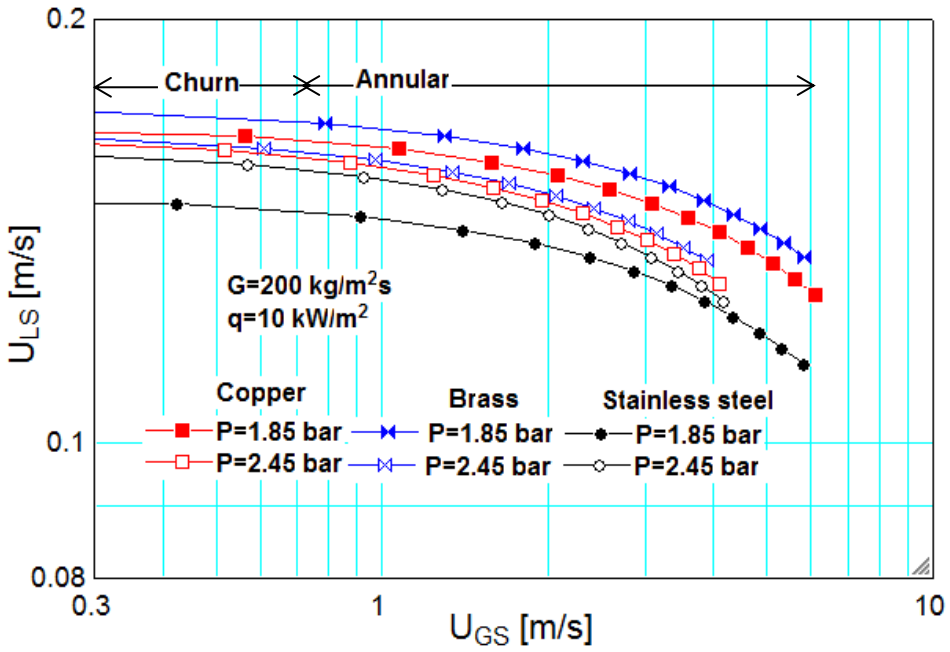

Figure 5.9. A comparison of the superficial velocities for copper, brass and stainless steel at inlet pressures of 1.85 and 2.45 bar.

The superficial velocities are a function of the mass flux, which is constant in this graph, and the vapour quality and density. Due to the differences in the flow patterns and hence heat transfer coefficient, the temperature at which the superficial velocities are calculated varies. For example, the percentage difference between the vapour density at both inlet pressures is 36% for stainless steel but only 25% for brass. As previously noted, the vapour qualities are also different between the materials. Stainless steel is seen to have lower vapour quality than for copper and brass. Interestingly, the effect of the inlet pressure does differ between the two materials, as seen in figure 5.9. For copper and brass, the increase in inlet pressure resulted in a shift to lower liquid superficial velocities which is not seen for stainless steel. For brass and copper, the superficial liquid velocities are similar for the last data points, with the differences seen in the superficial gas velocity. The vapour quality at this last point is similar between the inlet pressures for all three materials. The main differences seen are a consequent of the different vapour quality across the channel length which is a function of the channel material seen with the differing flow patterns.

5.4 Flow pattern maps

As previously discussed, the effect of hysteresis was evident for all materials with R245fa. As the flow pattern range is limited for increasing heat flux, the comparison with flow pattern maps is based on the data for decreasing heat fluxes for R245fa. Figure 5.10 presents a comparison of the experimental data for stainless steel, brass and copper compared with the transition lines presented by Revellin and Thome (2007). The transition lines are between isolated bubble (IB), coalescence bubble (CB) and annular (A) flow patterns. The transitions are based on a certain heat flux which for this purpose was taken to be 10 kW/m^2. At this heat flux, different flow patterns were seen depending on the mass flux. As these transitions are based on one heat flux, there are possible discrepancies on the flow transitions. This heat flux was chosen to give the best representation of two phase flow across all of the materials, inlet pressures and mass fluxes. However, if the transition lines were based on an alternative heat flux, the corresponding vapour quality would differ. For example, if plotted at a higher heat flux, the vapour quality values would be higher. The transitions lines show there is a threshold mass flux at which the flow patterns are vapour quality dependent, with the lines becoming horizontal with increasing mass flux, see figure 5.10.

For all of the materials, annular flow occurs at a much lower vapour quality than that predicted by Revellin and Thome (2007) across the mass flux range. Bubble flow was predicted best for brass, although the prediction becomes less accurate at higher mass fluxes. The Revellin and Thome (2007) transitions are calculated from the experimental conditions, including vapour quality. As such, there are slight variants seen in the predicted transitions between the materials but to a much smaller extent than seen with the experimental data. The same trend is seen in all cases, with annular flow not being predicted at low mass fluxes which is not in agreement with the experimental data, where annular flow dominated.

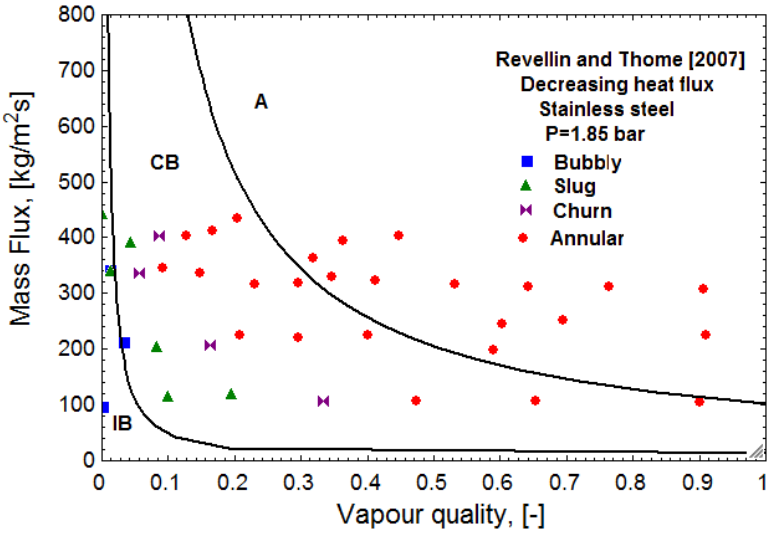

(a)

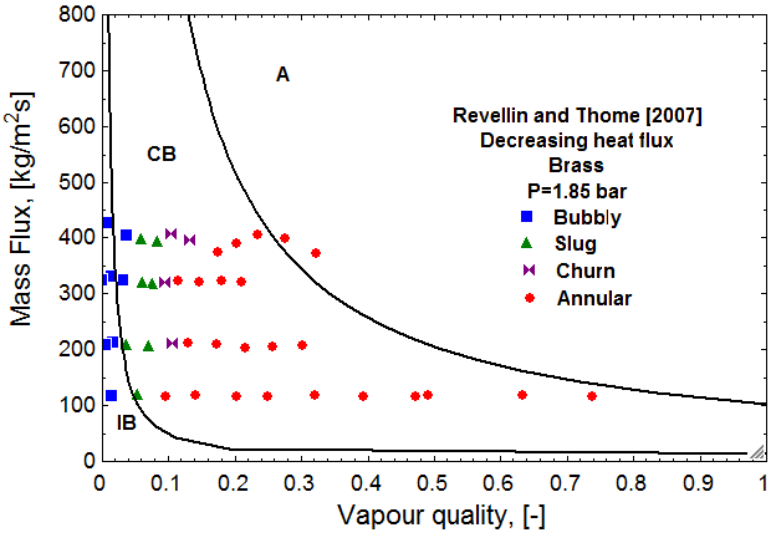

(b)

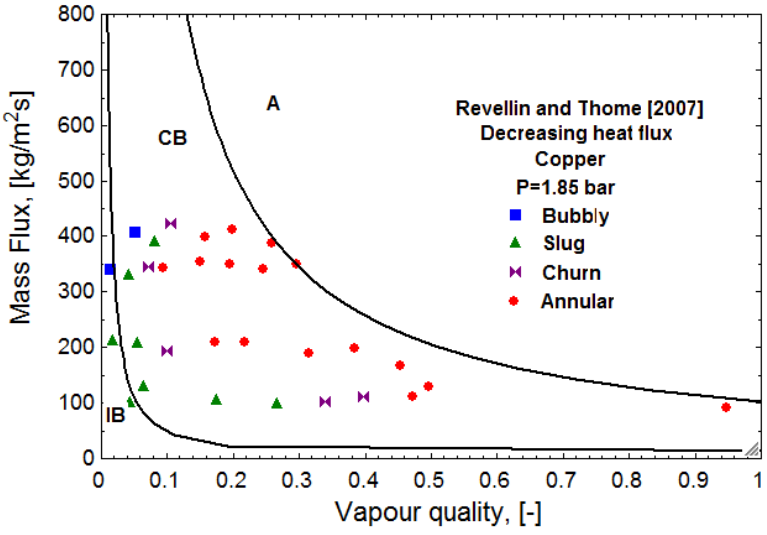

(c)

Figure 5.10. Comparison of experimental data with Revellin and Thome [2007] model for (a) stainless steel, (b) brass and (c) copper.

Figure 5.11 presents a comparison of the experimental R245fa data with the Ong and Thome (2009) model. The Revellin and Thome (2007) model presented an alternative method of defining flow pattern transitions based on the definitions of isolated bubble (IB), coalescence bubble (CB) and annular (A). This original model was based on data for R134a but has been updated to include a range of refrigerants. This adapted Ong and Thome (2009) model includes data for R245fa and R236fa and a further transition of plug-slug (P-S) flow. The Ong and Thome (2009) model accurately predicts the bubbly region, assuming that this corresponds to the IB region, for brass but the annular flow occurs at a lower vapour quality than predicted, with the accuracy of prediction decreasing with mass flux. This is also true for copper where all of the transitions occur at a lower vapour quality than predicted. The slug-plug line, which could be the slug region, was accurate at low heat fluxes but did not allow for slug flow at heat fluxes higher than 300 kg/m^2s.

A comparison of figure 5.10 and 5.11 shows that the experimental flow pattern transitions do not follow the same trend as those of Ong and Thome (2009). Copper shows the greatest similarity in the trend of the transitions, with larger differences seen at lower mass fluxes but the experimental transitions show a smoother decrease in vapour quality with increasing mass flux. Figure 5.8 shows that for the experimental results, the flow pattern transitions follow the same trend, which is material dependent. This is not seen for the Ong and Thome (2009) model, where the relationship between the mass flux and vapour quality is dependent on the flow pattern transition.

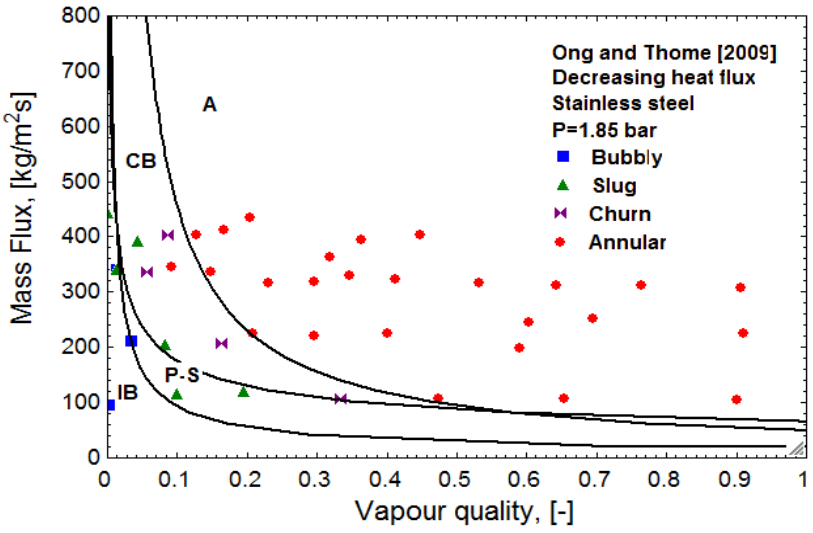

(a)

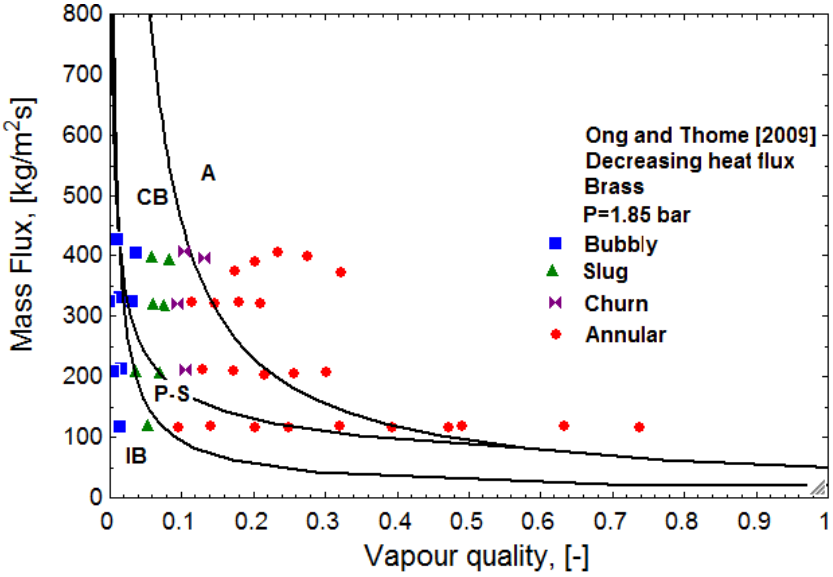

(b)

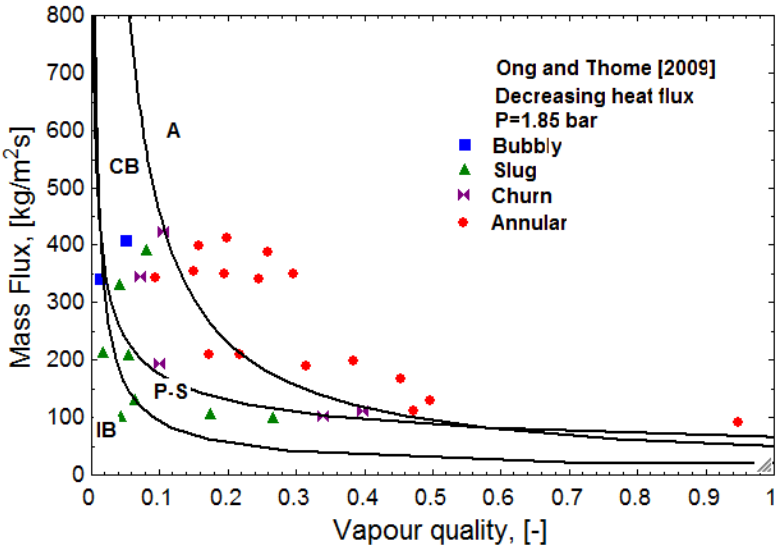

(c)

Figure 5.11. Comparison of experimental data with Ong and Thome (2009) model for (a) stainless steel, (b) brass and (c) copper.

Costa-Patry et al. (2012) presented a flow pattern based heat transfer coefficient model, which used a modified Thome et al. (2004) model for the intermittent region and a modified Cioncolini and Thome (2011) model for the annular flow and a transition model. Charnay et al. (2014) used this modified model to adapt the Revellin and Thome (2007) flow pattern map. Figure 5.12 presents a comparison of the experimental data and the Costa-Patry et al. (2012) model. The IB-CB transition remains the same as previously seen in figure 5.10 and 5.11. In comparison to the Revellin and Thome (2007) model, the CB-A transition has shifted to a lower vapour quality which improves the flow predictions. This model shows a worse prediction compared with Ong and Thome (2009) for the CB-A transition, with similar predictions at higher mass fluxes but a worse correlation at lower mas fluxes. This is especially evident with brass. The mass flux has a higher power for the Ong and Thome (2009) transition which is evident by the greater change in gradient with mass flux. The Costa-Patry (2012) model differs for having a function of the heat flux, with the transitions presented in figure 5.12 being at a heat flux of 25 kW/m^2. This does make the comparison of the models more complicated as the transition shifts to higher vapour qualities with an increase in heat flux. The Costa-Patry (2012) model does show good agreement with stainless steel and copper.

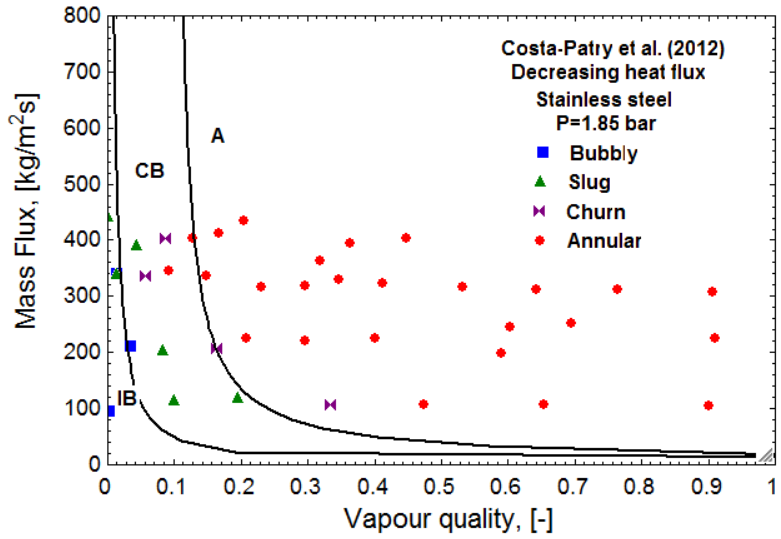

(a)

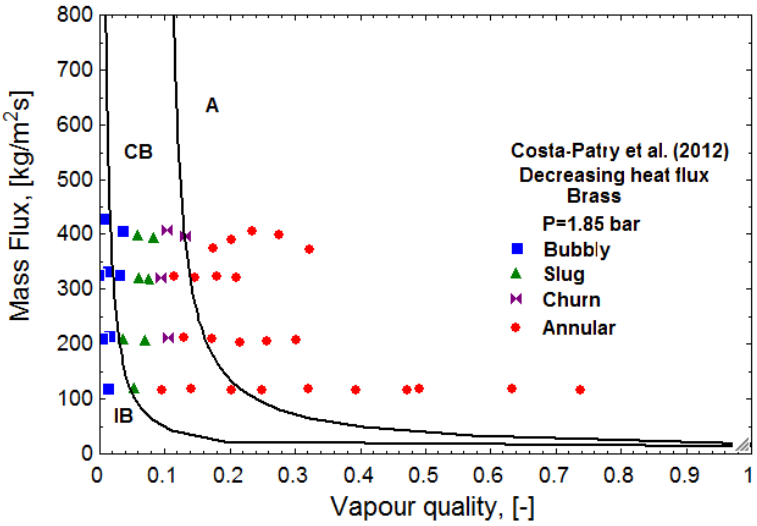

(b)

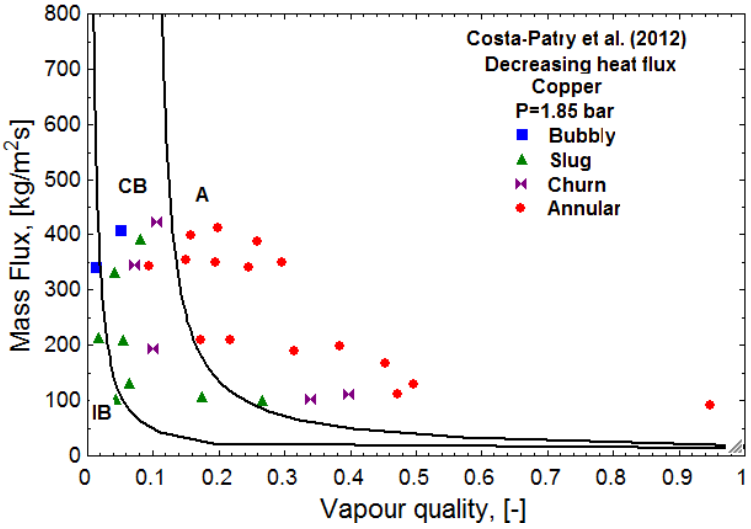

(c)

Figure 5.12. Comparison of experimental data with Costa-Patry (2012) for (a) stainless steel, (b) brass and (c) copper at a heat flux of 25 kW/m^2.

Figure 5.13 presents a comparison between the vertical flow pattern map of Hassan et al. (2005) which is plotted as a function of the superficial velocities. The experimental slug flow data was included under the intermittent region presented in figure 5.13. This map includes a larger range of superficial velocities than seen with the experimental data. The annular flow is predicted moderately well, with the prediction improving with the mass flux. The bubble and slug flow are predicted at a lower superficial gas velocity than seen experimentally. The slug and annular flow patterns are predicted well, especially for mass fluxes of 200 and 300 kg/m^{2}s. The bubbly flow occurs at a superficial gas velocity only slightly higher than predicted, besides at a mass flux of 400 kg/m^{2}s. A comparison of these figures shows a similarity in the predicted annular transition at lower superficial liquid velocities. The predicted transition for bubbly flow shows a similar gradient but shows a variance in the superficial liquid velocities magnitude.

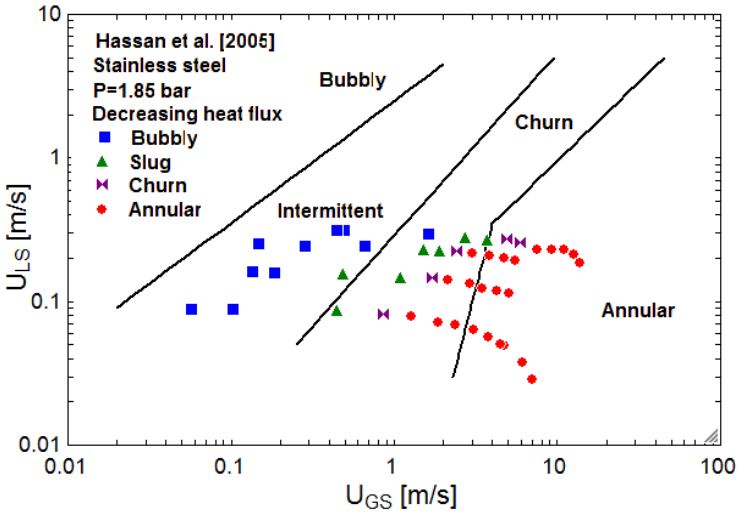

(a)

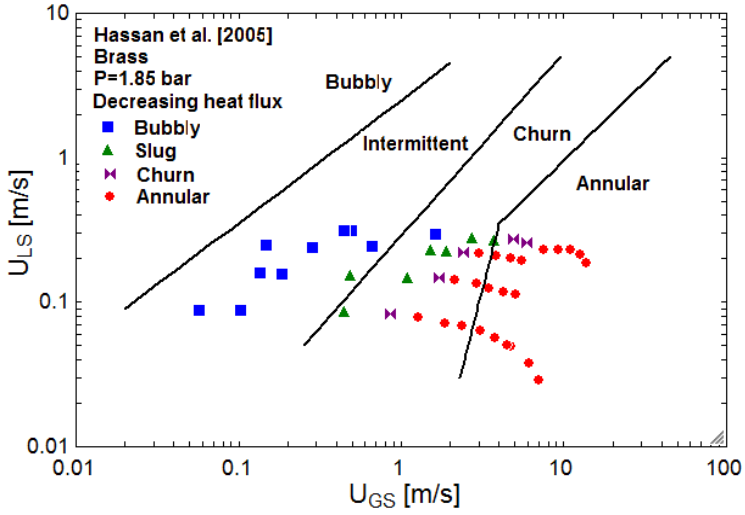

(b)

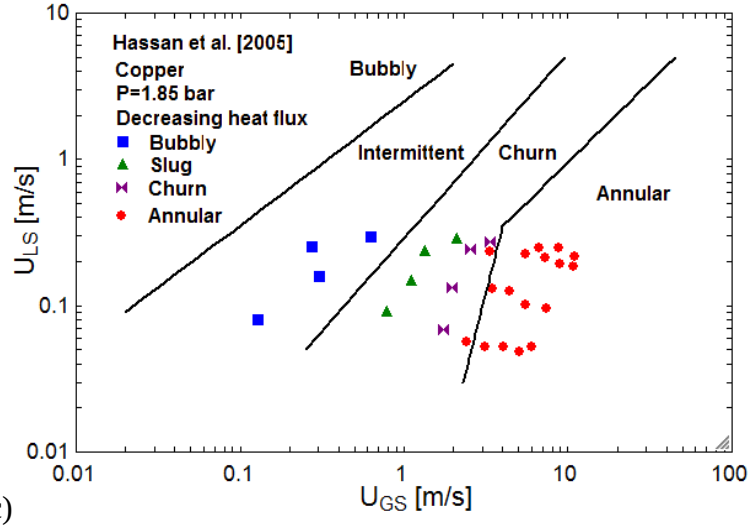

(c)

Figure 5.13. Comparison of experimental data with Hassan et al. (2005) for (a) stainless steel, (b) brass and (c) copper. Intermittent flow includes confined bubble and slug.

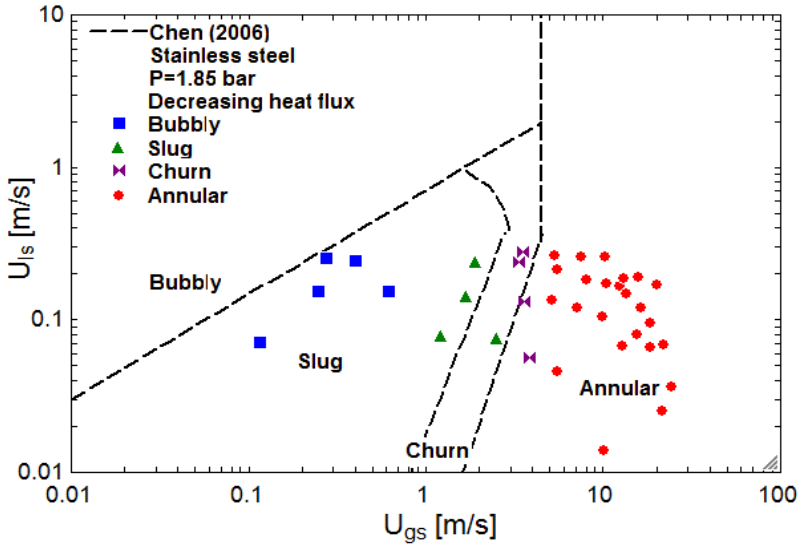

(a)

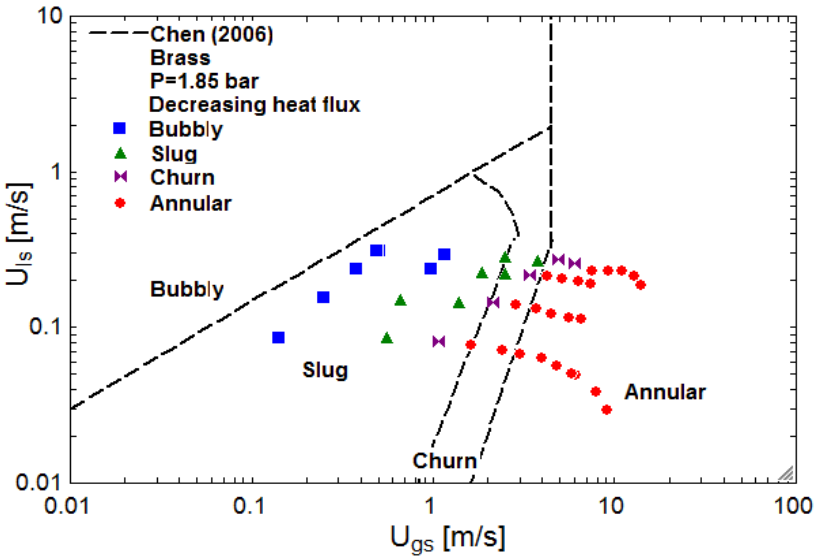

(b)

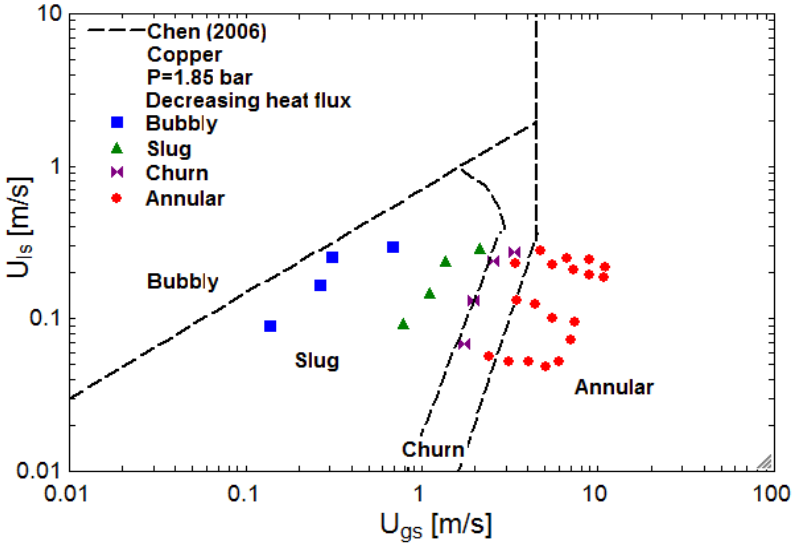

(c)

Figure 5.14. Comparison of experimental data with Chen (2006) for (a) stainless steel, (b) brass and (c) copper.

Chen (2006) produced a model predicting flow patterns based on the superficial gas and liquid velocities, which can be seen in figure 5.14. This figure shows that the surface characteristics have a greater influence on the superficial gas velocity over the superficial liquid velocity. The superficial liquid velocity is similar for all three materials but the flow transitions occur at different superficial gas velocities. The superficial velocities are calculated from the mass flux, density and vapour quality. The mass flux and density is relatively the same for all three materials, but the vapour quality differs. The Chen (2006) model is based on R134a, which has higher vapour density and consequently a lower superficial gas velocity. For all the materials, bubbly flow occurred at a higher superficial velocity than predicted, due to the change in refrigerant. The slug flow is predicted well for all three materials, but the churn flow is predicted best for copper. As seen in figure 5.8, the vapour quality at the copper flow transitions is greatly influenced by mass flux which in turn will influence the superficial velocities. The Chen (2006) model predicts a decrease in the superficial gas velocity with a decrease in the superficial liquid velocity. This relationship is seen with copper and brass to some degree but less so for stainless steel. The annular flow is predicted well for stainless steel and copper but less so for brass. Slug flow is predicted well for all of the materials.

Harirchain et al. (2012) suggested an alternative flow pattern map which was based on the phase change number (N_{pch}) and a convective confinement number ($Bo^{0.5}$ Re), see figure 5.15.

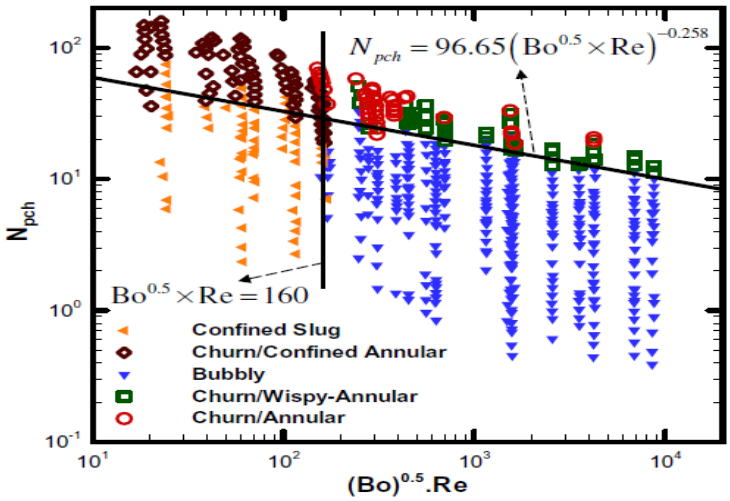

Figure 5.15. Flow pattern map presented by Harirchain et al. (2012).

This flow pattern map was deemed unsuitable for this investigation due to the relatively small convective confinement number range, ~1 – 25, of the current experiments in comparison to the work by Harirchain et al. (2012). Due to this difference in convective confinement number range, the experimental data for R245fa was grouped in the confined slug area of the map. This flow pattern map was produced from experimental data from rectangular channels with varying average surface roughness values and across a mass flux range of 214-1461.

5.5 Summary

Flow patterns were recorded for R245fa in a stainless steel channel and compared with those of R134a over a range of inlet pressures and mass fluxes. The flow patterns were classified as bubbly, confined, slug, churn and annular flow. All of these flow patterns were recorded for R134a, with both an increasing and decreasing heat flux. This is contrary to R245fa where only single phase and annular flow was recorded with an increasing heat flux but all of the flow patterns were evident when the heat flux was decreased, showing a strong effect of hysteresis. Annular flow was dominant for both refrigerants but occurred at a much lower vapour quality and heat flux for R245fa due to the changes in the thermophysical properties. These property changes were also reflected in the effect of inlet pressure, which was reduced for R245fa and showed a varying trend than that of R134a.

Stainless steel, copper and brass channels, using R245fa, were utilised to investigate the effect of surface characteristics on flow patterns. Figure 5.8 shows that the surface characteristics does have an effect on the flow transitions as a function of mass flux which is not represented in the flow pattern maps. Although the average surface roughness values do follow the same trend as superheat at the onset of nucleate boiling, this trend is not seen for the flow transitions. Each material shows a varying trend in the flow pattern transitions as a function of mass flux and vapour quality which cannot currently be related to a specific surface characteristic. This figure also shows the trends between the flow patterns to be similar for all flow transitions with mass flux, this is not the case for the Ong and Thome (2009) model. The Costa-Patry (2012) model also shows similar trends between the flow pattern transitions but over a larger vapour quality range than seen with the experimental data.

The effect of changes to the flow pattern transitions with difference materials is not as evident when plotted as a function of superficial velocities. Although there are small differences in the accuracy of the flow pattern maps between the materials, those flow pattern maps which were plotted as a function of superficial velocities performed better, with a smaller variance between the channel materials. The differences seen in the superficial velocities are due to the changes in vapour quality between the materials. This is due to changes in the surface characteristics affecting the onset of nucleate boiling, with annular flow occurring at considerably lower vapour quality than that of copper or brass. Surface characteristics play an important role in bubble nucleation and have been seen to effect the experimental conditions at which the flow patterns are evident. The relationship between the flow pattern transitions and the surface characteristics is still unclear, with no trend evident in the measured surface characteristics and the onset of nucleate boiling.

Chapter 6

6. Heat transfer results

6.1 Introduction

The heat transfer data presented in this chapter are steady state measurements, based on inlet fluctuations in the pressure and mass flux, which are time averaged over 90 second periods. The heat transfer coefficient is compared based on the working fluid and the channel material, in terms of the inlet pressure, heat flux and mass flux. The experiments were conducted at inlet pressures of 1.85 and 2.45 bar, equating to saturated temperatures of 31 and 39˚C, and a mass flux range of 100 – 400 kg/m^{2}s and an increasing heat flux. The materials are compared for the values of wall superheat and hence the onset of nucleate boiling. The heat transfer coefficients are compared with correlations in literature and evaluated based on the amount of data predicted within ± 30% and the mean absolute percentage error.

6.2 Flow oscillations and stability

The experimental data are recorded once the system was deemed to be stable, based on the inlet conditions. The stability of the system deteriorated with an increase in the heat flux. During the experimental procedure, time was taken between the increase in the applied heat flux and the measurements being taken, to allow for the system to stabilise. Although this does reduce some of the oscillations, the occurrence of two phase flow will cause an increase in the oscillations seen for the system parameters. A comparison of the flow oscillations was conducted at a heat flux of 1 kW/m^2, single phase flow, and 25 kW/m^2, two phase flow. This comparison includes both the inlet and outlet conditions of the heated section. The mass flux was recorded before the test section, but, as seen in figure 6.1, the flow oscillations increase with mass flux. The increased in the mass flux oscillations are not directly linked to the occurrence of two phase flow, as seen with the outlet system parameters. As the heat flux is increased, the

cooling applied to the system is increased. This is applied in small stages to try and reduce the fluctuations caused by the changes in temperature. The increase in the volume of R22 used in the condenser and sub cooler results in mass flux oscillations in the heating loop due to thermal shock. The amplitude of these fluctuations is dependent on the channel material, with copper and especially brass requiring a higher cooling capacity. This is partly due to a higher current being applied to the copper and brass channel. This is evident in figure 6.1 c, where the flow oscillations increase in amplitude with the higher heat flux, but with considerably higher standard deviations for copper and brass over stainless steel.

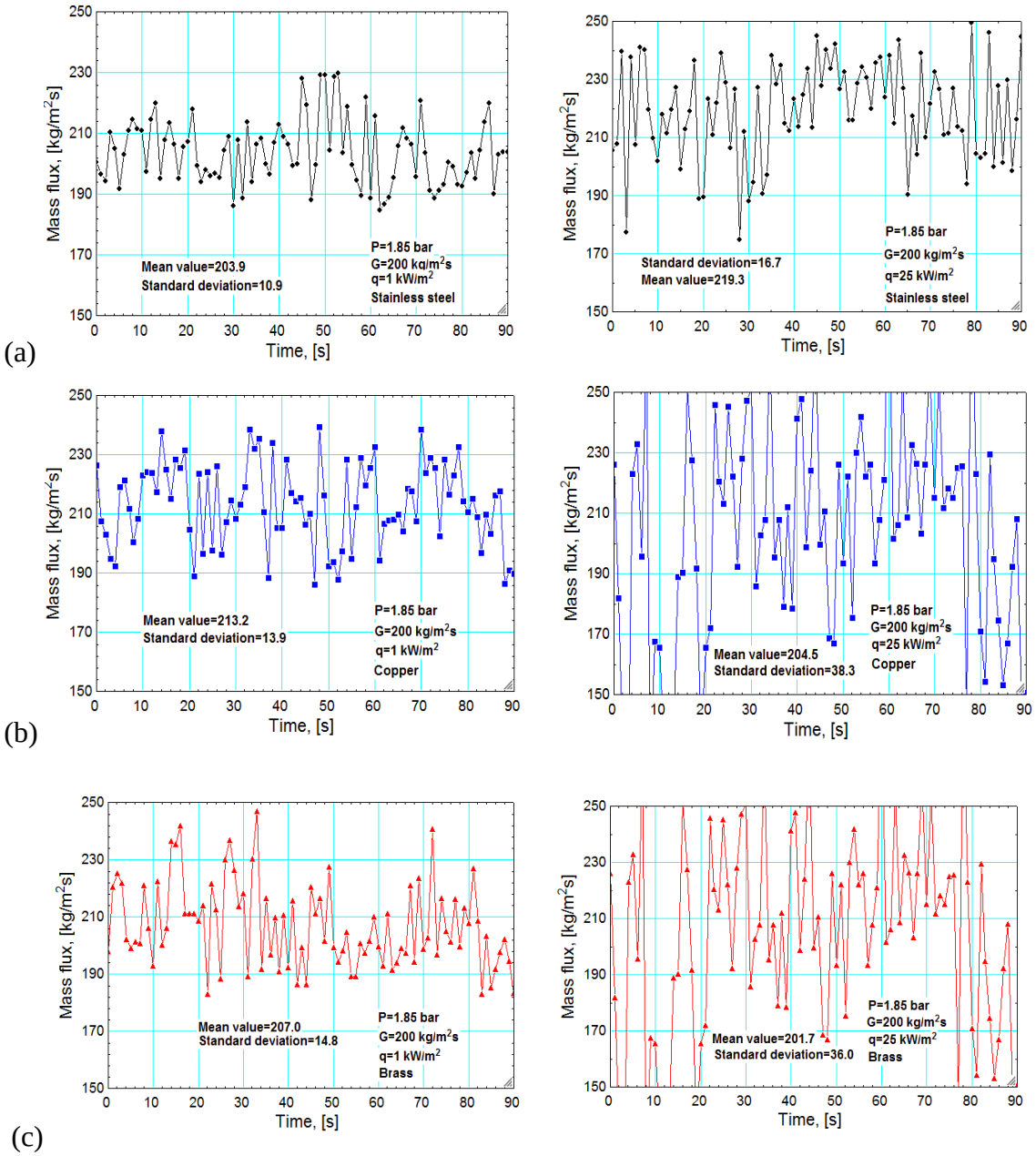

Figure 6.1. Mass flux oscillations at a heat flux of 1 and 25 kW/m^2 for (a) stainless steel, (b) copper and (c) brass.

The inlet temperature oscillations are seen to increase with heat flux, see figure 6.2. The oscillations are greater for stainless steel, with a standard deviation four times that of copper at the higher heat flux. The inlet pressure oscillations are also seen to be greater for stainless steel but to lesser extent, see figure 6.3. This increase in the oscillations seen for stainless steel are due to instabilities in the system, which could be a result of density wave oscillations. A study by Alam et al. (2012) on flow boiling in microgaps concluded that inlet pressure oscillations increased with average surface roughness (Ra) values for larger microgap sizes. This is not seen here, with stainless steel having the intermediate Ra value.

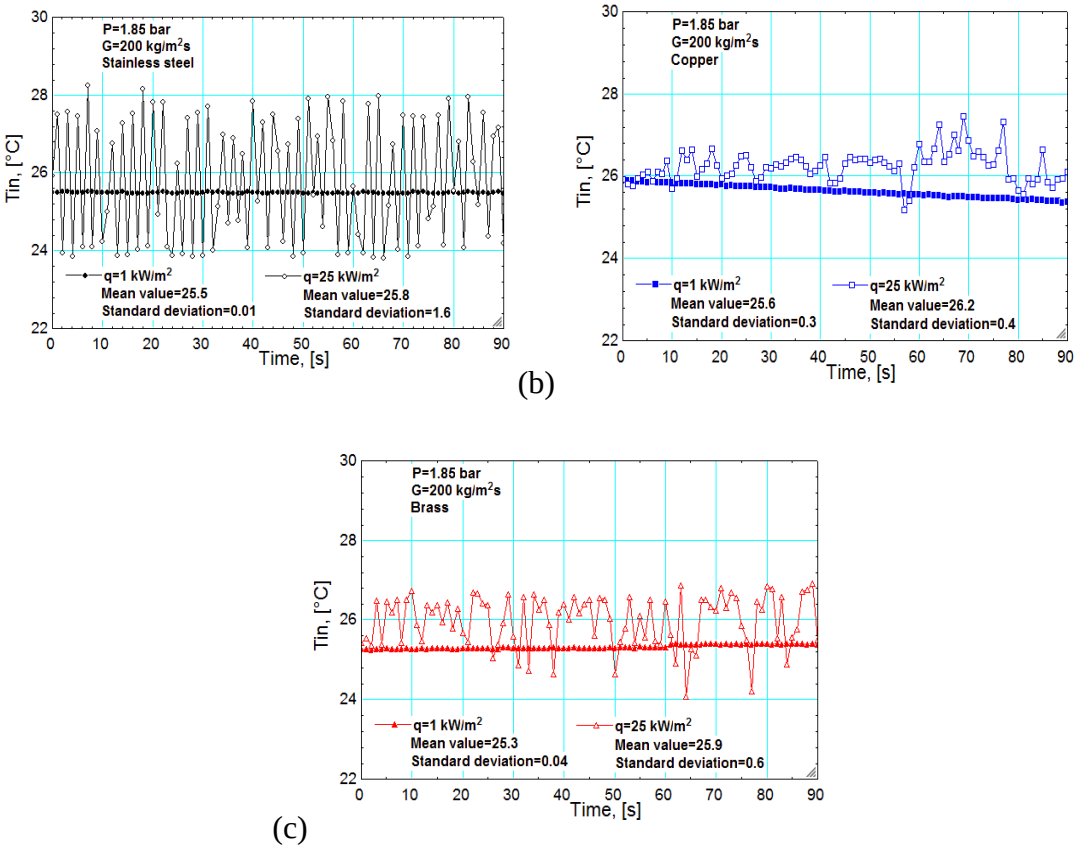

Figure 6.2. Inlet temperature oscillations at heat fluxes of 1 and 25 kW/m^2 for (a) stainless steel, (b) copper and (c) brass.

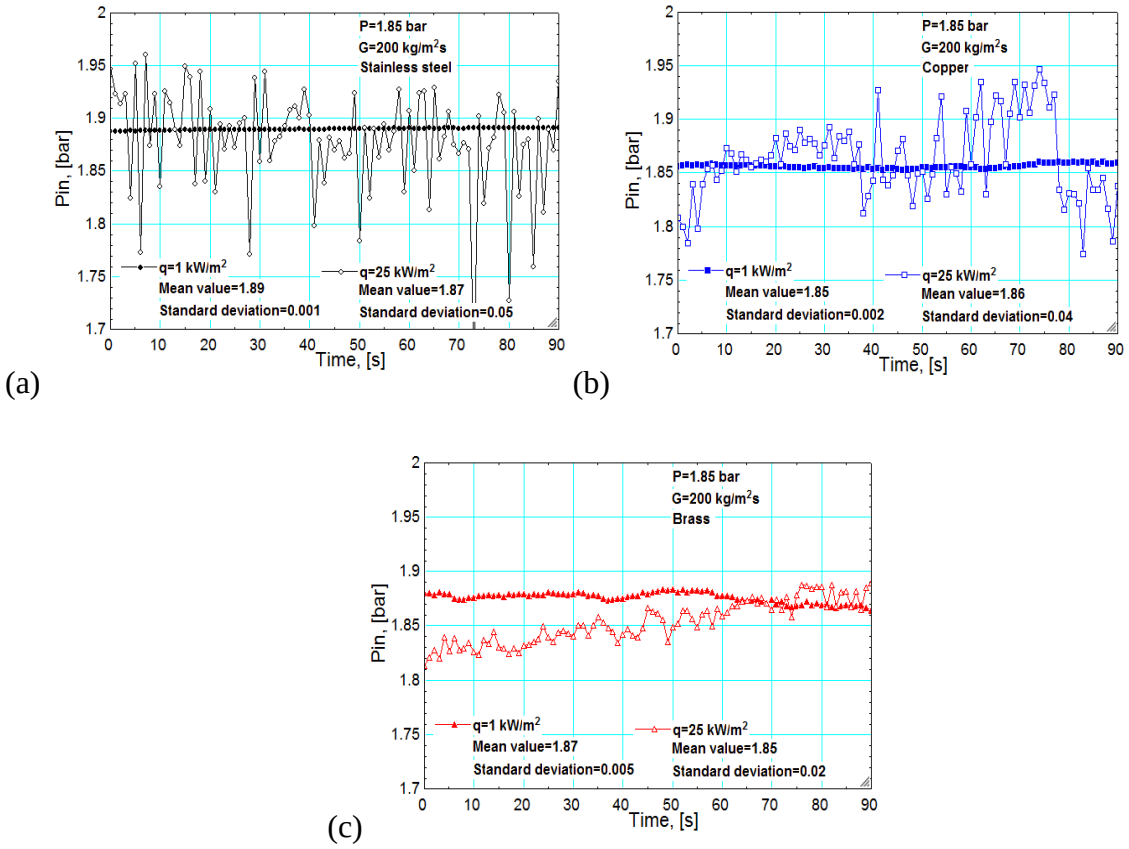

Figure 6.3. Inlet pressure oscillations at heat fluxes of 1 and 25 kW/m^2 for (a) stainless steel, (b) copper and (c) brass.

The oscillations at the outlet of the heated section are caused by the occurrence of two phase flow. This is evident by the low standard deviation of the outlet temperature during single phase flow, see figure 6.4. At a heat flux of 25 kW/m^2, annular flow is present in all of the channels but the annular flow structure can differ between channel materials. During annular flow, the flow consists of a vapour core and a liquid film. The liquid film thickness and stability will affect the wall temperature and pressure drop, both of which are a function of the surface characteristics. The same increase in flow oscillations is seen with the outlet pressure but with copper having half the standard deviation of stainless steel and brass, see figure 6.5. Copper has the lowest average surface roughness which suggests a smoother surface with fewer surface peaks which would disturb the liquid film and potentially result in higher oscillations.

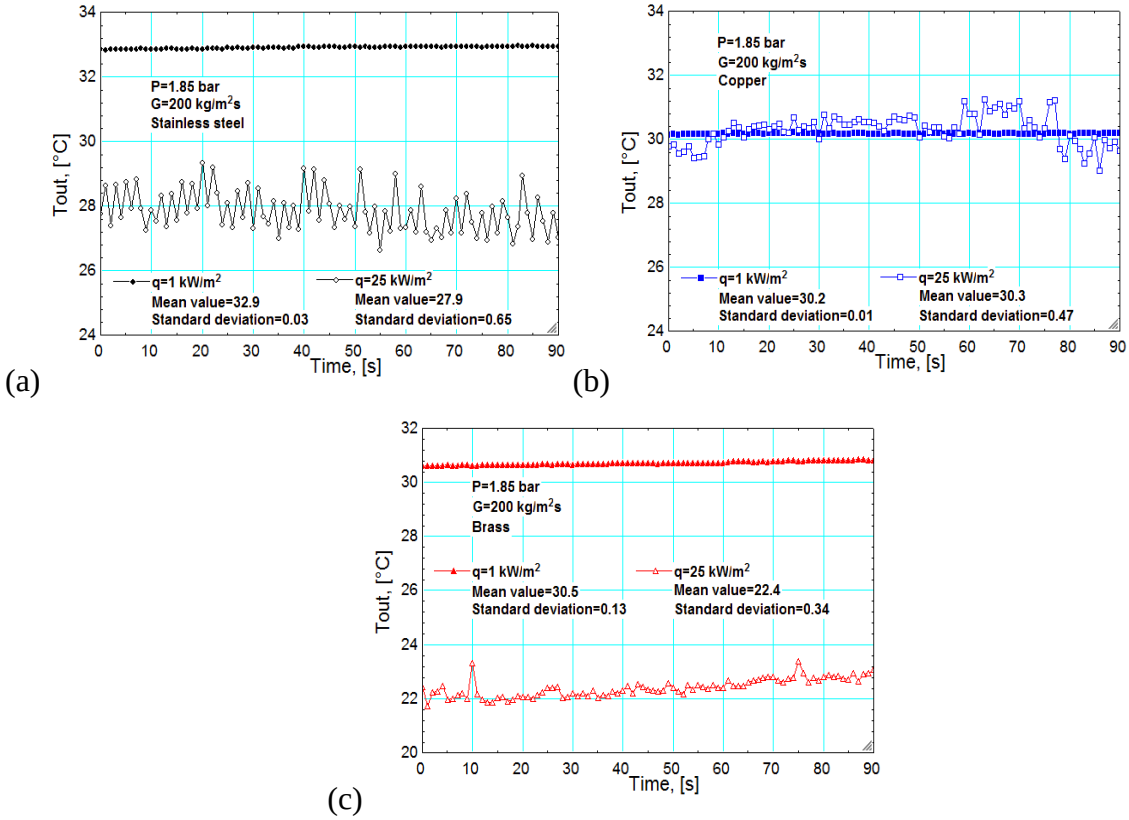

Figure 6.4. Outlet temperature oscillations at heat fluxes of 1 and 25 kW/m^2 for (a) stainless steel, (b) copper and (c) brass.

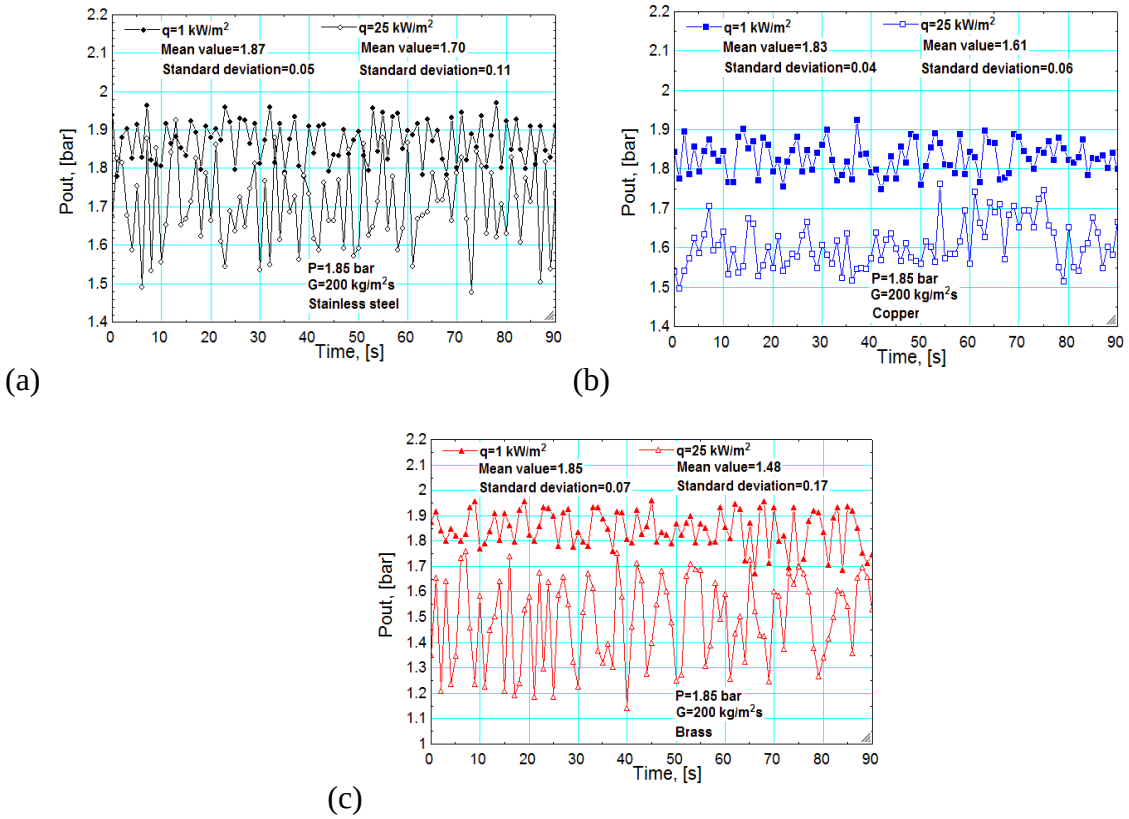

Figure 6.5. Outlet pressure oscillations at heat fluxes of 1 and 25 kW/m^2 for (a) stainless steel, (b) copper and (c) brass.

The wall temperature fluctuations will be greatly affected by the flow patterns within the channel. Although annular flow is present in all of the channels, the oscillations will vary depending on the liquid film thickness and disturbances in the film. Figure 6.6 b shows the wall temperature to drop due to these flow pattern oscillations which results in a larger standard deviation, from 0.08 during single phase to 0.45 at a heat flux of 25 kW/m^2.

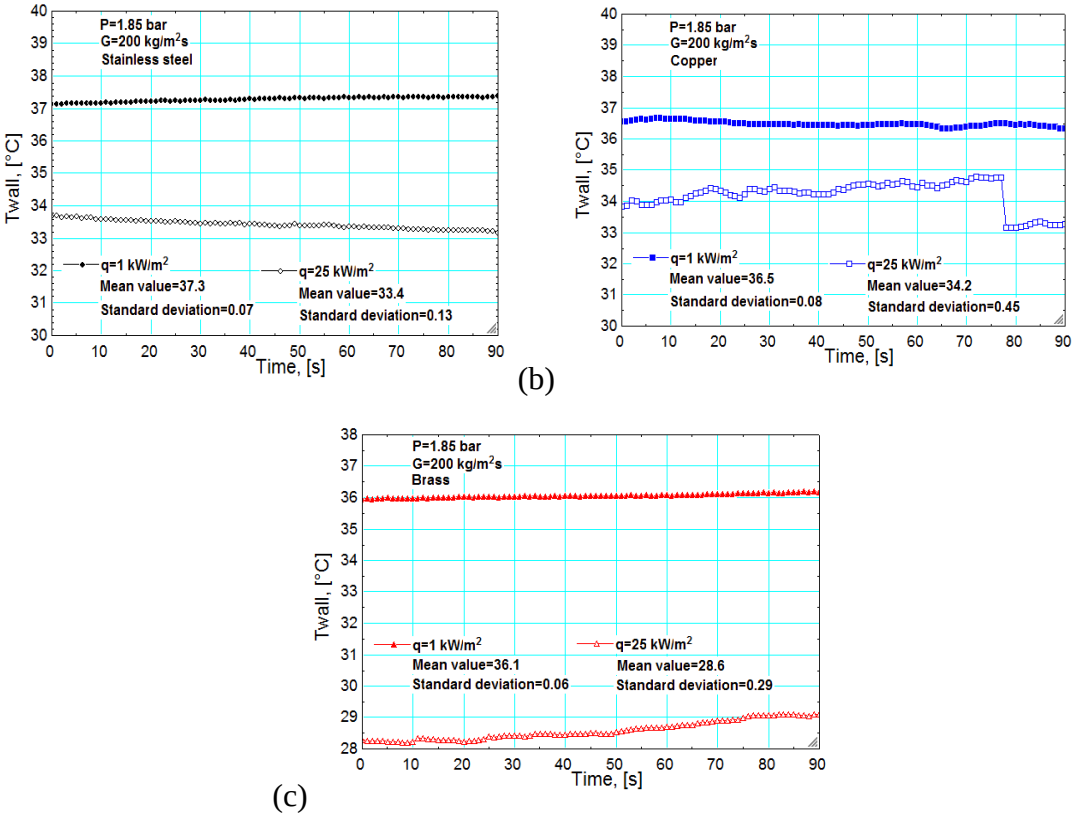

Figure 6.6. Wall temperature oscillations for the last thermocouple at heat fluxes of 1 and 25 kW/m^2 for (a) stainless steel, (b) copper and (c) brass.

A comparison of figures 6.1 - 6.6 show that the experimental data is recorded during stable conditions with the oscillations and standard deviations being small during single phase flow. The oscillations and standard deviations are still low at high heat fluxes but increase due to the occurrence of two phase flow and an increase in the cooling capacity. This comparison is conducted at an inlet pressure of 1.85 bar and mass flux of 200 kg/m^{2}s. At the higher inlet pressure and mass fluxes, the oscillations are greater which results in the experiments having to be stopped for copper and brass. For brass, the experiments were stopped at lower heat fluxes at mass fluxes of 400 kg/m^{2}s and at mass fluxes of 300 and 400 kg/m^{2}s for copper. The oscillations which prevented the experiments being completed were those of the inlet parameters caused by the increase in the cooling capacity required. The inlet pressure increases with the heat flux

which requires the cooling capacity to be increased in the condenser and the cooling coils in the R245fa tank. This results in oscillations in the flow which are too large for the experiments to be conducted. The flow oscillations are relatively similar for each experimental condition. This was validated by examining the reproducibility of the data.

6.3 Reproducibility

In order for the data to be validated and useable, the data needs to be repeatable. Each test is repeated on a different day and the results compared to ensure reproducibility.

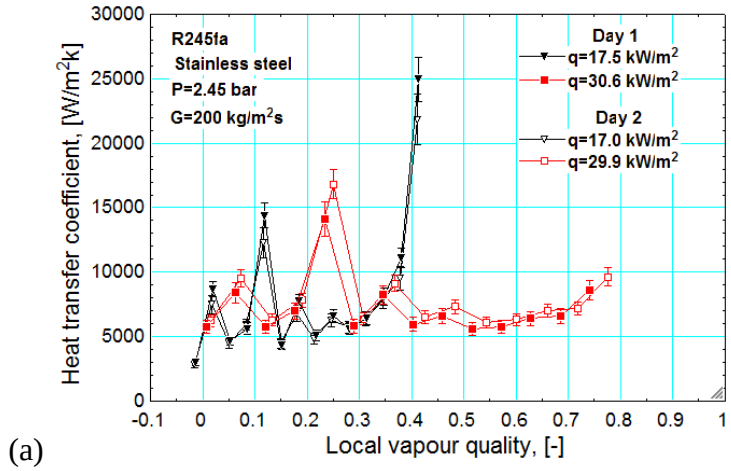

(a)

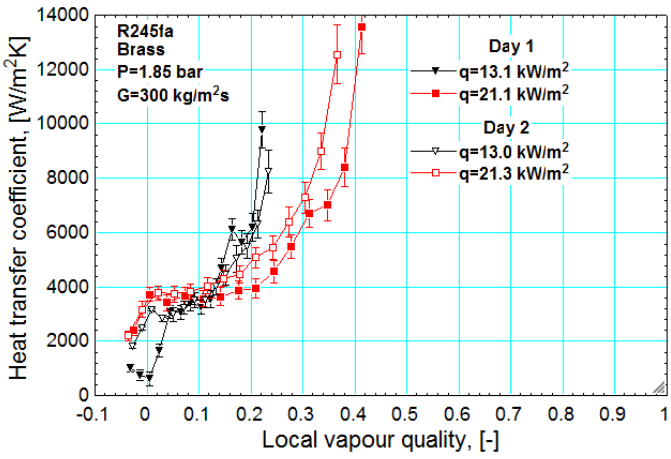

(b)

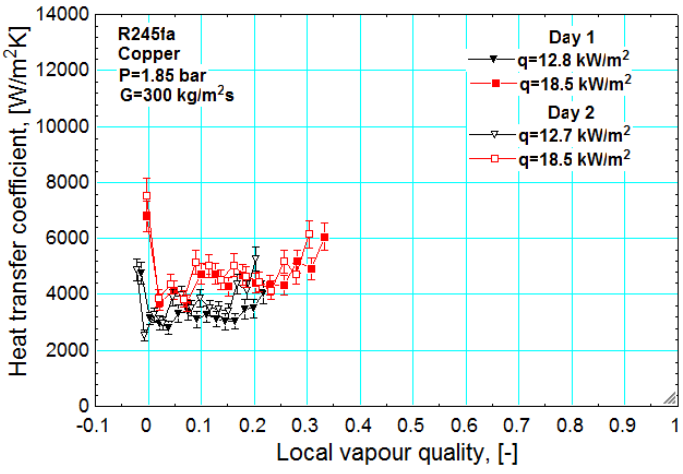

(c)

Figure 6.7. Reproducibility of experimental data for (a) stainless steel, (b) brass and (c) copper tubes.

Figure 6.7 compared the heat transfer coefficient for stainless steel, brass and copper across two days of testing. A comparison of the data shows good reproducibility for all of the materials, especially for the lower heat flux. This includes a comparison across a range of heat fluxes with which two phase flow occurs. This further validates that the oscillations seen are relatively constant at a given heat and mass flux. The

reproducibility is deemed to be good for these experiments with small standard deviations range in the system parameters for both single and two phase flow.

6.4 Heat transfer characteristics for R245fa and R134a

6.4.1 Effect of heat flux

The heat transfer coefficient is presented as a function of local vapour quality and axial location. The heat transfer coefficient data is plotted against the axial location to negate the effects of local vapour quality and more clearly present the effect of heat flux. From figure 6.8 a, the heat transfer coefficient is small with a decreasing trend for low heat fluxes. At these low heat fluxes, with $q<7$ kW/m^2, the flow is single phase according to the recorded flow patterns. The vapour quality is slightly above zero at this point which could suggest sub-cooled boiling which is not detected with the flow visualisation. As expected, the effect of heat flux on the heat transfer coefficient is shown to be negligible during single phase flow. As the heat flux increases, the flow becomes annular with an increase in heat transfer coefficient occurs. There is a sharp peak within these lines which is not seen in single phase flow and become less severe with increasing heat flux. It is thought that these peaks are a result of a surface flaw or imperfection which could be acting as a nucleation site. This could indicate that convective boiling is dominating at higher heat fluxes and therefore the effect of the nucleation site will diminish. For the heat flux range of 7 – 26 kW/m^2, the heat transfer coefficient increases from the first thermocouple to the second thermocouple and remains at a fairly level state, besides the peak, until near the end of the tube where the heat transfer coefficient begins to increase. The increase in the heat transfer coefficient at the end of the channel is thought to be due to the annular flow pattern. As the heat flux continues to be applied along the tube, the liquid film will become thinner and therefore offer less resistance and increases the heat transfer coefficient. At the point of dryout, $q=41$ kW/m^2, the heat transfer coefficient starts high, at 6000 W/m^{2}K, but decreases along the length of the tube. Dryout is considered to be the point at which the heat transfer coefficient drops and the wall temperatures increase rapidly.

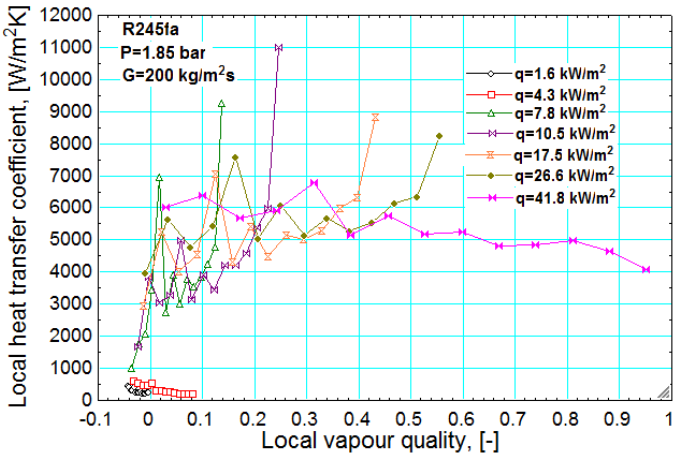

(a)

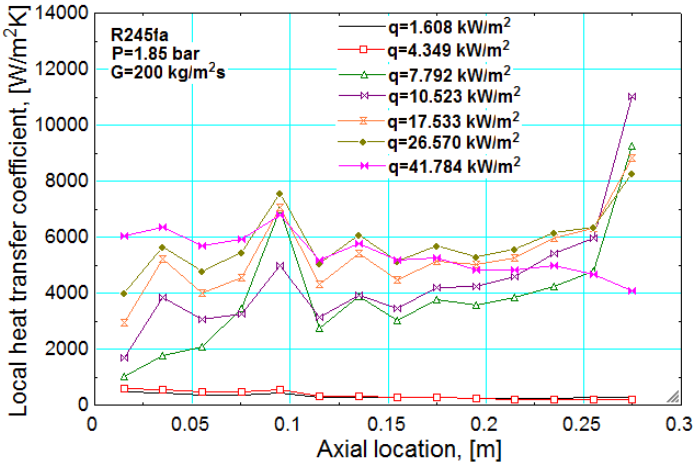

(b)

Figure 6.8. Local heat transfer coefficient for R245fa at a pressure of 1.85 bar and mass flux of 200 kg/m2s as a function of (a) local vapour quality and (b) axial location.

From figure 6.8 b, it can be seen that the heat transfer coefficient does increase with increasing heat flux before dryout, at a heat flux of 41 kW/m^2, for the majority of the tube length. At the end of the tube, as the heat transfer coefficient decreases, it does not show the same increasing trend with heat flux.

For R134a, the heat transfer coefficient shows a greater dependence on the heat flux, see figure 6.9 a. The increase in the heat transfer rates with heat flux is more convoluted when plotted as a function of the local vapour quality but is clearer when plotted as a function of axial location, see figure 6.9 b.

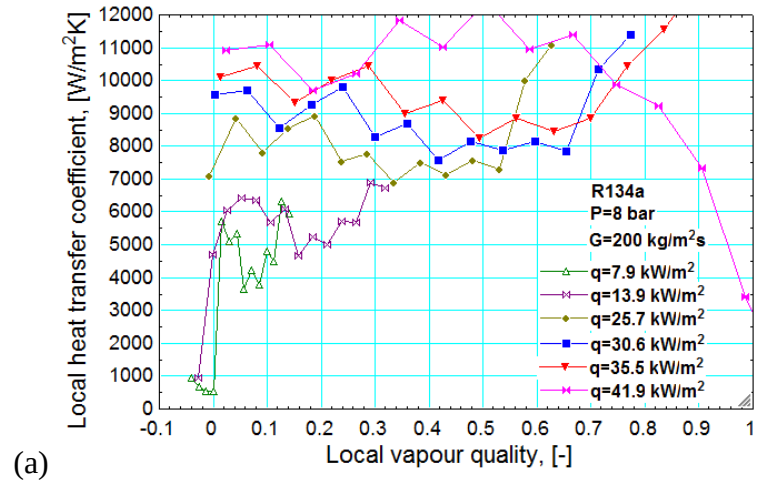

(a)

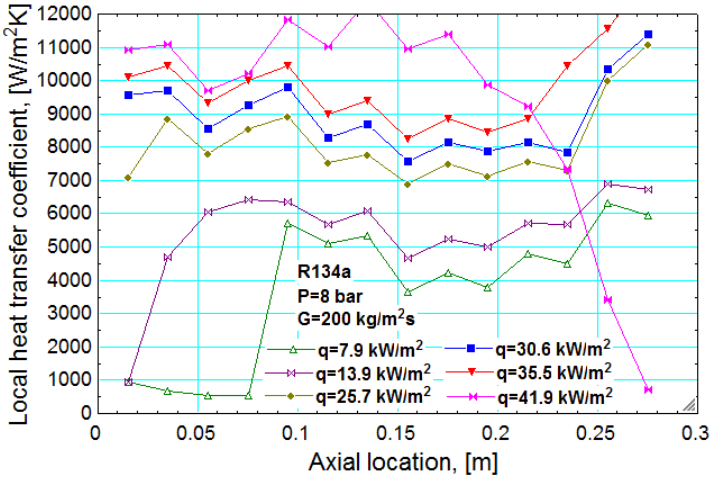

(b)

Figure 6.9. Local heat transfer coefficient for R134a at a pressure of 8 bar and mass flux of 200 kg/m2s as a function of (a) local vapour quality and (b) axial location.

Figure 6.9 b, shows a constant increase in the heat transfer coefficient with heat flux until dryout occurs. The same increase in the heat transfer coefficient near the channel exit is seen, assumed to be due to the thinning liquid film during annular flow. This increase is more gradual than seen with R245fa. For R134a, the onset of nucleation is seen to occur at an axial location of 0.075 m at a heat flux of 7 kW/m^2. The same heat flux value at the onset of nucleate boiling is seen for R245fa but the nucleation occurs at a location nearer to the channel inlet.

6.4.2 Effect of mass flux

The experiments were conducted over a mass flux range of 100 – 400 kg/m^{2}s for R245fa and 200 – 400 kg/m^{2}s for R134a. Figure 6.10 shows the effect of mass flux as a function of axial location. From this figure, it can be seen that there is no mass flux

effect with similar heat transfer coefficients for all mass fluxes up to an axial location of 0.2 m. After this point, the heat transfer coefficient for the lowest mass flux decreases due to dryout. For mass fluxes of 200 – 400 kg/m^{2}s, there is no clear mass flux effect across the channel length. The vapour quality is expected to change with mas flux, see figure 6. 11, due to the effect of mass flux on flow patterns (figure 5.8). The same trend is seen across all heat fluxes. No mass flux effect was seen for R134a with the heat transfer coefficient being similar in both trend and magnitude across all mass fluxes, figure 6.12 and 6.13.

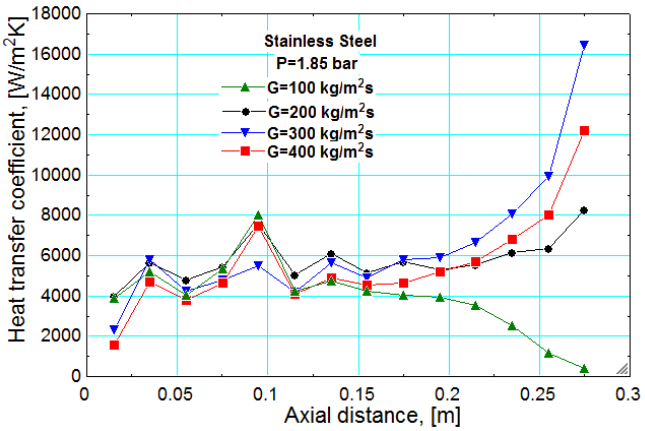

Figure 6.10. The effect of mass flux on the heat transfer coefficient as a function of axial location for a pressure of 1.85 bar and a heat flux of 25 kW/m^2 for R245fa.

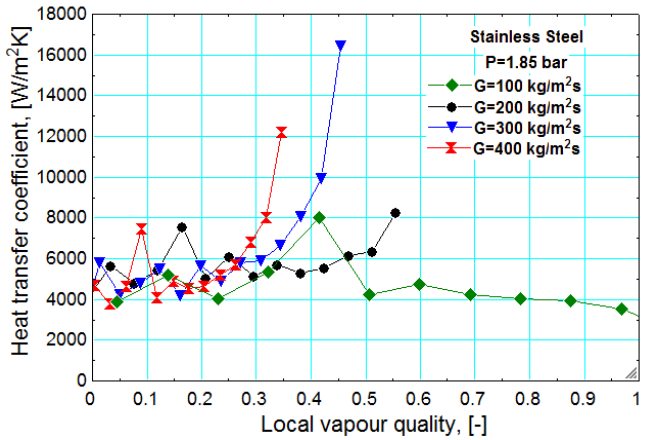

Figure 6.11. The effect of mass flux on the heat transfer coefficient as a function of local vapour quality for a pressure of 1.85 bar and a heat flux of 25 kW/m^2 for R245fa.

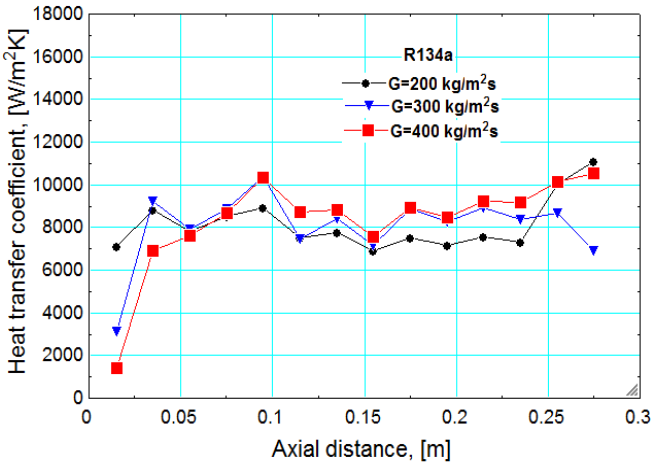

Figure 6.12. The effect of mass flux as a function of axial location for a pressure of 8 bar and a heat flux of 25 kW/m^2 for R134a.

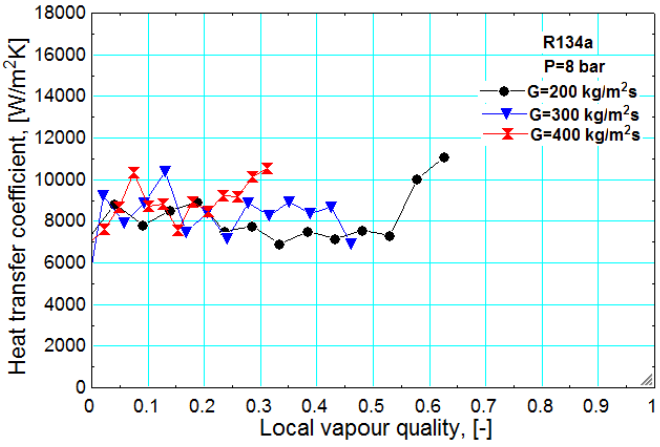

Figure 6.13. The effect of mass flux as a function of local vapour quality for a pressure of 8 bar and a heat flux of 25 kW/m^2 for R134a.

6.4.3 Effect of inlet pressure

The experiments were conducted at an inlet saturation temperature of 31 °C and 39 °C which equates to inlet pressures of 1.85 and 2.45 bar for R245fa and 8 and 10 bar for R134a. The results for stainless steel were compared at two inlet pressures and two heat fluxes. It can be seen from figure 6.14 that the heat transfer coefficient is higher for the higher inlet pressure, although this is more apparent with R134a. The inlet temperature will have an effect on the thermophysical properties of the refrigerant, namely the surface tension. The surface tension decreases with increasing pressure for both refrigerants, this will in turn affect the bubble dynamics and flow patterns which will have an effect on the heat transfer coefficient. The surface tension changed by 16% for R134a between the two pressure but only by 8% for R245fa which, may explain the

reduced effect of inlet pressure seen with R245fa. The effect of inlet pressure is greater at the higher heat flux, but with R134a once again showing a larger difference in magnitude. R245fa has a considerably higher surface tension nearly double that of R134a. A higher surface tension is thought to promote annular flow, once the flow is in the churn region. Annular flow is evident at both heat fluxes for both materials, see Chapter 5. As the thermophysical properties between the refrigerants is different, including the liquid viscosity and surface tension, the annular flow structure will be different. The higher liquid viscosity of R245fa should be conducive with a thinner liquid film (Kawahara et al. (2009)) during annular flow but also a lower Reynolds number and hence a less turbulent flow. The heat transfer coefficient trend for R134a at an inlet pressure of 10 bar and heat flux of 35 kW/m^2 suggests dry out and results in a larger difference in magnitude between the heat transfer coefficients of the two inlet pressures.

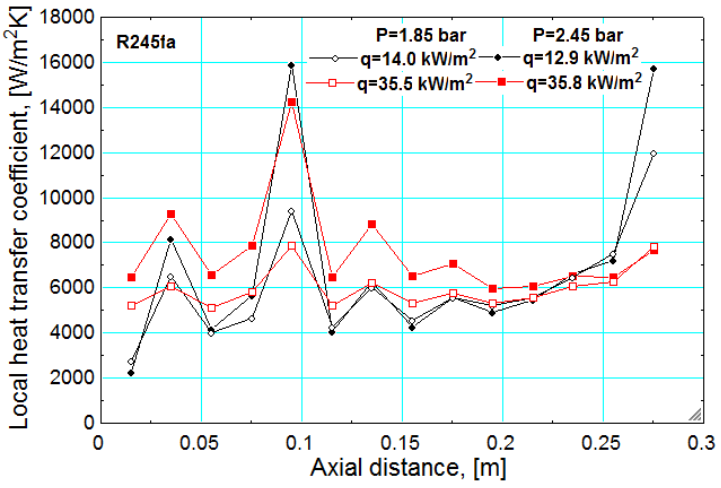

(a)

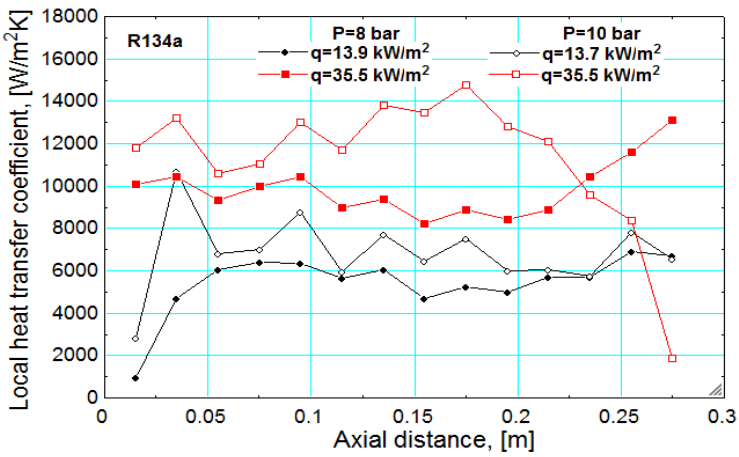

(b)

Figure 6.14. The effect of inlet pressure for G=200 kg/m^{2}s for (a) R245fa and (b) R134a.

6.5 Investigation into the surface peaks

The results in section 6.1.4 clearly show a peak in the heat transfer coefficient at the same axial location during two phase flow. This peak is thought to be from the result of a surface flaw acting as a nucleation site. To further investigate the nature of this peak, the test section was removed and replaced upside down. Figure 6.15 shows the heat transfer coefficient as a function of axial location for the original stainless steel tube and the "reversed" stainless steel tube. The onset of nucleate boiling occurs as at the same axial location, at a location of 0.095 m from the channel entrance for the original stainless steel channel and 0.095 m from the channel exit for the "reversed" channel orientation. The onset of nucleate boiling occurs at the reverse location of the heat transfer coefficient previously seen. This verifies the peak is due to a surface flaw and not the flow structure. This was seen to be true across the whole mass flux range. The effect of surface characteristics are also evident in the trend and magnitude of the heat transfer coefficient with the reversed tube. The original stainless steel results show a sharp increase in the heat transfer coefficient at the end of the test section, due to the thinning of the liquid film during annular flow. This sharp increase is not seen with the reversed stainless steel data. The heat transfer coefficient does increase across the length of the "reversed" test section but with a smoother gradient. The increase in the heat transfer coefficient for the "reversed" test section is considerably smaller than with the original channel orientation, with the heat transfer coefficient being more than half that of the original channel. This suggests that the flow pattern transition along the channel length differs between the two orientations. It can also be noted that the dry out occurs at a much lower heat flux for the reversed tube, from 41 kW/m^2 to 33 kW/m^2. Experiments were conducted until dry out with the original stainless steel tube up to a mass flux of 300 kg/m^2s. Experiments had to be stopped before dry out occurred at mass fluxes over 200 kg/m^2s due to instabilities at the inlet. Instabilities at the inlet were only seen at a mass flux of 400 kg/m^2s originally. Although the surface characteristics, i.e. Ra values, are the same, the location of the surface flaw has an important effect on the heat transfer coefficient. This could be due to how the two phase flow develops from these locations which subsequently may affect flow patterns and dry out.

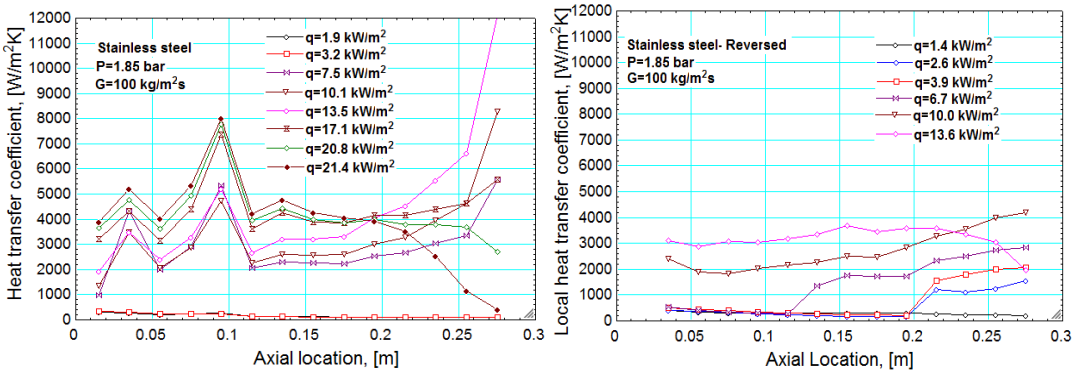

Figure 6.15. Comparison of the stainless steel and the reversed stainless steel tube at a pressure of 1.85 bar and mass flux of 100 kg/m^{2}s.

Figure 6.16 presents the heat transfer coefficients for the original and reversed stainless steel channels at three heat fluxes. The onset of nucleation occurs at an axial location nearer to the entrance for the original channel compared with the reversed channel but at the same heat flux. The effect of heat flux on the heat transfer coefficient is proportionally the same for both channel orientations.

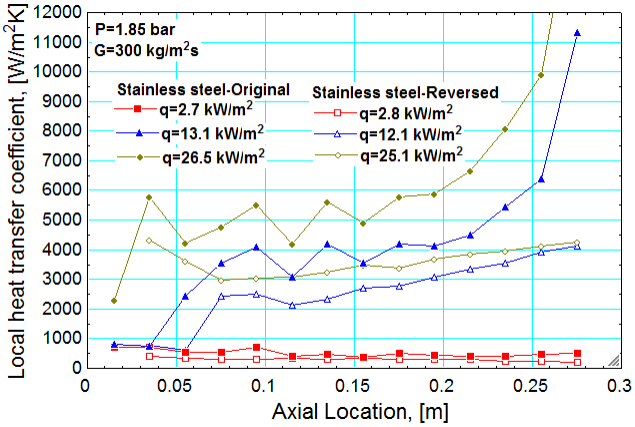

Figure 6.16. Heat transfer coefficient as a function of the axial location for the original and reversed channel orientation.

Annular flow was apparent for both channel orientations but the results suggest that the flow patterns vary across the channel length due to the surface flaw. This variation in flow patterns will results in differences in the heat transfer coefficient. The dependence of the heat transfer coefficient on mass and heat flux differs. The original stainless steel results showed no dependence on mass flux, with the difference in the heat transfer coefficient not following the same trend as that for mass flux. Figure 6.17 shows the effect of mass flux on the heat transfer coefficient for the "reversed" channel. After an axial location of 0.15 m, the heat transfer coefficient is similar for all mass

fluxes, with the decrease at a mass flux of 100 kg/m^{2}s due to the start of dryout. The differences seen in the heat transfer coefficient at an axial location less than 0.15 m is due to difference in the flow patterns. As seen in Chapter 5, the flow pattern transitions are a function of the mass flux. The heat flux at the onset of nucleate boiling changed with mass flux, see figure 6.18. However, there was no clear trend for this change.

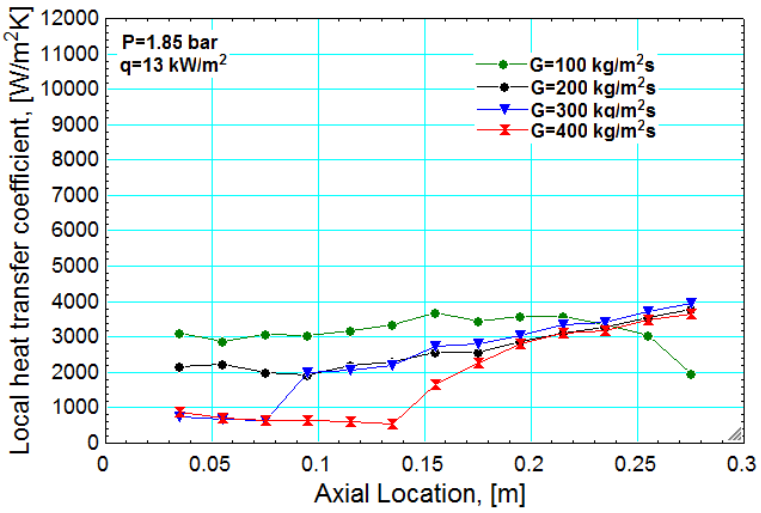

Figure 6.17. Effect of mass flux as a function of the axial location for the reversed orientation at a heat flux of 13 kW/m^2.

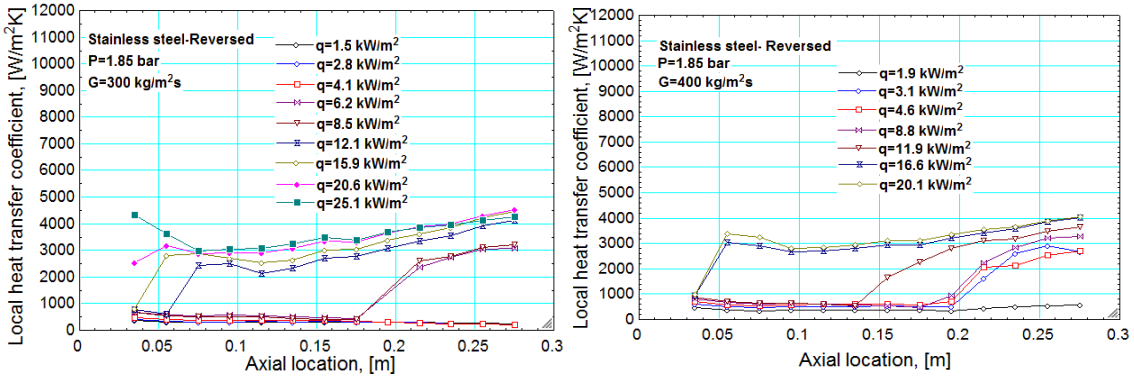

Figure 6.18. Heat transfer coefficient as a function of the axial location for the reversed stainless steel tube at mass fluxes of 300 and 400 kg/m^{2}s.

These results suggest that the surface characteristics are important, even if the peak in heat transfer coefficient is ignored, the magnitude of the heat transfer coefficient is different for the same tube reversed. The increase in the heat transfer coefficient, indicating the onset of two phase flow, at the same axial location suggest the dominance of nucleate boiling at lower heat fluxes. This is seen for heat fluxes up to 10 kW/m^2 for a mass flux of 100 kg/m^{2}s and heat fluxes up to 16.6 kW/m^2 for a mass flux of 400

kg/m^{2}s. The differences in the magnitude of the heat transfer coefficient and varying trends confirms that the surface characteristics is a controlling factor compared with the material properties, such as thermal conductivity. This also further validates that this is a potential reason for discrepancies in literature on the magnitude and trends of the heat transfer coefficient. Although this does lead to further questions on how to define a suitable heat transfer surface, as the surface parameter values are constants but the heat transfer coefficients vary.

As there is a difference in the magnitude and trend of the heat transfer coefficient, further validation was required to ensure that these changes were solely due to the change in channel orientation. The test section was reversed back to the original orientation and further experiments conducted. Figure 6.19, presents the comparison of the heat transfer coefficient at a heat flux of 17 kW/m^2 for the test section in the original position and for the repeat as a function of the axial location. The heat transfer coefficient for the repeat test is seen to be within the experimental error of the original heat transfer coefficient except for the end of the test section. For each rotation, the copper end pieces need to be removed and reattached which removes some test section length. As there is a longer length between the copper piece and the first thermocouple location (25 mm) this is less evident at the start of the test section. At the end of the test section, the distance between the copper piece and the last thermocouple location was originally 15 mm. As this length was reduced, the end thermocouple readings were affected by the direct current being applied, resulting in larger temperatures being recorded and a reduced heat transfer coefficient. These results further validate the occurrence of a surface flaw and the effect of this on the heat transfer coefficient.

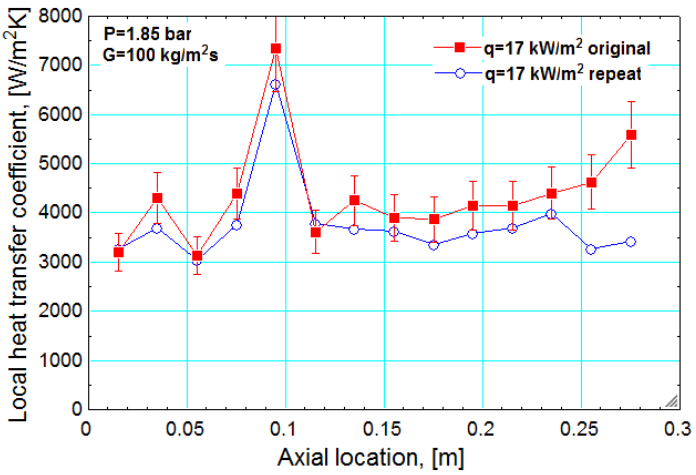

Figure 6.19. Heat transfer coefficient as a function of axial location for a heat flux of 17 kW/m^2 for the original and reversed channel orientation.

6.6 Heat transfer coefficient for Brass

The heat transfer coefficient for the brass test section is seen to steadily increase with vapour quality, see figure 6.20 a. The heat transfer coefficient does appear to increase slightly with heat flux, this is also evident when plotted as a function of the axial location, see figure 6.20 b. At a heat flux of 10.7 kW/m^2, the heat transfer jumps at an axial location of 0.05 m and then remains high, suggesting the onset of nucleate boiling. The heat transfer coefficient increases smoothly along the channel length, with this increase greater after a heat flux of 10.7 kW/m^2, after which annular flow dominates, see Chapter 5. The smooth gradient of increase in heat transfer coefficient is conducive with the thinning of the liquid film.

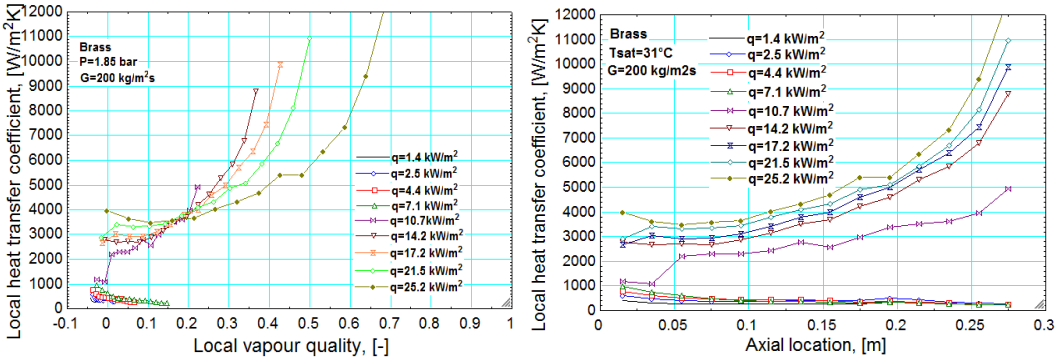

(a) (b)

Figure 6.20. Heat transfer coefficient for brass at a pressure of 1.85 bar and a mass flux of 200 kg/m^{2}s as a function of (a) local vapour quality and (b) axial location.

The heat transfer coefficient is seen to be independent of the mass flux, when plotted as a function of the vapour quality or axial location, see figure 6.21. The highest heat transfer coefficient was recorded for a mass flux of 200 kg/m^{2}s at a heat flux of 17 kW/m^2, and 100 kg/m^{2}s the lowest. It is clear from figure 6.21 b, that the heat transfer coefficients are very similar for mass fluxes of 300 and 400 kg/m^{2}s and they also show lower than the values at 200 kg/m^{2}s for most of the tube length. Note, figure 6.21 a shows the heat transfer coefficient for G=400 kg/m^{2}s relates to a smaller vapour quality.

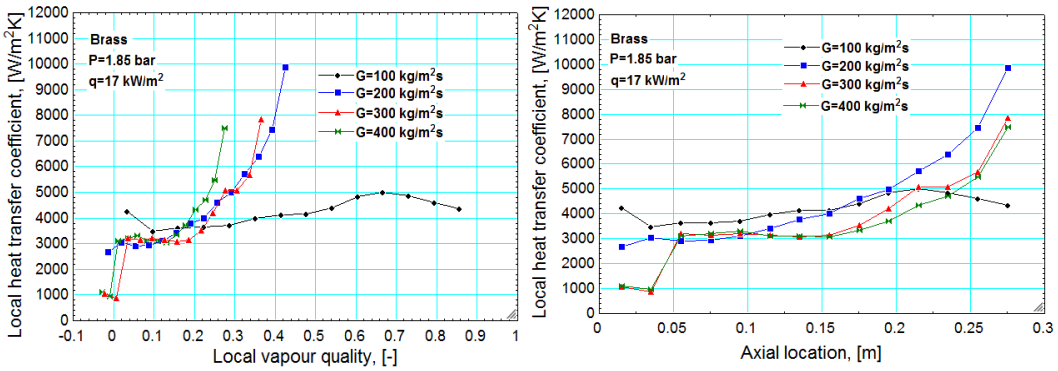

(a) (b)

Figure 6.21. Heat transfer coefficient for different mass flux rates at a heat flux of 17 kW/m^2 as a function of (a) local vapour quality and (b) axial location.

The inlet pressure was seen to have some effect on the heat transfer coefficient for both low and high heat fluxes, evident in figure 6.22. The heat transfer coefficient is slightly higher at the higher inlet pressure for both heat fluxes. The main difference seen between the two inlet pressure results is at an axial location of 0.225 m where a peak is seen at both heat fluxes at the higher inlet pressure. This peak is not seen at the lower pressure or during single phase flow which indicates a surface flaw, as opposed to faulty thermocouples. This was further validated by plotting the heat transfer coefficient as other mass fluxes for the higher inlet pressure. At the higher inlet pressure, the wall temperature is greater than that at the lower pressure, resulting in a higher wall superheat. The difference in wall superheat could allow for nucleation sites to be activated which were not activated at the lower inlet pressure. This would result in the heat transfer coefficient peaks seen only during two phase flow at the higher inlet pressure.

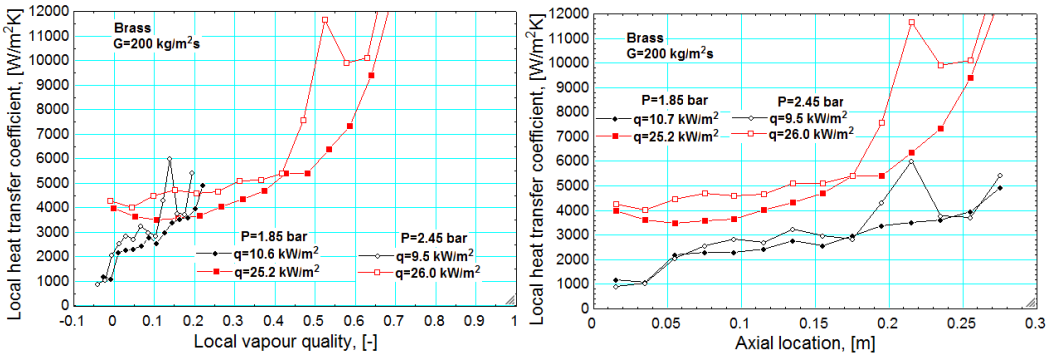

(a) (b)

Figure 6.22. Effect of inlet pressure at a mass flux of 200 kg/m^{2}s as a function of (a) local vapour quality and (b) axial location.

Figure 6.23 presents the heat transfer coefficient as a function of the axial location at an inlet pressure of 2.45 bar and mass fluxes of 300 and 400 kg/m^{2}s. At both mass fluxes, a peak in the heat transfer coefficient occurs at the same axial location. Figure 6.23 b shows the onset of nucleate boiling to occur at an axial location of 0.115 m at a heat flux of 6.9 kW/m^2. At heat fluxes from 6.9 – 11.6 kW/m^2, two phase flow is only evident at an axial location above 0.115 m. At higher heat fluxes, two phase flow is evident at axial locations greater than 0.035 m. Figure 6.23 b, also shows a change in the heat transfer coefficient at an axial location of 0.115m. As there is no effect of mass flux, this suggests the presence of a surface flaw or defect which results in an increase in the heat transfer coefficient, even after the onset of nucleation.

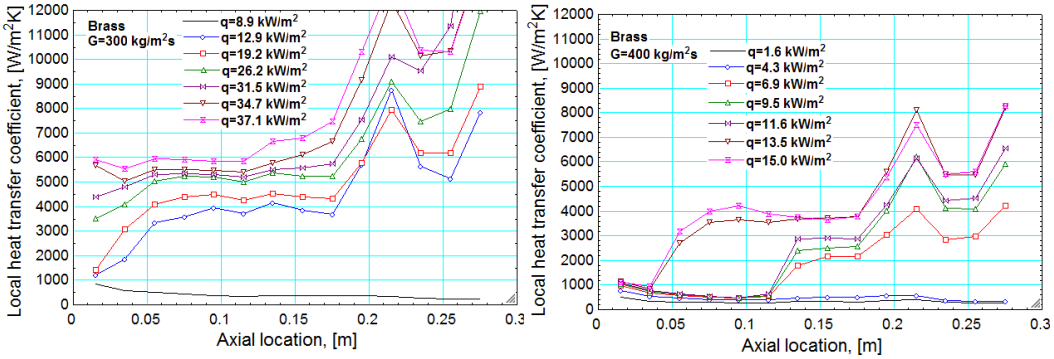

(a) (b)

Figure 6.23. Effect of mass flux for brass as a function of axial location at mass fluxes of (a) 300 and (b) 400 kg/m^{2}s.

The heat transfer coeffcient for the brass test section was seen to steadily increase with heat flux, although this increase is relatively small. The increase in the heat transfer coeffcient with vapour quality is smooth and follows an exponential trend. The heat

transfer coefficient showed little effect of inlet pressure, for either high or low heat fluxes, with the heat transfer rates showing a slight increase with inlet pressure. The main difference seen with pressure is that peak in the heat transfer coefficinet seen at an axial location of 0.225 m. This peak is seen across the mass flux range but only at the higher inlet pressure. A further fluctuation in the heat transfer coefficient is seen at an axial location of 0.115 m at an inlet pressure of 2.45 bar and the higher mass flux range. This suggests an effect of surface characteristics on the heat transfer coefficient under certain experiemental conditions for brass.

6.7 Heat transfer coefficient for Copper

The experiments conducted using the copper test section was stopped at heat fluxes over 25 kW/m^2 for the highest mass flux of 400 kg/m^{2}s, due to oscillations in the inlet parameters. Figure 6.24 presents the heat transfer coefficient results at an inlet pressure of 1.85 bar and a mass flux for 200 kg/m^{2}s, plotted as a function of the local vapour quality and the axial location along the heated section. The heat transfer coefficient trend can be seen to change with vapour quality in figure 6.24 a. The heat transfer coefficient peaks at low vapour qualities up to a heat flux of 18.6 kW/m^2, after which the heat transfer coefficient becomes relatively level. The same trend is seen for all of the copper results. The largest peak is seen to occur at a heat flux of 8.6 kW/m^2 at a vapour quality slightly above zero. At a heat flux of 10.1 kW/m^2, the vapour quality decreases and then increases again to the nearly the same value in a 'U' trend. Figure 6.24 b shows the heat transfer coefficient as a function of the axial location. This shows the heat transfer coefficient to increase with heat flux up to a location of 0.2 m, after which the heat transfer coefficient becomes independent of the heat flux. Copper is the smoothest channel which, in theory, would mean less nucleation sites. Therefore, flow may be less dominated by nucleate boiling and more convective boiling. The smoother channel would also have few peaks which could act as a restriction and disturb the liquid film during annular flow. The slight increase in the heat transfer coefficient at the end of the channel is indicative with thinning of the liquid film during annular flow. Although the channels were both thermally and electrically insulated, the relatively high heat transfer coefficient at the first thermocouple location during single phase flow could indicate that the first thermocouple reading is being artificially inflated due to the applied DC current.

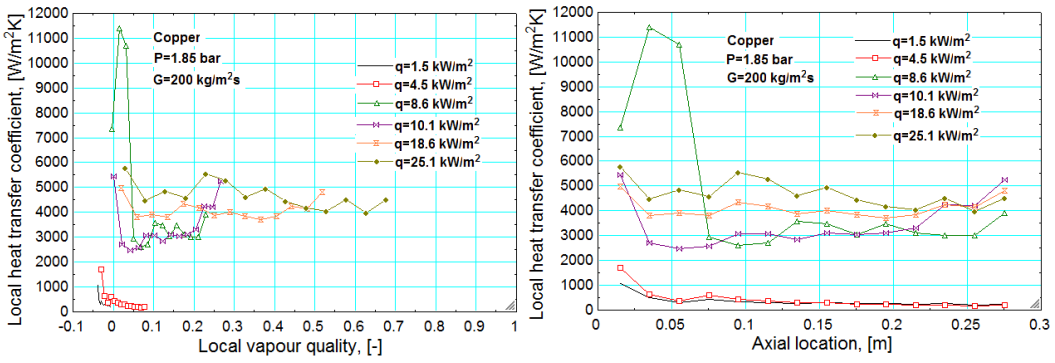

(a) (b)

Figure 6.24. Heat transfer coefficient for copper at a pressure of1.85 bar and mass flux of 200 kg/m^{2}s as a function of (a) local vapour quality and (b) axial location.

The heat transfer coefficients are also seen to be independent of mass flux, see figure 6.25, which shows the heat transfer coefficient as a function of local vapour quality at a heat flux of 17 kW/m^2. The heat transfer coefficients appear to vary in trend with the mass flux, especially for that of G=400 kg/m^{2}s, which shows a drop in the heat transfer coefficient at low vapour qualities. Plotting against the axial location shows that the trends are similar after an axial location of 0.1 m. The highest heat transfer coefficient was at a mass flux of 300 kg/m^{2}s followed by mass fluxes of 400, 200 and 100 kg/m^{2}s, thus the results are independent of the mas flux.

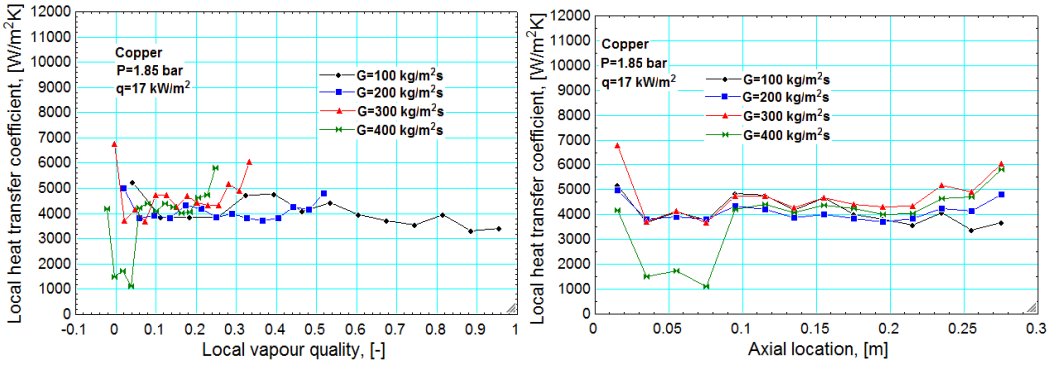

(a) (b)

Figure 6.25. Effect of mass flux for copper at a pressure of 1.85 bar and heat flux of 17 kW/m^2 as a function of (a) local vapour quality and (b) axial location.

Figure 6.26 shows the effect of inlet pressure on the heat transfer coefficient data. At the higher heat flux of 25 kW/m^2, the heat transfer is higher at the higher inlet pressure, with trends being similar for both inlet pressures. The trends are seen to vary between the two pressures at the lower heat flux value of 10 kW/m^2. At the lower vapour qualities, the heat transfer coefficient is lower at the higher inlet pressure and

higher at vapour qualities over 0.05. At the higher inlet pressure, the heat transfer coefficient plot is not as smooth as that at the lower inlet pressure. This can be more clearly seen when plotted as a function of the axial location, figure 6.26 b. This could be due to variations in which nucleation sites are active due to the different wall temperature and hence wall superheat.

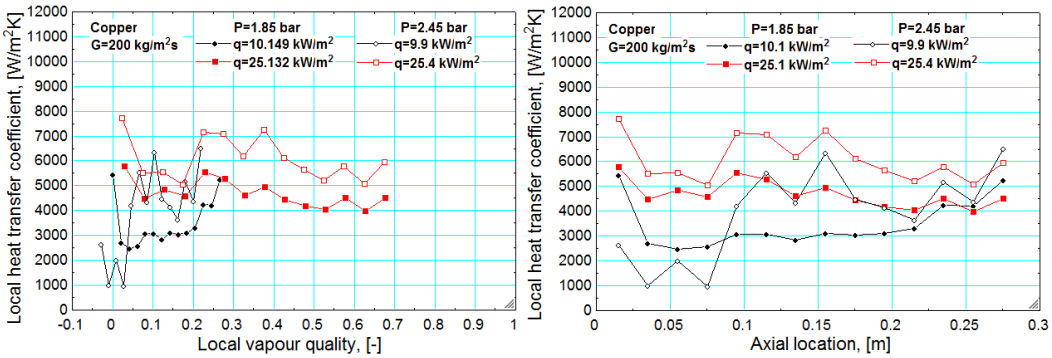

(a) (b)

Figure 6.26. Effect of inlet pressure for copper at a mass flux of 200 kg/m^{2}s as a function of (a) local vapour quality and (b) axial location.

The dependence of the heat transfer coefficient for the copper test section on heat flux and inlet pressure was seen to vary. The heat transfer coefficient increases with heat flux at higher heat fluxes but this trend is not seen at lower heat fluxes. The same is seen for the inlet pressure, where the heat transfer coefficient increases with inlet pressure at higher heat fluxes but the relationship is more convoluted for lower heat fluxes. The heat transfer coefficient was seen to be independent of the mass flux.

6.8 Comparison of materials

Similarities have been seen between the three materials investigated, mainly with all showing no mass flux dependence. Differences have been seen on the dependence of the heat transfer rates on the vapour quality and heat flux. This can be further investigated by analysing the heat transfer rates at different axial locations and the wall superheat.

6.8.1 Axial locations

The heat transfer coefficient will change across the channel length and will not remain consistent with heat flux. As the flow develops along the length of the channel, the local heat transfer coefficient will change. This can give an indication as to how the flow patterns change between the three materials. This can also make a direct comparison between the materials difficult, as the vapour quality is flow pattern dependent. A comparison of the heat transfer coefficient at the entry, middle and exit regions of the channel for all three materials can be seen in figure 6.27. Figure 6.27 a, shows that the heat transfer coefficient is highest at the end of the tube in the middle heat flux region for stainless steel. This is expected due to the thinning of the liquid film during annular flow. As the film continues to thin, dryout can occur causing,, the heat transfer coefficient to drop but this is only evident at the end of the tube. The same trend is not seen for copper, figure 6.27 b, where the end channel region is lower than that of the middle region, although the same reducing heat transfer coefficient is seen for the higher heat fluxes. The copper shows a more constant heat transfer coefficient across the channel length, suggesting less variation in the flow patterns along the channel length. The brass experiments were stopped prior to the occurrence of dryout and therefore the decrease in the heat transfer coefficient is not seen at the channel exit region, figure 6.27 c. The copper and brass channels show the middle channel region to have a higher heat transfer coefficient than the entry channel region which is contrary to the stainless steel channel which shows the middle channel region to be the lowest. The biggest difference between the entry and middle channel region is seen for brass. This could indicate the flow patterns developing across the channel length and hence annular flow occurring later along the channel length, with the increase in the heat transfer coefficient equating to the thinning of the liquid film. This is also seen in figure 6.20 where the heat transfer coefficient shows a smooth increase with vapour quality.

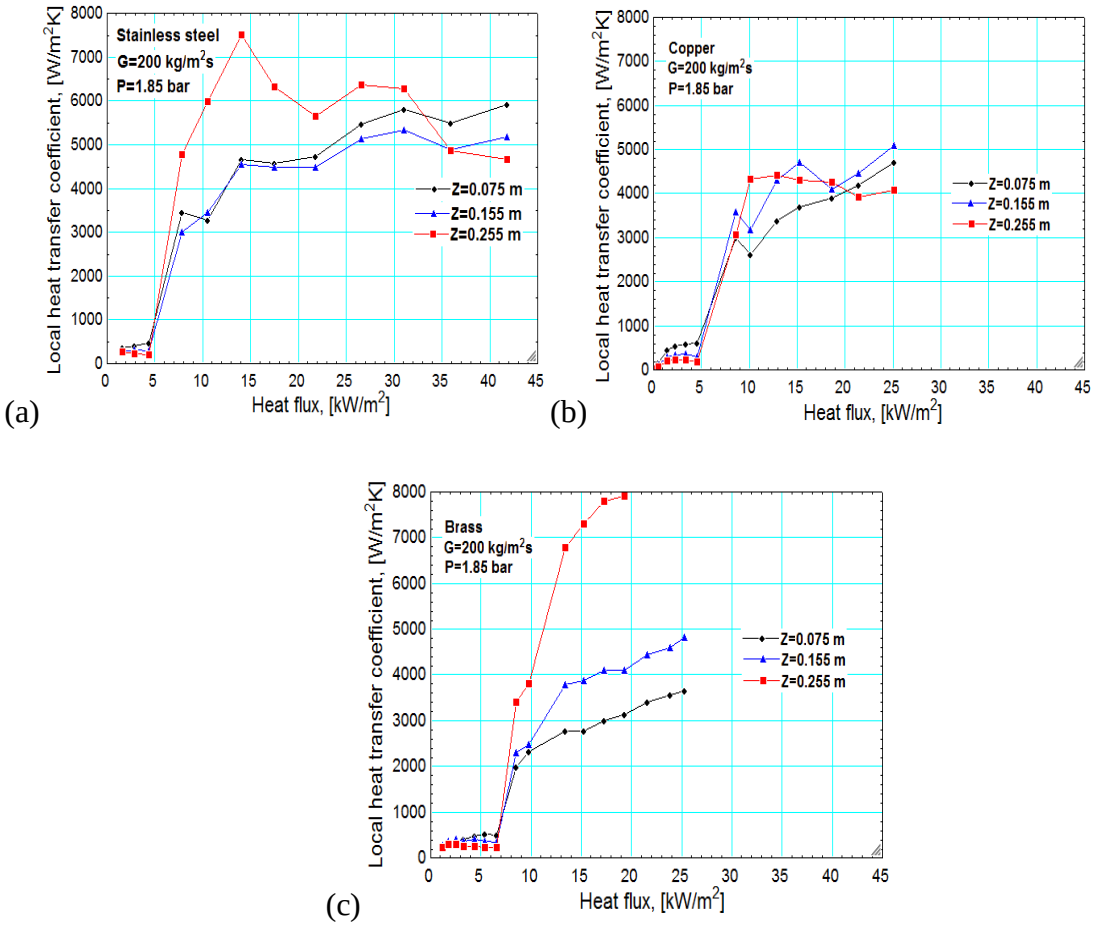

Figure 6.27. Heat transfer coefficient as a function of heat flux for (a) stainless steel, (b) copper and (c) brass.

6.8.2 Hysteresis

Hysteresis has been discussed in Chapter 5 in regards to the changes seen in the flow patterns which will directly affect the corresponding heat transfer coefficient. The heat flux is first increased and then decreased. For R134a, the hysteresis was only seen near the channel inlet, thought to be due to the subcooled liquid at the inlet affecting the stability of the nucleation sites (Mohamed, 2011). Hysteresis was evident across the whole length of the tube with R245fa, see figure 6.28, where hysteresis is evident at all of the axial locations. Hysteresis is a result of nucleation sites becoming activated during the increase in the heat flux which remain activated as the heat flux is reduced. The size of the nucleation sites which are activated will depend on the wall superheat, which is smaller for R134a than R245fa at comparable experimental conditions. Therefore, the nucleation sites which are activated would differ between the two fluids. The variations in the wall temperature are partially due to the differing flow patterns

between the fluids, see Chapter 5. R245fa has a higher surface tension, which promotes annular flow which aids in keeping the wall temperature lower than for R134a. The wall superheat is seen to be considerably higher than that predicted by equation 5.1, and vary with channel material. This equation is based purely on the fluid properties and does not account for surface characteristics.

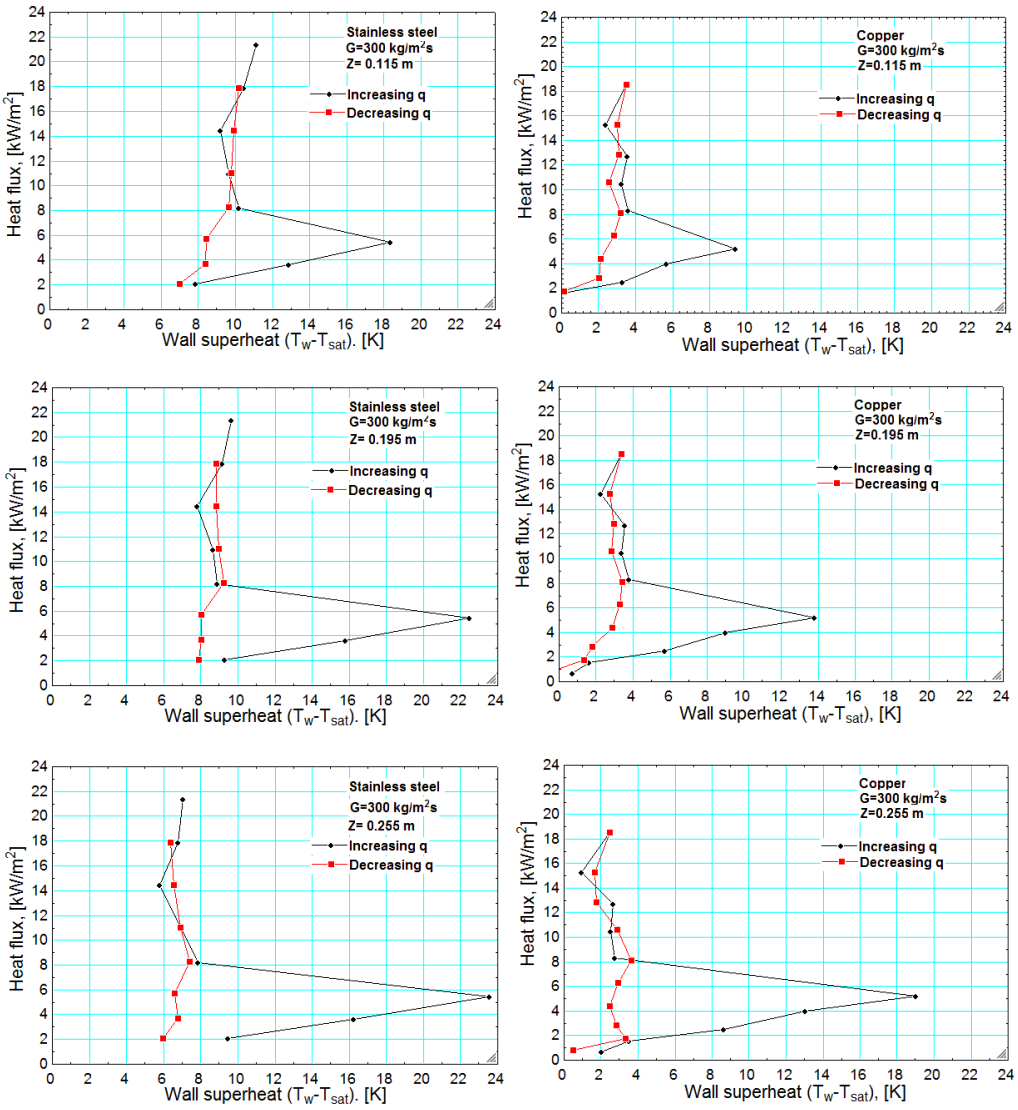

Figure 6.28. Hysteresis effect at axial locations of (a) 0.115 m, (b) 0.195 m and (c) 0.255 m for stainless steel and copper at a mass flux of 300 kg/m^{2}s.

Figure 6.29 shows that the wall superheat is relatively constant with a decreasing heat flux. This is expected due to the nucleation sites being activated during the process of increasing the heat flux. As the flow before this is in single phase, the heat transfer coefficients are very low and therefore the heat is not being removed from the channel wall. It is also for this reason that the wall superheat is lowest near the entrance at low heat fluxes. As two phase flow begins, the wall superheat decreases as the heat is being

removed from the channel wall. A comparison of the heat transfer coefficient with increasing and decreasing heat fluxes show that during two phase flow, the heat transfer coefficients are similar. Figure 6.29 shows that at a heat flux of 17 kW/m^2, during which annular flow is present, the heat transfer coefficient is the same. As a function of vapour quality, figure 6.29 a, the heat transfer coefficient is seen to vary, with the same trend occurring but at a lower vapour quality for the decreasing heat flux. The values do change at lower heat fluxes, which is expected due to the different flow patterns seen in this range. The heat transfer coefficient values are lower for the increasing heat flux as the flow is in single phase. As the nucleation sites are activated, bubbly and slug flow are seen in this heat flux region which results in a higher heat transfer coefficient with a decreasing heat flux.

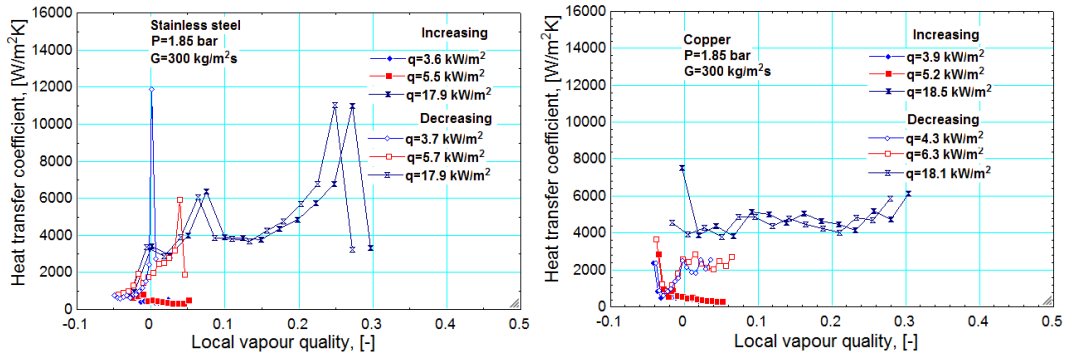

(a)

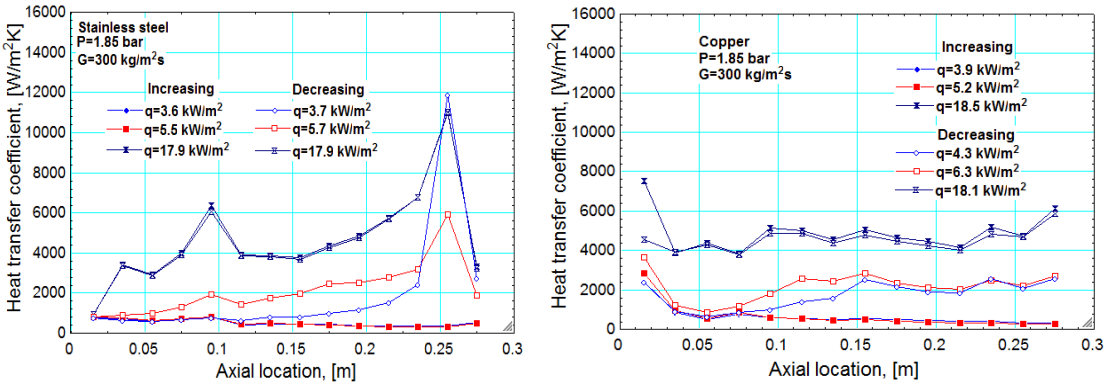

(b)

Figure 6.29. Effect of hysteresis for stainless steel and copper as a function of (a) local vapour quality and (b) axial location.

Figure 6.30 presents the effect of mass flux on the hysteresis for copper and stainless steel. The wall superheat at the onset of nucleate boiling is seen to be a function of the mass flux. A mass flux effect is predicted, with a higher heat flux required for the onset of nucleation at higher mass fluxes. However, there is no clear

trend for either material, with the highest mass flux of 400 kg/m^{2}s occurring at the highest wall superheat for both cases but not at the highest heat flux for copper. Stainless steel shows a greater dependence on mass flux in terms of both the heat flux and wall superheat at the onset of nucleate boiling. The wall superheat is highest for stainless steel at the highest mass flux, indicating higher wall temperature is required for the nucleation sites to be activated. As seen in figure 5.8, the effect of mass flux on flow transitions is material dependent, with copper showing a greater dependence. A complete investigation into the effect of mass flux on hysteresis is hindered by the comparison being based on a singular axial location, which as shown in figure 5.28, is a function of the wall superheat.

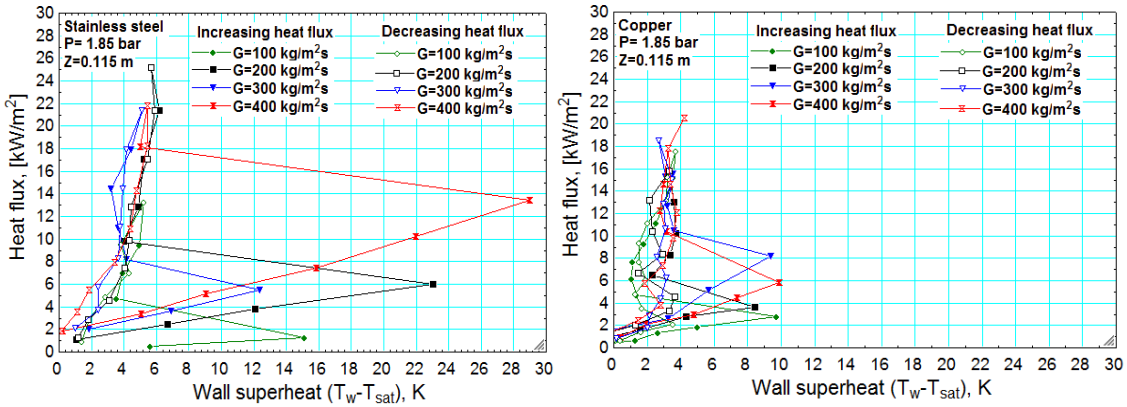

Figure 6.30. Effect of hysteresis for stainless steel and copper as a function of mass flux, at an axial location of 0.115 m, for (a) stainless steel and (b) brass.

There are contradicting conclusions in literature about the effect of hysteresis, with many researchers predicting no effect (Bortolin et al. (2011), Ong and Thome (2009)). This in turn may be one of the reasons for contradictory flow boiling results in literature, when using the same material and working fluid. It is not widely reported in literature how the heat flux is applied, increasing or decreasing, which is shown to have an effect of the heat transfer coefficient trends at the medium to low heat flux range. The effect of hysteresis is seen to be independent of the channel material and surface parameters.

6.8.3 Surface parameters

Wall superheat

The wall superheat is a measure of the difference between the wall temperature and the saturation temperature. Plotting the wall superheat as a function of the heat flux results in a boiling curve which shows the point of nucleate boiling and can be used to

indicate the size of the nucleation sites based on when those sites are activated. It is expected that the wall superheat will change as a function of the surface characteristics, due to differences in the size and geometry of the potential nucleation sites. There is no surface characteristic which can accurately represent this, see Chapter 5, but Ra and Rq can be used to give an indication. The average surface roughness parameter, Ra, would indicate the deviations of the surface from the mean line which could act as potential nucleation sites. Assuming a constant evaluation length, a higher Ra value could indicate more peaks and valleys which would trap vapour, but this value can be skewed by a small amount of large peaks and valleys. As shown in figure 2.10, the same Ra value can refer to multiple surface structures. The root mean square, Rq, used in conjunction with the Ra value can be used to further define the surface structure, as Rq is more sensitive to extreme peaks and valleys. Looking at both the Ra and Rq values indicates the uniformity of the surface which is desired for flow boiling. However, the multiple correlation in literature used to calculate the wall superheat at the onset of nucleate boiling are based on fluid properties. As the same working fluid, R245fa, is used for these experiments, a similar wall superheat is predicted for all of the materials. Hsu and Graham (1961) used a prediction equation which used the liquid thermal conductivity, surface tension, enthalpy and the heat transfer. The use of the heat transfer coefficient does result in some changes in the predicted wall superheat but these are minimal. Hsu and Graham (1961) and Sato and Matsumura (1964) developed a correlation, presented in Kandlikar (2004), which predicted a wall superheat of 3.8 K. Kandlikar (2006) also used a prediction method based on the enthalpy, surface tensions and thermal conductivity but also the heat flux. Similar heat flux ranges are used for all of the experimental data resulting in a similar predicted wall superheat of 3.5 K. Kandlikar et al. (2013) stated that if the experimental wall superheat is less than that of the predicted temperature for the onset of nucleate boiling, then nucleate boiling will not occur. Both of these correlations predict the wall superheat at which nucleate boiling will occur to be considerably smaller than the experimental wall superheat.

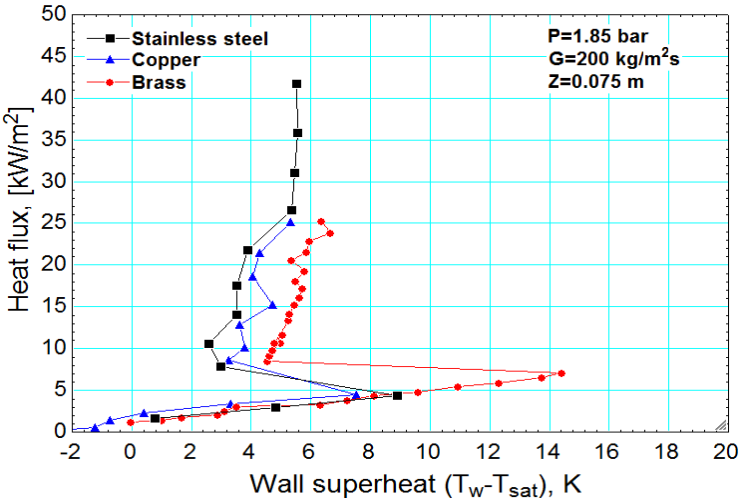

Figure 6.31. Boiling curves for stainless steel, copper and brass at a pressure of 1.85 bar, mass flux of 200 kg/m^{2}s and an axial location of 0.075 m.

Figure 6.31 presents the boiling curve for stainless steel, copper and brass at an axial location of 0.075 m, representing the entry region of the tubes. For stainless steel and copper, the heat flux at the onset of nucleate boiling is similar but higher for brass. Flow observation with these measurements showed differences in the flow patterns observed at the exit of the tube at the onset of nucleate boiling. For brass and copper, churn flow was evident at the channel exit at the corresponding heat flux. Annular flow was evident for stainless steel where all other conditions were the same indicating that the surface may have an effect on flow transitions. The same trend is seen for the wall superheat, with brass showing a considerably higher wall superheat compared with copper and stainless steel. This is not represented by the previously discussed prediction methods for the wall superheat.

The wall superheat is linked to the surface characteristics, which can be seen for all materials over heat fluxes of 5 kW/m^2, see figure 6.31. After the point of nucleate boiling, the wall superheat remains highest for brass and is lowest for stainless steel. Wall superheat is related to the surface characteristics in terms of the size of the active nucleation sites (Kandlikar et al. 1996). Larger nucleation sites require a smaller wall superheat to become active, suggesting that brass has smaller nucleation sites which require a higher wall superheat to activate. Cornwell and Brown (1978) found the relationship between the wall superheat and the active nucleation site density for pool boiling to be:

$$Na \sim \Delta T_w^{4.5} \tag{6.1}$$

Based on the above equation, brass would have a highest number of active

nucleation sites and copper the lowest. This trend is in agreement with the average surface roughness values. There is approximately 30% difference between the average roughness values and the wall superheat for stainless steel and copper, see table 6.1. Brass is over 200% higher in average roughness values and wall superheat. This suggests that there is some dependence on the average roughness but this can only be verified by a comparison over a wider range of average roughness values.

Table 6.1. Wall superheat and average surface roughness (Ra) values.

Material	Wall superheat, K	Ra, µm	Rq, µm
Stainless steel	8.9	0.716	0.928
Copper	7.5	0.524	0.722
Brass	14.4	1.249	1.743

Magnitudes and trends

The heat transfer coefficient is seen to vary with channel material, although the extend of these variations depends on the experimental conditions. Figure 6.32 presents a comparison of the heat transfer coefficient for the three materials as a function of both the vapour quality and the axial location. The copper results show a more linear heat transfer trend in comparison the to the stainless steel and brass results which show an exponential increase. The heat transfer coefficient starts at the same value for brass and stainless steel, with values over vapour qualities of 0.3 also similar between the two materials. The heat transfer coefficient between vapour qualities of 0 and 0.3 are higher for stainless steel, mainly due to the peaks seen at the surface flaw position. Figure 6.32 b further validates that the brass and stainless steel are similar in magnitude and trend with the exception of the peaks in stainless steel, before 0.15 m.

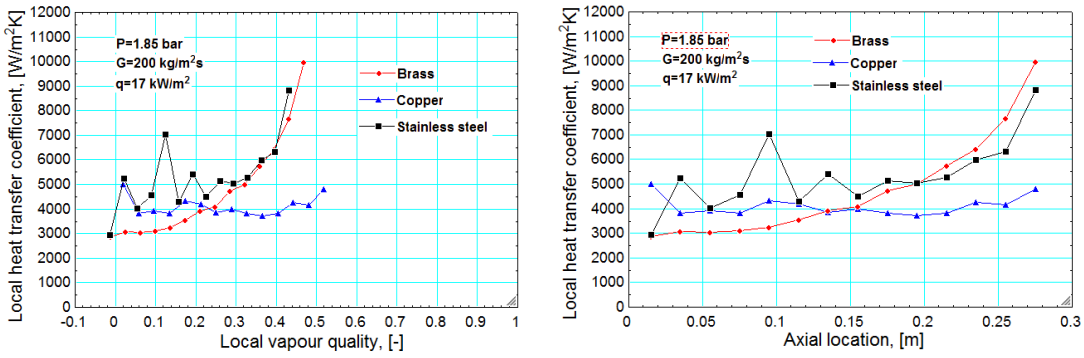

(a) (b)

Figure 6.32. Heat transfer coefficient at a pressure of 1.85 bar, mass flux of 200 kg/m^{2}s and heat flux of 17 kW/m^2 as a function of (a) local vapour quality and (b) axial location.

6.9 Summary

Heat transfer data was recorded for channels of stainless steel, copper and brass across two inlet pressures and a range of heat and mass fluxes for R245fa. The data for R245fa was compared with data for R134a which had been produced using the same stainless steel test section. A comparison of this data allowed for an evaluation of the effect of thermophyscial properties, excluding any effect of surface characteristics. Clear differences were seen in both the magnitude and trend of the heat transfer coefficient as well as the effect of vapour quality and heat flux. The heat transfer coefficient for R134a showed little dependence on vapour quality, being almost linear with increasing vapour quality. The results also showed a large increase in the heat transfer coefficients with increasing heat flux and inlet pressure. This is contrary to the R245fa results which showed an increase in the heat transfer coefficient with vapour quality and little effect of inlet pressure and heat flux. For both refrigerants, there was no mass flux effect. R245fa also showed large peaks in the heat transfer rates, thought to be caused by surface characteristics and the thinning of the liquid film during annular flow. As previously discussed, R245fa showed a greater dominance of annular flow as opposed to R134a.

Peaks seen in the heat transfer rates for stainless steel occurred at the same axial location which suggested the presence of a surface flaw. This was verified when the test section was reversed and the onset of nucleate boiling occurred at the same axial location. The channel was once again tested in the original orientation to ensure that the differences seen in the heat transfer coefficient were due to the surface flaw and that all other parameters had remained constant. This experiment further showed the complexity and limitations of defining a heat transfer surface. The surface parameters measured (Ra, Rp etc.) were unchanged but the orientation of the channel resulted in a change in the heat transfer coefficient. This shows that large discrepancies in both the magnitude and trend of heat transfer rates when using the same working fluid and channel material can be a result of the surface characteristics.

Further testing with R245fa in the brass and copper test sections showed an effect of surface characteristics on the heat transfer coefficient in magnitude and trend. The results for copper, which is the smoothest material, showed a lower and more linear heat transfer coefficient with increasing vapour quality. Stainless steel and brass both showed an increase in the vapour quality but the trends and gradients differed. The effect of the surface characteristics was a function of the vapour quality, with

differences seen in the low vapour quality region which relates to flow patterns prior to the dominance of annular flow. This is evident in figure 6.27, where the heat transfer coefficient trend is seen to differ with increasing heat flux along the channel length. The wall superheat also indicates a difference in the surface characteristics, with brass requiring a considerably larger wall superheat for the onset of nucleate boiling to occur.

The surface characteristics are seen to have an effect on the heat transfer coefficient but there is no clear trend between the surface parameters and the heat transfer rates. The copper results show a smooth trend at higher heat fluxes but peaks in the heat transfer coefficient are seen at low heat fluxes which would relate to the onset of nucleate boiling. The high peaks at the onset of nucleate boiling are not seen for stainless steel or brass but copper has the lowest Ra values. The brass channel shows signs of two surface flaws, one of which is only evident at a higher pressure, but this material shows the highest average roughness value. High Rp values could result in disturbances in the flow patterns and potential dryout spots but this is not seen for brass which has the highest Rp value. The wall superheat is seen to relate to the Ra values, with the same trend and percentage difference between the materials. Based on the wall superheat, the brass test section has the smaller nucleation sites which require a greater wall superheat to activate. The greater number of nucleation sites may results in a more evenly distributed nucleation and a smoother flow pattern transitions which may account for the smoother heat transfer coefficient trend. There are surface flaws evident in the brass test section, based on the location of the onset of nucleate boiling, figure 6.20, and the peak in the heat transfer coefficient seen at the higher inlet pressure, figure 6.23. The surface flaw, or nucleation site, seen at an inlet pressure of 2.45 bar may require a large wall superheat to activate which is only present at a higher inlet pressure. Surface flaws are evident with the stainless steel, which has the middle average surface roughness. The trend seen for the average surface roughness only matches the trend seen in the heat transfer coefficient after an axial location of 0.15 m. The heat transfer coefficient increases after this point which suggests annular flow with a thinning liquid film, where it is thought that the average surface roughness would not be important due to the dominance of convective boiling. The copper test section has the lowest heat transfer coefficient overall, with no heat transfer peaks which would indicate surface flaws, and also the lowest average roughness, Ra. This therefore suggests that the matching trends are a coincidence rather than a physical relationship. The point at which the average surface roughness should have most effect, during nucleate boiling, the trend does not match. The other surface parameters, namely that of Rp, Rv and Rt, show

no relationship with the heat transfer coefficients. Peaks and trends seen in the heat transfer coefficient, especially for stainless steel and brass, do show that surface characteristics are an important factor on the onset of nucleation and heat transfer rates. However, there is no clear trend seen for the surface parameters for these materials and the heat transfer rates.

Chapter 7

7. Heat transfer correlations

7.1 Introduction

There are a vast number of correlations readily available which aim to predict the heat transfer coefficient of flow boiling in channels. There are multiple ways to classify heat transfer correlations based on the form of the equation. Correlations can be defined as superposition model, asymptotic model and enhancement model, see Table 7.1, (Park et al. (2007)). These are the general forms of the equations, with the heat transfer correlations including further factors.

Table 7.1. Equation forms for the classification of heat transfer correlations, Park et al. (2007).

Classification	Equation form
Superposition model	$h = h_{nb} + h_{sp}$
Asymptotic model	$h = \left[(h_{nb})^n + \left(h_{sp}\right)^n\right]^{1/n}$
Enhancement model	$h = E \cdot h_l$

Other equation forms include empirical correlations which are based on the widely used dimensionless numbers (e.g. Weber number and boiling number) and the experimental conditions (e.g. channel diameter, mass flux and heat flux). Mechanistic models can also be used for heat transfer prediction, these are based on the flow structure in the channel. As presented in Chapter 2, flow boiling in small diameter (microscale) channels varies from that of large diameter (macroscale) channels, mainly due to bubble confinement and the dominance of surface tension. In order to accurately predict the heat transfer coefficient of microscale heat exchangers, new correlations based on small to micro channels were proposed. This chapter evaluates both the

macroscale and miscroscale correlations in relation to the ability to predict data with different thermophysical properties. The correlations are compared based on the percentage of data within ± 30% error bands (β) and the mean absolute error (MAE) which is calculated from equation 7.1, where N is the total number of experimental data points.

$$MAE = \frac{1}{N}\sum_{i=1}^{N}\frac{|h_{Pred,i}-h_{Exp,i}|}{h_{Exp,i}}X100 \quad (7.1)$$

The majority of correlations, both macroscale and microscale, are applicable for a specified experimental range. Experimental data after dryout had occurred were excluded as most of these correlations were not suitable to this range. The point at which dryout occurred varied based on the mass flux, inlet pressure and the refrigerant, see table 7.2. Due to instabilities at the inlet of the test section, it was not possible to achieve dryout at a mass flux of 400 kg/m^{2}s with R245fa.

Table 7.2. Vapour quality range at which dryout occurred

Refrigerant	Test section	Quality at dryout
R245fa	Stainless steel	0.8-0.95
	Brass	0.55-0.75
	Copper	0.6-0.75

All of the equations used are presented in Appendix A.

7.2 Cooper (1984) Correlation

The Cooper (1984) correlation is a pool boiling correlation which is often used in literature to calculate the nucleate boiling component for flow boiling heat transfer coefficient prediction. This correlation includes the reduced pressure, molecular weight, heat flux and the surface roughness. The surface roughness parameter used is the old Rp value defined in DIN 4762/1:1960, which has since been updated. Gorenflo (1993) suggested a conversion of Ra≈0.4Rp,$_{old}$. Based on this conversion the Rp,$_{old}$ values for the three materials can be found in table 7.3.

Table 7.3. Rp,$_{old}$ values based on converted Ra values from Gorenflo (1993).

Channel Material	Rp,old (μm) based on Gorenflo (1993)
Stainless steel	1.79
Copper	1.31
Brass	3.12

The predictive ability of this correlation should relate to the dominance of nucleate boiling in the channel. The best prediction was for that of stainless steel with 41.2% of the data predicted well and a low MAE value, see figure 7. 1. Figure 7.2 shows the heat transfer coefficient to be constant with vapour quality, thus under predicting the increase seen in the heat transfer coefficient with R245fa. The prediction values are lower for copper and brass, with higher MAE values. The brass results show the data to be over predicted. Contrary to this, the copper results show good agreement at low heat fluxes, but the data is under predicted at higher heat fluxes. Assuming that the Cooper (1984) correlation predicts the nucleate boiling well, this suggests a smaller nucleate boiling regime for copper and brass compared with stainless steel. This difference may also be due to the changes in the Rp values which as previously discussed, are open to interpretation. As the experimental conditions and working fluid are the same, the only variable between the materials is the Rp value, this equates to a larger difference in the predicted heat transfer coefficient.

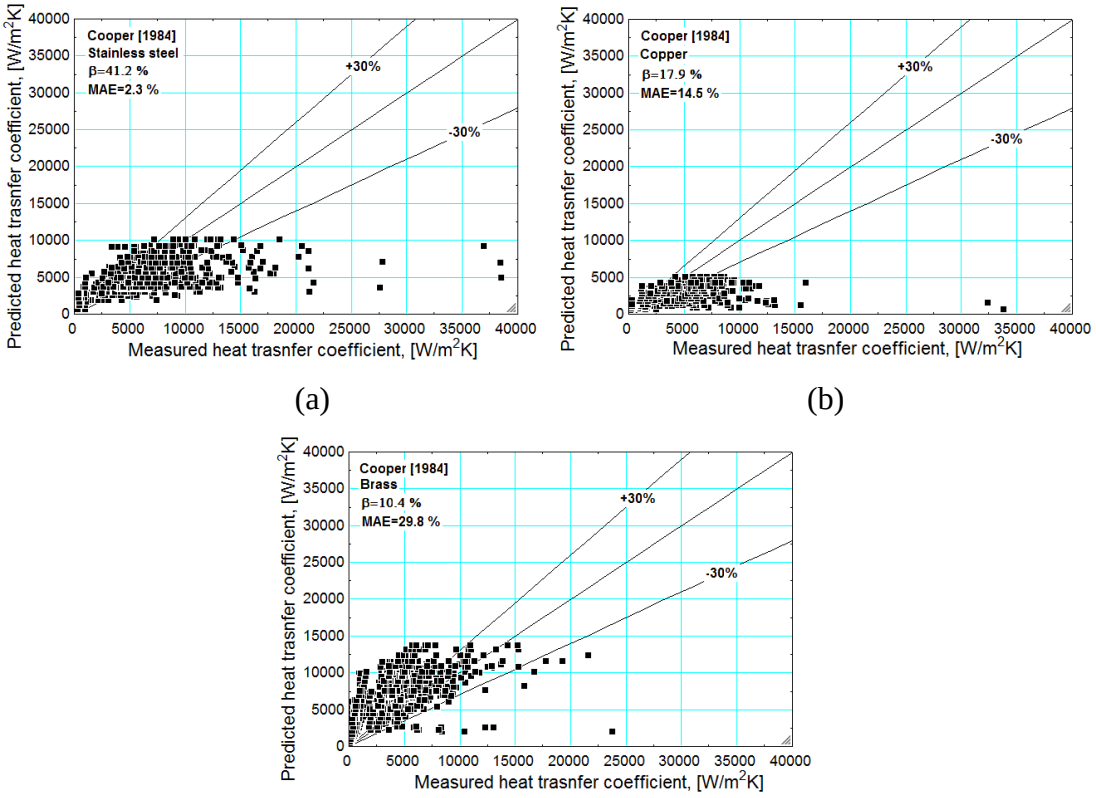

Figure 7.1. Comparison of the Cooper (1984) correlation with the experimental heat transfer coefficient for (a) stainless steel, (b) copper and (c) brass.

Figure 7.2 presents the predicted and experimental results at a heat flux of 10, 17 and 25 kW/m^2 and a mass flux of 200 kg/m^{2}s. This figure shows that at the lower heat

flux, the brass prediction is twice that of the stainless steel and three times that of the copper. A similar difference is seen at the higher heat fluxes, with the brass results over predicting the results by a considerable amount. This is not comparable with the measured heat transfer coefficient which, although does vary in magnitude, the surface roughness is not seen to have such a dramatic impact on the difference between the values.

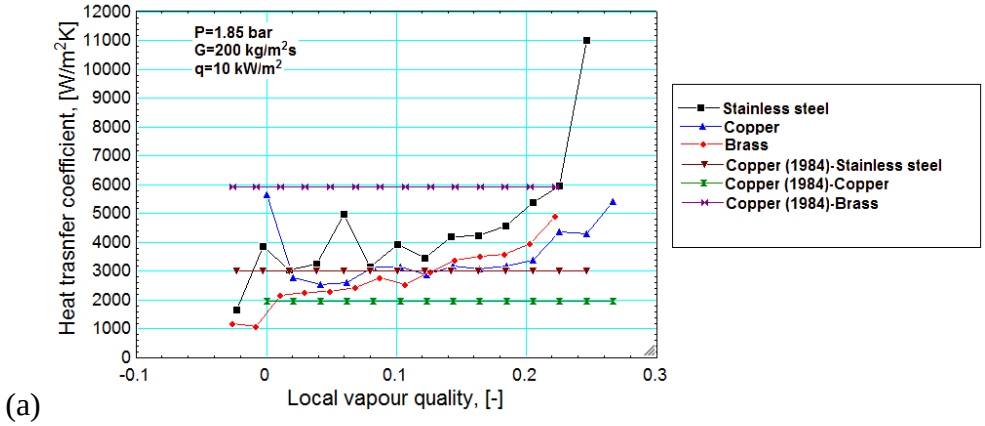

(a)

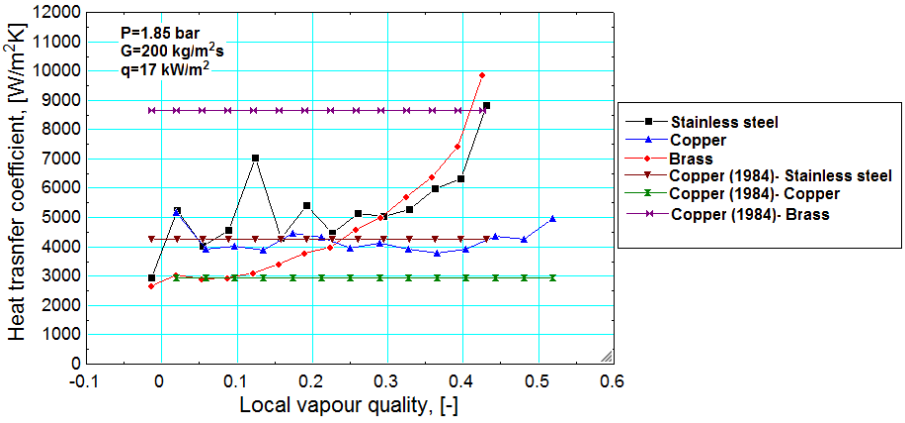

(b)

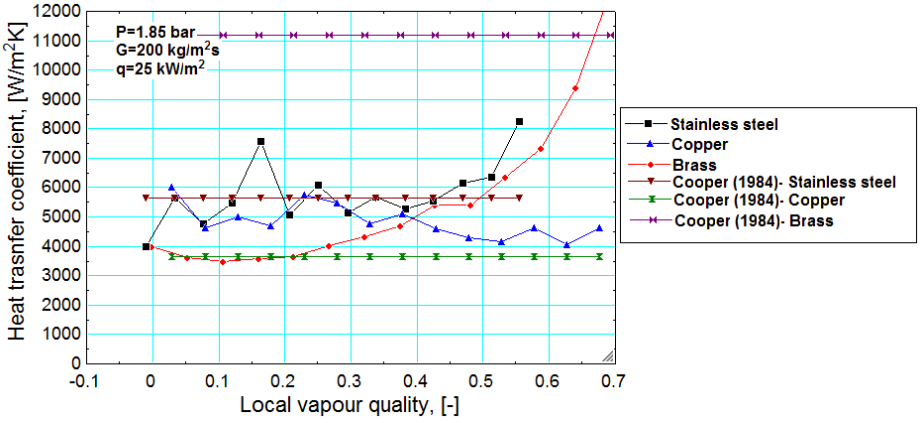

(c)

Figure 7.2. Copper (1984) predicted heat trasnfer coefficient as a function of the local vapour quality at heat fluxes of (a) 10, (b) 17 and (c) 25 kW/m^2.

7.3 Macroscale correlations

Although there are multiple methods of defining the difference between macro and micro scale channels, for the purpose of comparing correlations; macroscale correlations are deemed to be those which are designed for channels with diameters larger than 3mm.

As previously seen in Chapter 6, the effect of heat flux and vapour quality on the experimental heat transfer coefficient changes with material. The initial comparison of the correlations is based on the data at an inlet pressure of 1.85 bar, mass flux of 200 kg/m^2s and a range of heat fluxes. This is to show the general trend of the correlations with vapour quality and heat flux. As the correlations do not use any function of the surface characteristics, the correlations predict the same heat transfer coefficient for all of the materials. The whole data set will be used to fully evaluate the correlations individually.

Figure 7.3 presents the experimental data and the predicted data from four macroscale correlations across a range of heat fluxes. The correlation results depicted in figure 7.3 are based on the stainless steel. Due to the differences seen in the flow patterns between the materials, see Chapter 5, there are variations in the vapour qualities. Therefore, there are slight variations in the predicted heat transfer coefficient for copper and brass from those in figure 7.3. A comparison of the graphs show there is a clear difference between the experimental and predicted data depending on the heat flux. The heat transfer coefficient increases with heat flux for all materials, but with a greater extend for stainless steel. Figure 7.3a presents the data at a heat flux of 10 kW/m^2, showing a steep increase for stainless steel which is outside of the predicted results. All of the correlations show an increase in the heat transfer coefficient with vapour quality. The Chen (1993) correlation under predicts, with a lower heat transfer coefficient than the other correlations. At a heat flux of 17 kW/m^2, the same trend is predicted for each heat flux but with an increase in magnitude. The results appear to be better at this heat flux but the trends of the correlations do not match the trends of the experimental results. The Gungor and Winterton (1986, 1987) correlations predict an almost linear increase, both of which cross the paths for all three materials. The increase in the stainless steel and brass heat transfer rates is more of exponential trend, with a curve which starts lower than that predicted by the linear Gungor and Winterton (1986, 1987). Therefore, the heat transfer coefficients at lower vapour qualities are not predicted.

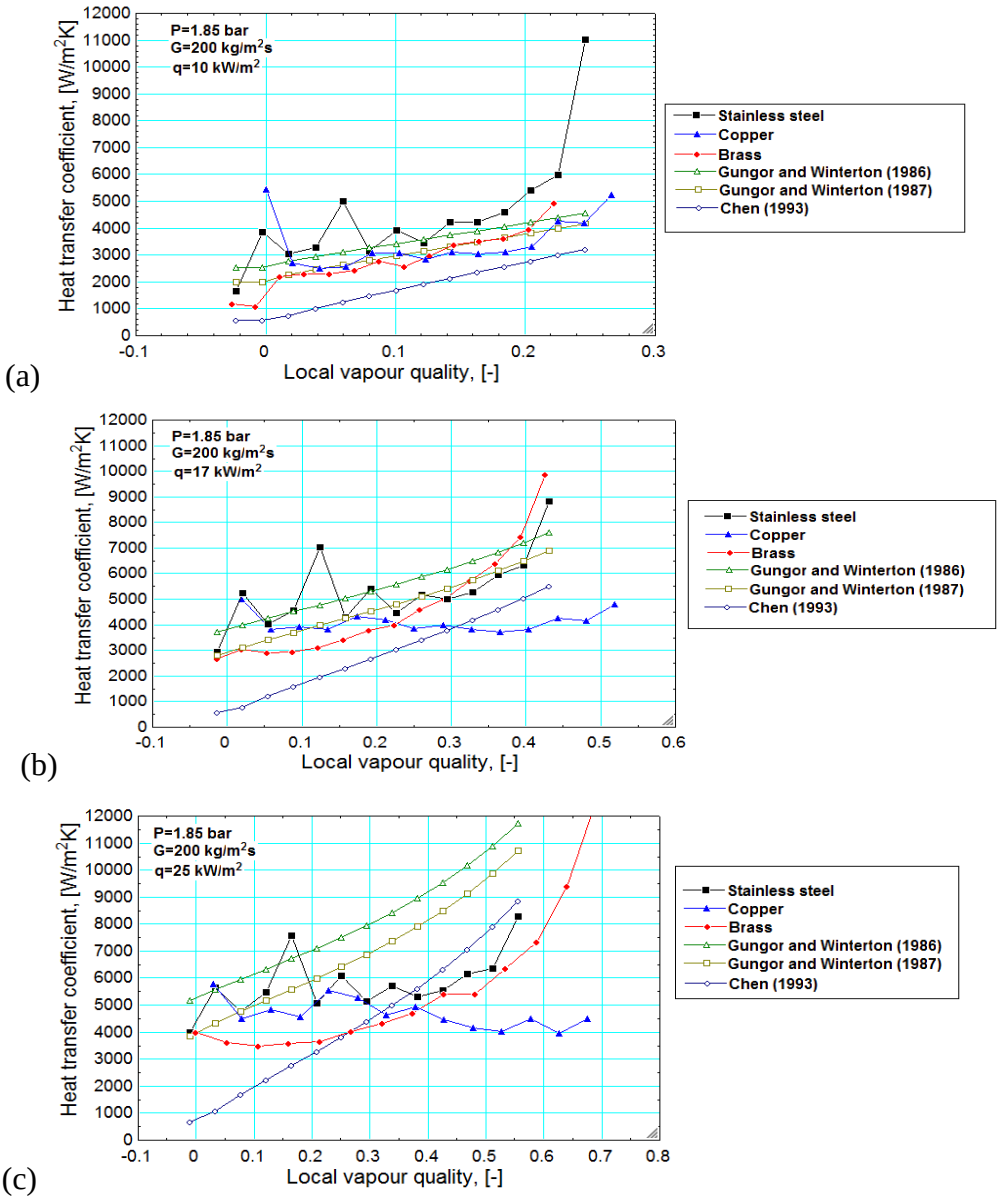

Figure 7.3. Predicted heat tranfer coefficient for Gungor and Winterton (1986), Gungor and Winterton (1987) and Chen (1993) at heat fluxes of (a) 10, (b) 17 and (c) 25 kW/m^2.

Figure 7.3 c presents the predicted and experimental data at a heat flux of 25 kW/m^2. The Chen (1993) correlation under predicts the data at low vapour qualities and over predicts at high vapour qualities. This over prediction at high vapour qualities is seen for all of the correlations besides Liu and Winterton (1991).

Chen (1963)

The Chen (1963) correlation is based on the heat transfer coefficient being the sum of the nucleate boiling and forced convection components in relation to two dimensionless factors, S and F, see equation 7.2. The suppression factor, S, is used to

account for the suppression of nucleate boiling due to the forced convection near the tube wall. The increase in convective turbulence due to the vapour phases is accounted for with the enhancement factor, F.

$$h_{tp} = Sh_{nb} + Fh_{sp} \quad (7.2)$$

This correlation was based on water, methanol, cyclohexane, n-pentane and benzene at 1 bar with vapour qualities from 0.01 to 0.71. It is deemed applicable for fluids before dry out occurs.

Figure 7.4 shows the stainless steel heat transfer coefficient to be under predicted, with β and MAE values of 18.9% and 41.3%, respectively. At low heat fluxes, corresponding to low heat fluxes, the heat transfer coefficient is over predicted. This was also seen for copper but not for brass. The copper results are similar to stainless steel, although with higher values of β=19.3 % and MAE=34.3 %, but with less of a spread of data. This is due to measured heat transfer coefficient being relatively linear for copper with fewer peaks than seen with stainless steel. The correlation performs best for brass with values of β=22.8 % and MAE=19.1 %. Figure 7.4 c shows the brass data to be most linear with no spread of data. The data follows the same trend of data as that of the predicted heat transfer coefficient but is under predicted which results in much of the data being just outside of the acceptable range at low heat fluxes with low MAE values.

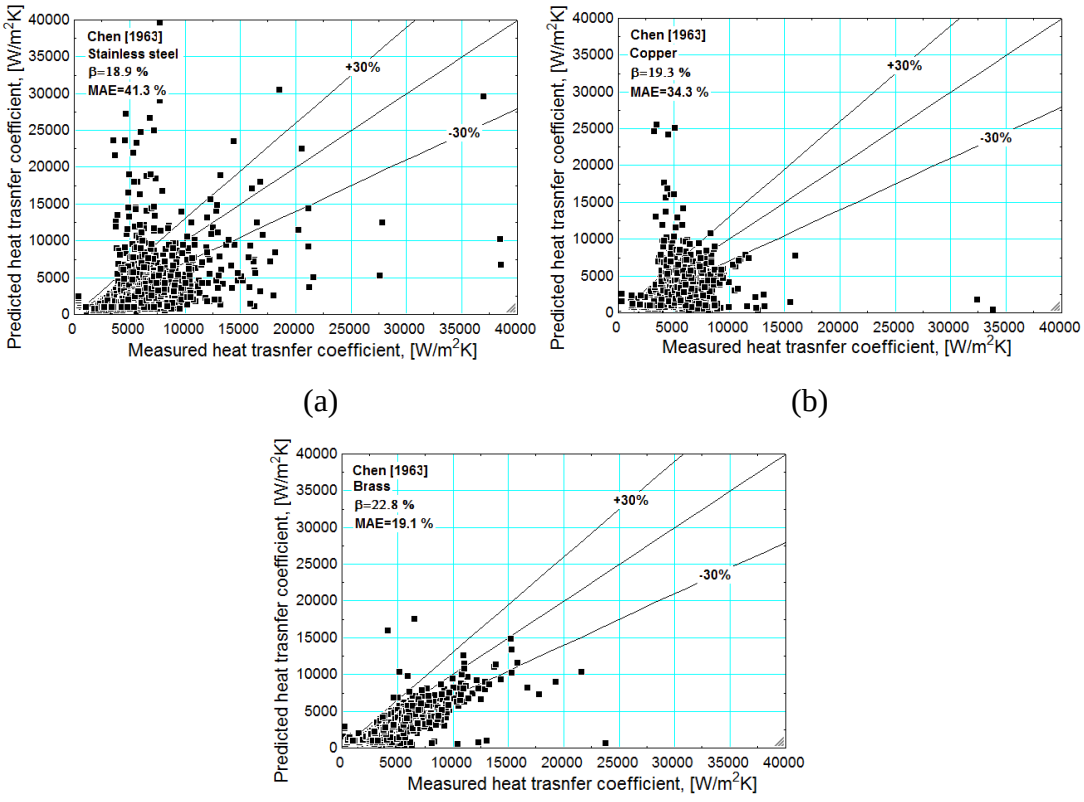

Figure 7.4. Comparison of the Chen (1963) correlation with the experimental heat transfer coefficient for (a) stainless steel, (b) copper and (c) brass.

Gungor and Winterton (1986)

Gungor and Winterton (1986) produced a correlation based on the Chen (1963) model from a data bank of 3700 data points. The data bank included heat transfer coefficients for water, refrigerants and ethylene glycol. The Chen (1963) model was modified in two ways, by changing the suppression factor and using the Cooper (1984) correlation for nucleate boiling as opposed to the Forster and Zuber correlation. The suppression factor was modified to include the Boiling number and uses the liquid Reynolds number as opposed to the two phase Reynolds number. These modifications were used to include disturbances in the boundary layer caused by vapour generation. Figure 7.5 shows the predicted heat transfer coefficient to give scattered results compared with the experimental data. This could be due to the change in the nucleate boiling equation, with the Forster and Zuber correlation including more functions of refrigerant properties. The magnitude difference between the predicted and the measured heat transfer coefficient is smaller for the Chen (1963) correlation, which predicts a lower heat transfer than Gungor and Winterton (1986). The same scatter in results at higher heat fluxes is seen for both correlations, relating to the sharp increases

in the measured heat transfer. Only a small amount of data was accurately predicted for stainless steel, with β and MAE values of 8.3 % and 29.1 %, respectively. The same increase in the measured heat transfer coefficient is seen for brass but not for copper but copper shows the scattering which brass does not. Brass has a smoother increase in the measured heat transfer coefficient, with less intermediate peaks. Figure 7.3 shows that the predicted heat transfer coefficient increases for both correlations but with the Gungor and Winterton (1986) predicting a higher heat transfer coefficient. The increase seen in the heat transfer coefficient for stainless steel, results in lower MAE value as the trends are similar but with a different gradient in increase and at a lower magnitude. The β results are best for stainless steel, although the difference between the materials is marginal with values of 7.4 % and 5.2% for copper and brass respectively. Brass shows the greatest agreement in trend, with the lowest β value due to the difference in magnitude between the predicted and measured heat transfer coefficient.

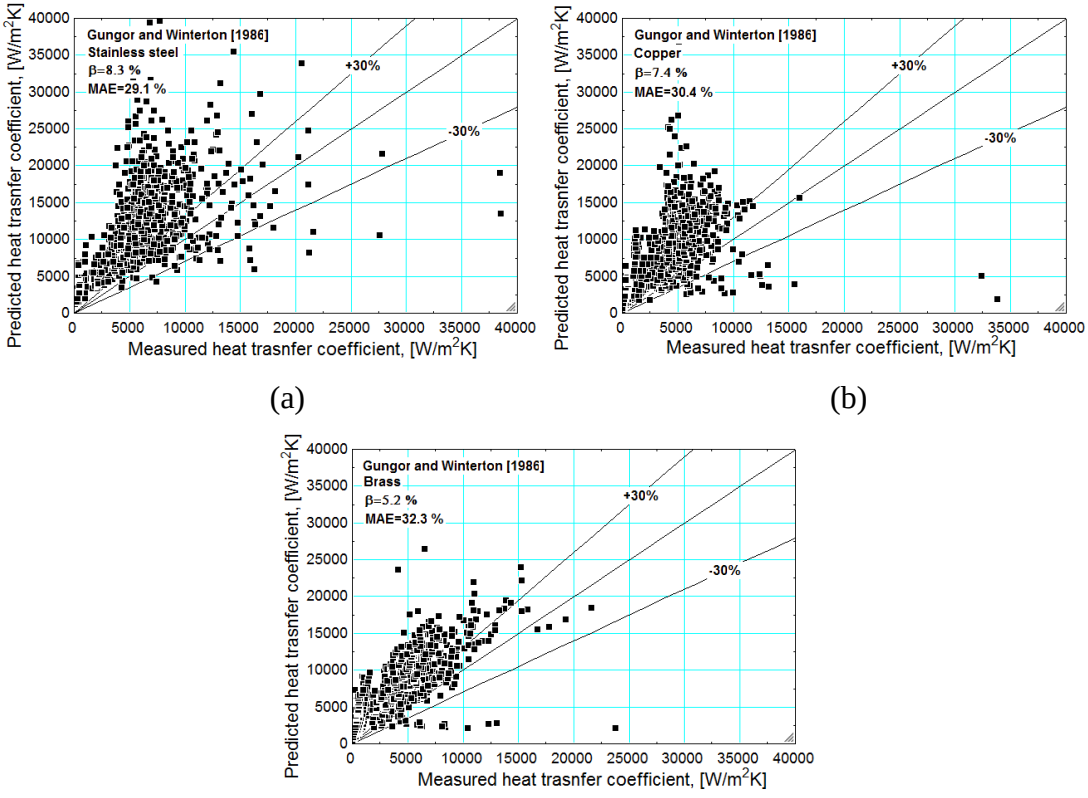

Figure 7.5. Comparison of the Gungor and Winterton (1986) correlation with the experimental heat transfer coefficient for (a) stainless steel, (b) copper and (c) brass.

Gungor and Winterton (1987)

The work by Gungor and Winterton (1986) was continued with a data bank including data from five refrigerants and water. The Gungor and Winterton (1987)

correlation uses the suppression and enhancement factors, modified from the previous correlation, with additional factors and the single phase heat transfer coefficient, see equation 7.3.

$$h_{tp} = (SS_2 + FF_2)h_{sp} \qquad (7.3)$$

The new factors, F_2 and S_2, values depend on the liquid only Froude number where values of F_2 and S_2 are equal to 1 when $Fr_{lo}<0.05$ or for vertical flow and a function of Fr_{lo} at higher values with horizontal flow. The Boiling number is still used for the suppression factor but with varying constants. This correlation is deemed suitable for both horizontal and vertical flows.

The prediction abilities of the Gungor and Winterton (1987) correlation is similar for all three materials, see figure 7.6. The predicted heat transfer coefficient shows a good grouping of data, but at values which are slightly lower than seen experimentally. This correlation showed a vast improvement from Gungor and Winterton (1986). This correlation is based on the single phase heat transfer coefficient, vapour quality, Boiling number and the ratio or liquid and vapour density which is far fewer variables than used in the original Gungor and Winterton (1986) correlation.

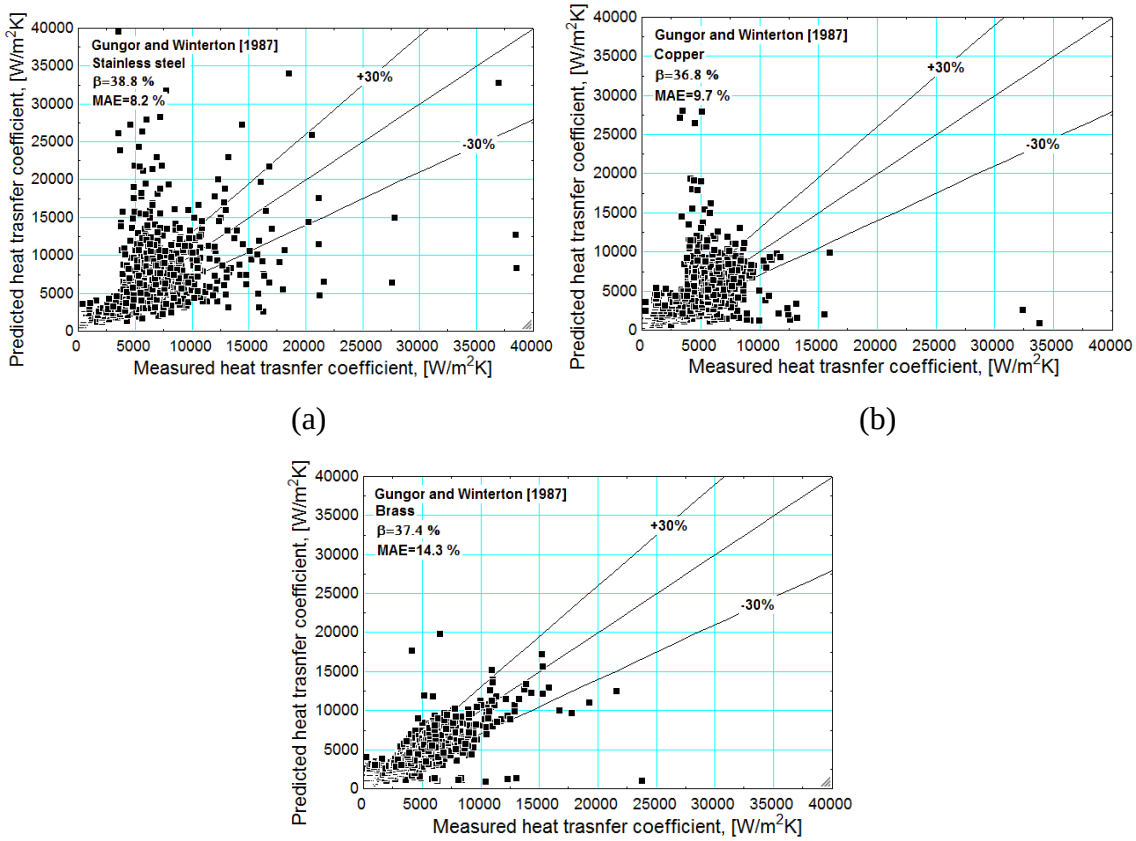

Figure 7.6. Comparison of the Gungor and Winterton (1987) correlation with the experimental heat transfer coefficient for (a) stainless steel, (b) copper and (c) brass.

Liu and Winterton (1991)

The Liu and Winterton (1991) correlation is based on the Chen (1963) model, with the nucleate boiling component calculated from the Cooper (1984) correlation. This correlation is recommended for subcooled and saturated flow boiling. This correlation differs from the previous correlations as it is an asymptotic model, see equation 7.4.

$$h_{tp}^2 = (Sh_{nb})^2 + \left(Fh_{sp}\right)^2 \qquad (7.4)$$

The suppression factor, S, is based on the enhancement factor and the Reynolds number. The enhancement factor, F, is calculated from the vapour quality, liquid Prandtl number and the ratio of liquid and vapour densities. The results showed the best agreement with stainless steel, with values of β=42.8 % and MAE=9.6 %, see figure 7.7. Similar results are seen for copper with values of β= 38.1 % and MAE=5.6. The results show a poor agreement with brass, with only 9.9 % of the data predicted and an MAE of 29.6 %. The data for stainless steel and copper is generally under predicted but over predicted for brass.

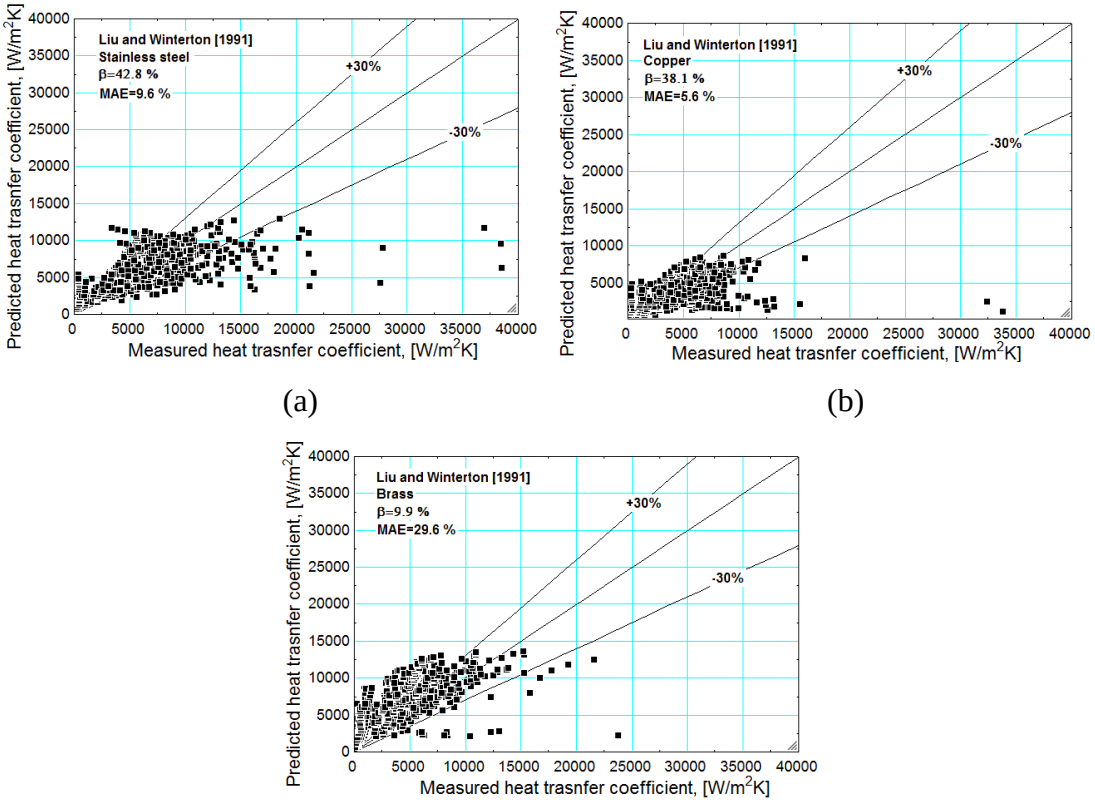

Figure 7.7. Comparison of the Liu and Winterton (1991) correlation with the experimental heat transfer coefficient for (a) stainless steel, (b) copper and (c) brass.

Figure 7.8 presents the Liu and Winteron (1991) correlation prediction for stainless steel, copper and brass at a heat flux of 10 and 25 kW/m^2. For all materials and heat fluxes, the heat transfer coefficient increases with vapour quality but the gradient of this increase and magnitude differs. The brass results are considerably higher than those of stainless steel and copper, and hence have a low β and MAE value. The brass results also show a shallower gradient, with less of an increase with vapour quality. The copper results show the least dependence on the heat flux, with the values being closest across the heat flux range. The copper surface has the lowest Rp value and hence the larger nucleate boiling component and consequently smaller heat transfer coefficient due to the asymptotic equation. The experimental results show less dependence on the Rp value, with a smaller heat transfer rate range. The brass results are largely over predicted and the stainless steel and copper results under predicted.

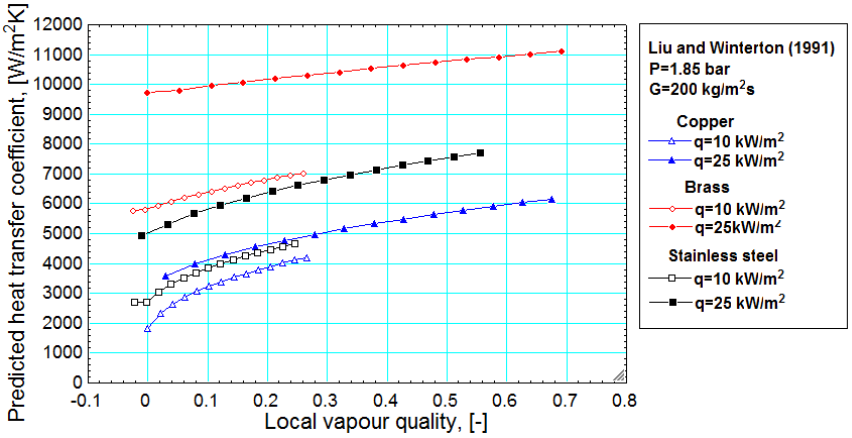

Figure 7.8. Predicted heat transfer coefficient for Liu and Winterton (1991) for copper, brass and stainless steel at different heat flux values.

7.4 Microscale correlations

Microscale correlations are those which are based on channel diameters of 3 mm or less. A comparison of the predicted heat transfer coefficient across difference heat fluxes is used to evaluate the trends and magnitudes of the correlations.

Figure 7.9 presents the predicted results for five heat transfer correlations across a heat flux range of 10 to 25 kW/m^2. The Zhang et al. (2004) correlation shows a linear increase in the heat transfer coefficient with vapour quality, the gradient of which increases with heat flux. The initial predicted heat transfer rate is low at low vapour qualities which results in poor agreement with the experimental results. Lazarek and Tran (1982) and Tran et al. (1996) predict a constant heat transfer rate with increasing

vapour quality, the magnitude of which increases with heat flux but still remains lower than the measured data. Warrier et al. (2002) shows a decreasing heat transfer coefficient with vapour quality, with the gradient increasing with heat flux. This is contrary to the trends seen for the experimental data. Kew and Cornwell does predict an increase in the heat transfer coefficient with vapour quality but the increase is small. These correlations, besides Zhang et al. (2004) all under predict the heat transfer coefficient and do not show the same increase in heat transfer coefficient with heat flux which is seen with the experimental results.

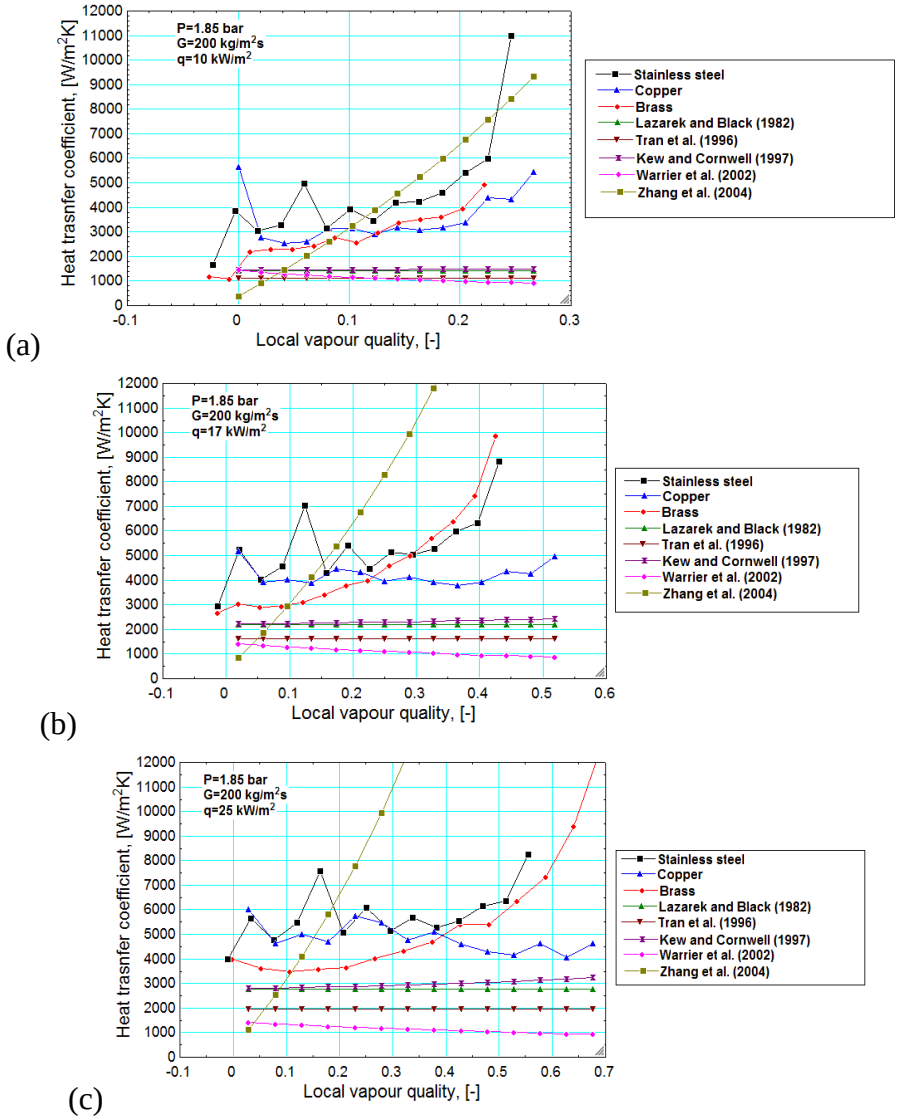

Figure 7.9. Predicted heat transfer coefficient for Lazarek and Black (1982), Tran et al. (1994), Kew and Cornwell (1997), Warrier et al. (2002) and Zhang et al. (2004) at heat fluxes of (a) 10, (b) 17 and (c) 25 kW/m^2.

Figure 7.10 shows Sun-Mishima (2009) correlation to predict a low heat transfer coefficient which is constant with the vapour quality. The increase in magnitude with heat flux is small, with an increase of less than 1000 W/m^{2}K over the heat flux range. The Saitoh et al. (2007), Lee and Mudawar (2005) and Li and Wu (2010) predict a decreasing heat transfer coefficient with vapour quality, although the Lee and Mudawar (2005) correlation does predict a peak at low vapour qualities, which the others do not. All of the correlations predict an increase in the heat transfer rates with heat flux but to different extents.

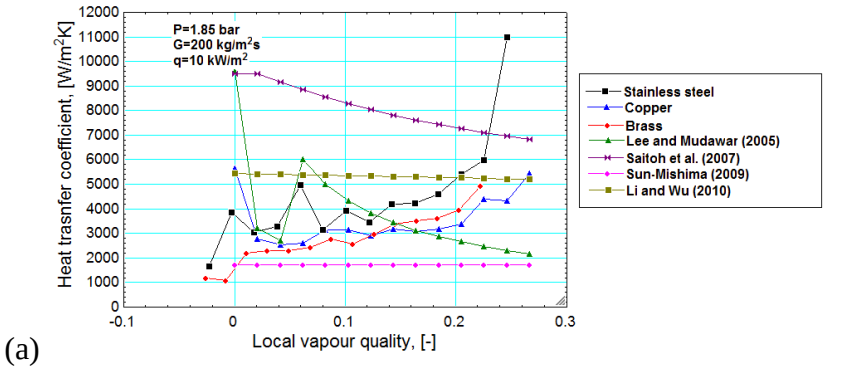

(a)

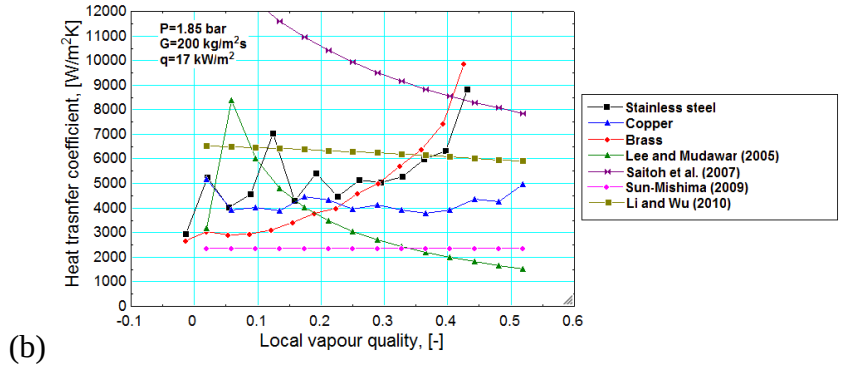

(b)

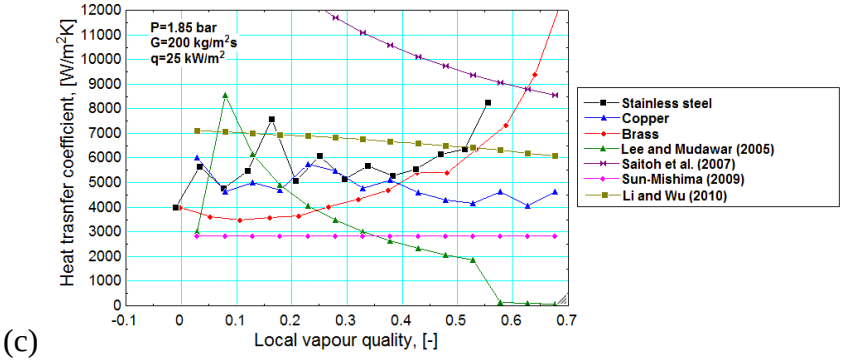

(c)

Figure 7.10. Predicted heat transfer coefficient for Lee and Mudawar (2005), Saitoh et al. (2007), Sun-Mishima (2009) and Li and Wu (2010).

The Mahmoud and Kayaiannis I (2012) correlation predicts a decreasing heat transfer coefficient with increasing vapour quality, see figure 7.11. This decrease is more prevalent with an increasing vapour quality and heat flux. The Li et al. (2013)

correlation shows an increase in the heat transfer rate with vapour quality. The gradient of this increase shows little dependence on heat flux. Kim et al. (2013) predicts an increase with vapour quality but with a much steeper gradient, which increases with heat flux.

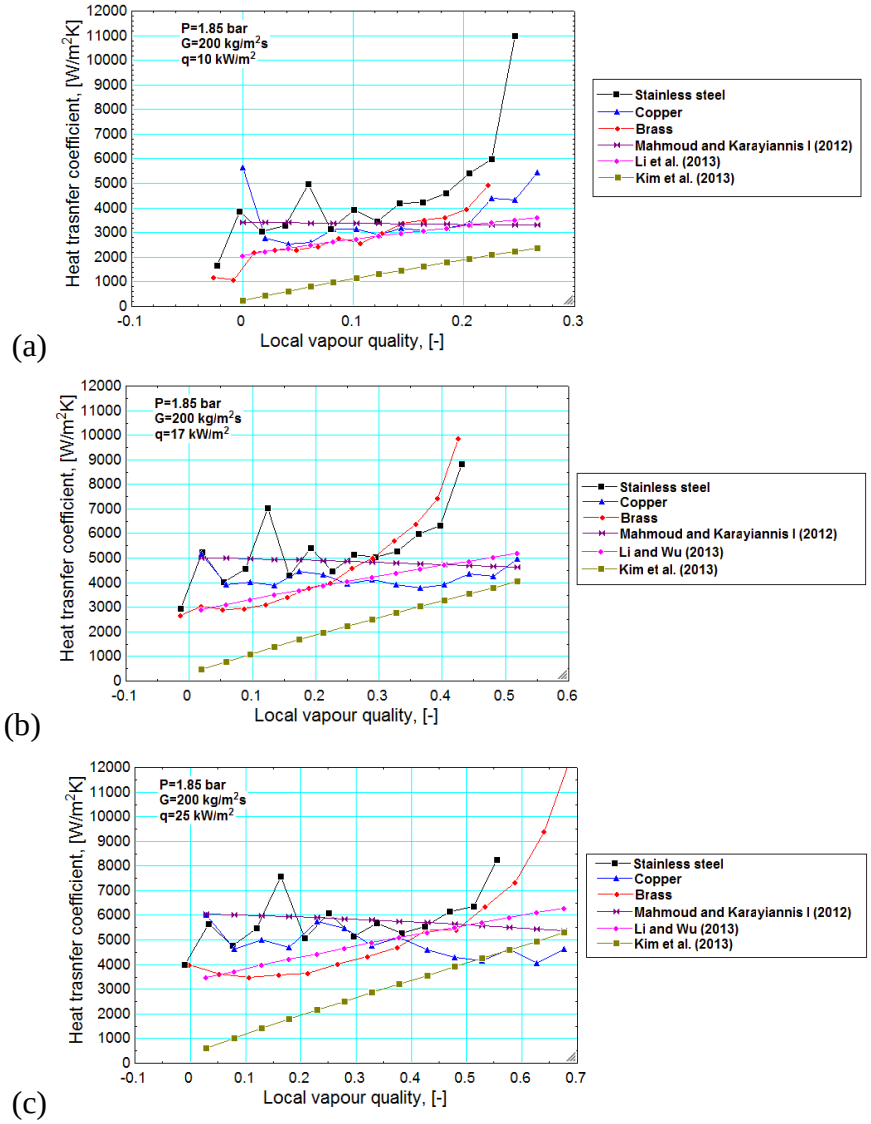

Figure 7.11. Predicted heat transfer coefficient for Mahmoud and Karayiannis I (2012), Li and Wu (2013) and Kim et al. (2013) at heat fluxes of (a) 10, (b) 17 and (c) 25 kW/m^2.

The heat transfer correlations investigated all show some dependence on the heat flux but do not all show a dependence on vapour quality. In general, the heat transfer correlations show an improvement with increasing heat flux, this is especially true for stainless steel. As the channel materials all show a different trend in heat transfer coefficient with vapour quality, none of the correlations could predict the differing trends as there is no function of the surface characteristics.

Lazarek and Black (1982)

The Lazarek and Black (1982) correlation was produced from a data bank of 738 data points for R113 in a 3.15 mm diameter tube. The proposed correlation, see equation 7.5, is an empirical equation based on the fluid properties and channel diameter.

$$h_{tp} = 30Re_l^{0.857}Bo^{0.714}\frac{k_f}{D_h} \quad (7.5)$$

This correlation is independent of vapour quality, showing a constant heat transfer coefficient in figure 7.9. The mass flux component is a small consideration in the Lazarek and Black (1982) correlation, with components equating to $G^{0.143}$. The prediction showed poor agreement for stainless steel, with β=12.7 % and MAE= 87.8 %, see figure 7.12. The majority of the data was under predicted, with the highest heat transfer coefficient being predicted at approximately 5 kW/m^2, lower than the mean measured heat transfer coefficient. The higher heat transfer coefficient resulting from the peaks in the heat transfer coefficient is not predicted which results in a large MAE values. The MAE values are smaller for copper and brass where these extreme peaks are not seen. The β values are similar to stainless steel at 10.9 % and 16.8 % for copper and brass respectively. Figure 7.12 b shows that the measured copper heat transfer coefficient is around the 5 kW/m^2 but the predicted heat transfer coefficient is lower.

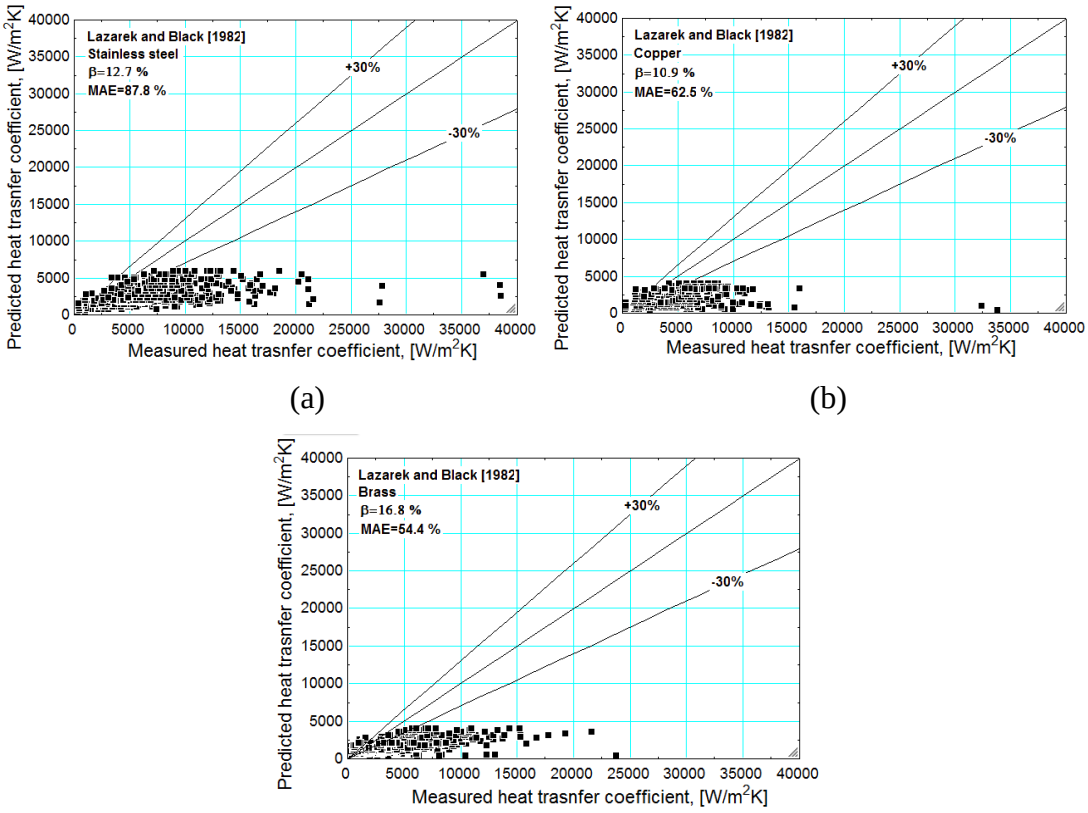

Figure 7.12. Comparison of the Lazarek and Black (1982) correlation with the experimental heat transfer coefficient for (a) stainless steel, (b) copper and (c) brass.

Tran et al. (1996)

The Tran et al. (1996) correlation is an empirical equation which is adapted from the Lazarek and Black (1982) correlation. The correlation is based on data from a circular and a rectangular brass channel, both with heated lengths of 870 mm. This investigation concluded that the dominant heat transfer mechanism is nucleate boiling. Therefore, the Reynolds number was replaced with the liquid Weber number. The liquid Weber number uses the total mass flux and does not include a function of the liquid vapour quality. The liquid vapour quality is not used in this correlation, showing a constant predicted heat transfer correlation with vapour quality, see figure 7.9. Contrary to the Lazarek and Black (1982) correlation, the liquid conductivity is not used here and the ratio of densities is used instead, see equation 7.6. The Boiling number exponent was reduced from 0.714 to 0.6. The liquid density is included in the density ratio and in the liquid Weber number, resulting in the exponent for this parameter being 0.7. The vapour density has a higher exponent of 0.4 showing more of a dependency. The use of the Weber number also allows for the inclusion of the surface tension.

$$h_{\square p} = 840000 We_l^{0.3} Bo^{0.6} \left(\frac{\rho_l}{\rho_g}\right)^{-0.4} \quad (7.6)$$

The correlation showed poor agreement with all three materials as the experimental heat transfer coefficient trend differs greatly from that of the predicted trend, see figure 7.13. This correlation does not predict any changes with vapour quality which is not seen experimentally.

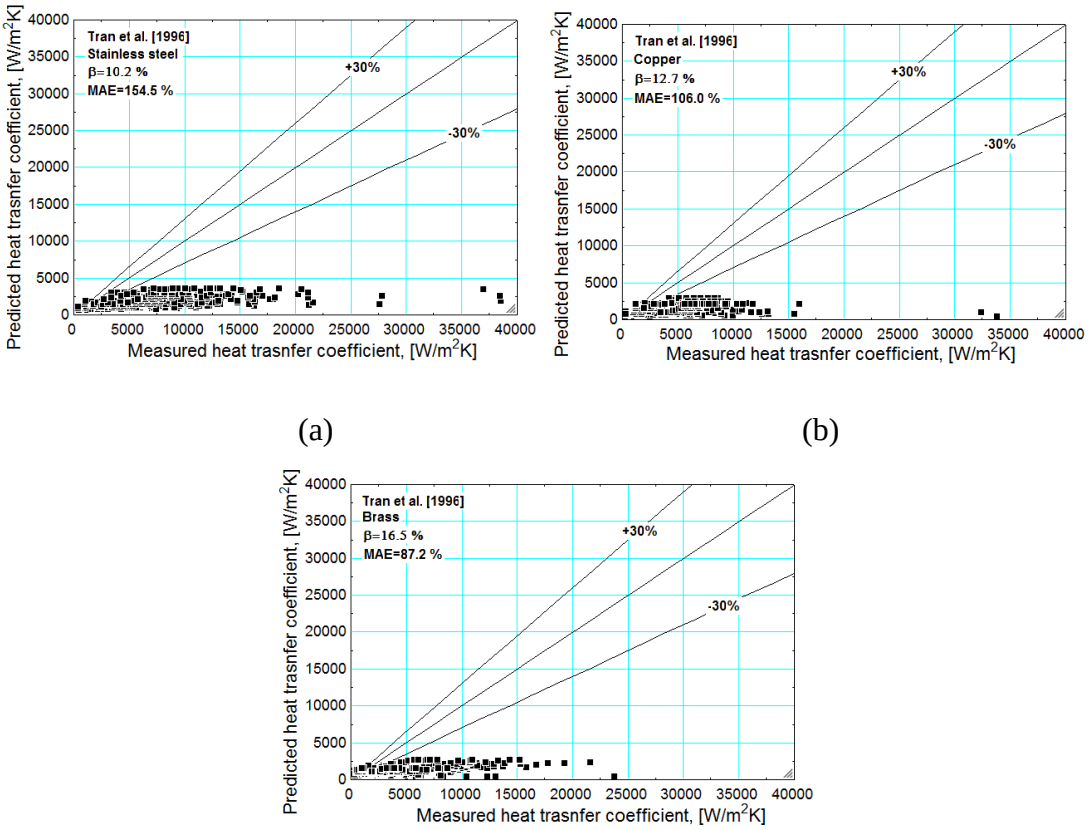

Figure 7.13. Comparison of the Chen Tran et al. (1996) correlation with the experimental heat transfer coefficient for (a) stainless steel, (b) copper and (c) brass.

Kew and Cornwell (1997)

The Kew and Cornwell (1997) correlation is based on the Lazarek and Black (1982) correlation but accounting for an increase in the heat transfer coefficient with vapour quality seen in larger tubes. This increase is accounted for with vapour quaility having a negative exponent, see equation 7.7. All other components of the equation are kept the same as Lazarek and Black (1982). Figure 7.9 shows that the predicted increase in heat transfer coefficient is small at a heat flux of 10 kW/m^2, this is due to the vapour qualities of <0.3. At the highest vapour quality of 0.95, the resulting value equates to a

50% increase in the value of the predicted heat transfer from that of Lazarek and Black (1982).

$$h_{tp} = 30\, Re^{0.857} Bo^{0.714} (1-x)^{-0.143} \frac{k_f}{D} \qquad (7.7)$$

The correlation shows a slightly better prediction from the Lazarek and Black (1982) correlation, for all materials, but this improvement is marginal. Figure 7.14 shows the heat transfer prediction to be lower than the experimental results. Although the correlation does predict an increase in the heat transfer coefficient with vapour quality, the increase is marginal compared with that seen in the experimental data, see figure 7.9. Only the data at the lower heat transfer coefficient, which equates to a lower heat flux is predicted, with the majority of the data being under predicted.

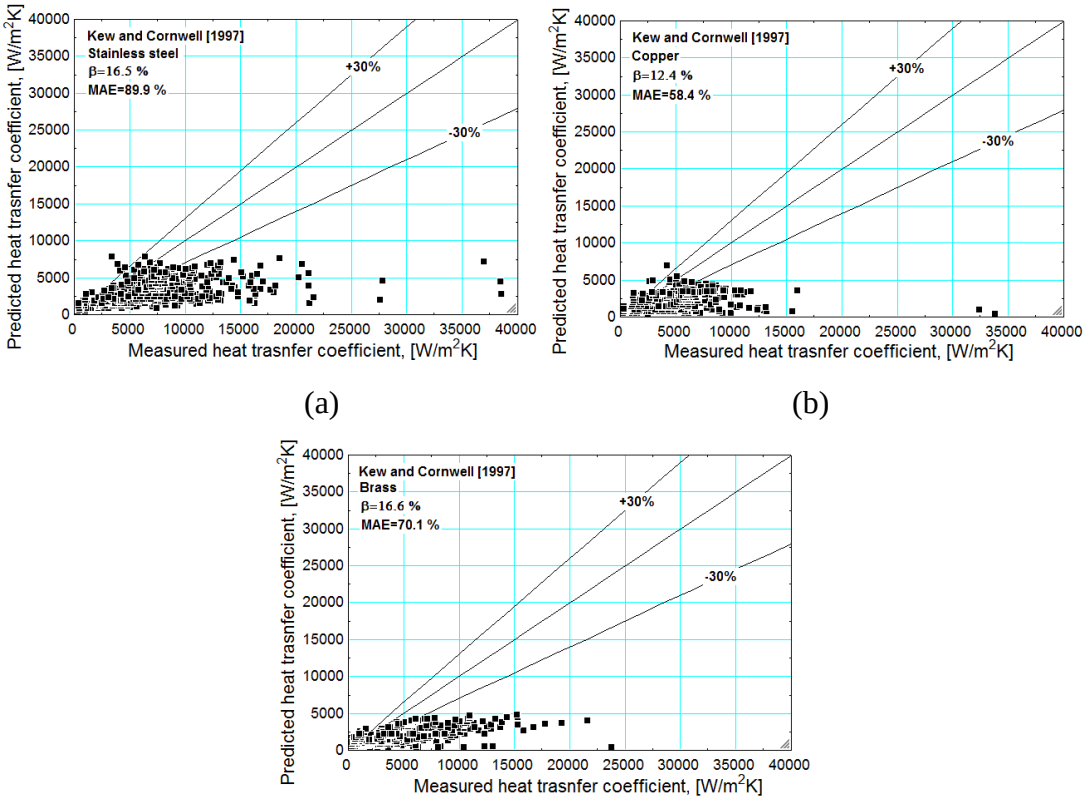

Figure 7.14. Comparison of the Kew and Cornwell (1997) correlation with the experimental heat transfer coefficient for (a) stainless steel, (b) copper and (c) brass.

Warrier et al. (2002)

Warrier et al. (2002) conducted experiments using FC-84 in a rectangular channel with a hydraulic diameter of 0.75 mm. The correlation is based on the enhancement model, where a function is multiplied by the single phase heat transfer

coefficient, see equation 7.10. The correlation includes a function of the vapour quality and the Boiling number. The quality is to an exponent of 0.65 which results in the predicted heat transfer coefficient decreasing with vapour quality. The correlation is valid for vapour qualities between 0.01 and 0.55.

$$h_{tp} = \left[1 + 6\,Bo^{1/16} - 5.3\,x^{0.65}(1 - 855\,Bo)\right]h_{sp} \qquad (7.10)$$

As the predicted heat transfer coefficient is low, with highs of 2500 W/m^{2}K at low vapour qualities, the increase in measured heat transfer coefficient results in a large MAE values, see figure 7.9. Figure 7.15 shows a poor agreement with the experimental data, with the range predicted similar to that seen during single phase flow. The trend also varies greatly from that of the experimental trend, which shows an increase in the heat transfer coefficient with vapour quality, which results in large MAE values.

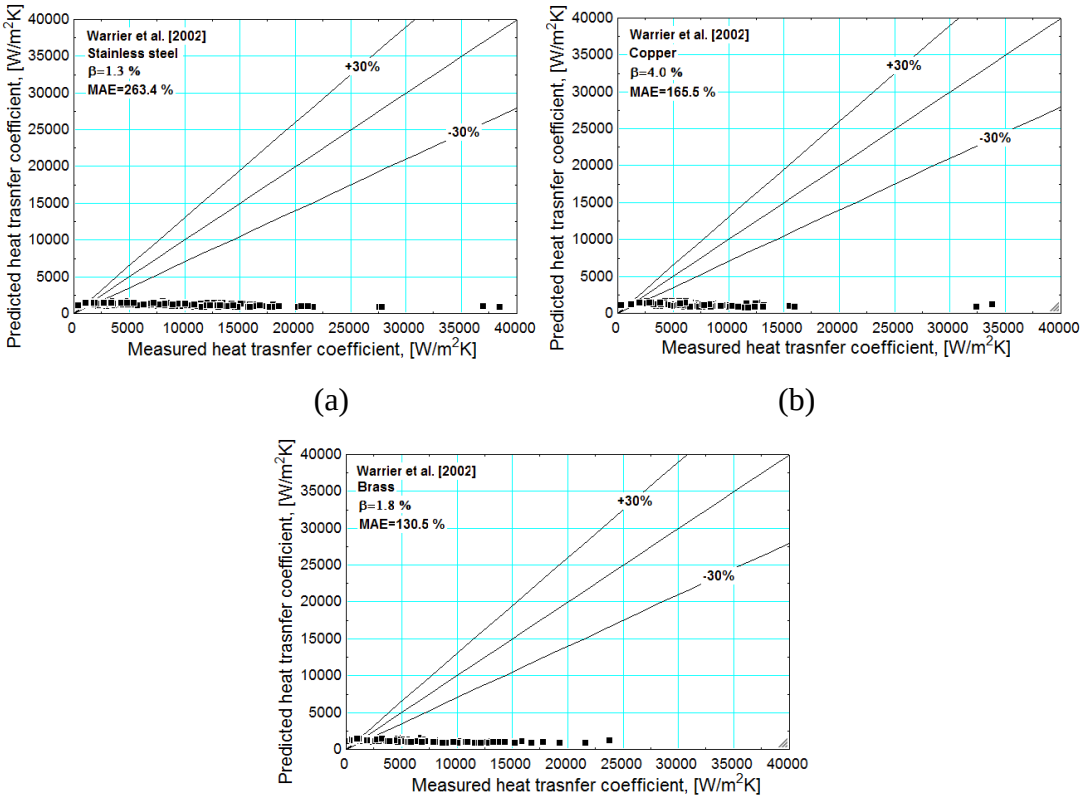

Figure 7.15. Comparison of the Warrier et al. (2002) correlation with the experimental heat transfer coefficient for (a) stainless steel, (b) copper and (c) brass.

Zhang et al. (2004)

Zhang et al. (2004) produced a superposition model based correlation from data of both water and refrigerants in channels ranging in diameter from 0.78 to 6 mm, see appendix A. The correlation is an adapted form of the Chen (1963) correlation to include minichannels and the laminar regime. The correlation is valid for vapour qualities of 0 to 0.7. The suppression factor is a function of the liquid Reynolds number and numerical constants. The single phase heat transfer coefficient is calculated from the Nusselt number, the value of which is a function the Reynolds number. The enhancement function, E, is the maximum value of 1 or E', where E' is a calculated from the two phase frictional multiplier. The same boundaries as the Lockhart-Martinelli (1945) correlation, see chapter 6, are employed, with the values changing depending on the turbulence for the liquid and vapour regimes. Due to the complexity of the correlation, a large number of flow conditions are considered, including the turbulence of the flow regimes which is not a factor in the other heat transfer correlations. Figure 7.9 shows that the Zhang et al. (2004) predicted heat transfer increases with vapour quality with a larger gradient than that of Chen (1963) correlation. The β values for stainless steel are similar between the Zhang et al. (2004) and Chen (1963) correlation at 17.1 and 18.9 % respectively. Although a similar percentage of data is predicted for both correlations, the MAE value is nearly half that of the Chen (1963) correlation at 22.7 %. This reduction in MAE is due to there being a reduced percentage difference between the predicted and measured heat transfer coefficient at the higher heat fluxes, see figure 7.16. The same reduction in MAE values, by two thirds, is seen with brass with similar β values. The β values are still similar for copper but the MAE value is considerably higher for the Zhang et al. (2004) correlation compared with the Chen (1963) correlation. The higher MAE values for copper are a result of the predicted heat transfer coefficient increasing with vapour quality which is not seen with the measured heat transfer coefficient.

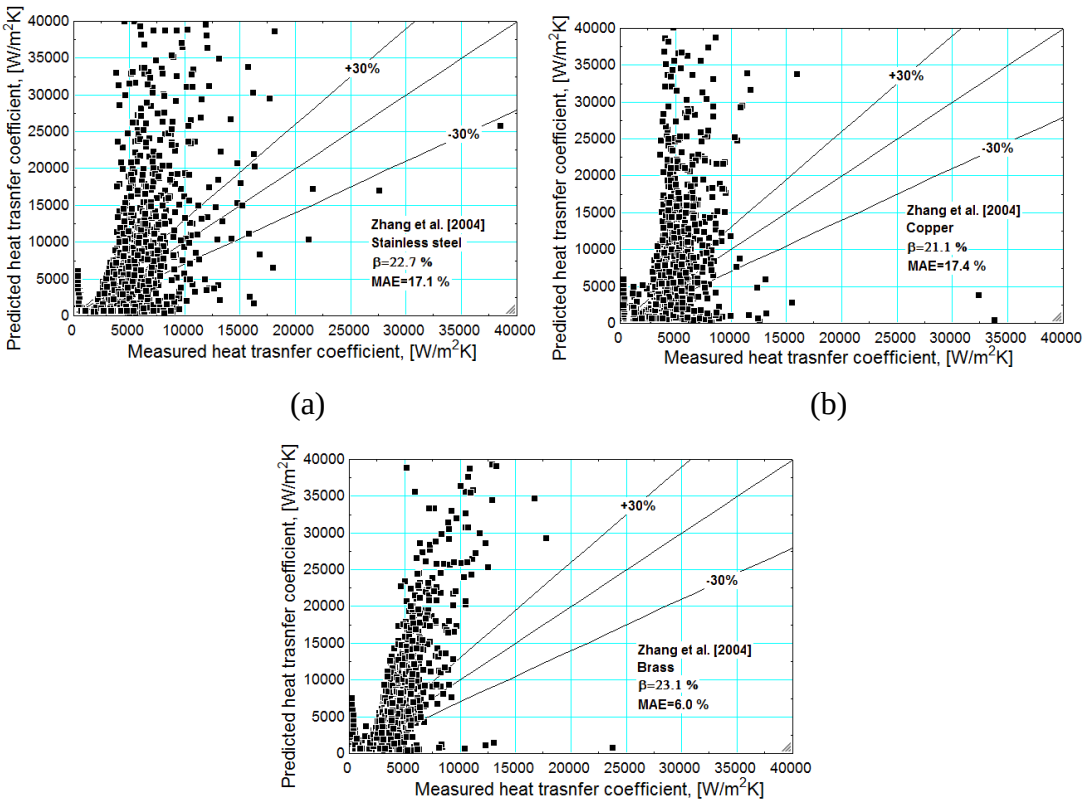

Figure 7.16. Comparison of the Zhang et al. (2004) correlation with the experimental heat transfer coefficient for (a) stainless steel, (b) copper and (c) brass.

A study by Shiferaw (2008) proposed modifying the Zhang et al. (2004) correlation, using the Cooper (1984) correlation as opposed to the Forster-Zuber (1955) correlation to represent the nucleate boiling component. Shiferaw (2008) and Mahmoud (2011) both noted an improvement in the prediction with this modification, with the increase in the predicted heat transfer coefficient resulting in higher β and MAE values. Figure 7.17 shows a comparison between the experimental heat transfer coefficient and the modified Zhang et al. (2004) predicted heat transfer coefficient. As the Zhang et al. (2004) correlation was seen to over predict the heat transfer coefficient, the increase seen with the modified correlation reduces the accuracy of the prediction. The work by Shiferaw (2008) and Mahmoud (2011) using R134a reported flow patterns which included bubbly and slug flow, where nucleate boiling dominants. This could be why an increase in the nucleate boiling component increased the accuracy of the prediction. Although the R245fa data shows a difference in the heat transfer coefficient with surface characteristics, which would indicate an influence of nucleate boiling, the increased surface tension of R245fa facilitates annular flow and therefore less sensitive to the nucleate boiling component. For all materials, the β and MAE values are lower for the modified Zhang et al. (2004) correlation.

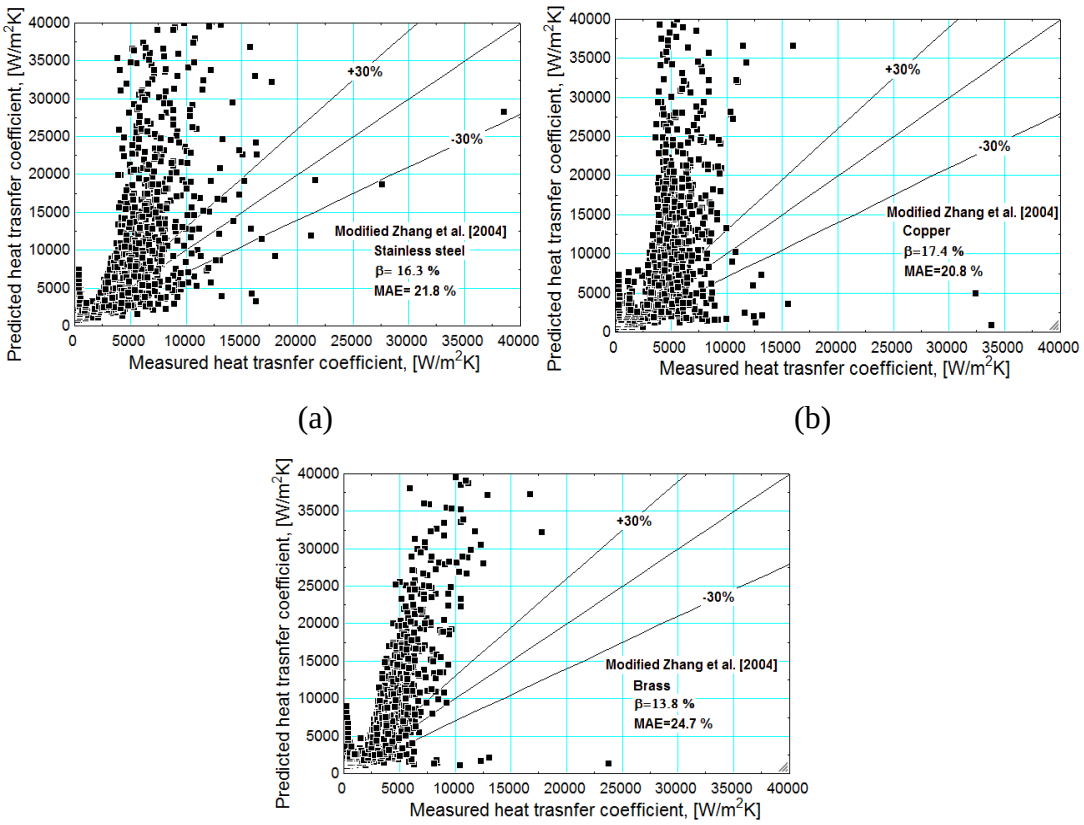

Figure 7.17. Comparison of the modified Zhang et al. (2004) correlation with the experimental heat transfer coefficient for (a) stainless steel, (b) copper and (c) brass.

Lee and Mudawar (2005)

Lee and Mudawar (2005) produced a heat transfer correlation based on a data bank of 318 data points, 111 data points from R134a and 222 data points from water, in a 0.35 mm hydraulic diameter channel. This study concluded that the micro scale correlations gave no improvement over macro scale correlations due to the dominance of slug and annular flow at high heat fluxes. Based on this, a correlation was produced which changes depending on the vapour quality range. For vapour qualities between 0 and 0.05, an enhancement model is used which is a function of the Lockhart-Martinelli (1945) parameter, X. The single phase heat transfer coefficient is calculated from the Nusselt number. A similar enhancement model is employed for vapour qualities between 0.05 and 0.55. The enhancement factor uses the Lockhart-Martinelli (1945) parameter, X, the liquid Weber number and Boiling number. For the vapour quality region of 0.55 and 1, the predicted heat transfer coefficient is the maximum value of a function of the Lockhart-Martinelli (1945) parameter and the single phase gas heat transfer coefficient or the single phase gas heat transfer coefficient alone. The calculation of the single phase gas heat transfer coefficient depends on the turbulence.

Figure 7.10 shows that this correlation changes with vapour quality, showing a peak in value at low vapour qualities and decreasing in magnitude with increasing vapour quality. The trend of heat transfer coefficient with vapour quality changes with heat flux due to the change in the experimental vapour quality. This correlation showed poor agreement for stainless with values β=15.5 % and MAE=147.5 %. Although much of the data is over predicted, the peaks seen with increasing vapour quality are not represented and are consequently under predicted, see figure 7.18. This is also true for brass but to a lower extent where the peaks only occur at a higher vapour qualities. This is not seen with copper where the data is mostly over predicted.

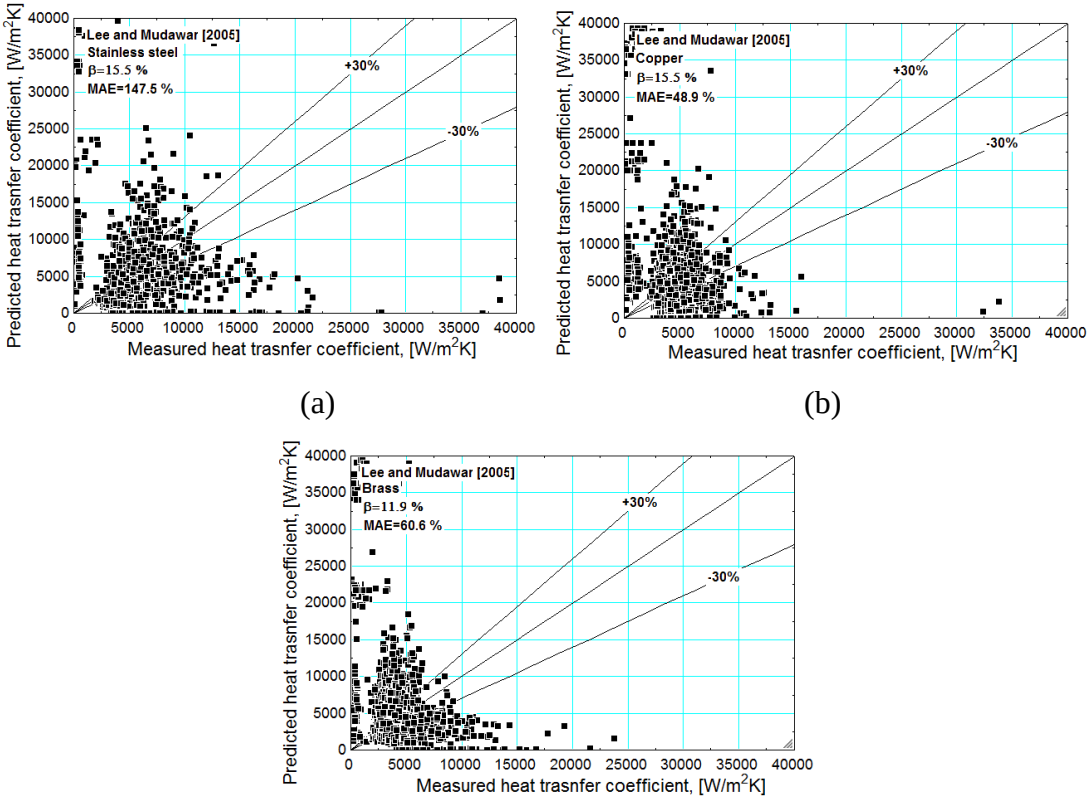

Figure 7.18. Comparison of the Lee and Mudawar (2005) correlation with the experimental heat transfer coefficient for (a) stainless steel, (b) copper and (c) brass.

Saitoh et al. (2007)

Saitoh et al. (2007) conducted experiments using R134a in channels with diameters of 0.51, 1.12 and 3.1 mm. This study found that for the larger channel of 3.1 mm, the heat transfer coefficient was a function of the both the heat and mass flux. For the smallest channel, 0.51 mm, the heat transfer coefficient increased with heat flux but had a low dependence on mas flux. The surface tension was seen to be a dominant factor for the small diameter channels, resulting in dry out at low qualities. A

superposition model was produced to account for the heat transfer coefficient trends seen. This model calculated the nucleate boiling based on the bubble diameter, heat flux, liquid conductivity, liquid temperature and the liquid and vapour density ratio. The suppression factor is based on numerical constants and the liquid Reynolds number. The enhancement factor is based on the Lockhart-Martinelli (1945) parameter, X, and the vapour Weber number. The single phase heat transfer coefficient is calculated from the Nusselt number for Reynolds numbers less than 1000. For Reynolds numbers greater than 1000, the single phase heat transfer coefficient is based on the experimental conditions. In general, this correlation over predicts the heat transfer coefficient, with the worst being for that of stainless steel, see figure 7.19. Only a small percentage of data was predicted in the ±30 %, 8.5%, but with a relatively low MAE of 28.6% due to the clumping of the data just outside of the acceptable range. The same clumping is seen for brass and copper with low β values but also low MAE values.

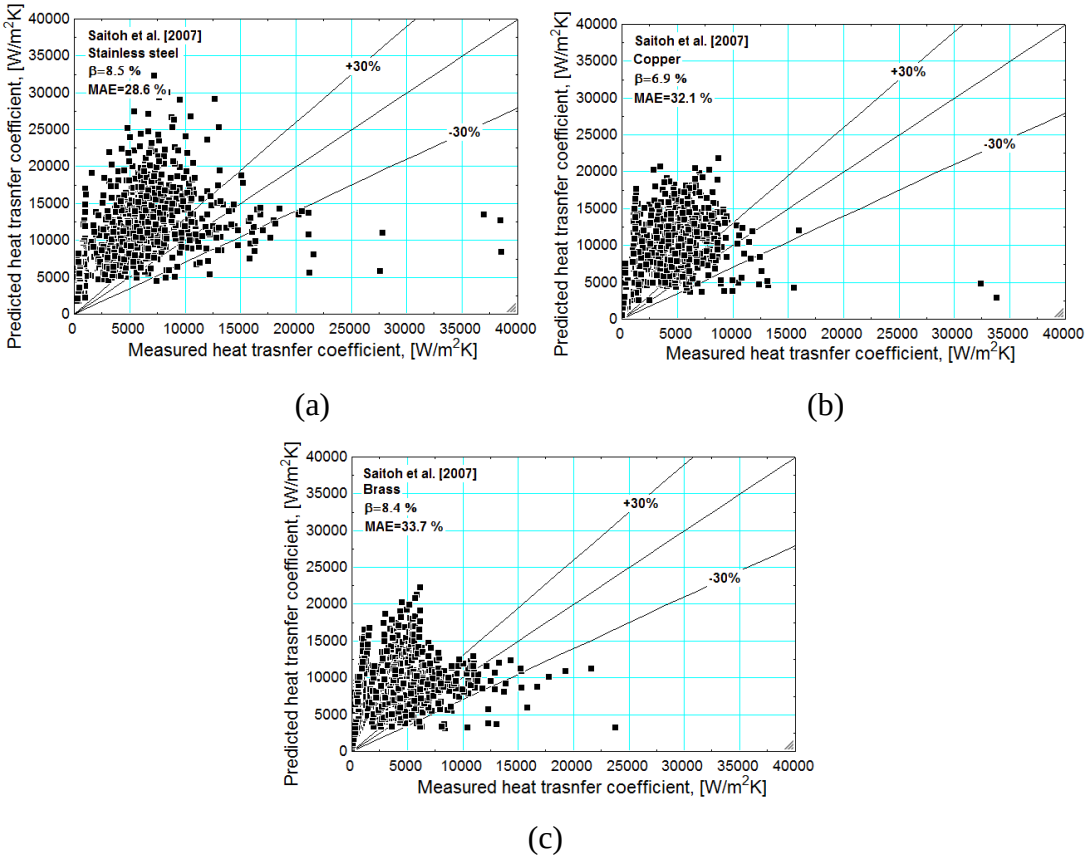

Figure 7.19. Comparison of the Saitoh et al. (2007) correlation with the experimental heat transfer coefficient for (a) stainless steel, (b) copper and (c) brass.

Bertsch et al. (2009)

Bertsch et al. (2009) developed a correlation based on a database of 3899 data points, including 12 fluids and hydraulic diameters from 0.16 to 2.92 mm, equating to

confinement numbers from 0.3 to 4. This correlation is similar to the superposition model but uses the convective heat transfer coefficient instead of the single phase heat transfer coefficient, see equation 7.9. The nucleate boiling heat transfer coefficient is calculated using the Copper (1984) pool boiling equation and. The suppression factor is equal to (1-x), due to the nucleate boiling suppression being a function of the vapour quality rather than the Reynolds number. The enhancement factor is a function of the confinement number and vapour quality. The convective heat transfer coefficient is calculated from the Dittus-Boelter equation for turbulent flow. For laminar flow, the convective heat transfer coefficient is calculated from the channel diameter, channel length, liquid thermal conductivity, Reynolds number and Prandlt number.

$$h_{tp} = Sh_{nb} + Fh_{conv} \qquad (7.9)$$

Figure 7.20 shows that the predicted heat transfer coefficient changes with vapour quality, with a slight dip in the predicted magnitude in the middle range of vapour quality for copper and stainless steel. The predicted heat transfer coefficient is seen to decrease with vapour quality for brass. The convective heat transfer coefficient is low and remains relatively constant across the experimental range. The enhancement factor, F, increases with vapour quality up to a vapour quality of approximately 0.8, after which it decreases. The suppression factor, S, is seen to decrease with vapour quality, resulting the predicted heat transfer coefficient showing a ‘dip’ at the intermediate vapour qualities. Figure 7.21 shows that the majority of the data for stainless steel is within the same heat transfer coefficient range, resulting in a low MAE value, besides that of the peaks seen in the experimental data. The predicted trend is similar to that of the experimental range in terms of the vapour quality, although the predicted data has a smaller gradient. The predicted data is seen to increase with heat flux to a larger extent that that of the experimental data which is why the β values is low.

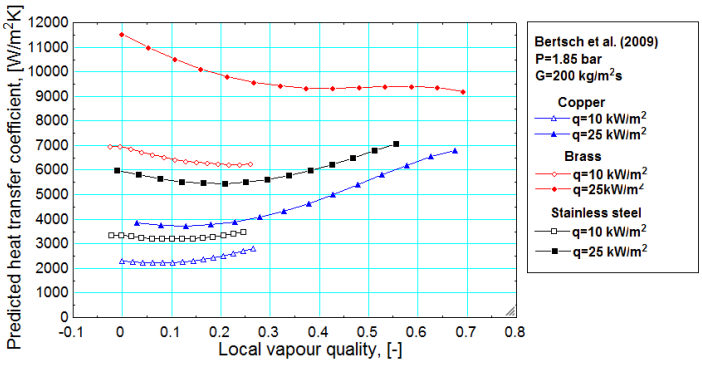

Figure 7.20. Predicted heat transfer coefficient for Bertsch et al. (2009) for copper, brass and stainless steel.

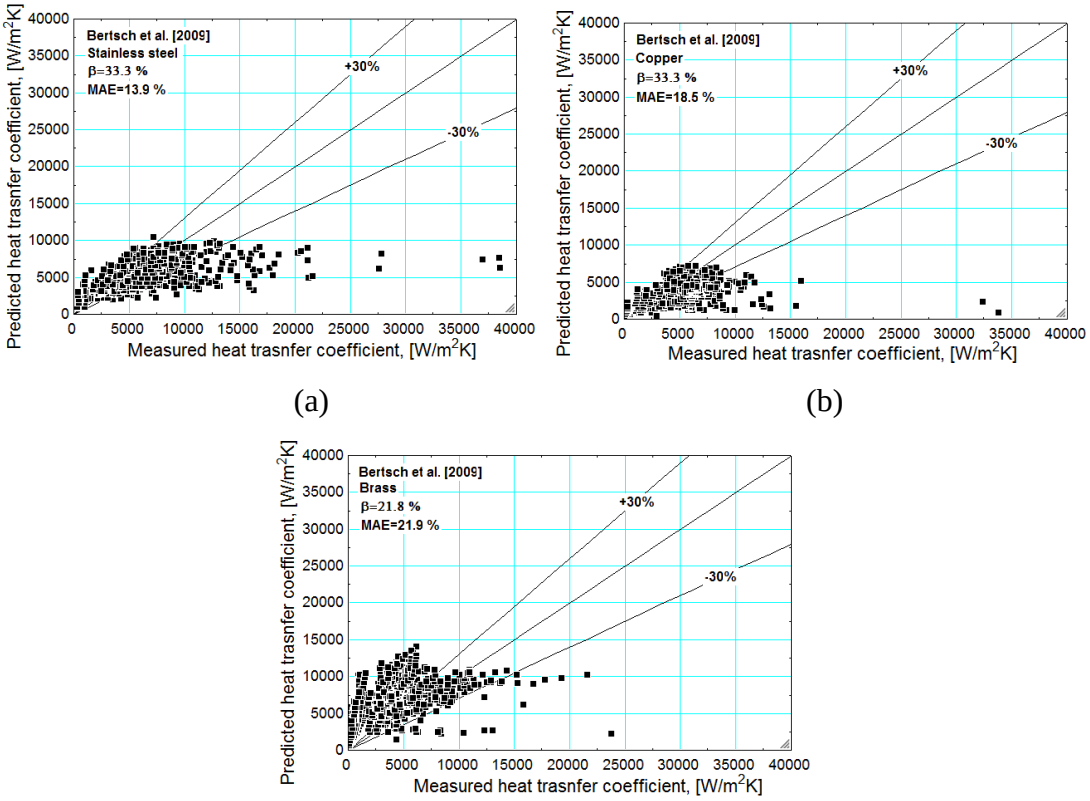

Figure 7.21. Comparison of the Bertsch et al. (2009) correlation with the experimental heat transfer coefficient for (a) stainless steel, (b) copper and (c) brass.

Sun-Mishima (2009)

Sun and Mishima (2009) developed a correlation based on a databank of 2505 data points which included 11 fluids and a diameter range of 0.21 to 6.05 mm. This investigation found Chen (1963) and Chen type correlations were not suitable for mini channels. The best performing correlations were found to be empirical correlations by Lazarek and Black (1982) and Kew and Cornwell (1997). The dominant heat transfer

mechanism was deemed to be nucleate boiling, with only a weak dependence of vapour quality. The correlation produced is based on the Lazarek and Black (1982) correlation but modified to include the Weber number, with the heat transfer coefficient showing a strong dependence on the Weber number, see equation 7.10. Figure 7.10 shows that the predicted heat transfer coefficient is constant with vapour quality and lower than that of Lazarek and Black (1982).

$$h_{tp} = \frac{6Re_{lo}^{1.05}Bo^{0.54}}{We_l^{0.191}\left(\rho_l/\rho_g\right)^{0.142}}\frac{k_f}{D} \tag{7.10}$$

The Sun-Mishima (2009) correlation shows lower β values for all materials compared with Lazarek and Black (1982) but also considerably lower MAE values. Therefore, although less data is predicted in the acceptable range, the difference between the predicted and measured heat transfer coefficient is less. Figure 7.22 shows that for all of the materials, the data is under predicted with the increase in heat transfer coefficient with vapour quality not being represented. The Sun-Mishima (2006) correlation has a greater function of the heat flux and enthalpy, as well as the addition of the liquid and vapour densities. The changes due to the thermophysical properties were predicted better for Sun-Mishima (2009) compared with Lazarek and Black (1982) due to the addition of the Weber number.

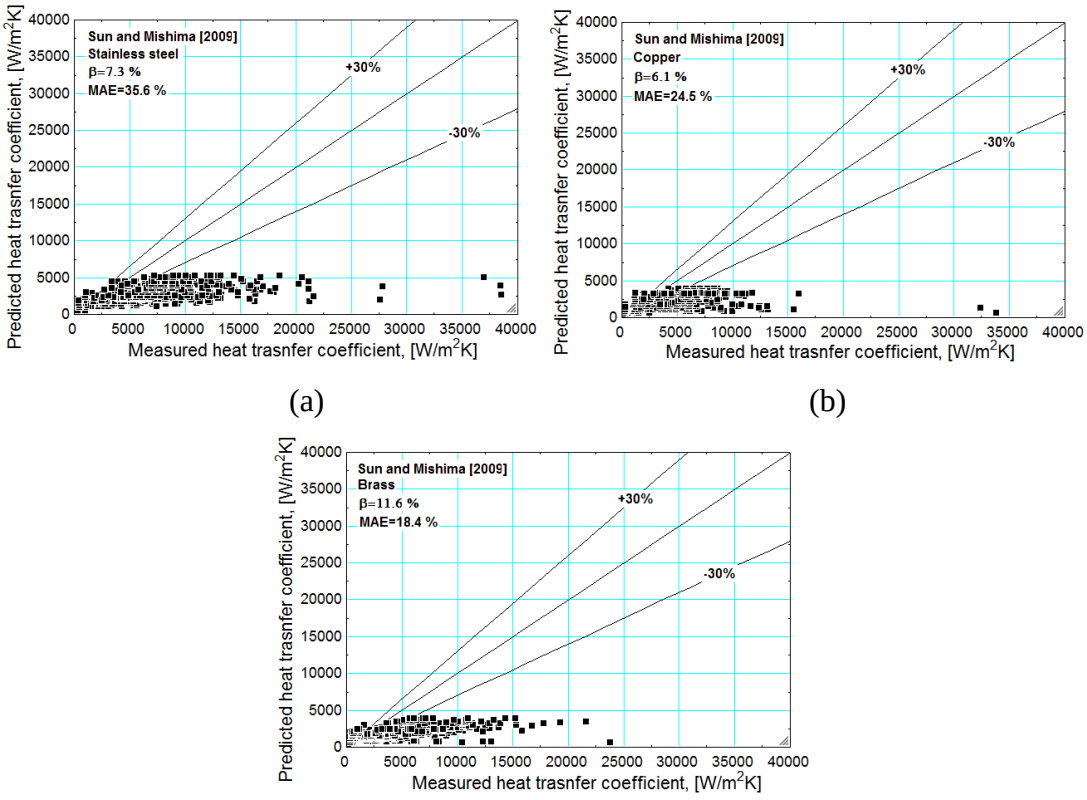

Figure 7.22. Comparison of the Sun and Mishima (2009) correlation with the experimental heat transfer coefficient for (a) stainless steel, (b) copper and (c) brass.

Li and Wu (2010)

Li and Wu (2010) collected a database of more than 3700 data points which covered a range of experimental conditions for both single and multi-channel configurations. This study found that previous correlations from literature could not accurately predict the whole databank, with the effects of small hydraulic diameters and liquid flow laminarization not being accounted for. The proposed correlation is based on the boiling number, Bond number and Reynolds number. The Bond number was used as a predictive method of defining micro and macro scale channels. The majority of the data points referred to the liquid laminar region of $Re_l < 2000$ and with Bond values less than 0.5. This was noted to be common in micro/mini scale channels and therefore required the use of the Bond number and liquids Reynolds number in the proposed correlation. The dimensionless parameters, Bond number and liquid Reynolds number, showed a strong relationship with the two phase Nusselt number and represented the importance of the ratio of surface tension and inertia forces. This was used in conjunction with the Boiling number, see equation 7.11.

$$h_{tp} = 334Bo^{0.3}(BdRe_l^{0.36})^{0.4}\frac{k_f}{D} \quad (7.11)$$

Figure 7.10 shows the Li and Wu (2010) correlation to decrease with vapour quality due to the liquid Reynolds number. This resulted in a poor agreement with all of the R245fa data. The R245fa measured heat transfer coefficient shows an increase with vapour quality, as well as peaks in the middle vapour region for stainless steel which results in the heat transfer coefficient being under predicted. At low vapour qualities and low heat fluxes, the heat transfer coefficient is over predicted, see figure 7.23. The data points are gathered within a narrow region which, although is outside of the acceptable range, does result in a low MAE value. Across the experimental range, the predicted heat transfer coefficient ranged from 2000-9000 W/m^{2}K. For vapour qualities up to 0.2, the heat transfer coefficient was predicted between 2000-6000 W/m^{2}K. This is in agreement with the experimental heat transfer coefficient, resulting in a low MAE but peaks in the heat transfer coefficient are seen in this vapour quality region, showing a low β value. The MAE values are considerably higher for copper and brass, 48.8 % and 54.8 %, respectively. These higher MAE values are due to the under prediction of the data at high vapour qualities, also resulting in lower β values.

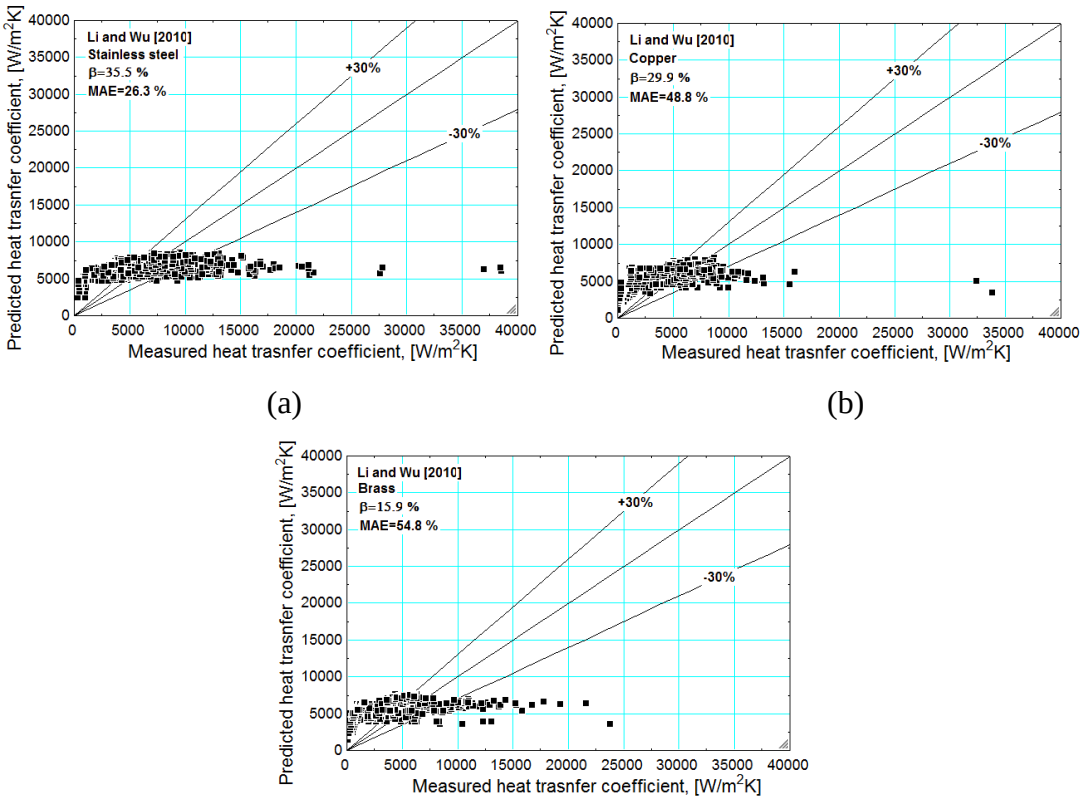

Figure 7.23. Comparison of the Li and Wu (2010) correlation with the experimental heat transfer coefficient for (a) stainless steel, (b) copper and (c) brass.

Mikielewicz (2010)

The Mikielewicz (2010) correlation is based on a theoretical study of the energy dissipation when boiling occurs. The energy dissipation is approximated from the viscous energy dissipation in the boundary later, assuming steady state conditions. The use of the two phase frictional multiplier is used to predict the convective flow, without nucleation, which is especially important for mini and micro channels. This correlation is appropriate for both macro and micro scale channels but it is suggested that the nucleate boiling term can be negated for micro channels due to the dominance of slug and annular flow. The most important factor was that of the two phase frictional multiplier, with accurate pressure drop measurements required for the correlation to be successful. The calculation of the two phase frictional multiplier is a function of the flow turbulence, with laminar flow including further thermophyscial properties in the calculation. The nucleate boiling component is calculated from the Cooper (1984) correlation. Equation 7.12 shows that a further parameter, P, is introduced which is calculated from the Reynolds number, Boiling number and the two phase frictional multiplier. The recommended two phase frictional multiplier is that of Muller-Steinhagen and Heck and the exponent, n, is 2 for turbulent flow and 0.9 for laminar flow.

$$\frac{h_{tp}}{h_l} = \sqrt{\phi_{MS}^n + \frac{1}{1+P}\left[\frac{h_{nb}}{h_l}\right]^2} \qquad (7.12)$$

As the channel is larger than 1 mm, at 1.1 mm, the nucleate boiling component was included in the calculation in the form of the Cooper (1984) correlation. Figure 7.24 shows the best agreement to be with stainless steel, with nearly half of the data, 41.7 %, being predicted within ± 30 %.The correlation shows a worse agreement with copper and brass which have lower β values and higher MAE values. The copper results, figure 7.24 b, shows the majority of data to be over predicted, especially at lower heat fluxes. This was also true for brass, figure 7.14 c, where only 25.5 % of the data was predicted in the acceptable range. The increase in heat transfer coefficient for all materials was not predicted with this correlation.

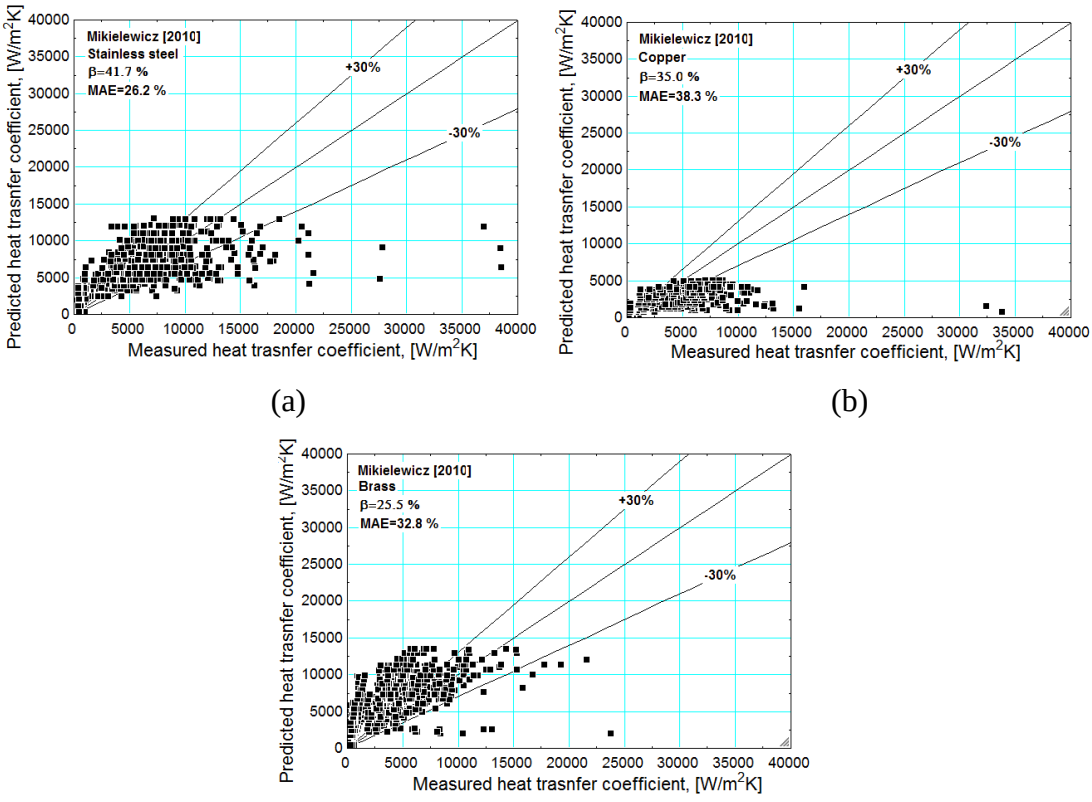

Figure 7.24. Comparison of the Mikielewicz (2010) correlation with the experimental heat transfer coefficient for (a) stainless steel, (b) copper and (c) brass.

Figure 7.25 presents the predicted heat transfer coefficients for all three materials at heat fluxes of 10 and 25 kW/m^2. This shows that the predicted heat transfer coefficient is almost linear with increasing vapour quality. The predicted heat transfer rates are very similar for stainless steel and copper, at both heat fluxes. This is seen to some extent with the experimental data at lower vapour qualities, although the effect of the heat flux is less. The large difference between the predicted heat tranfer rates due to the use of the Cooper (1984) correlations are not in agreement with the expeimental results and account for the lower accuracy of the brass predictions.

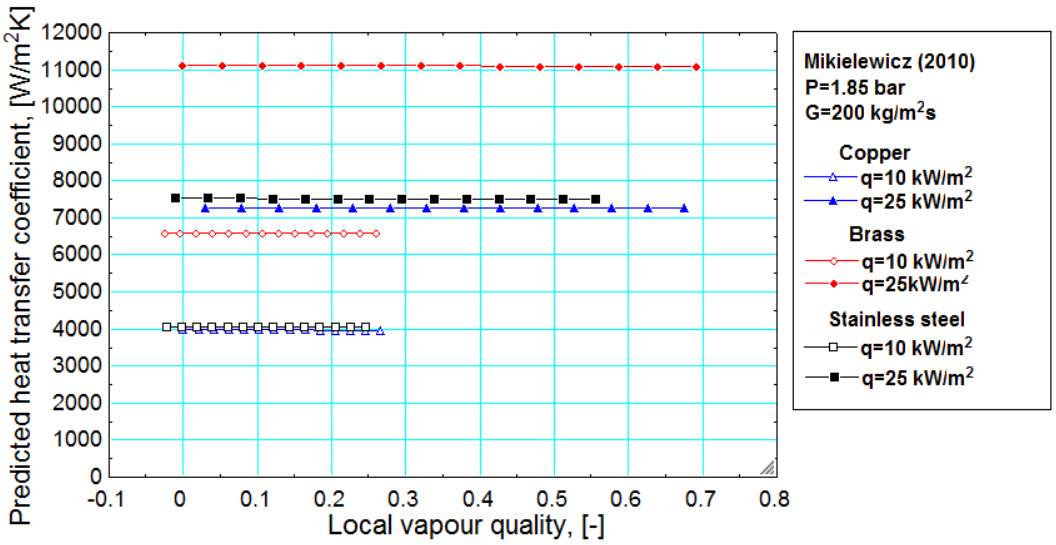

Figure 7.25. Predicted heat trasnfer coefficient for Mikielewicz (2010) for copper, brass and stainless steel.

Mahmoud and Karayiannis I (2012)

The Mahmoud and Karayiannis I (2012) is an empirical correlation which was developed based on data for R134a in channels with diameters ranging from 0.52 to 4.26 mm and over a range of inlet pressures, mass fluxes and heat fluxes, equating to 8561 data points. The correlation uses the boiling number to account for the heat and mass flux effects and the Weber number to account for the inertia and surface tension effects. The inertia and viscous forces were included with the use of the Reynolds number. The effect of channel diameter was accounted for from the confinement number. The correlation was formed based on a multi-parameter non-linear least square fitting to calculate the constants and function exponents. The Nusselt number was calculated as a function of the boiling number, liquid Weber number, liquid Reynolds number and confinement number. These functions are used in conjunction with the liquid thermal conductivity and channel diameter, see equation 7.13.

$$h_{tp} = 3414 \frac{Bo^{0.625} We_l^{0.2} Re_l^{0.1}}{Co^{0.6}} \frac{k_f}{D} \qquad (7.13)$$

This correlation is suitable for a mass flux range of 100-500 kg/m^{2}s and a pressure range of 6-14 bar. As the heat transfer coefficient in the 0.52 mm channel was found to be follow an alternative trend, a further correlation is recommended for vapour qualities higher than 0.3 with this channel diameter. This correlation showed one of the best agreements for all of the materials, but the values of β are relatively low at 42.2 % but with a low MAE value of 15.9 %. Figure 7.11 shows that the Mahmoud and

Karayiannis I (2012) correlation predicted a decreasing heat transfer coefficient with vapour quality which is not seen with R245fa. Data at vapour qualities less than approximately 0.7 is predicted well but the increase in the heat transfer coefficient at higher vapour qualities is not predicted. This is contrary to the brass results where higher vapour qualities show a better prediction than those at lower vapour qualities. The stainless steel results show a relatively constant heat transfer coefficient along the channel length before peaking, see figure 6.15. The brass results show an increasing trend in the heat transfer coefficient across the length of the tube where the values at lower vapour qualities are over predicted and data at high vapour qualities are under predicted. This is reflected in a low β value of 28.8 % and higher MAE of 32.1 %. The correlation gave slightly improved results for copper than stainless steel, with a β value of 46.4 %, see figure 7.26. There was no trend between the data which was predicted and the vapour quality or heat flux.

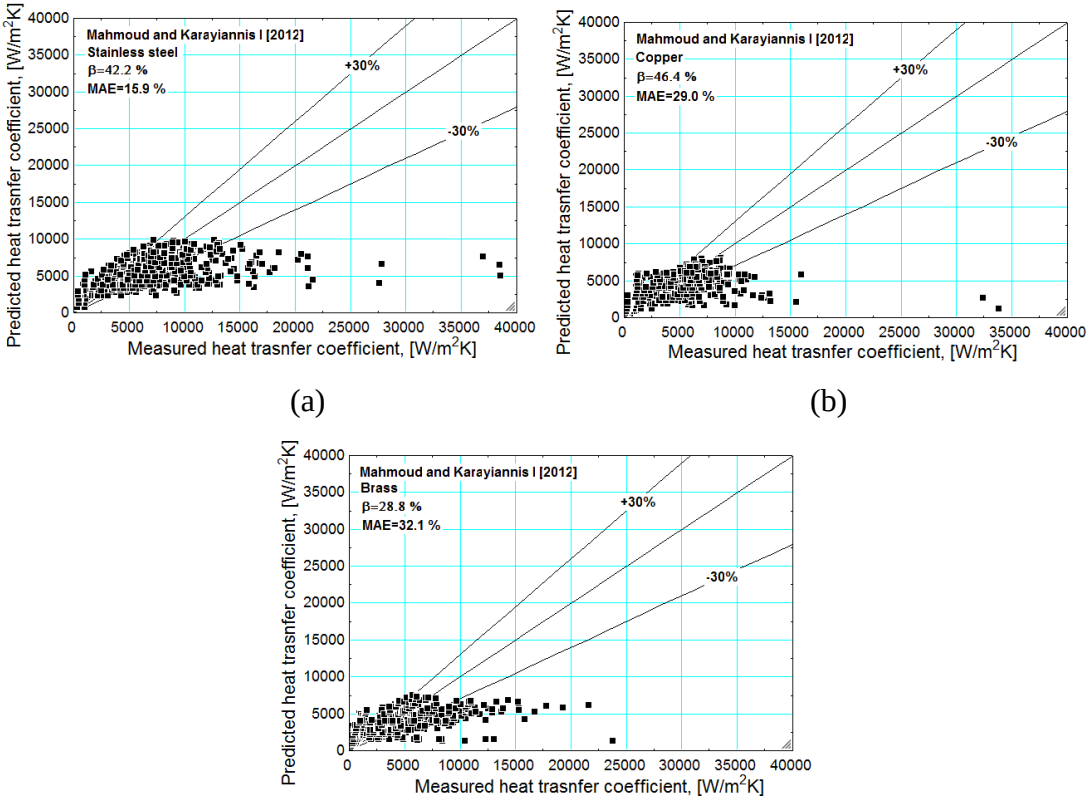

Figure 7.26. Comparison of the Mahmoud and Karayiannis I (2012) correlation with the experimental heat transfer coefficient for (a) stainless steel, (b) copper and (c) brass.

Mahmoud and Karayiannis II (2012)

The Mahmoud and Karayiannis II (2012) correlation is a superposition model, similar to that of Chen (1963). The same data bank of 8561 data points for R134a was used to develop this correlation. Contrary to the Chen (1963) model, the Cooper (1984) correlation is used to predict the nucleate heat transfer component, as opposed to the Foster and Zuber (1955) correlation. The single phase liquid heat transfer coefficient is calculated based on the Nusselt number, depending on the liquid Reynolds number, see equations 7.14 and 7.15. The suppression factor, S, and the enhancement factor, F, are adapted from the Chen (1963) correlation based on the experimental results. The enhancement factor equation is found from line fitting of the two phase fricitional multiplier data, resulting in an equation which is a function of the Lockhart-Martinelli parameter, X and a new function, A, see appendix A. This new function is based on the confinement number to a negative exponent. This equates to the value of the new function A, and hence the enhancement factor, decreasing with the channel diameter. The modified enhancement factor gives a larger value than the original Chen (1963) enhancement factor. The suppression factor is also evaluated based on line fitting of the experimental data in terms of the liquid Reynolds number and the enhancement factor. The original Chen (1963) suppression factor decreases steeply with the two phase Reynolds number. The modified suppression factor decreases with a smaller gradient, resulting in a larger value.

$$h_{tp} = S_{new} h_{cooper} + F_{new} h_l \tag{7.14}$$

$$h_l = \begin{cases} 4.36 \, \frac{k_f}{D} & Re_l < 2000 \\ 0.023 Re_l^{0.8} Pr_l^{0.4} \, \frac{k_f}{D} & Re_l > 3000 \end{cases} \tag{7.15}$$

For R245fa, this correlation shows lower heat transfer coefficient values than the previous Mahmoud and Karayiannis I (2012) correlation. For example, the stainless steel results showed a lower accuracy of β=32.2 % and MAE= 36.3 %. The increase in the heat transfer coefficient with vapour quality was not predicted and the magnitude generally under predicted, see figure 7.27. The data which was within the acceptable range was at lower heat fluxes, where the heat transfer coefficient values are lower. This was also seen for copper and brass, although copper also shows a large amount of data to be over predicted, see figure 7.27 b. It was expected that this correlation would perform better for copper than stainless steel and brass due to the more linear heat

transfer coefficient with vapour quality but this was only reflected in the lower MAE value.

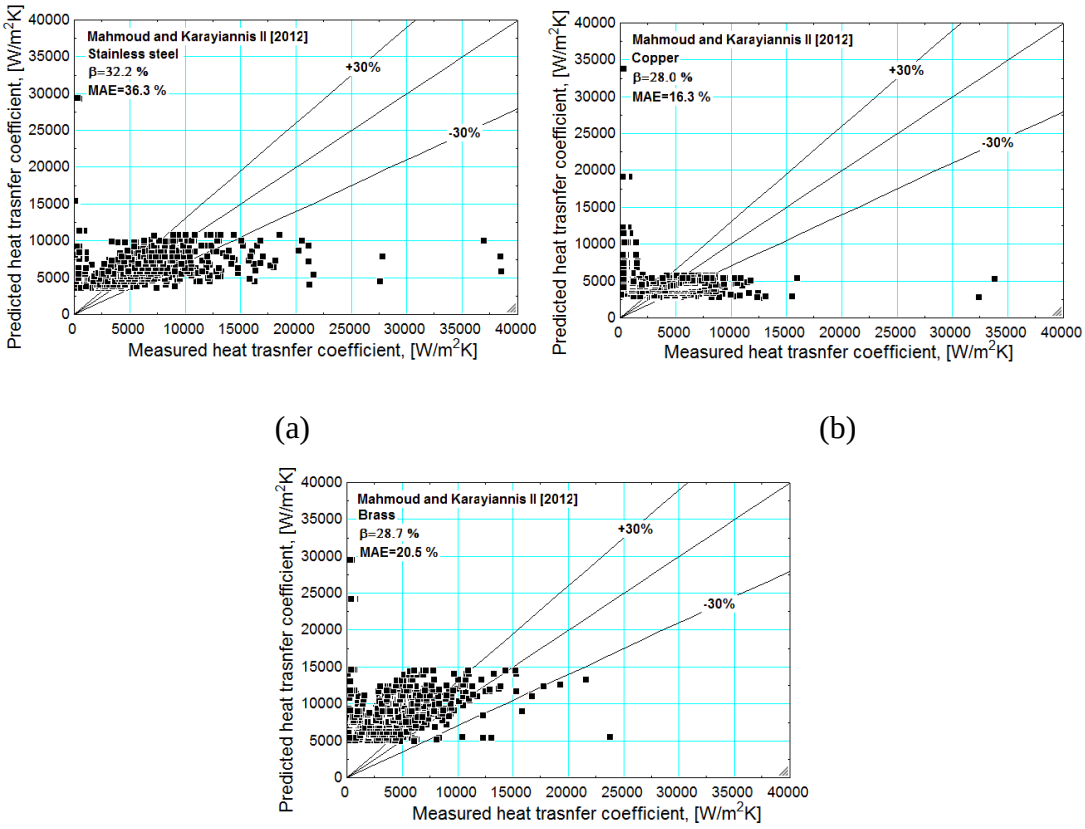

(a) (b)

(c)

Figure 7.27. Comparison of the Mahmoud and Karayiannis II (2012) correlation with the experimental heat transfer coefficient for (a) stainless steel, (b) copper and (c) brass.

As previously seen with the application of the Copper (1984) correlation for the prediction of the nucleate boiling, the higher the $Rp,_{old}$ value, the higher the predicted heat transfer coefficient. The effect of heat flux decreases with increasing $Rp,_{old}$ value which is not seen in the experimental results, with all materials having a low dependence on the heat flux, see figure 7.28. The predicted heat transfer coefficient is constant with increasing vapour quality. This correlation did not predict accurately the dependence of the heat transfer coefficient with vapour quality or heat flux.

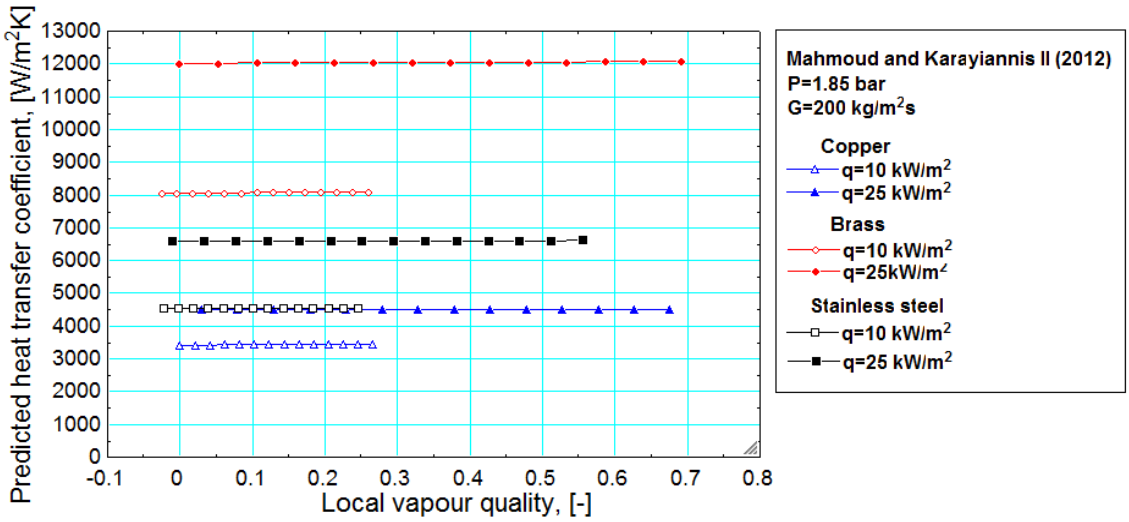

Figure 7.28. Predicted heat transfer coefficient for Mahmoud and Karayiannis II (2012) for copper, brass and stainless steel.

Li et al. (2013)

Li et al. (2013) conducted experiments with pure refrigerants, HFO1234yf and HFC32 and these refrigerants mixed as 80/20 and 50/50, by mass, in a smooth horizontal channel of 2 mm diameter. This study found that the 80/20 mixture heat transfer coefficient was over predicted and further adaptation to the correlation was required to account for the high temperature glide. This data was used to develop a correlation similar to the Chen (1963) correlation. The nucleate boiling correlation was predicted using the Cooper (1984) pool boiling correlation. The convective boiling component is calculated from the Dittus-Boelter correlation. Similar to other correlations, the enhancement factor, F, included the Weber number to account for the changes in surface tension with changing channel diameters. The suppression factor, S, uses the boiling number and two phase Reynolds number with exponents calculated from the experimental data.

Figure 7.11 shows the predicted heat transfer coefficient to increase with vapour quality. Although R245fa does show an increase with vapour quality, the magnitude predicted is considerably smaller than the measured heat transfer coefficient. The data which is predicted is at low vapour and low heat flux values where the measured heat transfer coefficient is at its lowest. Figure 7.29 shows a lower β values for the R245fa and higher MAE values. This is also seen with copper and brass, which have similar β values to stainless steel. Although the MAE values are very small for copper and also low for brass. The low vapour qualities for brass are predicted well with only the higher

vapour qualities being under predicted. The heat transfer coefficient for copper is lower and remains at lower values to the other materials which results in lower MAE values for this correlation.

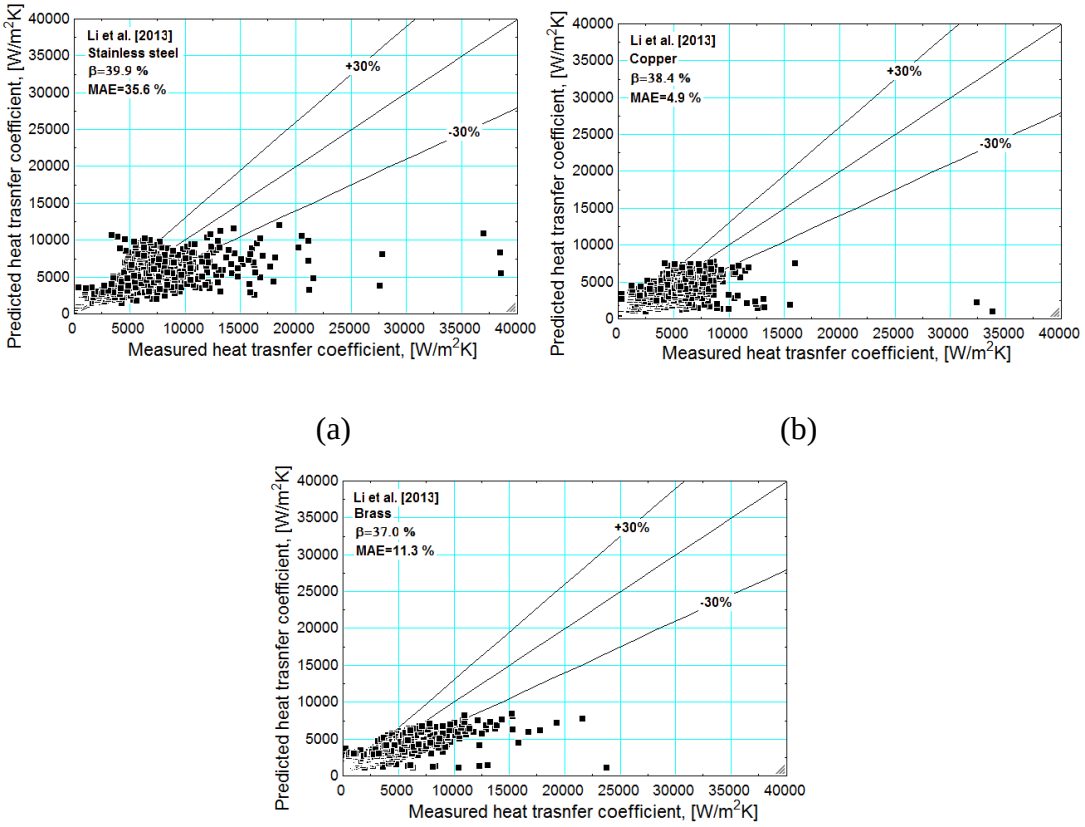

Figure 7.29. Comparison of the Li et al. (2013) correlation with the experimental heat transfer coefficient for (a) stainless steel, (b) copper and (c) brass.

Kim et al. (2013)

The Kim et al. (2013) correlation was produced from 10,805 data points from 31 sources and covering a range of 18 fluids and channel diameters from 0.19 – 6.5 mm inside diameter. The model produced is an asymptotic model which can be applied to both single and multi-channel configurations and circular and rectangular channels. The channel geometry is accounted for by using both the wetted perimeter and the heated perimeter in the calculation of the nucleate and convective boiling components. A study of other heat transfer correlations showed poor agreement at small channel diameters and high pressure ranges across the fluid base. This was accounted for with the reduced pressure component in the nucleate boiling equation. The Kim et al. (2013) correlation implements the Lockhart-Martinelli parameter into the convective boiling component.

Figure 7.30 shows the results to be largely under predicted for all R245fa experimental data. The main parameters include the Boiling number and the liquid only Reynolds number and Weber number. As the experimental conditions are the same, the same values were predicted for all of the materials. As this correlation was produced from a databank containing 18 fluids, the effect of fluid properties is expected to be more prevalent than the surface characteristics. Figure 7.30 shows that the predicted accuracy was similar for stainless steel, copper and brass. The database used to produce this correlation included a range of channel materials but no function of surface characteristics was included. Figure 7.11 shows the heat transfer coefficient to increase with vapour quality, which is agreement in trend with stainless steel and brass but not in magnitude. The predicted heat transfer coefficient is low, with the only data within the range of the experimental data being at higher vapour qualities. The vapour quality range at which this occurs increases with heat flux.

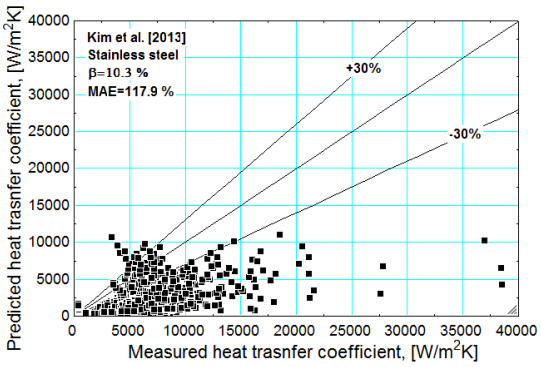

(a)

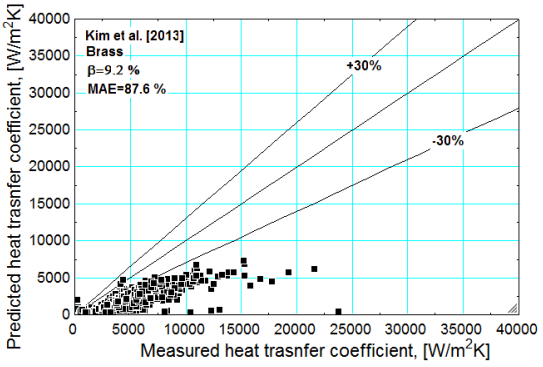

(b)

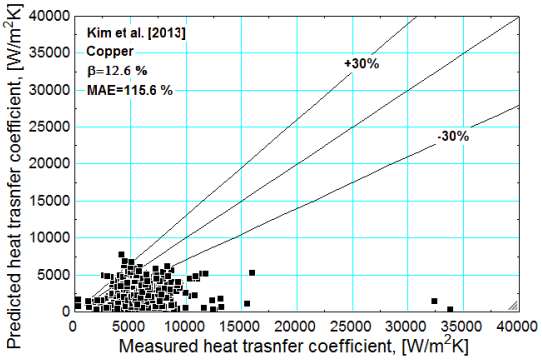

(c)

Figure 7.30. Comparison of the Kim et al. (2013) correlation with the experimental heat transfer coefficient for (a) stainless steel, (b) copper and (c) brass.

7.5 Three zone model

Thome et al. (2004) proposed a model which predicts the heat transfer coefficient at a fixed location on the channel based on the evaporation of an elongated bubble. The local time-averaged heat transfer coefficient is calculated from the sequential passage of a liquid slug, an evaporating elongated bubble and a vapour slug. The elongated bubble is modelled as a confined bubble with a thin liquid film between the bubble and the wall. This model illustrates the cyclic nature of the flow which will affect the heat transfer coefficient, with focus on the liquid film thickness and potential local dryout. The vapour slug occurs if the liquid film does dryout before the next liquid slug. The advantage of this model is that consideration for transient evaporation of the liquid film. This model assumes that a dominant factor in the local heat transfer coefficient is the bubble frequency and the liquid film thickness, with no nucleate boiling component. The model is time averaged at a specific location, (z), based on the residence time for the liquid slug, liquid film and dryout, see equation 7.16.

$$h(z) = \frac{t_{liquid}}{\tau} h_{liquid}(z) + \frac{t_{film}}{\tau} h_{film}(z) + \frac{t_{dry}}{\tau} h_{vapour}(z) \quad (7.16)$$

where τ refers to the pair period and,

$$\tau = \frac{1}{f_b} \quad (7.17)$$

$$f_b = \left(\frac{q}{q_{ref}}\right)^{1.74} \quad (7.18)$$

$$q_{ref} = 3328 \left(\frac{P_{sat}}{P_{crit}}\right)^{-0.5} \quad (7.19)$$

$$t_{liquid} = \frac{\tau}{1+\frac{\rho_f \ x}{\rho_g 1-x}} \quad (7.20)$$

$$t_{vapour} = \frac{\tau}{1+\frac{\rho_g 1-x}{\rho_f \ x}} \quad (7.21)$$

$$t_{dry\ film}(z) = \frac{\rho_f h_{fg}}{q} [\delta_0(z) - \delta_{min}] \quad (7.22)$$

The time periods applied to the model depend largely on the liquid film thickness (δ), where δ_{min} is set to 300 nm, as suggested by Dupont et al. (2004). The maximum duration at which the film can exists before the occurrence of dryout, at the

minimum film thickness, is calculated by $t_{dry\ film}$. If $t_{dry\ film} > t_{vapour}$, then dryout does not occur and therefore $\delta_0(z) = \delta_{end}$, hence $t_{film=}t_{vapour}$. If $t_{dry\ film} < t_{vapour}$, dryout occurs and therefore $\delta(z,t) = \delta_{end}$ and $t_{film=}t_{dry\ film}$.

The different film thicknesses can be calculated from;

$$\delta(z,t) = \delta_0(z) - \frac{q}{\rho_f h_{fg}} t \tag{7.23}$$

$$\frac{\delta_0(z)}{D} = C_{\delta_0}\left(3\sqrt{\frac{\upsilon_f}{U_p D}}\right)^{0.84}((0.07Bo^{0.41})^{-8} + 0.1^{-8})^{-1/8} \tag{7.24}$$

Where,

$$U_p = G_{tot}\left[\frac{x}{\rho_g} + \frac{1-x}{\rho_f}\right] \tag{7.25}$$

C_{δ_0} refers to the correction factor which was found to be 0.29 by Thome et al. (2004). The heat transfer coefficients for the liquid and vapour slugs are calculated from the local Nusselt numbers. The Nusselt numbers are calculated from the equivalent liquid and vapour slug lengths. The Shah and London (1978) correlations is used for Re< 2300 and Gnielinski (1976) for the transition and turbulent flow. An asymptotic method proposed by Churchill and Usagi (1975) is used to obtain the mean heat transfer coefficient as a function of the Reynolds number. The heat transfer coefficient for the film is calculated from equation 7.26.

$$h_{film} = \frac{k_f}{\delta_0 - \delta_{end}} \ln\left(\frac{\delta_0}{\delta_{end}}\right) \tag{7.26}$$

This model does not use a function of the surface characteristic and therefore the same heat transfer is predicted for the three materials. Figure 7.31 presents the predicted heat transfer coefficient at heat fluxes of 10, 17 and 25 kW/m^2 at a mass flux of 200 kg/m^{2}s and an inlet pressure of 1.85 bar. The predicted heat transfer rates increase with heat flux and show a decreasing trend with increasing vapour quality.

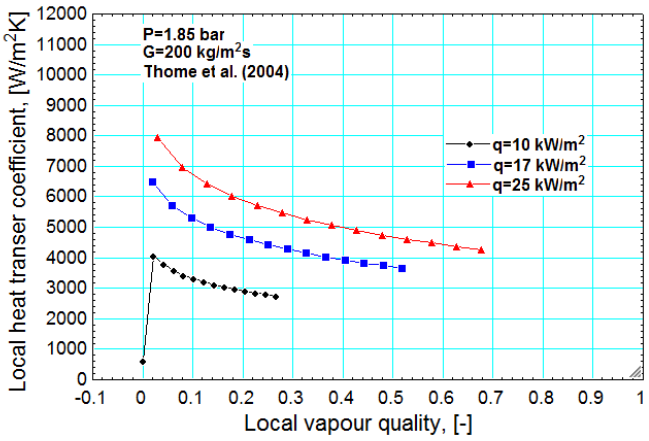

Figure 7.31. Predicted heat transfer coefficient for Thome et al. (2004) at heat fluxes of 10, 17 and 25 kW/m^2.

The trend seen for the predicted heat transfer coefficient does not match the experimental results where the heat transfer increases with vapour quality. This increase is thought to be due to the thinning of the liquid film during the dominance of the annular flow. As discussed in Chapter 5, only a limited amount of slug flow was evident in the channels. This may account for the low amount of data predicted within ±30%. Figure 7.32 shows the comparison of the predicted and experimental heat transfer data. The MAE values are also low, with the data having only a small scatter at higher heat fluxes. The data is mostly under predicted but only by a small magnitude. A slightly larger scatter is seen for the brass, figure 7.32 c, due to the large peaks at the end of the channel at higher heat fluxes. The MAE values expected to be low due to the trend seen in figure 7.31, where the predicted data does not follow the same trend but is in the same heat transfer magnitude range.

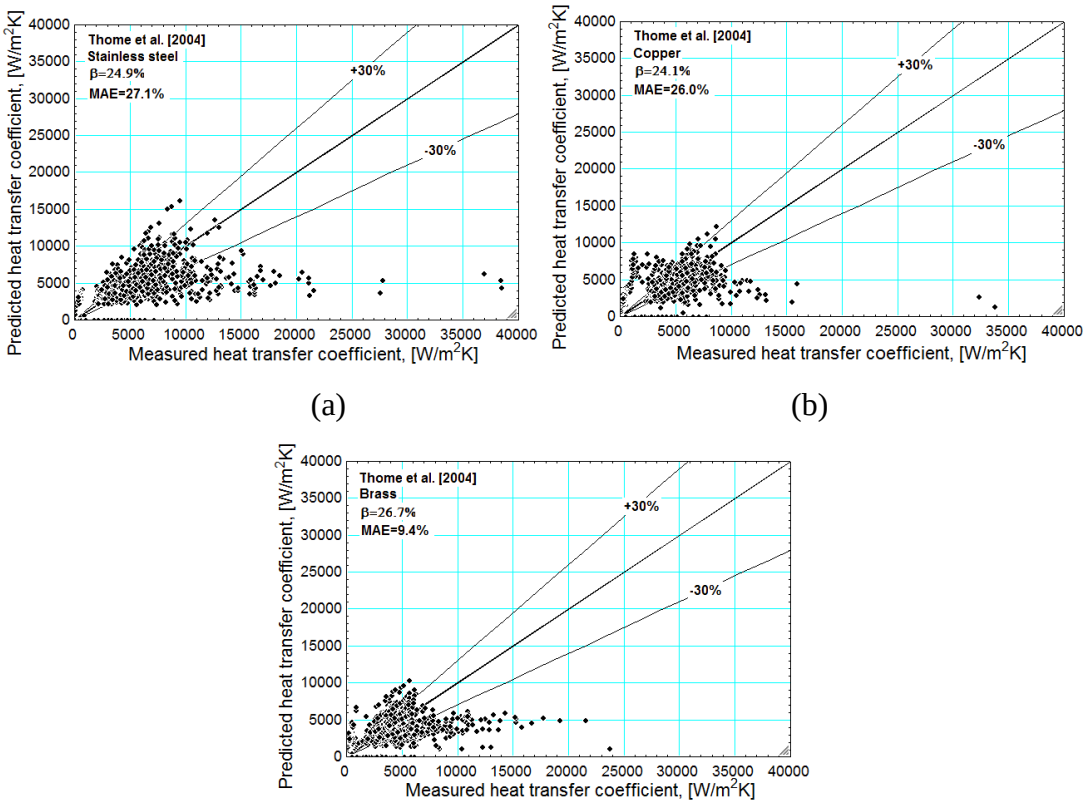

Figure 7.32. Comparison of the Thome et al. (2004) correlation with the experimental heat transfer coefficient for (a) stainless steel, (b) copper and (c) brass.

7.6 Costa-Party et al. (2012)

As discussed in 7.4, the Thome model is limited in the annular flow regime predictions. Costa-Party et al. (2012) proposed a model which was flow pattern dependent, with a modified Thome model being used for the intermittent flow patterns and a modified Cioncolini and Thome (2011) model for the annular flow regime. The transition between these models is based on the vapour quality calculated from;

$$x_{transition} = 425\left(\frac{\rho_g}{\rho_f}\right)^{0.1} \frac{Bo^{1.1}}{Co^{0.5}} \tag{7.27}$$

The Thome et al. (2004) model is modified in terms of the Nusselt number equations used. For laminar flow, the Nusselt number is 4.36 and the equation used for the turbulent Nusselt number is modified to use the frictional pressure drop coefficient instead of the drag coefficient. The transitional Reynolds number was also reduced to 1500. The film heat transfer coefficient also adapted to add a nanometer to the denominator, see equation 7.28.

$$h_{film} = \frac{k_f}{\delta_0 - \delta_{end} + 1x10^{-9}} \ln\left(\frac{\delta_0}{\delta_{end}}\right) \quad (7.28)$$

The Cioncolini and Thome (2011) model used for the annular flow is based on the adiabatic and evaporating annular flow, particularly that of the heat transfer in the annular liquid film. The annular heat transfer coefficient is predicted from the liquid Prandtl number, liquid thermal conductivity, average film thickness and dimensionless film thickness, see equation 7.29. The dimensionless film thickness is calculated from the mass flux, fluid viscosity, channel diameter, vapour quality and entrained liquid fraction. The entrained liquid fraction is calculated from the core flow Weber number. The core flow parameters, including the density and velocity which are used in calculating the wall shear stress are calculated from known fluid properties and the vapour quality. The average film thickness is calculated from the dimensionless film thickness and the radial co-ordinates.

$$h_{annular} = \frac{k_f}{\delta_{avg}}(0.0776\delta^{+^{0.9}} Pr_f^{0.52}) \quad (7.29)$$

The transition zone between the two models is based on the vapour quality range from equation 7.30. Based on this, the heat transfer coefficient entering the transition region should be equal to Thome et al. (2004) and exiting at an equal value as the Coincolini and Thome (2011) model. The heat transfer coefficient for this transition region is calculated from equation 7.31.

$$x_{trans} \pm \frac{x_{exit}}{5} \quad (7.30)$$

$$h_{trans} = (1 - r)h_{Thome} + \frac{rh_{annular}}{(1-r)h_{Thome} + rh_{annular}}(rh_{annular} - (1 - r)h_{Thome}) \quad (7.31)$$

where,

$$r = \frac{x - x_{trans}}{0.4\, x_{exit}} + 0.5 \quad (7.32)$$

Figure 7.33 shows the predicted heat transfer coefficient at heat fluxes of 10, 17 and 25 kW/m^2 at a mass flux of 200 kg/m^{2}s and an inlet pressure of 1.85 bar. The predicted values are lower than those of the Thome et al. (2004) model, see figure 7.31. The heat transfer coefficient increases with heat flux but the increase is smaller than the

Thome et al. (2004) model. The decrease with vapour quality has a shallower gradient than that of the Thome et al. (2004) model.

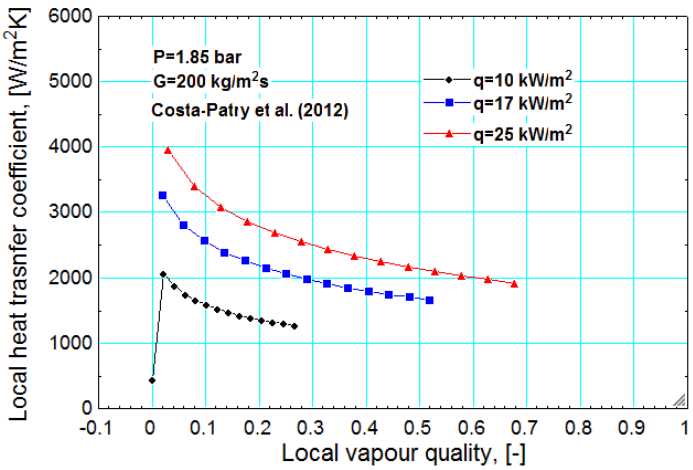

Figure 7.33. Predicted heat transfer coefficient for Costa-Patry et al. (2012) at heat fluxes of 10, 17 and 25 kW/m^2.

In comparison to the Thome et al. (2004) model, the β values are higher but the MAE values are higher as the data is under predicted and has a greater scatter, see figure 7.34. R245fa shows a dominance of annular flow but the Coincolini and Thome (2011) predicts a decreasing heat transfer coefficient during this regime which is contradictory to the experimental results.

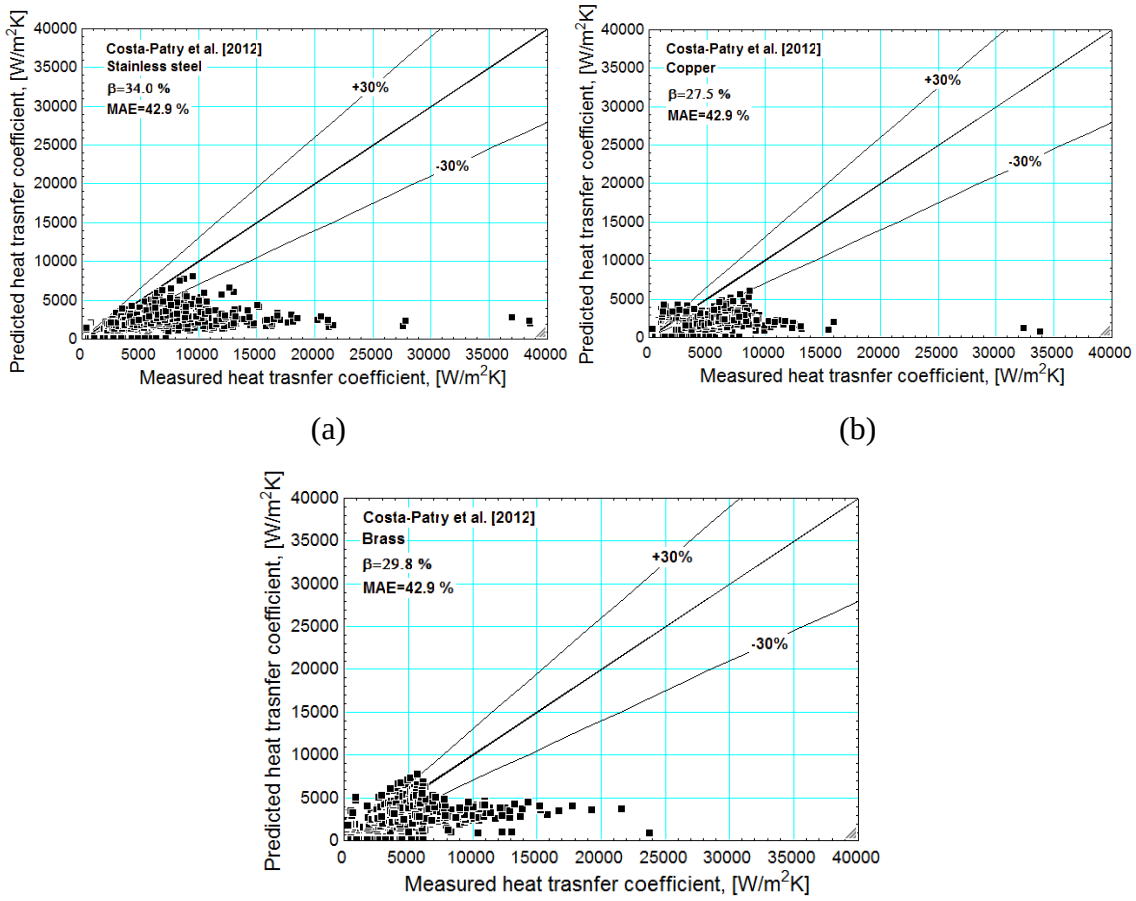

Figure 7.34. Comparison of the Costa-Patry et al. (2012) correlation with the experimental heat transfer coefficient for (a) stainless steel, (b) copper and (c) brass.

7.7 Summary

Flow boiling heat transfer correlations from literature were evaluated based on the experimental data of R245fa in three channels, of stainless steel, brass and copper. Note, that this comparison was based on the original stainless steel channel orientation only. This evaluation was based on the percentage of data predicted within ± 30%, β, and the mean absolute error, MAE. The experimental heat transfer coefficient changed in trend and magnitude between the three materials, see Chapter 6. As a result of this, there are differences seen in the accuracy of the heat transfer correlations between the materials, see table 7.4.

Correlations in literature can use many equation forms, but for this study, the most important factor is whether a function of the surface is included. Those correlations which do not include a function of the surface parameter predicted the same heat transfer coefficient for all three materials, which is not seen in the experimental data. Any variations in the predicted heat transfer coefficients, for those correlations

which do not include a surface parameter, are due to variations in the vapour quality, see Chapter 5. The surface parameter, $Rp_{,old}$, is included in the Cooper (1984) correlation, which can be used to predict the nucleate boiling component in flow boiling. Heat transfer correlations which used the Cooper (1984) correlation to predict the nucleate heat transfer component showed varying degrees of dependence on Rp,old. The structure of the correlations played a large part in the effect of the surface parameter. For example, Liu and Winterton (1991) produced an asymptotic correlation where a smaller $Rp_{,old\ value}$ would equate to a larger nucleate boiling component but a smaller overall heat transfer coefficient. However, Bertsch et al. (2009) used a superposition model which meant that the smaller the Rp,old value, the smaller the nucleate boiling component and overall predicted heat transfer. The Rp,old value would relate to the nucleate boiling regime, but the experimental results show no agreement in the trend of the Rp,old value and the heat transfer magnitude in this region. The difference in the materials is due to changes in the nucleate boiling regime but annular flow dominants for all materials. The three zone model proposed by Thome et al. (2004) performed poorly for all three materials which is expected due to the dominance of annular flow. The Costa-Patry (2012) correlation did account for this with the use of an annular flow component. The results showed slight improvement from the Thome et al. (2004) model but the agreement is poor. As seen, due to the difference in the flow patterns, see Chapter 5, the vapour quality is a function of the heat transfer coefficient for all of the materials. For all of the R245fa experimental data, the heat transfer coefficient increased with vapour quality to some degree, but many correlations show either a decreasing heat transfer coefficient with vapour quality (Lee and Mudawar (2005), Saitoh et al. (2007), Li and Wu (2010)) or no effect of vapour quality (Tran et al. (1996), Lazarek and Black (1982), Sun-Mishma (2009)). This difference in the experimental and predicted heat transfer coefficient is a result of discrepancies in reported data in literature and the correlations being based on a limited experimental range.

Considering all of the materials, the three best correlations are Liu and Winterton (1991), Mahmoud and Karayiannis I (2012) and Li et al. (2013). Although the Liu and Winterton (1991) correlation is poor for copper, but shows good agreement with stainless steel and brass. The worst performing correlation for all materials were Warrier et al. (2002), Gungor and Winterton (1986) and Tran et al. (1996). A further correlation investigated was that of Fang et al. (2013). This correlation focused on R134a, with the prediction based on 2286 data points from 19 sources. This correlation

was deemed to be unsuitable due to the fluid temperature being greater than the wall temperature for a large percentage of the data. The heat transfer coefficient is calculated from the Nusselt number, see equation 7.33, which utilises the liquid viscosity at the fluid temperature ($\mu_{l,f}$) and the inside wall temperature ($\mu_{l,w}$).

$$Nu = \frac{0.00061(S+F)Re_l Pr_l^{0.4} Fa^{0.11}}{\ln\left(\frac{1.023\mu_{l,f}}{\mu_{l,w}}\right)} \quad (7.33)$$

When the fluid temperature is higher than the wall temperature, the ln function equates to a negative value and the predicted heat transfer coefficient is also negative. Therefore, this correlation was excluded from the correlation evaluation.

To fully evaluate the heat transfer correlations, further data from literature should be considered. Therefore, the correlation results from the R134a data for Shiferaw (2008) and Mahmoud (2011) are also included in the evaluation. The heat transfer coefficient varies in both trend and magnitude between the two refrigerants, see Chapter 6, which results in a difference in the accuracy of the heat transfer correlations. There is agreement on the Tran et al. (1996) and Warrier et al. (2002) correlations being unsuitable. The Mahmoud and Karayiannis I (2012) correlation is also seen to perform well for both refrigerants. Annular flow was the dominate flow pattern for R245fa, which suggests convective boiling dominates but no improvement was seen from convective boiling correlations. The differences seen between the different materials suggests that nucleate boiling does have an effect, suggesting future correlations should include both convective and nucleate boiling components.

There are many correlations available in literature, with no clear recommendation on which is the most suitable for heat exchanger design. There was no clear trend on which correlation type was most suitable for R245fa, with no improvement in microscale correlations over macroscale correlations or those correlations which included a function of surface characteristics. There was only one correlation which performed well for both R245fa and R134a, Mahmoud and Karayiannis I (2012), although this correlation did perform better for R134a. There was no correlation which performed exceedingly well for R245fa, with the highest β across all materials being 46.4 %, which was Mahmoud and Karayiannis I (2012). There is some agreement on which correlations should be negated from future research, those of Tran et al. (1996) and Warrier et al. (2002). Further research is required to develop correlations which are suitable for both a change in working fluid and heater surface.

Table 7.4. The β and MAE values for all of the correlations evaluated.

Correlation	Stainless Steel		Copper		Brass	
	β, %	MAE, %	β, %	MAE, %	β, %	MAE, %
Cooper (1984)	41.2	2.3	17.9	14.5	10.4	29.8
Chen (1963)	18.9	41.3	19.3	34.3	22.8	19.1
Gungor and Winterton (1986)	8.3	29.1	7.4	30.4	5.2	32.3
Gungor and Winterton (1987)	38.8	8.2	36.8	9.7	37.4	14.3
Liu and Winterton (1991)	42.8	9.6	9.9	29.6	38.1	5.6
Lazarek and Black (1982)	12.7	87.8	10.9	62.5	16.8	54.4
Tran et al. (1996)	10.2	154.5	12.7	106.0	16.5	87.2
Kew and Cornwell (1997)	16.5	89.9	12.4	58.4	16.6	70.1
Warrier et al. (2002)	1.3	263.4	4.0	165.5	1.8	130.5
Thome et al. (2004)	24.9	27.1	24.1	26.0	26.7	9.4
Zhang et al. (2004)	22.7	17.1	21.1	17.4	23.1	6.0
Modified Zhang et al. (2004)	16.3	21.8	17.4	20.8	13.8	24.7
Lee and Mudawar (2005)	15.5	147.5	15.5	48.9	11.9	60.6
Saitoh et al. (2007)	8.5	28.6	6.9	32.1	8.4	33.7
Bertsch et al. (2009)	33.3	13.9	33.3	18.5	21.8	21.9
Sun-Mishima (2009)	7.3	35.6	6.1	24.5	11.6	18.4

Li and Wu (2010)	35.5	26.3	29.9	48.8	15.9	54.8
Mikielewicz (2010)	41.7	26.2	35.0	38.3	25.5	32.8
Costa-Party (2012)	34.0	42.9	27.5	42.9	29.8	42.9
Mahmoud and Karayiannis I (2012)	42.2	15.9	46.4	29.0	28.8	32.1
Mahmoud and Karayiannis II (2012)	32.2	36.3	28.0	16.3	28.7	20.5
Li et al. (2013)	39.9	35.6	38.4	4.9	37.0	11.3
Kim et al. (2013)	10.3	117.9	12.6	115.6	9.2	87.6

Chapter 8

8. Pressure drop results and correlations

8.1 Introduction

The ability to accurately predict the two phase pressure drop is a vital factor in the application of microchannels. The magnitude of the pressure drop determines the pumping power and consequent energy consumption, which is used when evaluating the system performance. The measured pressure drop presented in this chapter refers to the flow boiling pressure drop across the heated section. The analysis of the measured pressure drop is conducted in two parts; the effect of the refrigerant and the effect of the surface characteristics. These experimental results are compared with pressure drop correlations from literature, for both macro and micro scale sizes. The total measured pressure drop is the sum of the frictional, gravitational and acceleration components, which can be individually calculated from pressure drop correlations. There are no restrictions at the inlet or outlet of the test section, therefore no allowances were needed for entry or exit pressure changes. The single phase pressure drop resulting from the flow being subcooled is subtracted from the measured pressure drop.

8.2 Measured pressure drop-Effect of fluid properties

The effect of fluid properties is investigated at two saturation temperatures and a range of heat and mass fluxes. The pressure drop readings are only recorded when the inlet pressure is deemed to be stable, as discussed in Chapter 6.2. Chapter 6 shows the increase in inlet pressure oscillations with increasing heat flux for R245fa, which shows oscillations of~0.05 bar at the higher heat fluxes. Similar magnitudes of inlet pressure oscillations were seen for R134a. Figure 8.1 presents the total measured pressure drop for both R134a and R245fa at a mass flux of 300 kg/m^{2}s at inlet saturation temperatures of 31 and 39 ˚C. As previously discussed in Chapter 2, R245fa is a low pressure refrigerant and so the comparison is based on the inlet saturation temperatures of 31 and 39 ˚C which equates to pressures of 8 and 10 bar and 1.85 and 2.45 bar for R134a and

R245fa respectively. This shows there are both similarities and differences between the pressure drop for both refrigerants. The measured pressure drop increases with heat flux for both refrigerants, although the gradient of increase for the heat flux range of this figure is different. The increase in the pressure drop with heat flux is attributed to the change in the flow patterns and void fraction. A change in the measured pressured pressure drop is predicted with mass flux. The mass flux term in the acceleration and frictional components is squared, showing a quadratic increase with an increase in mass flux. A further similarity is in the effect of inlet saturation temperature, with a difference only seen at higher heat fluxes. The increase in inlet pressure results in a lower measured pressure drop, this is due to the changes in thermophysical properties with temperature. As the inlet pressure increased from 1.85 to 2.45 bar, the liquid to vapour viscosity ratio decreased by 12 %. This in turn reduces the frictional, gravitational and acceleration components of the pressure drop. The vapour density increase by up to 30% with the decrease in inlet pressure with a resulting effect of up to 25% decrease in the frictional component. The magnitude of the pressure drop is vastly different, with that of R245fa being up to 300% higher than R134a. This difference in the magnitude of the two phase pressure drop is due to difference in thermophysical properties of the two refrigerants, see figure 8.2. The liquid viscosity is 110% higher for R245fa at the lower inlet pressure and the vapour density is 75% lower. The magnitude of this pressure drop difference is expected for to the large differences seen in the properties which, as previously discussed, relate to the acceleration and frictional pressure drop. The equations which are widely used to predict the frictional, acceleration and gravitational components, based on the Lockhart-Martinelli (1949) correlation, are presented below.

$$\Delta P_f = \int_0^{x_e} \frac{2 f_l G^2}{D \rho_f} \phi_f^2 \, dx \tag{8.1}$$

$$\phi_f^2 = 1 + \frac{C}{X} + \frac{1}{X^2} \tag{8.2}$$

$$X = \left(\frac{1-x}{x}\right)\left(\frac{\rho_g}{\rho_f}\right)^{0.5}\left(\frac{f_f}{f_g}\right)^{0.5} \tag{8.3}$$

$$\Delta P_g = g \int_0^{x_e} \left[\alpha \rho_g + (1-\alpha)\rho_f\right] dx \tag{8.4}$$

$$\Delta P_{acc} = \frac{G^2}{\rho_f}\left[\frac{x_e^2}{\alpha_e}\frac{\rho_f}{\rho_g} + \frac{(1-x_e)^2}{(1-\alpha_e)} - 1\right] \tag{8.5}$$

$$\alpha = \frac{1}{1+0.28X_m} \tag{8.6}$$

$$X_m = \left(\frac{1-x}{x}\right)^{0.64} \left(\frac{\rho_g}{\rho_f}\right)^{0.36} \left(\frac{\mu_f}{\mu_g}\right)^{0.07} \quad (8.7)$$

These equations show that the differences seen in the liquid viscosity and vapour density between R134a and R245fa will change the pressure drop. For example, the X_m value is up to 50 % higher for R134a which equates to a smaller α value and reduced gravitational and acceleration pressure drop values for R134a. The vapour density, which is larger for R134a, results in a X value which is over 25% higher. This results in a two phase frictional multiplier, ϕ_f^2, which is 50 % higher for R245fa. Although the experimental data shows a far larger percentage difference in the pressure drop between R245fa and R134a, the influence of the fluid properties can clearly been seen.

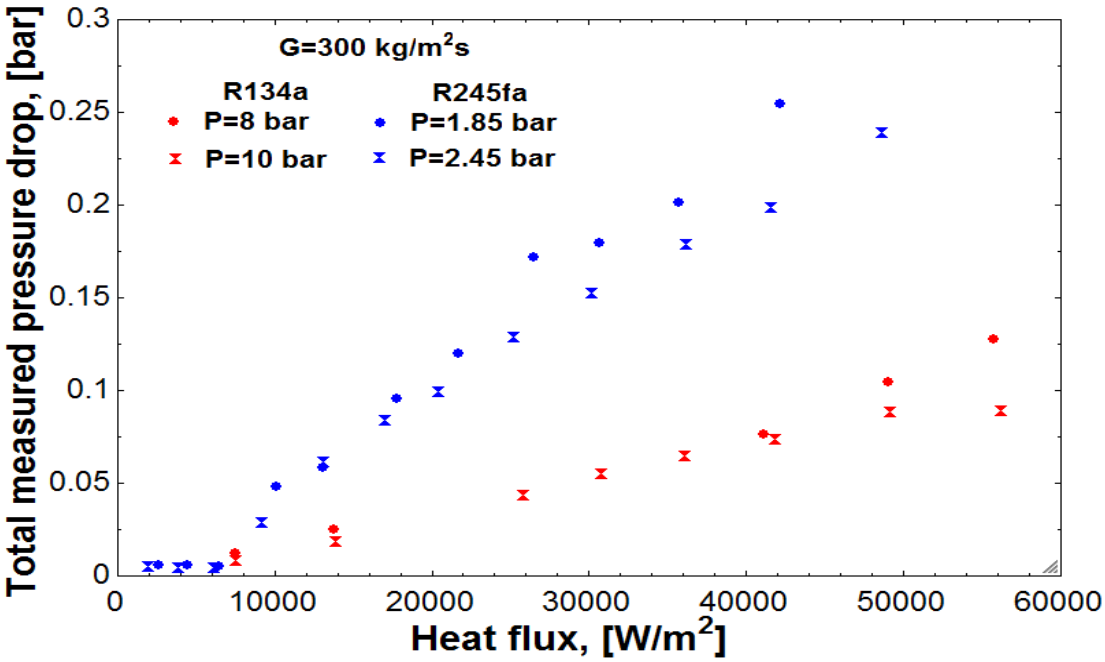

Figure 8.1.Tthe measured pressure drop of R245fa and R134a in a stainless steel tube at a mass flux of 300 kg/m^{2}s.

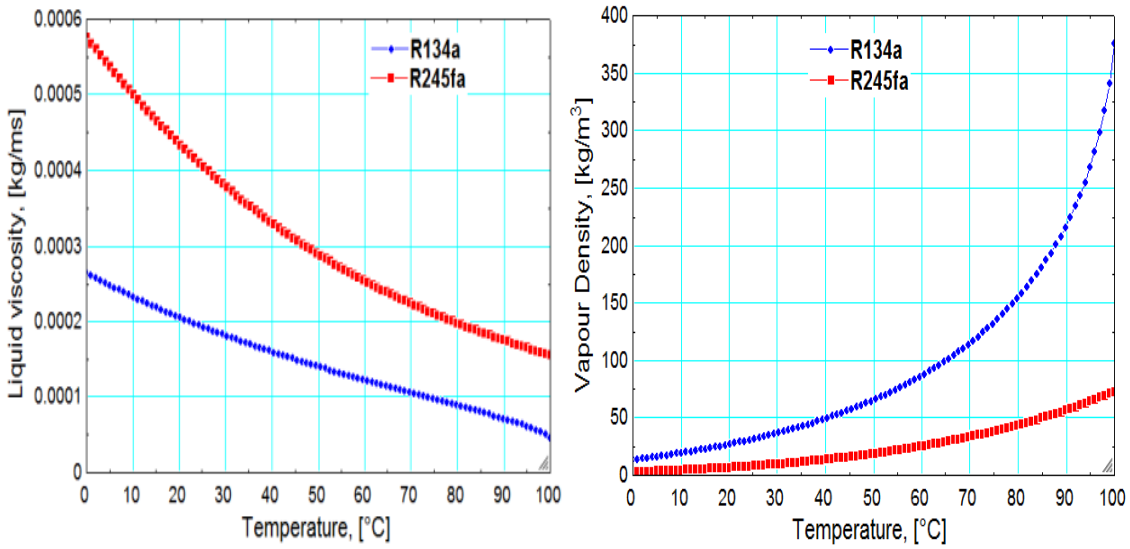

Figure 8.2. The change in liquid viscosity and vapour density for R134a and R245fa.

Figure 8.3 shows the measured pressure drop increases with mass flux for both refrigerants. The heat fluxes achievable were higher for R134a as the experiments were stopped due to instabilities for R245fa. The magnitude of the increase in the pressure drop with mass flux is similar for both refrigerants. This increase with mass flux is expected, where the frictional and acceleration components are a function of G^2.

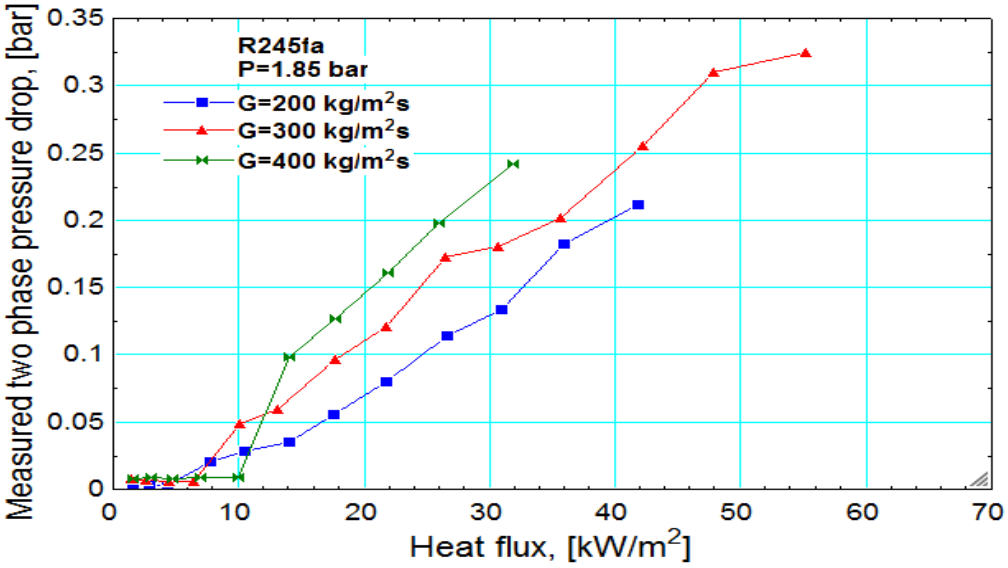

(a)

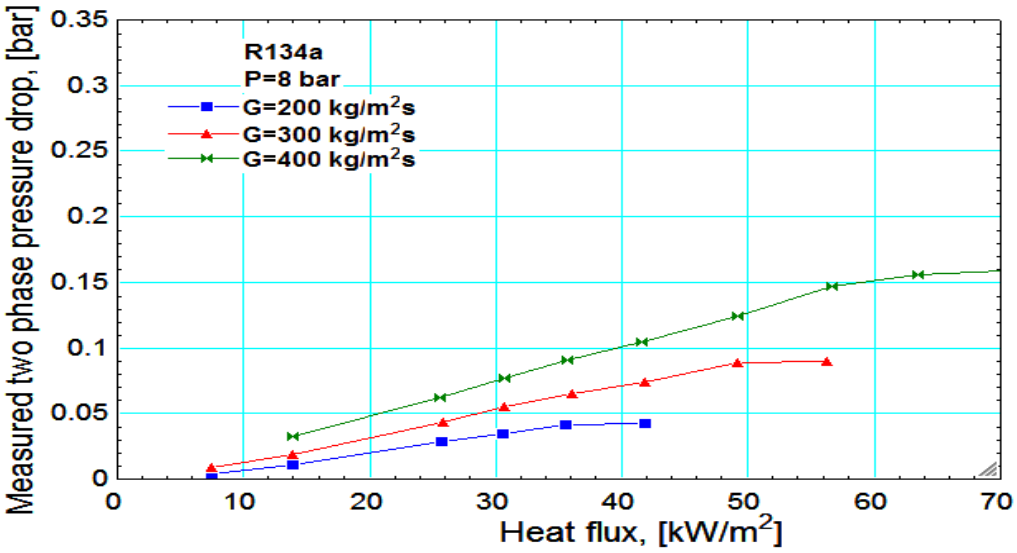

(b)

Figure 8.3. The effect of mass flux on pressure drop for (a) R245fa and (b) R134a.

The difference in the measured pressure drop is due to the properties of the refrigerant as all other parameters were kept constant. As pressure drop correlations are based on the properties of the refrigerant, these changes should be reflected in the pressure drop correlations. Figure 8.4 presents frictional pressure drop as predicted by the homogenous model. The two phase frictional multiplier is based on the liquid and vapour viscosities and specific volumes, see equation 8.8. The refrigerant properties are vastly different between R245fa and R134a, resulting in a two phase frictional multiplier for R245fa, which is over three times that of R134a.

$$\phi_L^2 = \left[1 + x\left({}^{\upsilon_{fg}}/_{\upsilon_f}\right)\right]\left[1 + x\left({}^{\mu_{fg}}/_{\mu_g}\right)\right]^{-1/4} \tag{8.8}$$

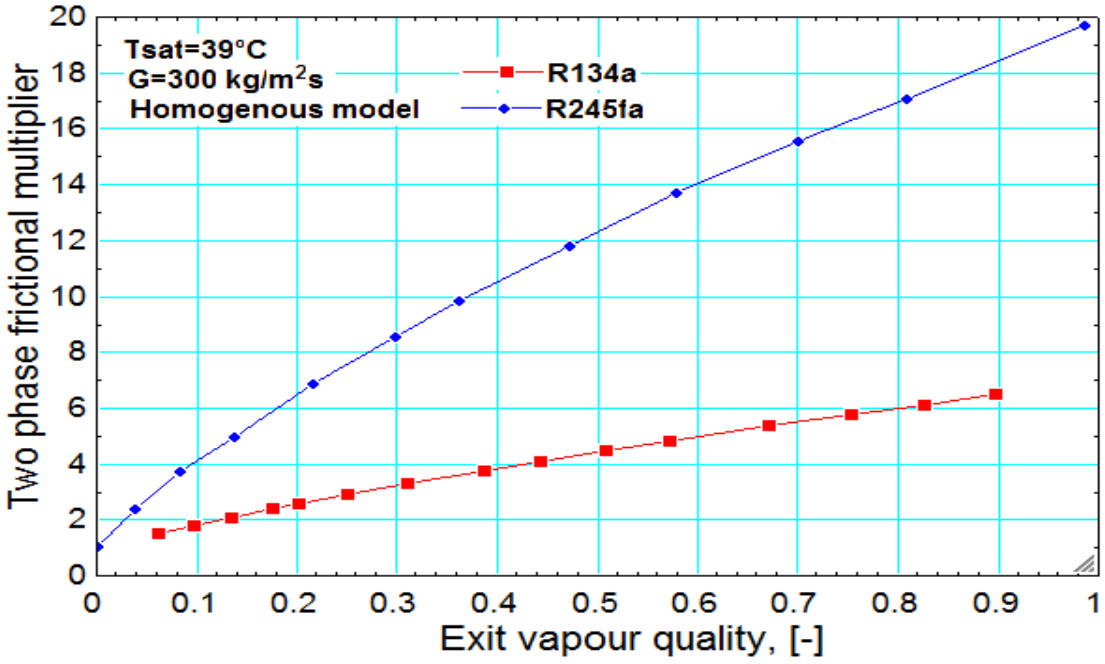

Figure 8.4. Two phase frictional multiplier as a function of exit vapour quality for R245da and R134a at an inlet saturation temperature of 39˚C.

8.3 Effect of material on pressure drop

The effect of the channel material on pressure drop was investigated using stainless steel, copper and brass test sections. The working fluid, R245fa, was used for all three materials. The pressure drop correlations used for prediction are based on fluid properties and are therefore constant for all three materials. The pressure drop was seen to once again increase with heat flux but to varying magnitudes, see figure 8.5. Stainless steel had the lowest measured pressure drop of the three materials and brass the highest. As previously seen with the refrigerant comparison, the pressure drop decreases with an increase in the inlet pressure but the magnitude of this increase differs between the materials. The decrease in the stainless steel is relatively linear compared with brass and copper where the decrease was less clear. For copper, the effect of inlet pressure is only seen at heat fluxes above 20 kW/m^2 but the subsequent pressure difference increases in magnitude with heat flux. The increase in pressure drop, associated with the occurrence of two phase flow, occurs at a much higher heat flux with the higher inlet pressure. At the occurrence of two phase flow, the pressure drop shows a sharp increase. The pressure drop is expected to decrease with an increase in the inlet pressure due to changes in the thermophysical properties of R245fa, mainly the decrease in the liquid

and vapour density ratio which will decrease the frictional pressure drop. This anticipated relationship is only evident for stainless steel and copper at higher heat fluxes. This suggests that changes in the properties of the working fluid are less important to the measured pressure drop than the surface structure. The difference in the heat flux at which two phase flow occurs can be seen in figure 8.6. The effect of inlet pressure for the single phase to two phase flow pressure drop differs between materials. The magnitude is similar for both inlet pressures for all materials which is expected in the single phase region. The heat flux at which two phase flow occurs is similar for the stainless steel but is higher for the copper and brass. For copper, the heat flux is nearly double at the higher inlet pressure but, as with stainless steel, the increase in pressure drop is gradual after this occurrence. At both inlet pressures for brass, the increase is sharp and occurs at more than double the heat flux for the higher inlet pressure. This is in agreement with the work of Kandlikar and Schmitt (2005) who found surface roughness had an effect on the single phase pressure drop due to the changing surface structures acting as a restriction to the flow. The onset of boiling is a function of both heat flux and surface structure, due to the differences seen in the flow patterns discussed in Chapter 5. Proportionally, the differences seen in the pressure drop between the materials is similar before and after the onset of two phase flow. This further implies that the surface structure is an important factor in the measured pressure drop. The frictional and acceleration pressure drop components are almost identical in value, based on the equations 8.1-8.7. Therefore the differences seen are due to the effect of the surface structure, restricting the flow and increasing the frictional pressure drop. Figure 8.5 shows that the channel material changes the effect of the inlet pressure on the measured pressure drop. For stainless steel and copper, the measured pressure drop is higher for the lower inlet pressure, after heat fluxes of 15 kW/m^2 and 20 kW/m^2, respectively. Based on Chapter 5, it is known that this is the heat flux range at which annular flow is prevalent. As previously discussed, this reduction in measured pressure drop with increasing inlet pressure is expected due to the changes in fluid properties with saturated temperature. This same trend is not seen with brass, where there is no effect of inlet pressure on the measured pressure drop. This could be a result of the rougher surface structure which increases the pressure drop. The rougher surface can disturb the liquid film and the potentially higher number of nucleation sites can result in bubbles in the liquid film. Copper, the smoothest surface, has the largest difference between the inlet pressures. The difference between the two inlet pressures is smaller

for stainless steel. This suggests that as the surface roughness increases, this dominates over the change in fluid properties.

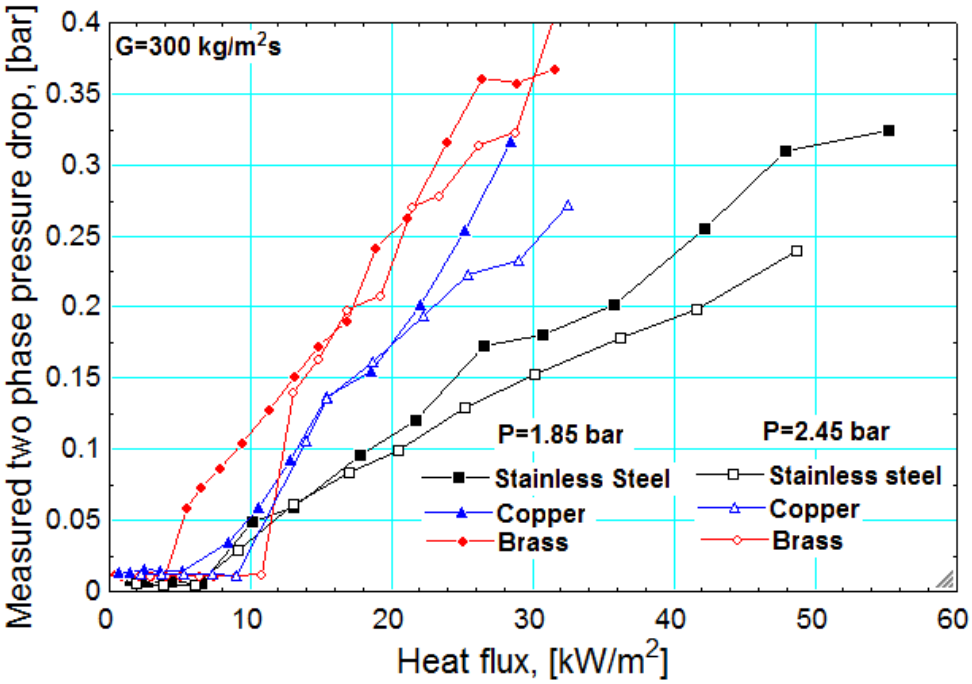

Figure 8.5. Measured two phase pressure drop as a function of the heat flux at inlet pressures of 1.85 and 2.45 bar for stainless steel, copper and brass.

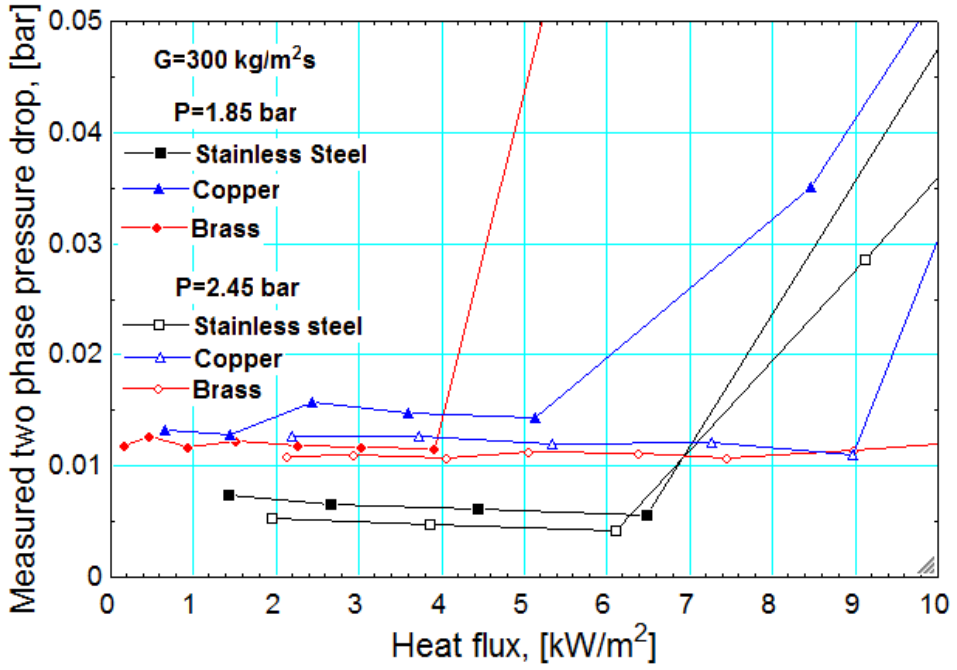

Figure 8.6. Measured pressure drop at low heat flux values at inlet pressures of 1.85 and 2.45 bar for stainless steel, copper and brass.

Figure 8.7 shows that for all of the materials, the measured pressure drop is a function of the mass flux. However, this function of mass flux is not consistent for the three materials. The stainless steel shows a clearly defined increase with mass flux, as

does the copper, although the increase is smaller. The brass test section shows an overlap with mass fluxes of 200 and 300 kg/m^{2}s. The pressure drop is directly linked to the flow patterns which, as seen in Chapter 5, are material dependent. At higher heat fluxes, greater than 10 kW/m^2, annular flow dominates for all of the materials. The liquid film of annular flow can be disturbed by surface roughness, with surface peaks acting as a constriction to the flow, which would increase the frictional losses. Chapter 6 showed the brass test section to have a smooth increase in the heat transfer coefficient which would equate to a thinning of the liquid film. Figure 6.21 shows the heat transfer coefficient, which is linked to the liquid film thickness and hence pressure drop, is not mass flux dependent.

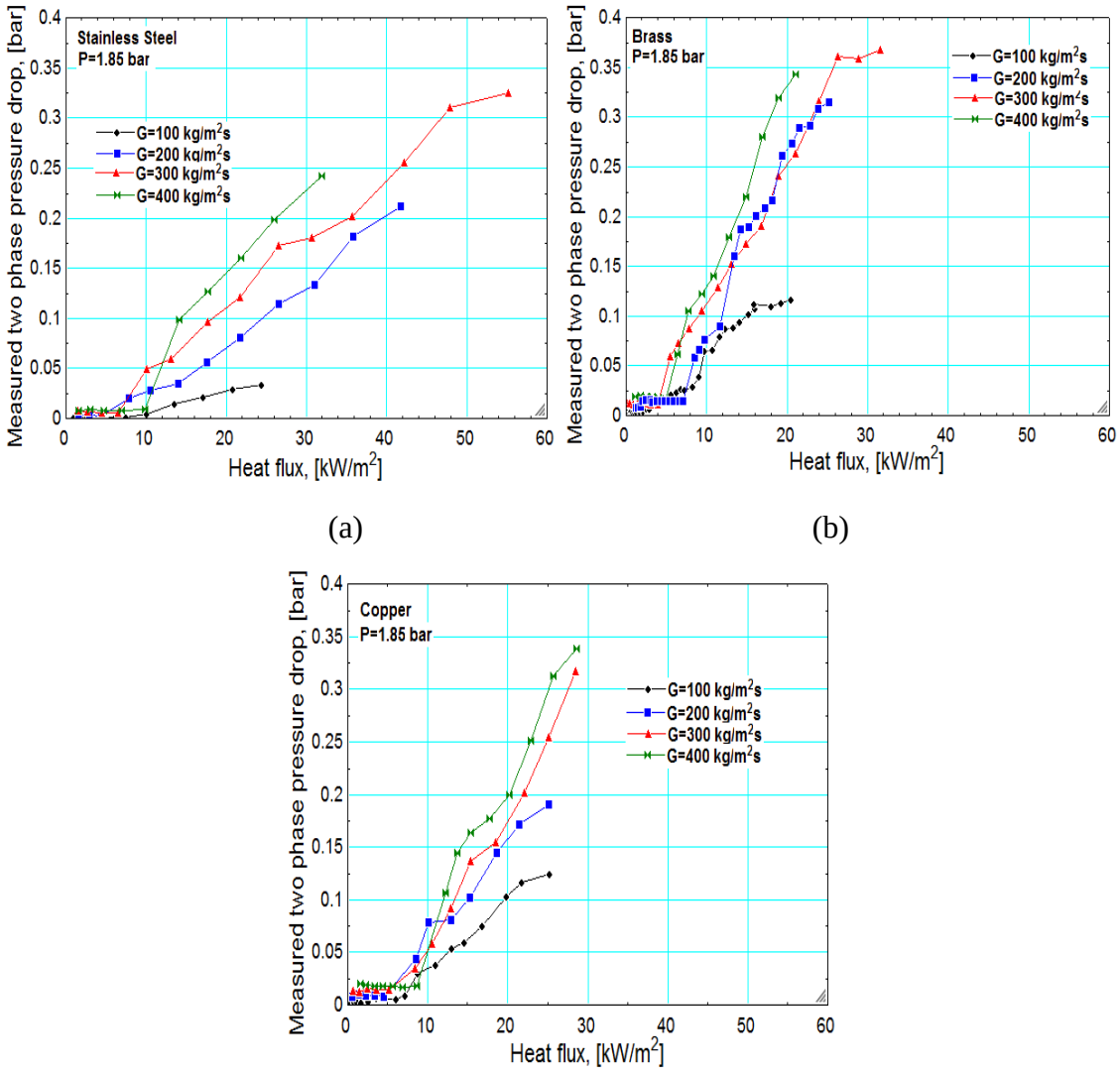

Figure 8.7. Measured two phase pressure drop as a function of heat flux for mass fluxes of 100-400 kg/m^{2}s for (a) stainless steel, (b) brass and (c) copper.

In theory, a rougher surface should equate to a higher pressure drop, due to the surface peaks acting as a restriction and increasing the frictional pressure drop. Although brass does have the steepest pressure drop and the highest surface roughness, copper has the intermediate pressure drop but the lowest surface roughness. This suggests that an increase in the surface roughness does not equate to an increase in the pressure drop. This may be due to the shape of the surface peaks not being considered, only the height of the peak. Croce and D'Argaro (2005) concluded that the shape of the peak was a defining factor in the pressure drop, with cylindrical pressure drop peaks having a larger pressure drop than triangular peaks. An alternative method of categorising the surface in terms of the pressure drop is to use the Fp variable, discussed in Chapter 2. This parameter is also the lowest for copper at 2.4 μm and 2.9 μm for brass and stainless steel which does not agree with the trend seen here. There is a clear effect of surface characteristics on the two phase pressure drop which is not represented by the current surface parameters presented. The only surface parameter which does follow the same trend as the experimental pressure drop is that of Rp, the maximum profile peak. Although higher surface peaks result in a flow constriction and consequently a higher pressure drop, the Rp value refers to the height of the largest singular peak and is not representative of the whole surface. Therefore, it is more likely a coincidence that the experimental pressure drop follows the same trend as that of Rp. The limitations of Rp can be addressed by using the RHSC, which is the high spot count which refers to the number of complete profile peaks above a given line for the evaluation length. This line can be set as the mean line or parallel to the mean line to allow for focus on larger peaks. This gives a value of peaks which is only relevant if the evaluation length is known. However, the RHSC value is not widely used and is not represented by the surface topography methods used in this study. The RHSC value can be estimated from the raw data, which followed the same trend as that for the average surface roughness in this instance. Stainless steel had an equal number, 6 of each, of small peaks and larger peaks. The larger peaks were not necessarily higher but were over a longer surface length. The copper surface had 9 peaks over the given line, 5 of which covered a larger surface length than 0.05 mm. Brass had the highest ratio of larger peaks, with 12 of the 14 peaks covering a longer surface length. This change in peak length was reflected in the Rsm values, with brass having the smallest value (0.732 μm) and stainless steel the highest (0.865 μm). This trend suggests that the shape of the peak has a greater effect on the pressure drop than the height of the peak itself.

The pressure drop along the tube length is assumed to be linear, based on the measured inlet and outlet pressure readings. This assumption is widely used in flow boiling (Qu et al. 2003, Maqbool et al. 2013). A study by Copetti et al. (2011) of R134a in a horizontal minichannel concluded that there was only a small variation between the actual pressure drop and the assumption of a linear pressure drop and therefore did not have a significant effect of the data. This was validated by Tibiriçà et al. (2010) for adiabatic flow based on a comparison of the assumed linear pressure drop and the pressure drop calculated from the local thermocouple measurements. However, the actual pressure drop is unlikely to be truly linear, with a greater pressure drop near the tube entry at the occurrence of nucleate boiling. This in turn results in the assumption of a higher fluid temperature and a recorded heat transfer coefficient than in real terms. This is also largely dependent on the working fluid employed. Bortolin et al. (2011) stated that low pressure refrigerants, such as R245fa, are less likely to show a linear pressure gradient, resulting in discrepancies for the saturated temperature and consequently, the heat transfer coefficient. The Bortolin et al. (2011) investigation accounted for this by using the Friedel (1979) pressure gradient correlation, with a multiplying factor to ensure that the inlet and outlet pressures were matched. Figure 8.8 presents a comparison of the linear pressure drop and the Friedel (1979) correlation for the stainless steel channel. A multiplying factor of 0.43 was applied for the outlet pressures to be equal. The Friedel (1979) correlation predicts a smooth curve which is lower than that of the linear pressure drop, which in turn would result in a lower recorded heat transfer coefficient. This is based on the experimental results for R245fa at an inlet pressure of 1.85 bar, a mass flux of 200 kg/^{2}s and a heat flux of 17 kW/m^2. The difference between the pressures is a function of the heat flux. At a lower heat flux of 10 kW/m^2, the difference between the linear and Freidel (1979) pressure drop is smaller, see figure 8.8. For both heat fluxes, the Friedel (1979) correlation shows a higher pressure drop near the entry to the channel, compared with the linear pressure drop, with the lower heat flux having a smaller pressure drop. This is most likely due to the flow patterns seen at the entry to the channel, with annual flow occurring at the channel exit for both heat fluxes. The local pressure drop is similar for both heat fluxes after an axial location of 0.075 m, with the lower heat flux having a slightly lower pressure drop than at the higher heat flux. As the channel length increased, the difference between the linear and Friedel (1979) pressure drop reduces.

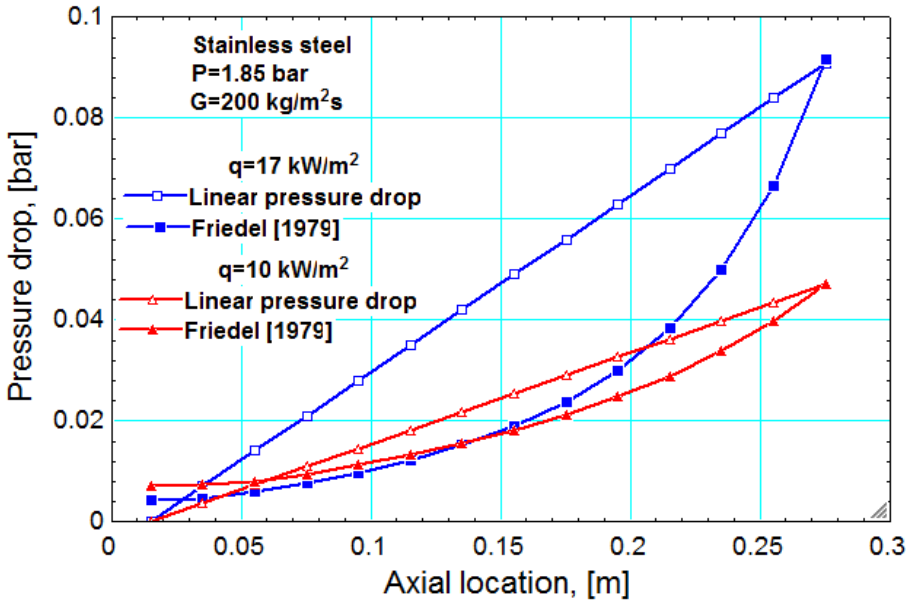

Figure 8.8. Comparison of the experimental linear pressure drop and the Friedel (1979) correlation.

8.4 Pressure drop correlations

Pressure drop correlations from literature are evaluated in terms of the ability to predict the effect of the changes in refrigerant and the changes in surface material. As previously discussed when evaluating the heat transfer correlations, see Chapter 6, the correlations are generally produced from a limited experimental data set. The correlations are based on either the homogenous or separated flow model. Other types of model include semi-mechanistic models, such as the Shiferaw (2009) model. This model is based on slug flow being the dominant flow pattern and is not deemed suitable for annular flow. As annular flow dominates for R245fa in all of the test sections, this model was not used. The separated flow model assumes that both the liquid and vapour phases have different properties and flow velocities, as opposed to the homogenous model which assumes the same flow velocity for both. For this experimental range, the liquid phase was in the turbulent region and the vapour phase in the laminar region. The applicability of these models will vary depending on the flow pattern. The homogenous model can be applied to bubbly flow, where the liquid and vapour phases will be flowing in unison. The separated flow model can apply to the remaining flow patterns where the vapour core flows at a different velocity to the liquid film. The separated flow model is limited by the accuracy of the void fraction calculations for the acceleration and gravitational losses, although these are small for microchannels, see equations 8.9 – 8.12.

$$\Delta P_g = g\frac{L_{tp}}{x_e}\int_0^{x_e}\left[\alpha\rho_g + (1-\alpha)\rho_f\right]dx \tag{8.9}$$

$$\Delta P_{acc} = \frac{G^2}{\rho_f}\left[\frac{x_e^2}{\alpha_e}\frac{\rho_f}{\rho_g} + \frac{(1-x_e)^2}{(1-\alpha_e)} - 1\right] \tag{8.10}$$

$$\alpha = \frac{1}{1+0.28X_m} \tag{8.11}$$

$$X_m = \left(\frac{1-x}{x}\right)^{0.64}\left(\frac{\rho_g}{\rho_f}\right)^{0.36}\left(\frac{\mu_f}{\mu_g}\right)^{0.07} \tag{8.12}$$

In 1949, Lockhart and Martinelli (1949) stated that the two phase frictional pressure drop can be found by multiplying the measured single phase pressure drop and a two phase frictional multiplier, equation 8.13. The two phase frictional multiplier is used to calculate the frictional pressure losses due to the liquid and vapour interaction.

$$\left(\frac{dP}{dz}\right)_{TP} = \phi_l^2\left(\frac{dP}{dz}\right)_{SP} \tag{8.13}$$

Where ϕ_l^2 is equal to;

$$\phi_l^2 = 1 + \frac{C}{X} + \frac{1}{X^2} \tag{8.14}$$

And X to;

$$X = \left(\frac{f_l}{f_g}\right)^{0.5}\left(\frac{\rho_g}{\rho_l}\right)^{0.5}\left(\frac{1-x}{x}\right) \tag{8.15}$$

The value for C depends on the liquid and vapour regimes, ranging from 5-20. The above equation for ϕ_l^2 was produced by Chisholm (1967) after plotting curves of the Lockhart-Martinelli (1949) study. Consequently, C is referred to as the Chisholm constant. The Chisholm constant is usually modified to suit the pressure drop correlation accordingly. This can be done in many forms, either taking into consideration the effect of laminar and turbulent liquid and vapour phases or with a set C function for all flow regimes. Some correlations, including Friedel (1979), Muller-Steinhagen and Heck (1986), Waarier et al. (2002) and Del Col et al. (2013), also refer to the liquid only two phase frictional multiplier, ϕ_{lo}^2. The two phase frictional multiplier is the main consideration as friction is the greatest contributor as seen in figure 8.9. The pressure drop components for R245fa can be seen for both inlet pressures and are similar in trend. The frictional component increases with exit vapour quality while the gravitational and acceleration components decrease. The gravitational

component is the smallest contributor, which is in agreement with Kandlikar and Balasubramanian (2004), who stated that due to the dominance of surface tension, the gravitational effect can be negated for small diameter channels.

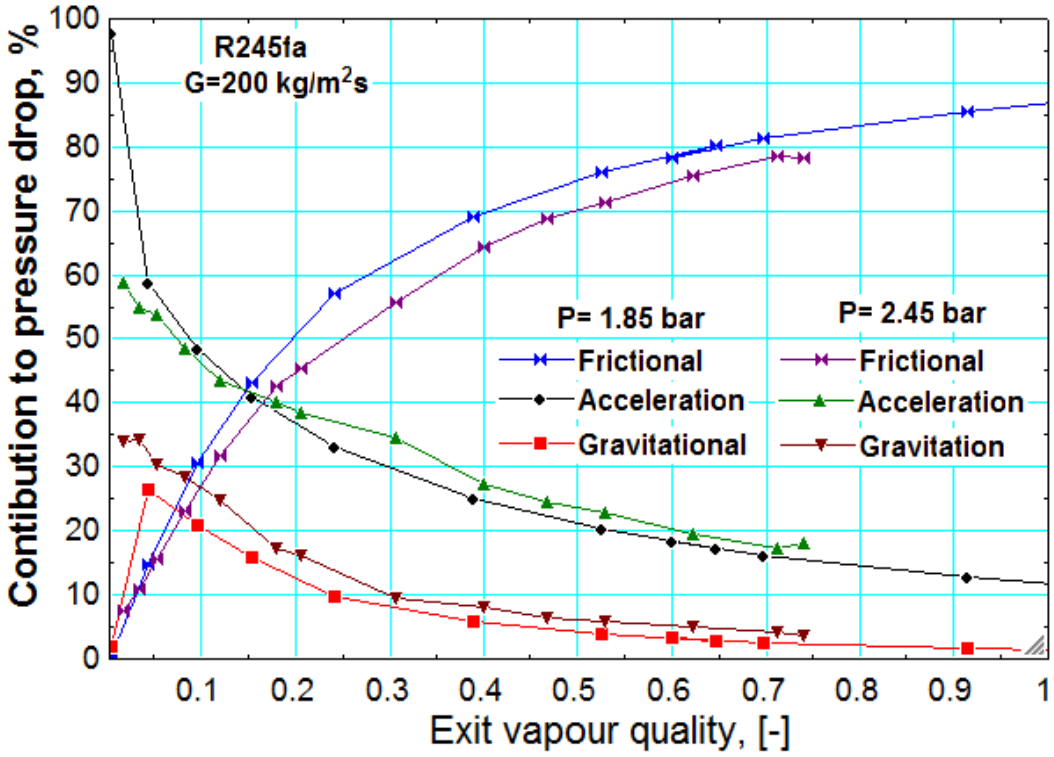

Figure 8.9. Frictional, gravitational and acceleration components as a function of the percentage contribution for R245fa at inlet pressures of 1.85 and 2.45 bar.

Macroscale and microscale pressure drop correlations were evaluated in terms of the effect of refrigerant and channel material. The correlation equations can be found in Appendix B. This evaluation is based on the amount of data predicted within ±30%, β, and the mean absolute percentage error, MAE, see equation 8.16. The values for each correlation can be found in Table 8.2.

$$MAE = \frac{1}{N}\sum_{i=1}^{N}\frac{\left|h_{Pred,i}-h_{Exp,i}\right|}{h_{Exp,i}} x\ 100 \qquad (8.16)$$

8.5 Macroscale correlations

Homogenous model

As discussed above, the homogenous model assumes that the liquid and vapour phases are of equal velocity. For all of the materials, annular flow dominates and therefore the phases are moving at difference velocities, with a faster flowing vapour

core. For this reason, the homogenous model is expected to give poor accuracy. The experimental pressure drop does not follow the same trend as the predicted pressure drop, resulting in different gradients for the pressure drop and low β values, see figure 8.10. The low pressure drop values, corresponding to low heat fluxes, are lower than predicted with this model. The pressure drop at intermediate heat fluxes are predicted well but the prediction accuracy then decreases with heat flux due to the differing gradients. The best results are seen for stainless steel, predicting just over a third of the data within an acceptable range. Copper data shows a similar trend to that of the predicted pressure drop but the values are out by a magnitude resulting in a low accuracy. The change in gradient seen with stainless steel is also seen with brass, although the difference is much greater with only a small heat flux range being predicted well.

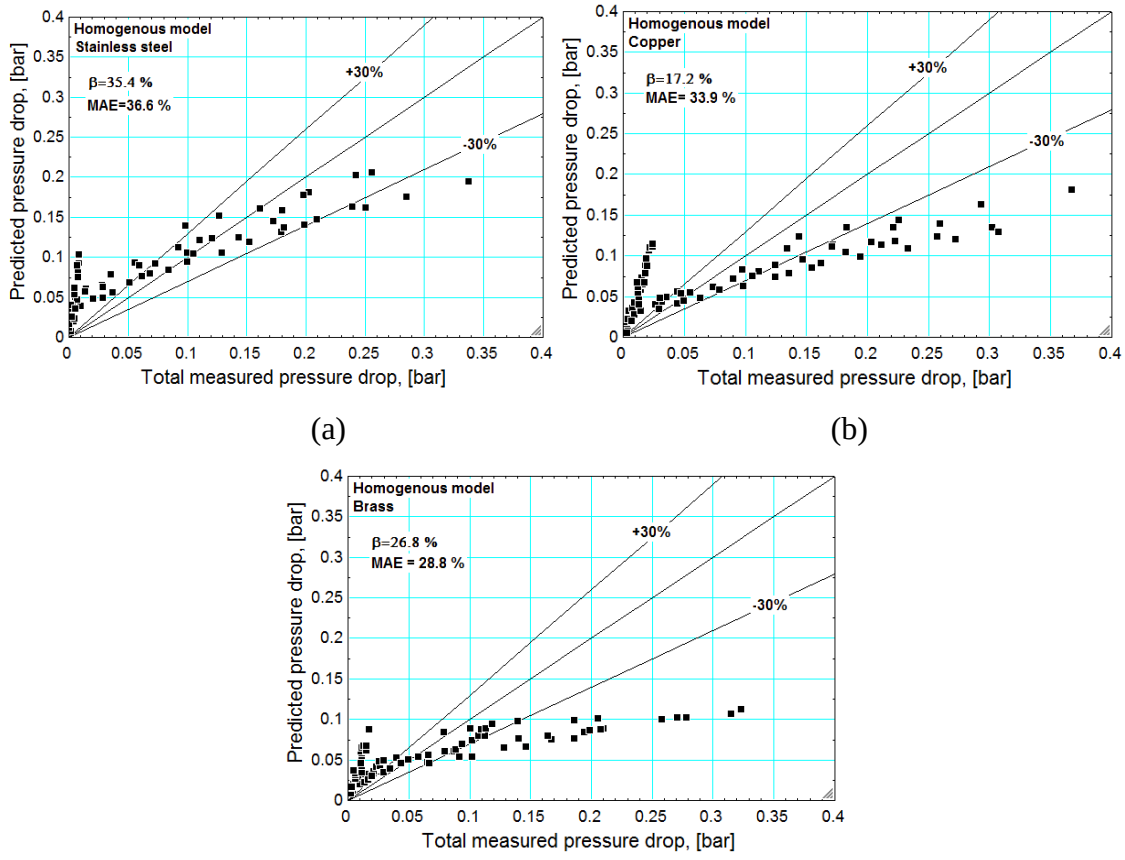

Figure 8.10. Comparison of the Homogenous model with the experimental pressure drop for (a) stainless steel, (b) copper and (c) brass.

Lockhart-Martinelli (1945) correlation

This correlation was produced from experimental data of water, benzene, kerosene and oil in channels of 1.49- 25.83 mm. This correlation uses values which equates to the Chisholm constants seen in Table 8.1. The values of 'C' depend on the turbulence of the liquid and vapour phases. For these experimental conditions, the liquid phase is always within the laminar region but the vapour phase ranges from laminar, at low heat fluxes, to turbulent at higher heat fluxes.

Table 8.1. Chisholm constant values for Lockhart-Martinelli (1945) correlation.

Liquid phase	Vapour phase	C values
Laminar	Laminar	5
Laminar	Turbulent	12
Turbulent	Laminar	10
Turbulent	Turbulent	20

The accuracy of the pressure drop correlation improves with heat flux for the stainless steel, where the Chisholm constant is 12. This correlation showed the best accuracy with stainless steel, predicted the higher heat fluxes well, but under-predicting the pressure drop at low heat fluxes. The correlation under predicted the pressure drop for copper and brass, with a very low prediction value for these materials compared with that of stainless steel, see figure 8.11. The difference in the predicted pressure drop between the materials is due to variations in the exit vapour quality, see Chapter 5.

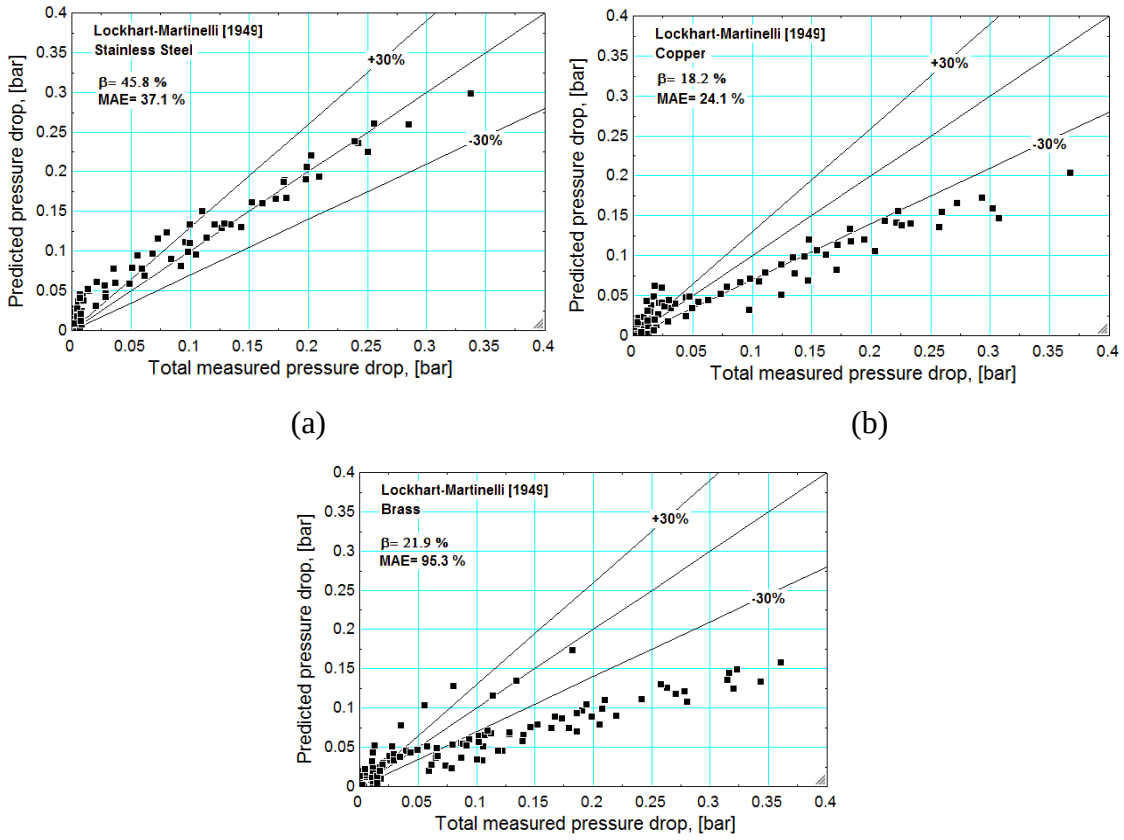

Figure 8.11. Comparison of the Lockhart-Martinelli (1949) correlation with the experimental pressure drop for (a) stainless steel, (b) copper and (c) brass.

Friedel (1979) correlation

The Friedel (1979) correlation uses the Froude number and the Weber number as well as the liquid and vapour density, specific volume, friction factor and viscosity. The accuracy increase with measured pressure drop, with good agreement for stainless steel at higher pressure drops, see figure 8.12. This is not seen with copper and brass where the lower measured pressure drop, equating to lower heat fluxes are more accurately predicted and the pressure drop is under predicted at higher heat fluxes. The β values follow the reverse trend of the measured pressure drop, with brass having the lowest β value followed by copper. This correlation performs considerably better for stainless steel in comparison to brass and copper.

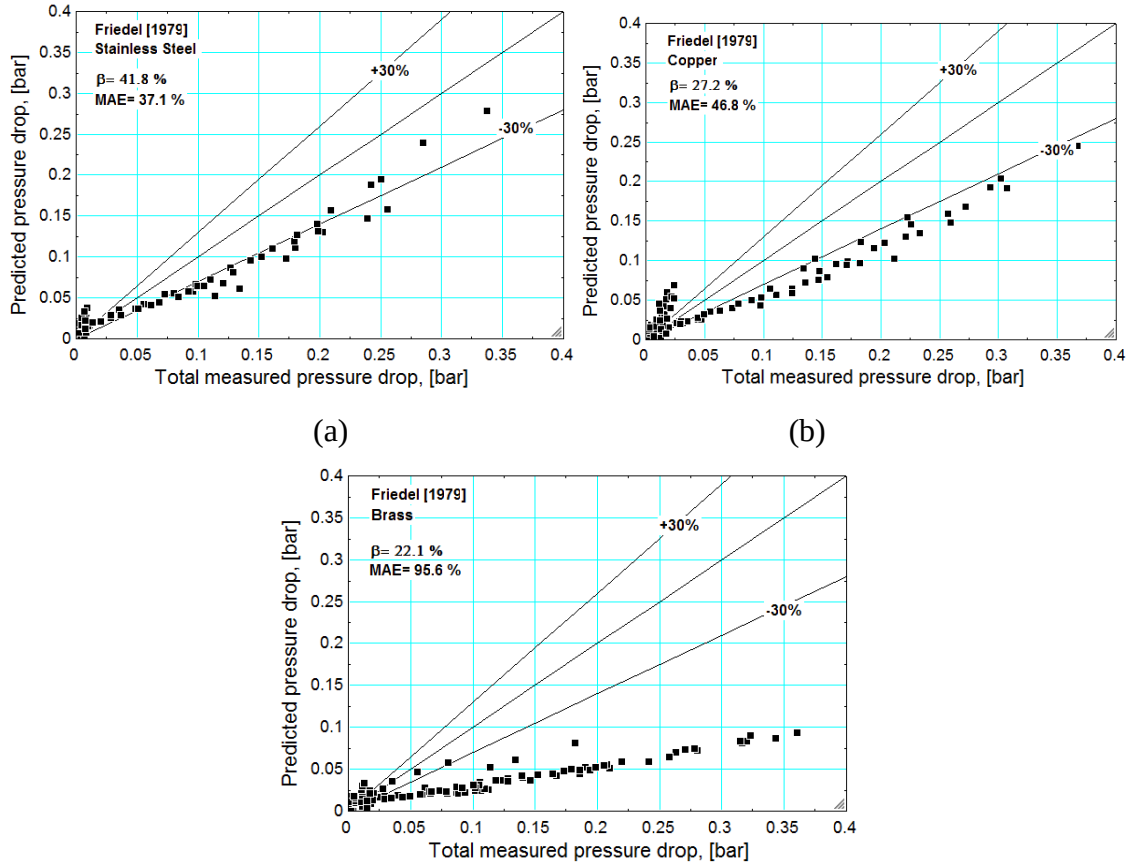

Figure 8.12. Comparison of the Friedel (1979) correlation with the experimental pressure drop for (a) stainless steel, (b) copper and (c) brass.

Muller-Steinhagen and Heck (1986) correlation

The Muller-Steinhagen and Heck (1986) correlation is based on the channel diameter, mass flux and liquid and vapour friction factors and density. The correlation was developed from a data bank of 9300 points from a range of working fluids and experimental conditions. In general, the correlation shows poor agreement for all of the R245fa experimental data. The main difference is seen at the higher pressure drop values, with the low pressure drop values being similar across the three materials. Brass has the highest measured pressure drop followed by copper. The same trend is not seen in figure 8.13, where the results are best for copper and then brass, based on the β and MAE. The frictional pressure drop is calculated based on the vapour only and liquid only pressure drop across the channel length, as well as the vapour quality. Chapter 5 shows a difference in the flow patterns, and consequently pressure drop, with vapour

quality between the materials. These changes in vapour quality between the materials results in differences in the predicted pressure drop.

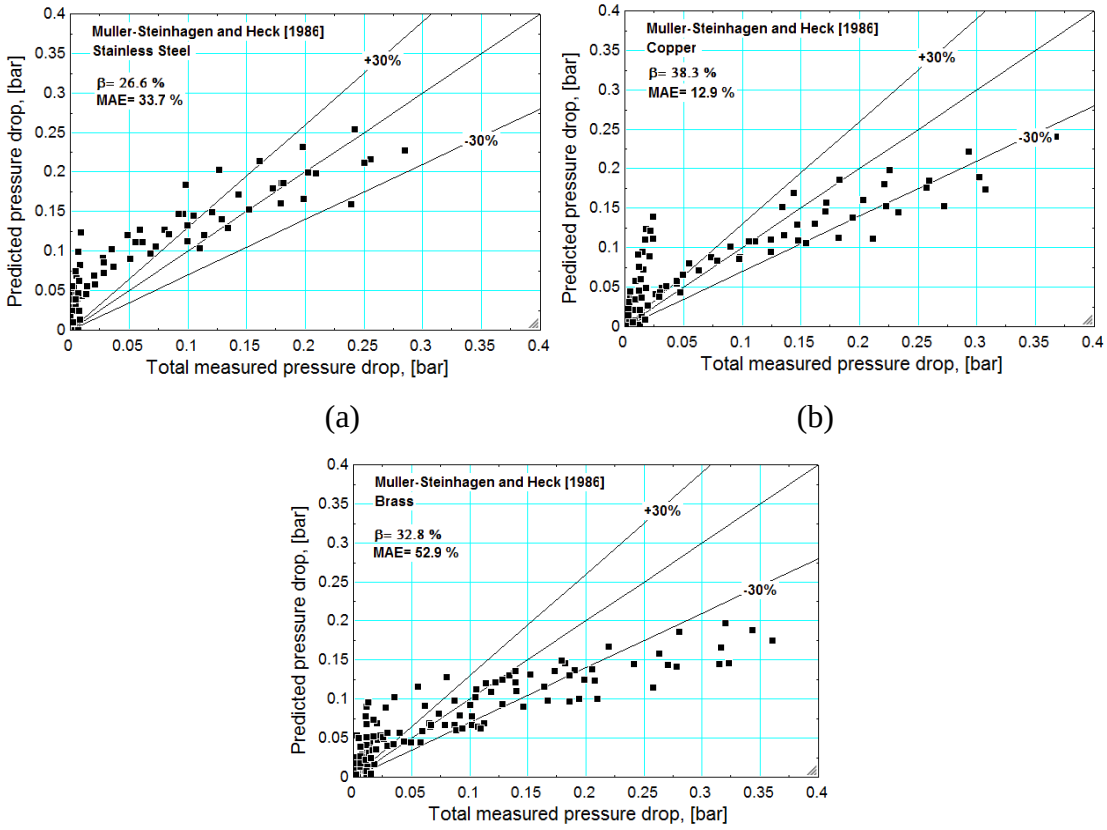

Figure 8.13. Comparison of the Muller-Steinhagen and Heck (1986) correlation with the experimental pressure drop for (a) stainless steel, (b) copper and (c) brass.

Wang et al. (1997)

The Wang et al. (1997) correlation is based on experimental data from R22, R134a and R407C in a 6.5 mm channel. This correlation consists of two frictional pressure drop equations, which depend on the range of mass flux. For mass fluxes lower than 200 kg/m^{2}s, the frictional pressure drop uses a Chisholm constant (C) function which is based on the fluid properties, with liquid only Reynolds number and ratios of the liquid and vapour density and viscosity. For higher mass fluxes, the equation is based solely on the Lockhart-Martinelli parameter X. Figure 8.14 shows that the pressure drop values corresponding to low heat fluxes are over predicted for all materials. The correlation shows poor agreement for copper and brass, in comparison with stainless steel. Nearly half of the data was predicted within an acceptable range,

although the pressure drop is predicted in the lower half of the range, at -30 %. Brass and copper show a poor agreement with β values of only 15.6% and 12.4% respectively.

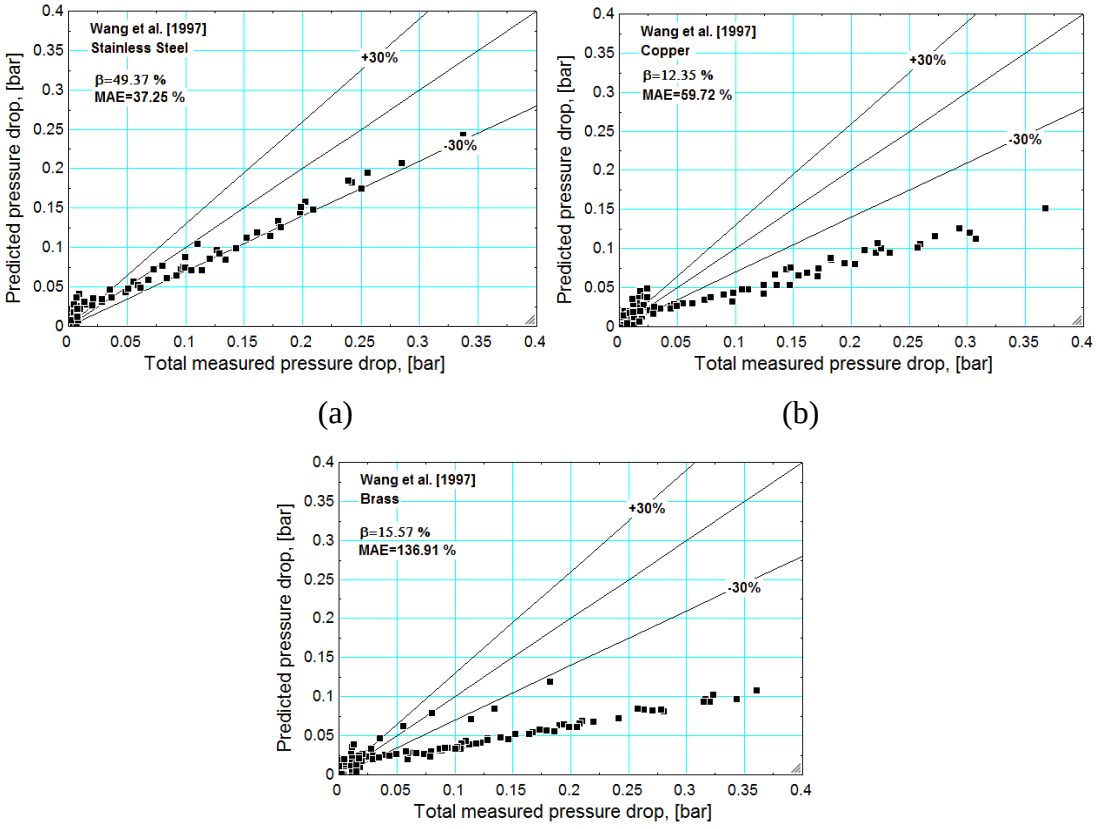

Figure 8.14. Comparison of the Wang et al. (1997) correlation with the experimental pressure drop for (a) stainless steel, (b) copper and (c) brass.

8.6 Microscale correlations

Mishima and Hibiki (1996)

The Mishima and Hibiki (1996) correlation is based on experimental data for air/water in channels ranging in diameter from 1.05 to 4 mm. The frictional pressure drop uses a C function which is based solely on the channel diameter. This correlation shows poor agreement for all of the materials, see figure 8.15. Stainless steel has the lowest β value but all the lowest MAE value. The Mishima and Hibiki (1996) correlation underpredicts the pressure drop and is one of the worst performing correlations.

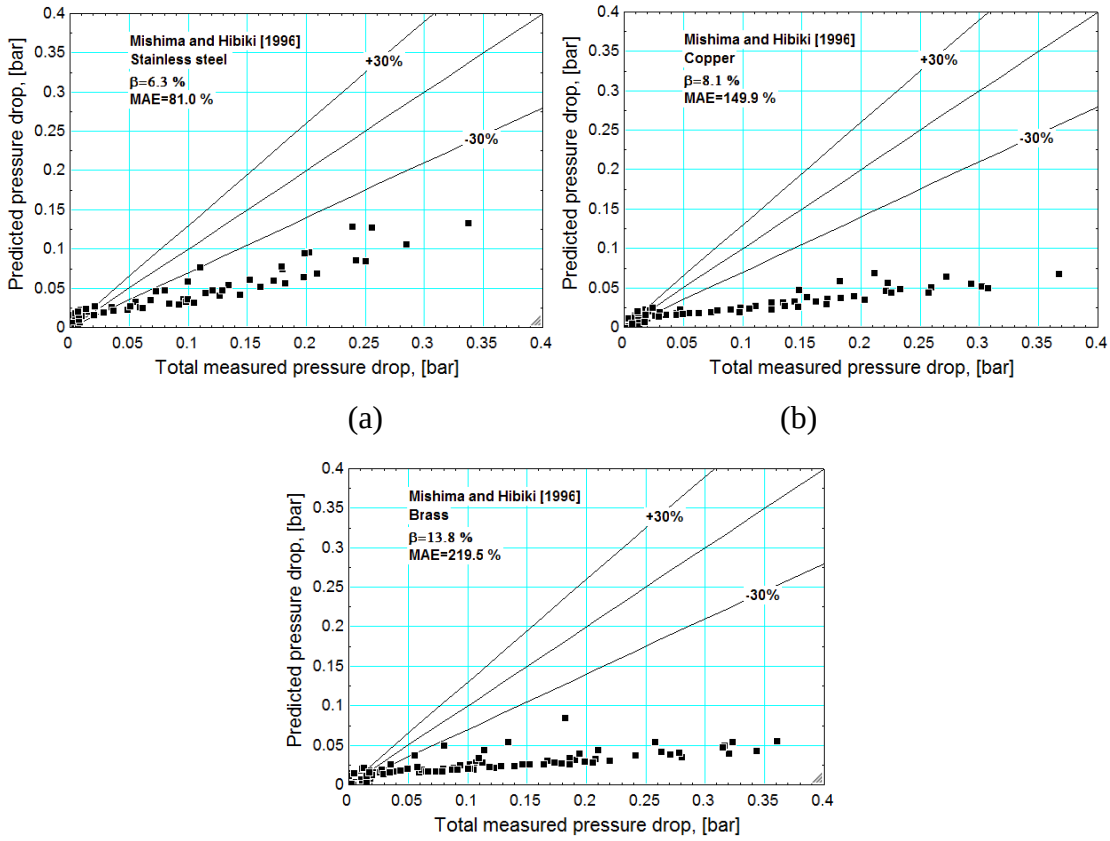

Figure 8.15. Comparison of the Mishima and Hibiki (1996) correlation with the experimental pressure drop for (a) stainless steel, (b) copper and (c) brass.

Tran et al. (2000)

The Tran et al. (2000) correlation was produced using data from both two circular and one rectangular channel, with hydraulic diameters ranging from 2.4- 2.92 mm, and working fluids of R134a, R12 and R113. This study produced a data bank of 610 data points, concluding that macroscale correlations were not applicable due to the elongated bubble, only seen in microscale channels. The confinement number was used to account for the changes seen at the microscale. This was included in a modified version of the Chisholm (1983) correlation. Only a quarter of the data was predicted within ± 30% for stainless steel. Figure 8.16 shows that as the experimental pressure drop increases, the predicted pressure drop does not increase at the same rate and therefore the data is underpredicted. This is also true for copper and brass but with more of the data underpredicted. The spread of results is greater than with many of the other correlations which show relatively straight lines of data. The spread in data refers to the change in mass flux. The effect of mass flux was more defined for stainless steel than

copper and brass. This may explain why the spread appears larger for copper and brass as the predicted changes with mass flux were not seen with the experimental data.

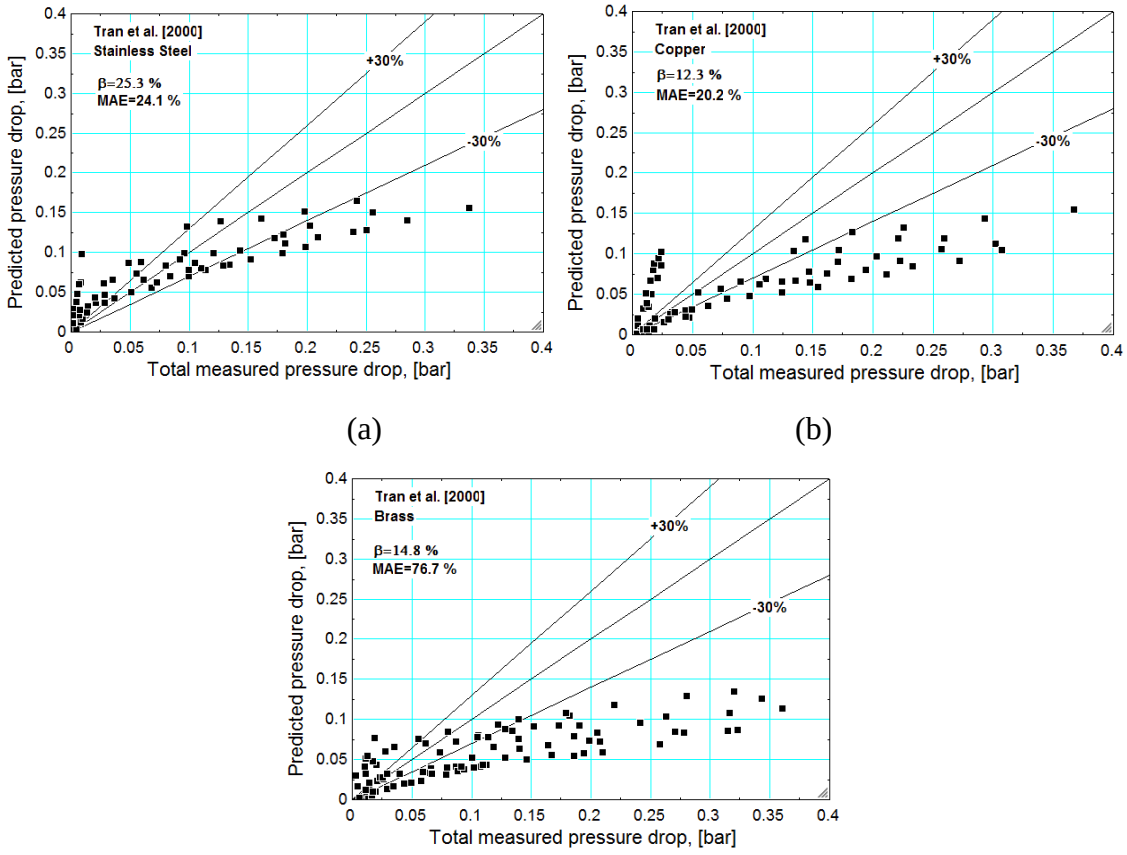

Figure 8.16. Comparison of the Tran et al. (2000) correlation with the experimental pressure drop for (a) stainless steel, (b) copper and (c) brass.

Lee and Lee (2001)

The Lee and Lee (2001) correlation was developed based on a study using air and water in channels with hydraulic diameters ranging from 0.78 to 6.67 mm which includes both micro and macro scale data. This correlation is focused on the liquid properties, including the liquid only Reynolds number, viscosity, superficial velocity and density, see Appendix B. These functions are used in dimensionless groups to form the Chisholm's constant. The dimensionless groups and indexes applied depend on the turbulence of the liquid and gas phases. The results show the best agreement for stainless steel, with a β value of 59.9 % and MAE= 32.2 %. From figure 8.17a, it can be noted that these results show very good agreement, with the β value being lower than expected due to an overprediction of the pressure drop in the low heat flux region. The correlation is less successful for copper and brass, with the results being better at low

heat fluxes but under predicted at higher heat fluxes. The experimental and predicted pressure drop follows the same trend with only a small magnitude difference for the copper results. The brass results are slightly higher with β=24.6% and 20.9 %, respectively.

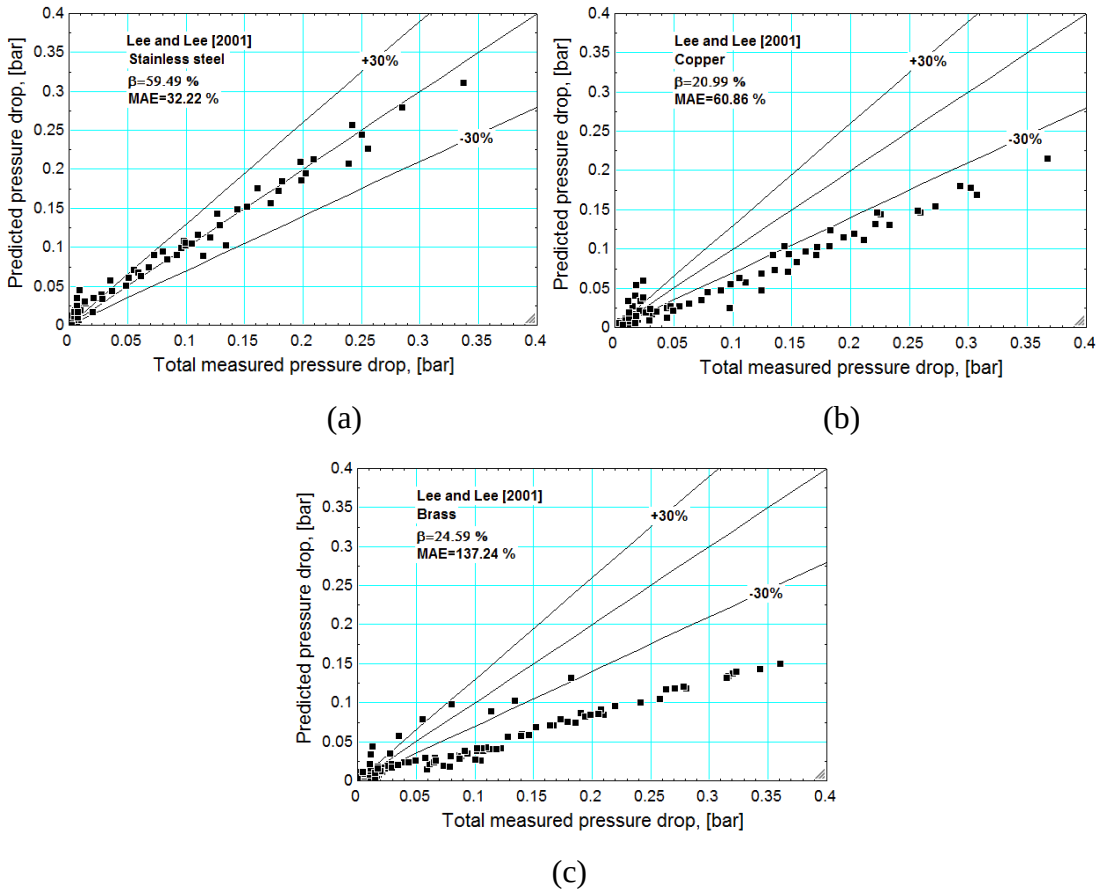

Figure 8.17. Comparison of the Lee and Lee (2001) correlation with the experimental pressure drop for (a) stainless steel, (b) copper and (c) brass.

Warrier et al. (2002)

The Warrier et al. (2002) correlation is based on experimental data of FC-84 in rectangular multi-channels with a hydraulic diameter of 0.75 mm. This study found that the flow quickly became annular and set the C function to be 38 for all flow regimes. The Warrier et al. (2002) correlation shows very poor agreement with stainless steel, with no data predicted in the acceptable range, see figure 8.18. The results were slightly better for copper and brass, this is most likely due to the pressures being higher for these materials. Brass showed the best results, with the accuracy increasing with heat flux. This correlation, although showing a poor prediction with experimental data, differs from the majority of the correlations by overpredicting the data. This correlation has a

considerably higher ‘C’ function, compared with other correlations, of 38 which results in a higher frictional pressure drop.

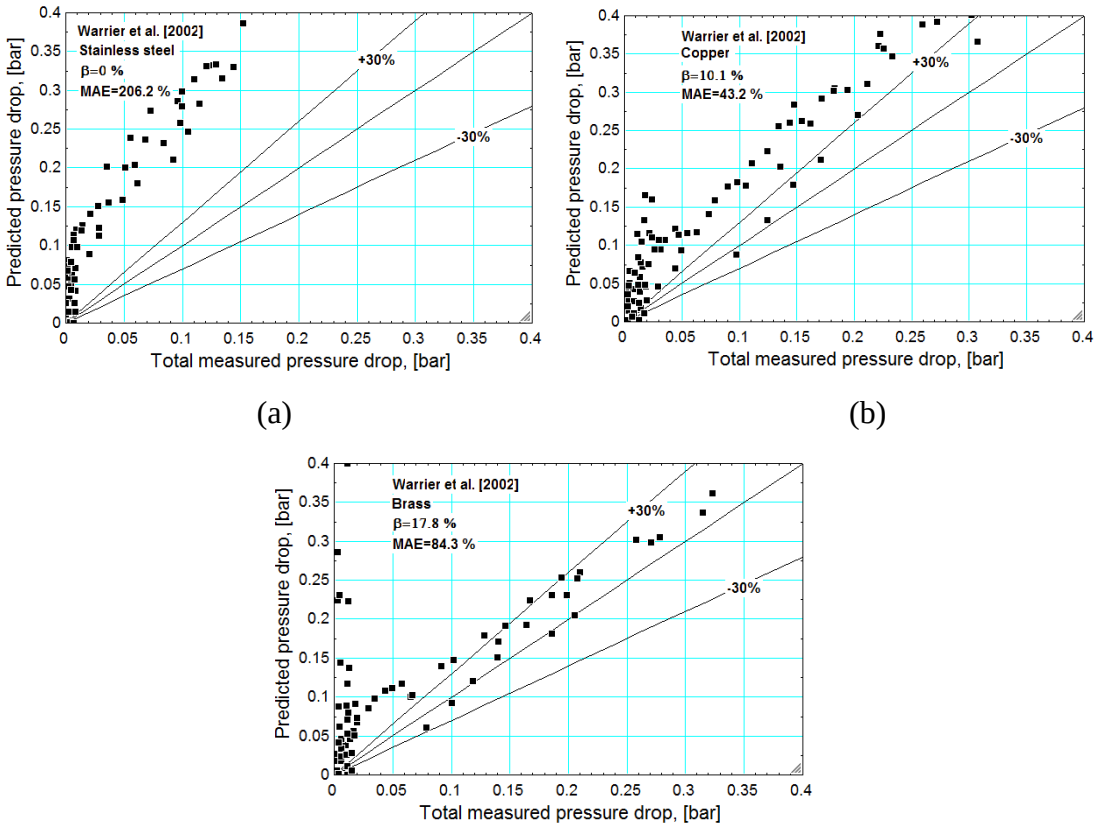

Figure 8.18. Comparison of the Warrier et al. (2002) correlation with the experimental pressure drop for (a) stainless steel, (b) copper and (c) brass.

Yu et al. (2002)

The Yu et al. (2002) correlation was produced from pressure drop data for water in a 2.98 mm diameter circular channel. This investigation found that slug flow was dominant in smaller channels as opposed to annular flow, thus requiring a different pressure drop correlation to a macro scale channel where annular flow dominates. They concluded that the Lockhart-Martinelli parameter X could be adapted to predict the smaller pressure gradient associated with slug flow, since the previous Lockhart-Martinelli parameters were over predicting the pressure drop for micro scale channels. Figure 8.19 shows the random nature of the correlation, where those data points within the ±30% boundary do not follow a linear trend. This scattering is seen for all of the materials. The best prediction is for stainless steel, predicting only 21.5 % of the data in the ± 30 % range.

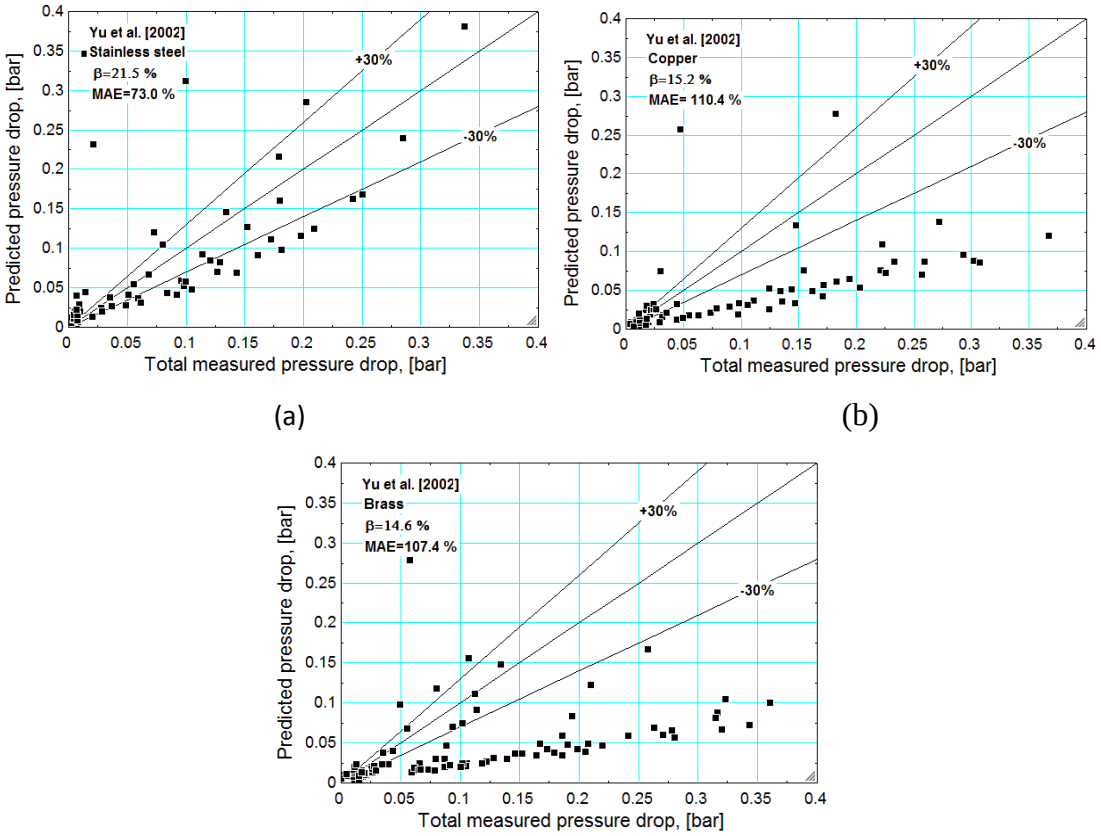

Figure 8.19. Comparison of the Yu et al. (2002) correlation with the experimental pressure drop for (a) stainless steel, (b) copper and (c) brass.

Qu and Mudawar (2003)

Qu and Mudawar (2003) produced a correlation based on an experimental study of water in a channel of 0.35 mm. This correlation is once again based on the Chisholm constant C and modified the Mishima and Hibiki (1996) correlation to include the effect of mass flux as well as that of the channel diameter which was deemed to be important based on previous studies. Figure 8.20 shows nearly a third of the data is predicted for the stainless steel, but with a high MAE value due to the poor performance at low measured pressure drop. This is contrary to the copper and brass results which show the pressure to be under predicted besides that of low measured pressure drop, of less than 0.15 bar.

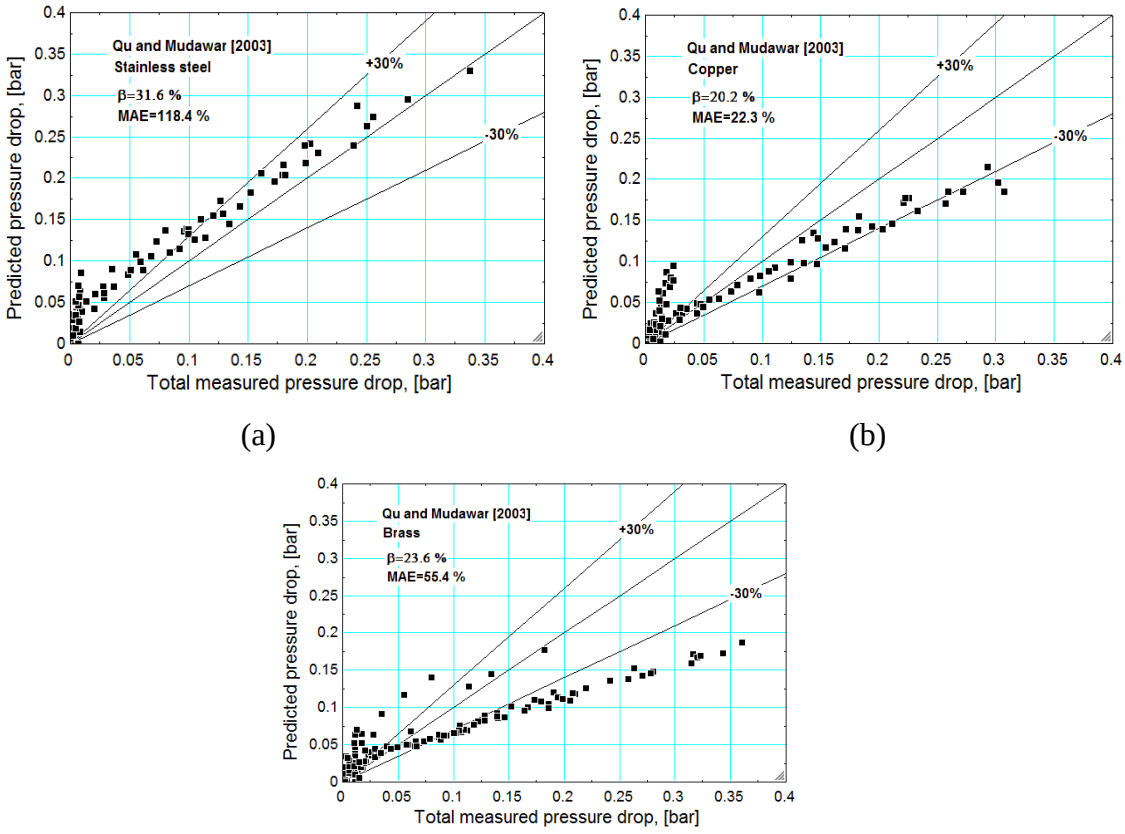

Figure 8.20. Comparison of the Qu and Mudawar (2003) correlation with the experimental pressure drop for (a) stainless steel, (b) copper and (c) brass.

Hwang and Kim (2006)

Hwang and Kim (2006) conducted an investigation into two phase pressure drop using R134a in channels with internal diameters of 0.244, 0.430 and 0.792 mm. This study focused on flow where Re_{fo}<2000. The correlation uses a modified Chisholm constant which includes Re_{fo} and the confinement number. All of the data produced with R245fa was within the range of Re_{fo}<2000. This correlation showed good results for stainless steel with a β value of 50.6% and MAE value of 30.6%. The correlation shows a good prediction over a measured pressure drop of 0.05 bar, but is underpredicted at lower measured pressure drops. The correlation shows worse agreement with copper and brass, with data being underpredicted, see figure 8.21 b and c. Copper has the lowest MAE value due to the low measured pressure drop values, less than 0.075 bar being predicted well. The MAE value is high for brass, even with a similar β value as copper, with an increasing deviation between the experimental and predicted pressure drop with heat flux.

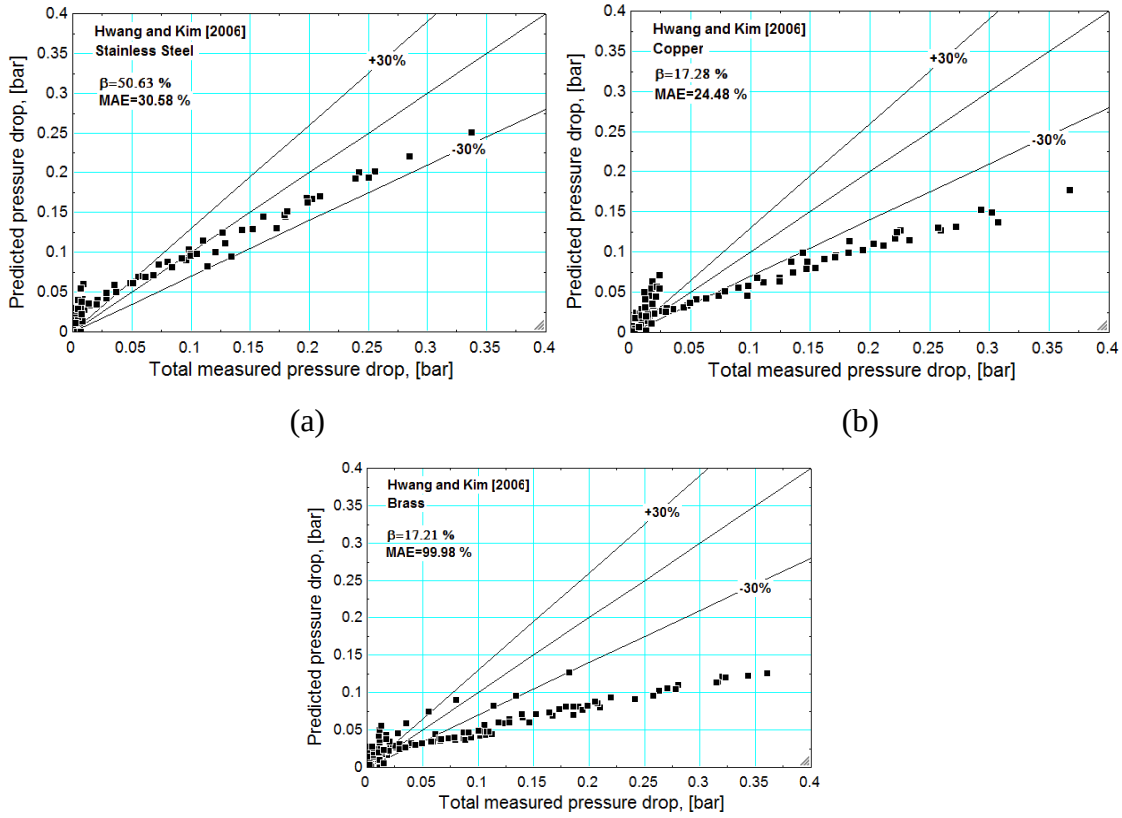

Figure 8.21. Comparison of the Hwang and Kim (2006) correlation with the experimental pressure drop for (a) stainless steel, (b) copper and (c) brass.

Lee and Garimella (2008)

The Lee and Garimella (2008) correlation was based on an experimental study of rectangular mutli-channels with hydraulic diameters ranging from 0.16 to 0.571 mm using water. The study investigated flow within the laminar liquid and laminar vapour flow region. The Chisholm parameter (C) was adapted from the Mishima and Hibiki (1996) model to include a further function of hydraulic diameter and the mass flux. Figure 8.22 shows a scattering of the results, due to the mass flux function. Figure 8.7 shows the effect of mass flux to vary between the materials, with brass and copper having a reduced function of mass flux. Due to this, the copper and brass show less scattering than that of the stainless steel. The low measured pressure drop, less than 0.05 bar, were over predicted for all three materials. The correlations show poor agreement for the brass and copper, with both having similar β values, 17.1% and 18.2%, and MAE values, 39.9% and 24.9%, respectively. For both materials, the low to medium heat fluxes, with a measured pressure drop between 0.05 and 0.1, were the only values within the acceptable range.

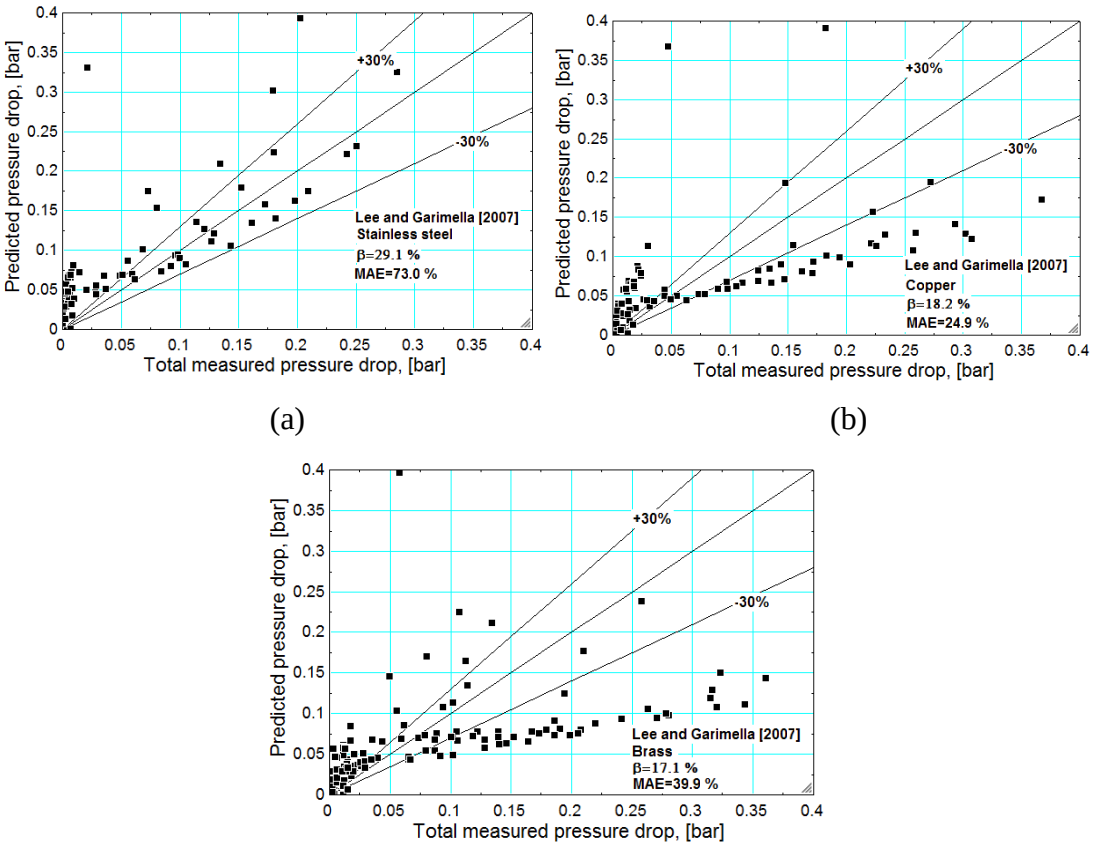

Figure 8.22. Comparison of the Lee and Garimella (2007) correlation with the experimental pressure drop for (a) stainless steel, (b) copper and (c) brass.

Sun and Mishima (2009)

Sun and Mishima (2009) used a data base consisting of 2092 data points, including data for water and refrigerants and diameters of 0.506 to 12 mm, which covers the micro and macro range. This data was used to produce a correlation based on modifying the Chisholm constant, C, see appendix B. Two modified Chisholm constant (C) equations were proposed, one for the laminar flow regime and one for the turbulent flow regime. For both flow regimes, the liquid Reynolds number is used and the gaseous Reynolds number for the turbulent regime. The Laplace function is used for the laminar regime which accounts for the surface tension, change in density, gravity and channel diameter. The laminar flow regime modifications are based on the importance of the liquid Reynolds number, based on the experimental data, and the Zhang (2006) conclusion that the Laplace number strongly influences the laminar region. This correlation showed the best agreement with stainless steel, predicted nearly half of the data within the ±30% range, see figure 8.23a. The correlation showed good agreement at higher heat fluxes but over predicted at low heat fluxes. The correlation showed poor

agreement for copper and brass, with the only data being predicted at low heat fluxes, at measured pressure drops less than 0.1 bar. The MAE values are considerably higher for brass over copper, with a large discrepancy in data at higher heat fluxes.

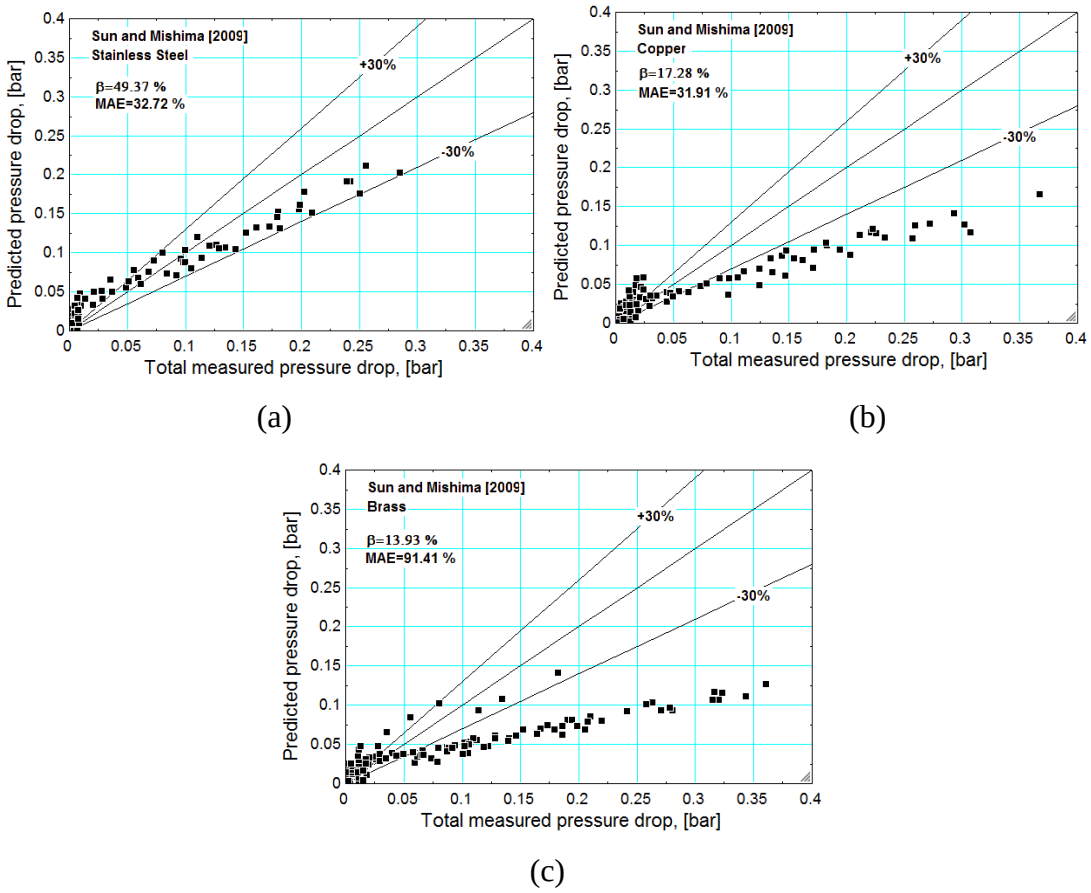

Figure 8.23. Comparison of the Sun and Mishima (2006) correlation with the experimental pressure drop for (a) stainless steel, (b) copper and (c) brass.

Lee et al. (2010)

A data bank consisting of 484 data points, including both water and refrigerants, from 9 sources, was used to produce the Lee et al. (2010) correlation. The data bank consisted of pressure drop results from micro channels only, with hydraulic diameters less than 3 mm. The experimental data points included data from both circular and rectangular channels and single and multi-channel configurations. The Chisholm constant (C) was adapted to include the Bond number and exit quality, see Appendix B. The Bond number was seen to be an important factor in the interactions between the phases. A low Bond number was associated with confined bubbles and consequently a reduced phase interaction. Higher Bond numbers corresponded to more phase interactions, such as seen in bubbly flow. This is in agreement with the data seen for R245fa, where the Bond value is relatively low and bubbly flow is rarely seen, see

Chapter 5. This adapted Chisholm constant gives considerably higher values than those of the original Lockhart-Martinelli constant. Figure 8.24 shows a scattering of the data, with only 20% of the data predicted within ± 30%. For stainless steel, this is mainly for the higher heat flux data. The results for copper and brass, although still scattered, presented a more defined trend, see figure 8.24 b and c. The highest agreement was seen for copper but with a low value of β=27.2% and a slightly higher MAE value than stainless steel of 53.3%. As seen with stainless steel, the results are spread across being under and over predicted but contrary to stainless steel, both copper and brass have more data under predicted.

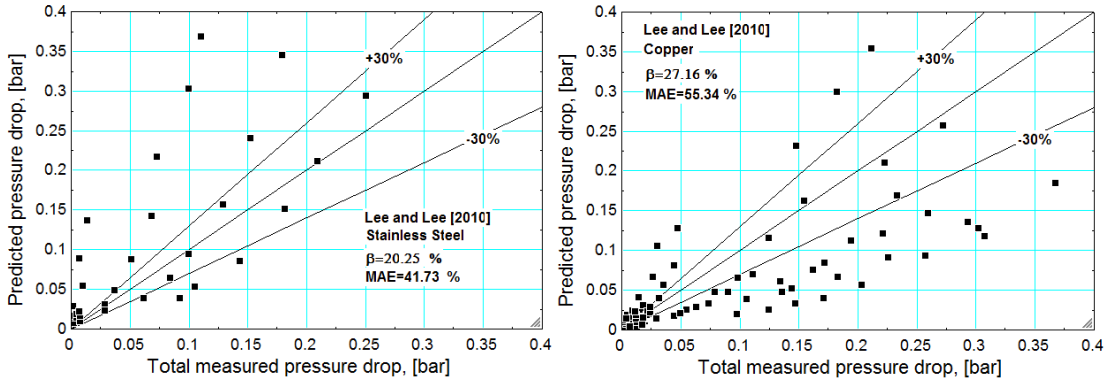

(a)

(b)

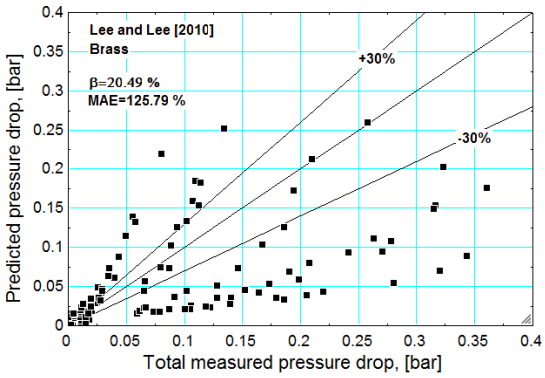

(c)

Figure 8.24. Comparison of the Lee and Lee (2010) correlation with the experimental pressure drop for (a) stainless steel, (b) copper and (c) brass.

Li and Wu (2010)

Li and Wu (2010) produced a data bank consisting of 769 data points, including 12 refrigerants and diameters of 0.148 to 3.25mm. The databank also includes the relative roughness of the channels, ranging from 0.011% to 0.435 %. The effect of the relative roughness on the pressure drop was not investigated. In agreement with the Lee and Lee (2010) correlation, the Bond number was deemed to be an important factor in

micro channel pressure drop. The Li and Wu (2010) correlation included two modified Chisholm constants, with the applied 'C' function depending on the Bond number. For Bond numbers ≤1.5, the C function is based on the Bond number only. For 1.5 < Bd ≤11 the C function used both the Bond number and the Reynolds number. This correlation showed poor agreement with stainless steel, with the data being scattered and over predicted. The correlation is seen to over predict at all heat fluxes for R245fa, see figure 8.25a. This over prediction results in an improved agreement for copper and brass which have higher measured pressure drop. The best agreement is with brass in terms of the β value but has the highest MAE value as those data points which are outside of the ±30% show a large discrepancy between the predicted and experimental pressure drop. As opposed to the stainless steel results which are over predicted, brass shows more data under predicted except at low pressure drop values were results are over predicted.

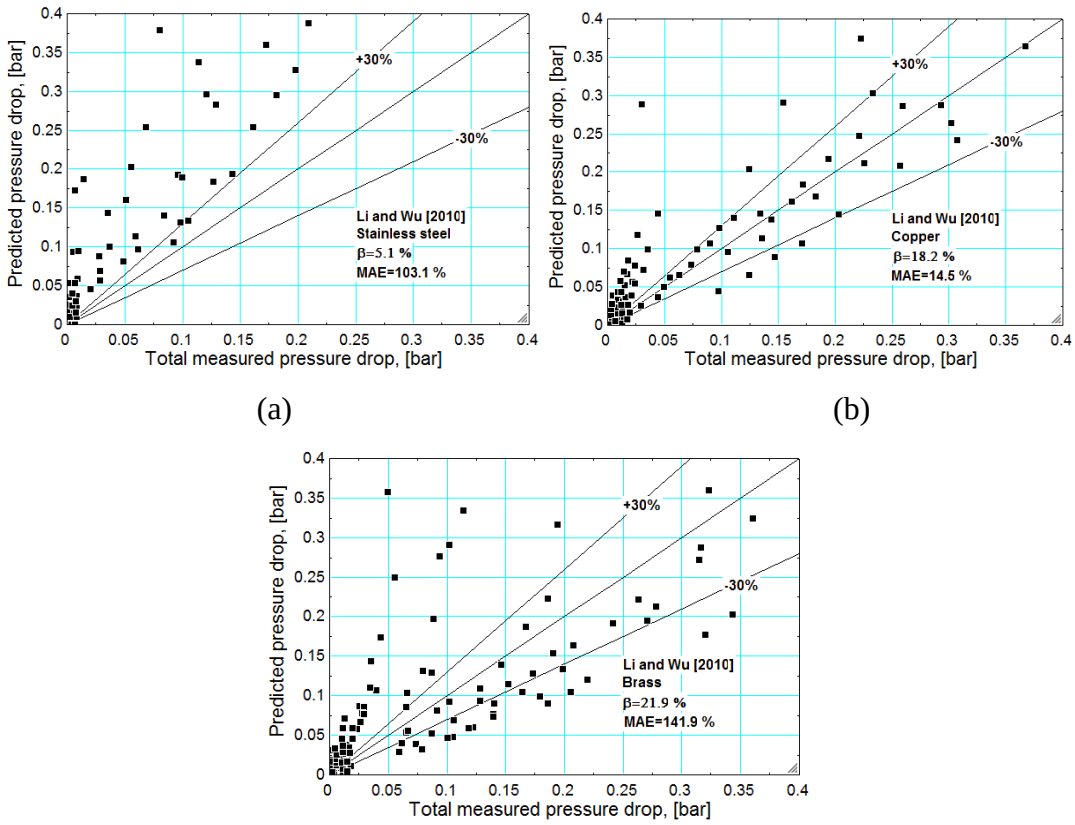

(a) (b)

(c)

Figure 8.25. Comparison of the Li and Wu (2010) correlation with the experimental pressure drop for (a) stainless steel, (b) copper and (c) brass.

Zhang et al. (2010)

Zhang et al. (2010) used a data bank of 2201 points, with both water and refrigerants, to construct an artificial neural network to analyse the most important parameters for frictional pressure drop. The databank consists of multiple channel materials, including aluminium, brass, copper and stainless steel. This investigation concluded that the diameter and dimensionless Laplace function were deemed to be the most important function, over the channel diameter alone and vapour quality, see Appendix B. This resulted in a modified Chisholm constant which used a function of Laplace, which includes the diameter. This correlation is not recommended for turbulent flow and is suitable for channel diameters of 0.014 to 6.25 mm. The Laplace function includes the surface tension, gravity, change in density and channel diameter. Figure 8.26 a shows that for stainless steel, the data at higher heat fluxes is underpredicted, with the data falling outside of the acceptable range as the heat flux increases. Data at medium heat fluxes, relating to measured pressure drops of 0.1 – 0.25 bar, is predicted well resulting in a β value of 40.5 %, which is more than double that of the other materials. The correlation predicts poorly the pressure drop for copper and brass, with the pressure drop being under predicted except at low measured pressure drop values. Similar β values are seen for copper and brass, 14.1% and 16.2%, respectively, but brass has a higher MAE value.

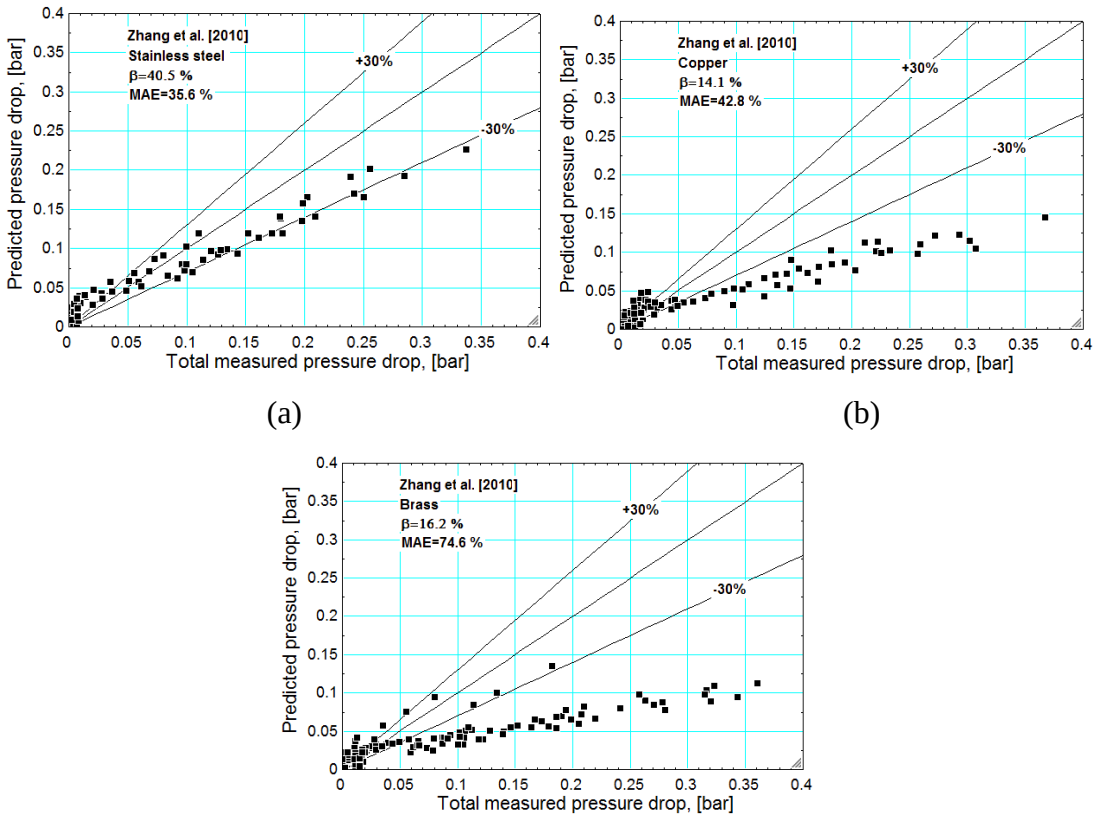

Figure 8.26. Comparison of the Zhang et al. (2010) correlation with the experimental pressure drop for (a) stainless steel, (b) copper and (c) brass.

Kim and Mudawar (2012)

Kim and Mudawar (2012) concluded that pressure drop correlations in literature were based on a narrow experimental range resulting in poor agreement. A data base was formed from 36 sources which included 17 working fluids and channel diameters from 0.0695 to 6.22 mm. The resulting correlation was deemed suitable for both single and multi-channel configurations for mini to micro diameters. The correlation was based on the Lockhart-Martinelli (1949) correlation, with the Chisholm constant (C) changing based on the turbulence for both the liquid and vapour phases. The range of turbulence for laminar or turbulent flow depends on whether the channel is circular or rectangular. For the whole range, the C function uses the liquid only Reynolds number, ratio of liquid and vapour density and the vapour only Suratman number, Su. The Suratman number is defined Appendix B and is a function of the vapour density, surface tension, diameter and vapour viscosity. This correlation showed the best agreement with stainless steel, predicting 51.2% of the data within ±30%. The β values are considerably lower for copper and brass, of 12.4% and 14.8%, respectively. However, the MAE

value is large for brass at 110.9%, see figure 8.27 c. The pressure drop is over predicted at low measured pressure drop values and under predicted for measured pressure drops over 0.05 bar for copper and brass.

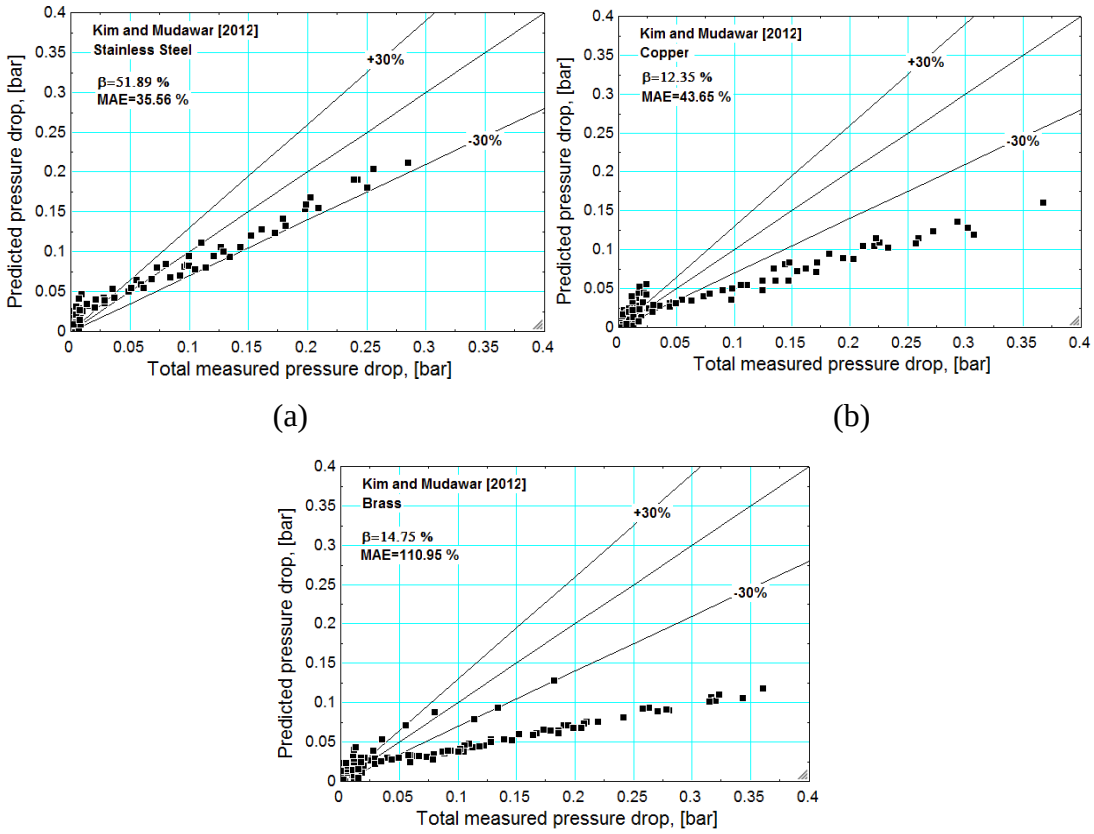

Figure 8.27. Comparison of the Kim and Mudawar (2012) correlation with the experimental pressure drop for (a) stainless steel, (b) copper and (c) brass.

Del Col et al. (2013)

The Del Col et al. (2013) correlation uses the average surface roughness, Ra, in the calculation of the liquid only friction factor, with the dependence of the average roughness varying with the liquid Reynolds number. An adapted liquid only Reynolds number, based on Ra value and numerical constants, is used to define the range at which further surface roughness equations are applied. When the adapted liquid only Reynolds number is greater than the liquid only Reynolds number, the value is reduced to zero, resulting in no surface roughness effect on the pressure losses. High values of liquid only Reynolds number, greater than 3500, the flow is fully developed and the effect of the surface roughness is balanced by the corrective coefficient, X_{Del}. For values between these ranges, the X_{Del} value is based on the surface roughness parameter. The surface roughness parameter is the relative roughness, which equates to double the average

surface roughness divided by the diameter, see Appendix B. The two phase frictional multiplier is calculated from the Cavallini et al. (2009) method which applies a combination of the entrainment ratio, E, and new parameters . The entrainment ratio varies between 0 and 0.95, with values between these values ranging with the homogenous gas core density, liquid density, liquid viscosity, surface tension and the superficial gas velocity. The new parameters, see Appendix B, include functions of the reduced pressure, density ratios and viscosity ratios. As the Ra value is only a factor in the liquid only friction factor, the influence of the surface characteristics was seen to be small. The liquid only friction factor is larger for brass, more than double that for copper, but the measured pressure drop only shows a slight variance. For stainless steel, the data is overpredicted, with only 1.3 % of the data predicted within ± 30%. The correlation showed a slight improvement for copper, predicting 11.1 % of the data and again for brass, predicting 25.4 % of the data. The trends in the predicted pressure drop vary between the materials, see figure 8.28. The effect of the average roughness on the pressure drop is dependent on the liquid only Reynolds number, see appendix B. All of the experimental data is in the $Re_{lo}^{+} < Re_{lo} < 3500$ range, which equates to the effect of Ra not being fully developed. The effect of Ra increases with liquid only Reynolds number and hence mass flux. The brass results show a wider scatter due to this mass flux effect. The measured pressure drop shows only a moderate dependence on the mass flux compared with copper and stainless steel. This correlation predicts a greater increase in pressure drop with mass flux then seen for any of the experimental results. This in turn results in a larger scatter seen for the brass results.

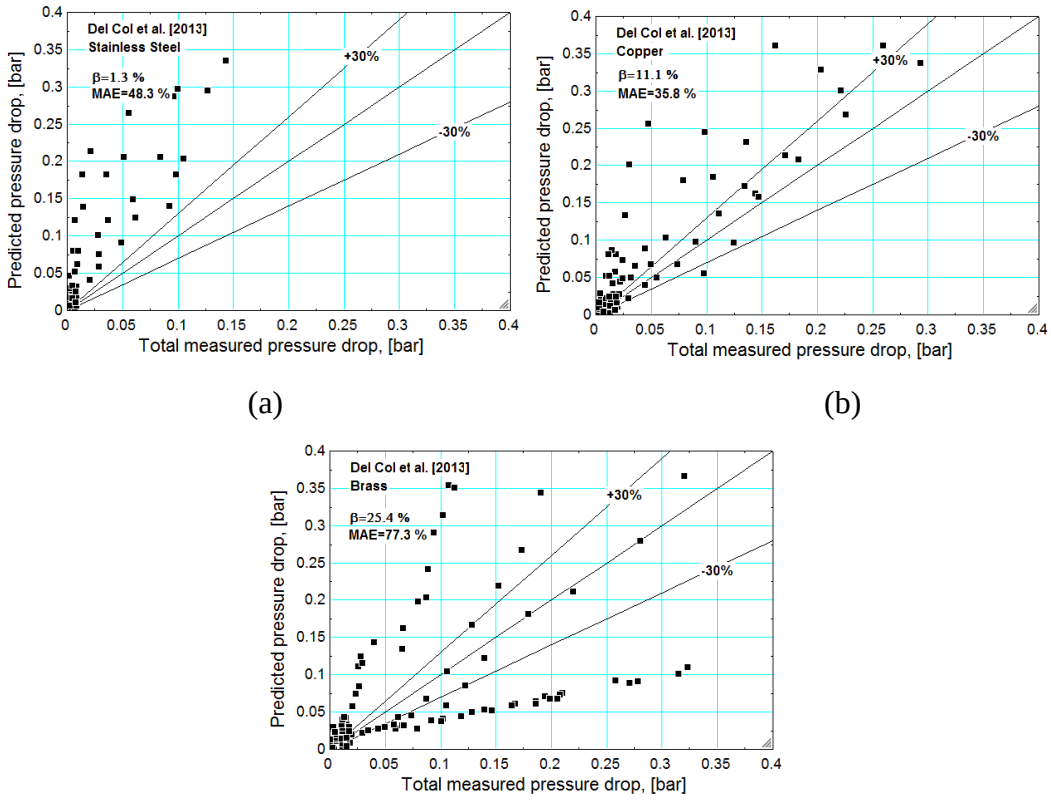

Figure 8.28. Comparison of the Del Col et al. (2013) correlation with the experimental pressure drop for (a) stainless steel, (b) copper and (c) brass.

8.7 Summary of correlations

Macroscale and microscale pressure drop correlations were evaluated based on R245fa data from tubes of three different materials. The total measured pressure drop was seen to be a function of the surface characteristics, with brass having the highest pressure drop and stainless steel the lowest. This effect was not captured with any of the correlations considered, with all bar one not including a function of surface characteristics. Although the Del Col et al. (2013) does include a function of the average surface roughness, the predicted pressure drops were similar between the materials, resulting in poor agreement. This is due to the structure of the correlation, where the influence of the surface roughness changes with the liquid only Reynolds number. The experimental liquid only Reynolds number is within the range where the surface effects are not fully developed and therefore only account for a small change in the frictional pressure drop. The average surface roughness, Ra, values were not seen to follow the same trend as the measured pressure drop which further explains the poor agreement with the Del Col et al. (2013) correlation. There was no one correlation which was best for all of the materials. Lee and Lee (2001) gave the best prediction for stainless steel

with values of β=59.5% and MAE=32.2%. Muller-Steinhagen and Heck (1986) was the best performing correlation for both copper and brass with β values of 38.3 % and 32.8 % and MAE values of 12.9 % and 52.9 %, respectively. There was no improvement from using correlations produced with microscale data or that of data which covered both micro and macroscale data for copper and brass. The best performing correlations for these channels were those produced for macroscale tubes, namely those of Muller-Steinhagen and Heck (1986) and Friedel (1979). Kim and Mudawar (2012), Lee and Lee (2001) and Hwang and Kim (2006) showed the best agreement for stainless steel. These correlations all have C values which focus on the liquid properties, mainly that of Re_{fo}. These correlations also include fluid properties, such as the density, viscosity and surface tension as well as the vapour quality. There was no obvious relation to the size or variety of the data bank used and the correlation results. Those correlations with a large data bank of varying diameters and working fluids (Kim and mudawar (2012), Zhang et al. (2010), Li and Wu (2010), Lee et al. (2010), Sun and Mishima (2009)) showed no improvement over those which are based on only one fluid or one channel diameter. The database used by Li and Wu (2010), Zhang et al. (2010) and Kim and Mudawar (2012) include the use of different channel materials. Although, for all of these studies, the effect of the channel material on pressure drop was not investigated. There was no improvement in the performance of these correlations, with all but the Li and Wu (2010) performing worse for copper and brass. As previously discussed, the pressure drop is assumed to be linear across the length of the channel. This results in a discrepancy between the predicted and linear pressure drop, especially at the entrance to the channel. This may result in the discrepancies seen at low pressure drop values.

The measured pressure drop was seen to be a function of the inlet pressure; this is most evident at higher heat fluxes. The difference was less evident for stainless steel than with copper and brass. The effect of pressure was correlation dependent, with the effect being smaller for correlations which included refrigerant properties which change with pressure. Those correlations which are not based on the fluid properties and remain constant show a difference in prediction results between pressures. The effect of heat flux is evident for all of the correlations for all materials and both inlet pressures. These factors were a function of how well the correlations performed at low or high heat fluxes. The method used for correlation analysis, based on β and MAE, can be skewed by data of different heat fluxes. There are some correlations (Lockhart-Martinelli (1949), Friedel (1979), Lee and Lee (2001)) which show a good agreement at higher measured pressure drops, relating to higher heat fluxes.

Figure 8.29 presents the two phase frictional multiplier, see Appendix B for appropriate equations, plotted as a function of the exit vapour quality for the three best and worst performing correlations for stainless steel with R245fa. All of the frictional multipliers follow the same trend, increasing with exit vapour quality. The three best performing correlations (Hwang and Kim (2006), Kim and Mudawar (2012), Lee and Lee (2001)) are shown to have only a small discrepancy from each other. The worst performing correlation, Warrier et al. (2002), which predicted none of the data within the ±30% range shows a considerably higher frictional multiplier. This larger frictional multiplier corresponds to the over prediction of two phase pressure drop, this was also shown with Li and Wu (2010), although to a reduced degree. The Mishima and Hibiki (1996) correlation under predicts the data which is shown by a smaller frictional multiplier. As the materials are tested under the same experimental conditions, the frictional multiplier is calculated to be the same for each test section (although there are slight variations due fluctuations in the temperature and pressure at which the fluid properties are taken). As seen in figure 8.5, the measured pressure drop varies between the materials which is not captured in the correlations. It can be clearly seen that for all of the pressure drop correlations, there is a distinct change in gradient between the experimental and predicted pressure drop. This is due to equal frictional multipliers being used for all materials. The magnitude difference between the results for different materials is also reflected in the β and MAE values. The pressure drop has been over predicted for stainless steel, thus resulting in poor β and MAE values and the predictions are better for copper and brass as these have a higher measured pressure drop. This accounts for the materials all following the same trend when plotted as the measured pressure drop versus predicted pressure drop but with varying gradients.

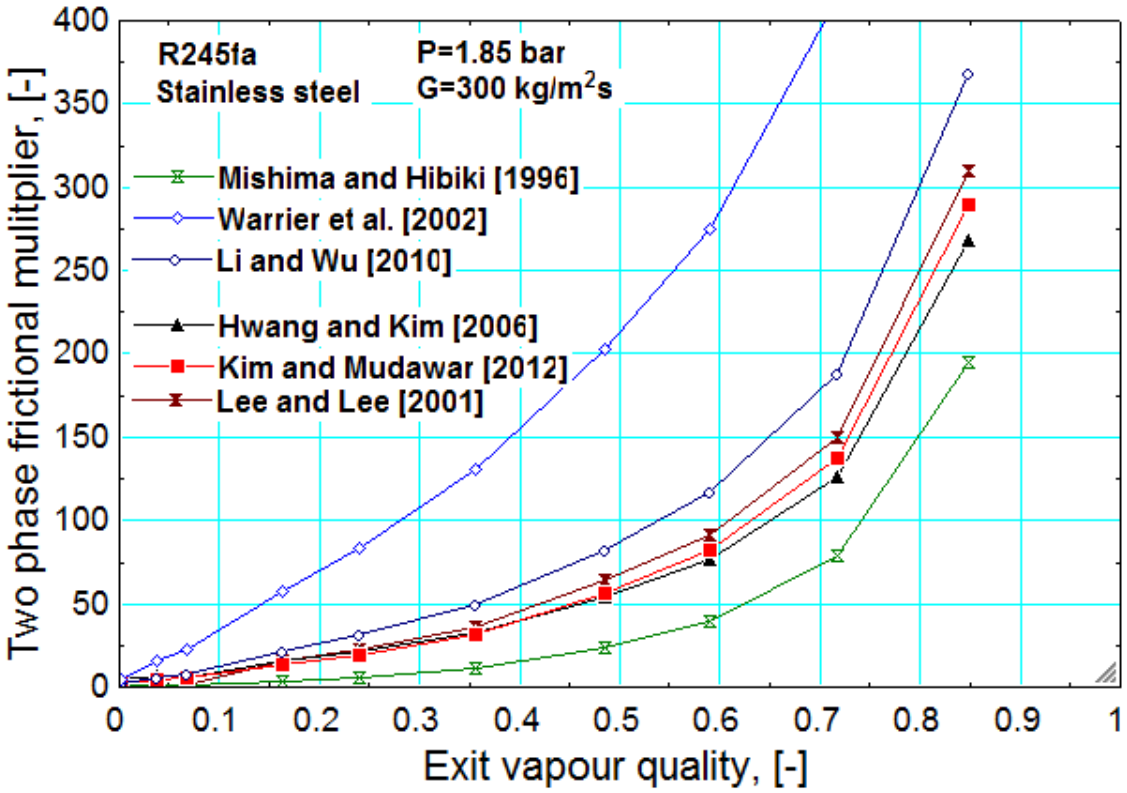

Figure 8.29. Two phase frictional multipliers as a function of exit quality for stainless steel at P=1.85 bar and G=300 kg/m^{2}s.

The magnitude difference between the different frictional multipliers is not equal to the magnitude difference between the predicted pressures. This is due to variations in the structure of the frictional equations. For example, Lee and Lee (2001) included the liquid friction factor, mass flux, diameter and liquid density into the integration of the frictional multiplier, see equation 8.17. This is in contrast to Warrier et al (2002) who excluded these factors from the integral, using the liquid only friction factor, see equation 8.18. Although both use the same variables, the difference in equation structure accounts for a 10% difference in the predicted pressure drop after taking into account the difference in the frictional multiplier.

$$\Delta P_f = \frac{L_{tp}}{x_e}\int_0^{x_e}\frac{2f_{lo}G^2}{D\rho_l}\phi_L^2 dx \tag{8.17}$$

$$\Delta P_f = \frac{2f_lG^2}{D\rho_l}\frac{L_{tp}}{x_e}\int_0^{x_e}\phi_{Lo}^2\, dx \tag{8.18}$$

It can be noted that correlations which only integrate the frictional multiplier used the liquid friction factor and all those which include more functions use the liquid only friction factor.

Evaluating the pressure drop correlations based on the trends seen when plotted as a function of the measured pressure drop show Lee and Lee (2001) and Lockhart-Martinelli (1949) to show a good agreement with R245fa in a stainless steel tube. Although both of these have relatively high β and MAE values, these values can be skewed by low heat flux values. These two correlations both consider the whole flow range, combinations of laminar and turbulent flow for both liquid and vapour phases for the Chisholm constant.

The correlations were further evaluated based on the wok by Mahmoud (2011) who conducted flow boiling experiments using R134a. In general, the correlations performed better for R134a in comparison with the R245fa. This is thought to be due to the high pressure drop seen with the low pressure refrigerant. Also, most correlations did not include R245fa in their databank. The best correlation for R134a was Mishima and Hibiki (1996), with β and MAE values of 83.6 and 21.8 %, respectively. This shows a much better agreement compared with R245fa, where the highest performing correlation had β and MAE values of 59.5 and 32.2 %, respectively.

8.8 Summary

Two phase pressure drop experiments were conducted using R245fa for a mass flux range of 100-400 kg/m^{2}s and inlet pressures of 1.85 and 2.45 bar. The effect of refrigerant was investigated using R134a, in the same stainless steel tube, at corresponding inlet saturation temperatures of 31 and 39˚C. Copper and brass test sections were used with R245fa to investigate the effect of surface characteristics. The results show that, regardless of fluid and channel material, that the two phase measured pressure drop increases with heat flux but the extent of this increase is fluid and material dependent. For all cases, the effect of inlet pressure is only evident at higher heat fluxes. Although the two phase pressure drop increases with mass flux, this increase is less evident with brass. The differences seen between the two refrigerants and the surface characteristics are attributed to a change in the frictional component. The difference in thermophysical properties is reflected in the two phase frictional multipliers which are up to 3 times larger for R245fa. In general, the pressure drop correlations performed better for R134a than for R245fa, with R245fa being under predicted.

The pressure drop varies with the channel material, with brass having the highest pressure drop and stainless steel the lowest. The change in surface structure will affect the frictional losses, with the most important parameters relating to the shape and size of the surface peaks. The pressure drop correlations evaluated do not include a function of

surface characteristics. Those surface characteristics which do follow in the same trend as the measured pressure drop include Rp and Rsm, both of which have limitations in surface definition. The pressure drop correlations showed better results for the stainless steel compared with the copper and brass tubes. This is expected as, in general, the correlations under predict the pressure drop for R245fa and stainless steel has the lowest measured pressure drop. Copper has the intermediate pressure drop and brass the highest but this trend is not reflected in the correlation results. On the whole, the pressure drop correlations under predicted the experimental pressure drop.

Table 8.2. Correlation results for stainless steel, copper and brass.

Correlation	Stainless Steel		Copper		Brass	
	β, %	MAE, %	β, %	MAE, %	β, %	MAE, %
Homogenous model	35.4	36.6	17.2	33.9	26.8	28.8
Lockhart-Martinelli (1945)	45.8	37.1	18.2	24.1	21.9	95.3
Friedel (1979)	41.8	37.1	27.2	46.8	22.1	95.6
Muller-Steinhagen and Heck (1986)	26.6	33.7	38.3	12.9	32.8	52.9
Wang et al. (1997)	29.4	37.3	12.4	59.7	15.6	136.9
Mishima and Hibiki (1996)	6.3	81.0	8.1	149.9	13.8	219.5
Tran et al. (2000)	25.3	24.1	12.3	20.2	14.8	76.7
Lee and Lee (2001)	59.5	32.2	20.9	60.9	24.6	137.2
Warrier et al. (2002)	0	206.2	10.1	43.2	17.8	84.3
Yu et al. (2002)	21.5	73.0	15.2	110.4	14.6	107.4
Qu and Mudawar (2003)	31.6	118.4	20.2	22.3	23.6	55.4
Hwang and Kim (2006)	50.4	30.6	17.3	24.5	17.2	99.9
Lee and Garimella (2007)	29.1	73.0	18.2	24.9	17.1	39.9
Sun and Mishima (2009)	49.4	32.7	17.3	31.9	13.9	91.4
Lee et al. (2010)	20.3	41.7	27.2	55.3	20.5	125.8
Li and Wu (2010)	5.1	103.1	18.2	14.5	21.9	141.9

Zhang et al. (2010)	40.5	35.6	14.1	42.8	16.2	74.6
Kim and Mudawar (2012)	51.9	35.6	12.4	43.7	14.8	110.9
Del Col et al. (2013)	1.3	48.3	11.1	35.8	25.4	77.3

Chapter 9

9. Conclusions and recommendations

9.1 Conclusions

Flow boiling experiments were conducted using R245fa in channels of 1.1 mm internal diameter. A stainless steel channel was used for a comparison of R134a, with data from a previous study conducted by Mahmoud (2011) and R245fa. Two further channels, of copper and brass with the same diameter, were used to investigate the effect of surface characteristics. The 300 mm long channels were heated directly using DC current. A calming section of 150 mm was positioned before the heated length to ensure that the flow was fully developed. A borosilicate glass channel, of 1.1 internal diameter, was positioned after the heated channel to allow for flow visualisation. The experiments were conducted over a mass flux range of 100 – 400 kg/m^{2}s, a vapour quality range of 0-0.95, and inlet pressures of 1.85 and 2.45 bar. The effect of refrigerant and surface characteristics on the heat transfer coefficient, two phase pressure drop and flow patterns was evaluated directly and in comparison with R134a. The effect of hysteresis was also investigated. The experimental data were also compared with flow pattern maps and correlations in literature.

9.2 Surface measurements

The inner surface of three channels were analysed using Scanning Electron Microscopy (SEM) and Confocal Laser Microscopy (CFSLM). SEM is widely used in industry as a form of visually analysing the surface. This method allowed for a comparison of the surface structure, which differed between the materials. All of the channels were seamless cold drawn and therefore the differences seen on the surfaces were due to the material and not the manufacturing method. Distinct differences were seen between each material, which could result to differences in the nucleation sites. SEM however does not allow for any tangible data, i.e. surface parameter values, of the surface which can be used for comparison.

CFLSM produces 3D surface profiles and surface parameter data for the surfaces which can be used in comparisons. Unlike SEM, there are many scan variables which can affect the surface parameter data as the results are subject to interpretation.

a. The scan is conducted over a mesh or grid, with the values in each grid being averaged to give the surface parameters. A large grid

system, equating to a low resolution, will give different values from that of a small grid or high resolution. In general, the surface parameters values decreased with the resolution. This is due to the increase averaging of the surface structure.

b. The scan size or scan area will also have an effect on the surface parameter readings, as the surface parameter values are averaged. A change in the scan area was seen to affect all of the surface parameters. This was partly due to surface peaks and flaws being excluded when the scan area was decreased.
c. The scan size and scan resolution were evaluated separately but are linked. A change in the scan size will change the scan resolution as the grid sizes will change. Therefore, an appropriate scan size for the desired resolution should be considered.
d. The only parameter, if any, which is reported with surface parameter data is that of the cut-off value. The cut-off value refers to how the surface data is filtered and which data is considered to the profile, the waviness and the roughness. A large cut-off value can give inflated roughness values as a large amount of data is considered to be within the finer range which is associated with roughness. This was evident when the cut-off value was increased from 0.08 to 0.8 mm, where the Ra, Rq and Rv values increased with cut off. The appropriate cut-off value will depend on the geometry of the sample and the application.
e. The CFLSM readings were conducted using two different profilers, a TaiCaan surface profiler and an Olympus Lext 3100 microscope. The same trend was seen for the different tube materials with both profilers but the values were different. Although both utilise confocal microscopes, the set up and parameters which can be varied are different between the two profilers which results in difference surface parameter values. Rp did show a difference in trend, being lowest for stainless steel using the TaiCaan but lowest for copper using the Olympus Lext 3100. This could be a result of variations in the surface area used for evaluation.

The limitations of SEM and CFLSM can result in difficulties or inconsistencies in comparing surface characteristic data between laboratories. This is partly due to the differences seen between the two surface profiling machines. Further issues arise from

the lack of information which is reported in literature, i.e. with surface data reported with no information regarding the cut off value or scan set up resulting in incomparable data.

9.3. Flow patterns

Flow patterns were recorded simultaneously to the heat transfer and pressure data for both increasing and decreasing heat fluxes. Differences were seen between the flow patterns for R134a and R245fa due to differences in the thermophysical properties.

a. For increasing heat flux, bubbly, slug, churn and annular flow were evident for R134a with no hysteresis effect.
b. For R245fa, annular flow dominated for an increasing heat flux, with only churn and annular flow seen. The higher surface tension, 80 % higher, of R245fa facilitates transition into annular flow from churn flow.
c. Hysteresis was evident for R245fa, with bubbly, slug and churn flow evident for a decreasing heat flux. Hysteresis is a result of nucleation sites activating when the heat flux is increased and remaining activated as the heat flux is decreased. The wall superheat, linked to activation of nucleation sites, is lower for R245fa.
d. The effect of inlet pressure with heat flux, at saturation temperatures of 31 and 39 ºC, was the same for both fluids but to different extents. The change in inlet temperature changes the fluid properties, decreasing the surface tension by 16 % and 8 % for R134a and R245fa, respectively.

The surface characteristics were seen to have an effect on the exit vapour quality and heat fluxes at which the flow patterns occurred due to the differences in the potential nucleation sites, evident from the SEM and CFLSM comparison.

a. Mass flux had an effect on the flow transitions, with an increase in the mass flux shifting flow transitions to lower vapour qualities. The trend of this shift was material dependent, with the flow pattern transitions for brass occurring at a higher vapour quality than stainless steel, but having similar trends. For copper, the gradient of the flow transitions, plotted as a function of mass flux and vapour quality, is shallower with the highest vapour quality for the transitions.

b. The differences seen in flow transitions between the three materials with mass flux were evident when comparing the flow pattern maps for each tube. Due to the dominace of annular flow with increasing heat flux, flow pattern maps were evaluated based on the decreasing heat flux data.
c. The Chen (2006) flow pattern map, originally based on R134a experiemental data, gave the best agreement, for slug, churn and annular flow. Bubbly flow occurred at higher superficial gas velocities than predicted by Chen (2006).
d. The onset of nucleate boiling and experimental conditions at which certain flow patterns occurred, namely exit vapour quality and heat flux, were seen to be material dependent. This is a result of changes in the number of potential nucleation sites and differences in the wall superheat. The channel material and consequent surface characteristics should be considered as one of the important parameters for future flow pattern maps. The main differences seen were a result of the onset of nucleate boiling, which is a function of the average surface roughness, Ra. Although a larger range of Ra values need to be tested to verify this connection.

9.4. Heat transfer characteristics

9.4.1 Effect of refrigerant

The effect of refrigerant on the heat transfer coefficient was conducted using R134a and R245fa in a stainless steel channel. The comparison was based on the effect of heat flux, mass flux and inlet pressure on the heat transfer coefficient plotted as a function of the vapour quality and axial location.

a. The R134a heat transfer coefficient data reported by Mahmoud (2011) were seen to increase at low heat fluxes, 7 – 13 kW/m^2, after which the heat transfer coefficient is at higher values, between 7000 and 12000 W/m^{2}K before dry out occurs at which point it decreases. This is based on a mass flux of 200 kg/m^{2}s and saturated temperature of 31˚C. The heat transfer coefficient is seen to remain relatively flat with both vapour quality and axial location.

b. For the same mass flux and inlet saturation temperature, the onset of two phase heat transfer coefficient occurred at 7 kW/m^2 for both refrigerants. The dry out, signified by a decreasing heat transfer coefficient, occurred at 41 kW/m^2 for both R134a and R245fa. The heat transfer coefficient was seen to increase with vapour quality, with highs of 11 kW/m^2, with peaks in the heat transfer coefficient. The heat transfer coefficient increases at the channel exit, due to the thinning of the liquid film during annular flow.
c. There was no mass flux effect for either R134a or R245fa when the heat transfer coefficient is plotted as a function of vapour quality or axial location.
d. For both R134a and R245fa, the higher inlet pressure resulted in a higher heat transfer coefficient, but with a larger difference for R134a. This is due to the thermophysical properties changing by a greater extent for R134a than for R245fa. The surface tension changed by 16 % for R134a and 8 % for R245fa.

9.4.2 Effect of surface characteristics

a. When the heat transfer coefficient for R245fa is plotted as a function of axial location, it is evident that peaks occur at the same axial location in the stainless steel channel. The same heat transfer coefficient peak is evident across all mass fluxes, inlet pressures and mass fluxes. This suggests that this is a result of a surface flaw. This flaw was not evident with R134a which could be due to the differences in the wall superheat resulting in the nucleation site not being activated with R134a. The occurrence of a surface flaw was validated by reversing the orientation of the channel. The magnitude of the heat transfer coefficient was lower for the reversed channel with a 'flatter' trend. The channel was returned to the original orientation and the same peaks occurred and an increase in the heat transfer coefficient was seen. Therefore, the changes seen with the reversed orientation are a result of changes in surface conditions which is directly linked to flow patterns and heat transfer coefficients. This validated a clear

effect of the surface characteristics. However, this further highlights a limitation in the use of surface parameters to define a heater surface. The same channel was used, and therefore the surface parameters were constant, but the direction of flow over these surface flaws had an effected on the heat transfer coefficient.

b. The heat transfer coefficient for brass was seen to change in trend and magnitude compared with stainless steel. The heat transfer coefficient increased from 10 kW/m^2 but, due to the occurrence of instabilities, testing was stopped before dry out could occur. When plotted as a function of both vapour quality and axial location, the heat transfer coefficient shows a smooth increase, with a higher local heat transfer coefficient than stainless steel.
c. Peaks were seen in the brass heat transfer coefficient at a constant axial location, which were evident when plotting it as a function of axial location. This peak was only seen at the higher inlet pressure. This is thought to be a result of a nucleation site activating at different wall superheats.
d. The copper channel has a large heat transfer coefficient peak at a heat flux of 8 kW/m^2 and increases with vapour quality at a heat flux of 10 kW/m^2. After which, the heat transfer coefficient remains relatively constant with vapour quality at a lower heat transfer coefficient of between 3000 and 5000 W/m^2K.
e. There was no mass flux effect evident for any of the channels.
f. The heat transfer coefficient increased with inlet pressure for all materials.

A clear effect of surface characteristics on the heat transfer coefficient was evident. This is in terms of both the magnitude and trend of the heat transfer coefficient. However, there was no clear trend between the surface parameter values and the magnitude of the heat transfer coefficient. There was a trend between the average surface roughness, Ra, and the onset of nucleate boiling. A comparison of the boiling curves showed the same ratio between the wall superheat and the Ra values for the three materials.

9.5. Heat transfer correlations

There are multiple correlations in literature for the prediction of the heat transfer coefficient, for both macro and microscale channels. A selection of correlations was evaluated based on the percentage of data predicted within ± 30 %, β, and the mean absolute error, MAE.

a. There was no one correlation which showed good agreement with both R134a and R245fa, with correlations generally performing better for R134a. The increase in the heat transfer coefficient with vapour quality for R245fa was not predicted. This could be due to R245fa data not being widely used in the data banks used to produce the correlations and partly due to discrepancies in both the trend and magnitude of the reported heat transfer coefficient as a function of vapour quality for R245fa in literature.
b. The best performing correlation both refrigerants was that of Mahmoud and Karayiannis I (2012) which predicted 42.2 % of the R245fa data and 92.8 % of the R134a data to within ± 30 %.
c. The Cooper (1984) correlation performed well for stainless, with a β value of 41.2 %. This is a pool boiling correlation based on nucleate boiling. Cooper (1984) includes a function of the surface characteristics, incorporating the $Rp_{,old}$ value. This verifies that the surface characteristics and hence the nucleate boiling component is important to flow boiling.
d. There was no one correlation which was suitable for all three materials, with considerably lower β values for copper. Considering all of the channel materials, the three best correlations are Liu and Winterton (1991), Mahmoud and Karayiannis I (2012) and Li et al. (2013). There was no clear improvement in the use of microscale correlations over macrsocale correlations.
e. There was no correlation in literature which could be recommended to predict the effect of changes in the working fluid and channel material on heat transfer coefficient. Further work is required in producing correlations which include larger data banks which can evaluate a larger range of experimental conditions.

9.6. Pressure drop characteristics

The pressure drop along the tube is assumed to be linear, based on pressure readings at the inlet and outlet of the heated channel. Although the pressure drop will realistically not be linear, the differences seen between this assumption and that of the Friedel (1979) correlation are small. The measured pressure drop is compared between the two fluids and three channel materials as a function of heat flux. The measured pressure drop is the sum of the frictional, acceleration and gravitational components. The acceleration and gravitational components decrease in contribution with the increase in the exit vapour quality, as the frictional component increases.

9.6.1 Effect of refrigerant

a. The measured pressure drop for R245fa was seen to be 300 % higher than for R134a, while the pressure drop for both refrigerants increased with heat flux. The liquid viscosity is 110 % higher and vapour density is 75 % lower for R245fa, resulting in the difference in magnitude seen between the measured pressure drop.
b. The measured pressure drop is higher with a higher inlet pressure, with the difference between the two inlet pressures increasing with heat flux. This is due to the reduction in the liquid to vapour density ratio and liquid to vapour viscosity ratio with changes to the inlet conditions.
c. For both fluids, the measured pressure drop increases with mass flux. The acceleration and frictional components are calculated from the square of the mass flux, resulting in a quadratic increase with mass flux.

9.6.2 Effect of surface characteristics

Surface characteristics are an important consideration in pressure drop, mainly that of the frictional component. Surface flaws or peaks can act as a channel restriction and can disturb the liquid film. Both the number and the shape of the peaks are a consideration for the frictional pressure drop.

a. The measured pressure drop increases with heat flux for all three surfaces, but with different gradients. Brass, the roughest surface, has the highest pressure drop, with the steepest gradient. However,

copper, the smoothest surface, has the second steepest increase with heat flux. The pressure drop trend does not follow the surface parameters, which may be due to the surface parameters not considering the geometry of the surface characteristics.

b. The measured pressure drop decreases with inlet pressure, due to the changes in the thermophyscial properties, but to a different extent between the materials. The smoothest channel, copper, has the largest difference between the measured pressure drops for the two inlet pressures and the roughest surface, brass, has the smallest. This suggests that the surface characteristics dominate over the change in fluid properties.
c. Differences were seen in the single phase pressure drop between the materials. The single phase pressure drop for copper was double that of stainless steel, showing surface characteristics are important during single phase flow. The differences in the inlet pressures were more evident in the single phase region. The difference in the heat flux at which the single phase pressure drop changed into two phase pressure drop was largest for brass and the smallest for stainless steel.
d. The measured pressure drop showed a clear increase with mass flux for stainless steel and copper. The pressure drop for brass shows an overlap at mass fluxes of 200 and 300 kg/m^2s.

9.7. Pressure drop correlations

Pressure drop correlations from literature were evaluated based on the β and MAE values.

a. In general, the pressure drop correlations performed better for the R134a data reported by Mahmoud (2011). The pressure drop was considerably higher for R245fa which was not captured by the majority of the correlations. The best performing correlation for R245fa was Lee and Lee (2001), with values of β=59.5% and MAE=32.2%.
b. Although the Li and Wu (2010), Zhang et al. (2010) and Kim and Mudawar (2012) correlations used databases which included a variety of channel material, the effect of this difference in material

was negated. The only correlation which used a function of the surface roughness was that of Del Col et al. (2013). The extent to which the relative roughness impacted the predicted pressure drop was a function of the Reynolds number, with the correlation equations changing with Reynolds number range. The experimental Reynolds number was in the range of the surface roughness not being fully developed and was therefore only a small percentage of the equation and there was little difference between the predicted pressure drops for the three materials.

c. Muller-Steinhagen and Heck (1986) was the best performing correlation for both copper and brass with β values of 38.3 % and 32.8 % and MAE values of 12.9 % and 52.9 %, respectively. In general, the correlations performed worst for copper and brass over stainless steel. This is due to the higher pressure drop of copper and brass not being predicted.

9.8. Recommendations

After an evaluation of the current experiments, the following future work is recommended.

a. Further investigation into defining a suitable heater surface is required. Differences are seen in the surface structure between the materials but the heat transfer and pressure drop experimental results don't follow the same trend as the surface parameter data. This could be a result of the differences in the shape of the surface flaws, which is not currently reported. Current work in this area has only included numerical modelling. As current surface profilers are limited and unable to define the shape, artificial surfaces can be constructed for experimental validation.
b. The effect of channel characteristics dominated over that of the change in thermophysical properties for the pressure drop. Test sections which include a larger range of roughness' can be used to investigate the boundary at which surface roughness dominates over the fluid properties. This can include the use of different fluids to fully understand which fluid properties are dominated by the effect of surface characteristics.

c. The effect of the manufacturing process on stainless steel channels was conducted by Mahmoud (2011). The current study found that, with the same manufacturing method, the surface finish was a function of the material. Further investigations could include further combinations of materials and manufacturing methods.
d. The reversal of the channel orientation was seen to change the heat transfer coefficient. This suggested that not only the surface characteristics are an important consideration but also the direction of the flow over the these characteristics. Further experiments into the effects of reversing the flow direction is needed to fully clarify this.
e. Discrepancies in literature were associated with the effect of surface characteristics and flow instabilities. Surface characteristics have been shown to have an influence on two phase flow boiling. Flow instabilities were evident during the experiments but were not investigated. Further work on the control of these instabilities, potentially with inlet restrictions, could allow for a larger range of experimental conditions to be examined for copper and brass, where flow instabilities resulted in the experiments being stopped at relatively low heat fluxes.
f. Pressure drop and heat transfer correlations are generally based on experimental databanks, found in published literature. These databanks include a range of refrigerants, diameters and materials but as data is from multiple sources, there can be inconsistences. Therefore, constructing a large databank from one source which included a large range of channel materials and fluids would be beneficial for correlation developments.

References

Agostini, B., Thome, J.R., Fabbri, M., Michel, B., Calmi, D. and Kloter, U., High heat flux flow boiling in silicon multi-microchannels – Part II: Heat transfer characteristics of refrigerant R245fa, International Journal of Heat and Mass Transfer,51(21–22):5415-5425, 2008.

Ahn, S., Choi, I., Kwon, O. J., Kim, J. J., Hydrogen production through the fuel processing of liquefied natural gas with silicon-based micro-reactors, Chemical engineering journal, 247: 9-15, 2014.

Akbar, M.K., Plummer, D.A., Ghiaasiaan, S.M., On gas–liquid two-phase flow regimes in microchannels. Int. J. Multiphase Flow 29, 855–865, 2003.

Alam, T., Lee, P. S., Yap, C. R., Investigation of lfow boiling instabilities in silicon microgap heat sink, Electronics packaging technology conference (EPTC), 14th IEEE, Singapore, 2012.

Alam, T., Poh Seng Lee, Yap, C. R., Investigation of flow boiling instabilities in silicon microgap heat sink. Electronics Packaging Technology Conference (EPTC), 2012 IEEE 14th, 519-524, 2012.

Ali, R., Palm, B. and Maqbool, M.H., Experimental Investigation of Two-Phase Pressure Drop in a Microchannel, Heat Transfer Engineering, 32(13-14): 1126-1138, 2011.

Ali, R., Palm, B. and Maqbool, M.H., Flow Boiling Heat Transfer of Refrigerants R134a and R245fa in a Horizontal Micro-Channel, Experimental Heat Transfer, 25(3): 181-196, 2012.

Amon, C. H., Murthy, J., Yao, S. C., Narumanchi, S., Wu, C-F., Hsieh, C-C., MEMS-enabled thermal management of high-heat-flux devices EDIFICE: embedded droplet impingement for integrated cooling of electronics, Experimental thermal and fluid science, 25, 231-242, 2001.

Baek, S., Hwang, G., Kim. J., Jeong, S., Development of compact heat exchanger for LNG FPSO, Proceedings of the twenty-first (2011) International Offshore and Polar Engineering Conference, Maui, Hawaii, USA, June 19-24, 2011.

Baek, S., Lee, C., Jeong, S., Effect of flow maldistribution and axial conduction on compact microchannel heat exchanger, Cryogenics, 60: 49-61, 2014.

Bajus, M., Microchannel-Technologies, Petroleum and Coapricess imprices l, 54 (3) 294-300, 2012.

Balasubramanian, K., Jagirdar, M., Lee, P. S., Teo, C. J., Chou, S. K., Experimental investigation of flow boiling heat transfer and instabilities in straight microchannels, International journal of heat and mass transfer, 66: 655-671, 2013.

Bao, Z. Y., Fletcher, D. F., Haynes, B. S., Flow boiling heat transfer of Freon R11 and HCFC123 in narrow passages, International journal of heat and mass transfer, 43: 3347-3358, 2000.

Barnea, D., Luninski, Y., Taitel, Y., Flow pattern in horizontal and vertical two phase flow in small diameter pipes. The Canadian Journal of Chemical Engineering, 61(5), 617-620, 1983.

Bejan, A., Kraus, A. D., Heat transfer handbook, volume 1, Wiley and Sons, 2003.

Benati, F. Effect of surface topography upon the quality of autobody panels, PhD thesis, Brunel University London, 2003.

Bertsch. S. S., Groll, E. A., Garimella, S. V., A composite heat transfer correlation for saturated flwo boiling in small channels, International Journal of heat and mass transfer, 52: 2110-2118, 2009.

Bewoor, A. K., Metrology and measurement, Tata McGraw-Hill Education, pp. 271-286, 2009.

Biswas, J., Greenfield, P., Two phase flow through vertical capillaries—existence of a stratified flow pattern. International Journal of Multiphase Flow, 11(4), 553-563, 1985.

Blunt, L., Jiang, X., Advanced techniques for assessment surface topography: Development of a Bassis for 3D surface texture standards “Surfstand”, Elsevier, 2003.

Bobbo, S., Zilio, C., Scattolini, M., Fedele, L., R1234yf as a substitute of R134a in automotive air conditioning. Solubility measurements in two commercial PAG oils, International journals of refrigeration, 40: 302-308, 2014.

Bortolin, S., Col, D.D. and Rossetto, L., Flow Boiling of R245fa in a Single Circular Microchannel, Heat Transfer Engineering, vol. 32 (13-1): 1160-1172, 2011.

Brackbill, T. P., Kandlikar, S. G., Effect of sawtooth roughness on pressure drop and turbulent transition in microchannels, Heat transfer engineering, 28 (8-9):662-669, 2007.

Brauner, N. and Moalem-Maron, D., Identification of the range of small diameter conduits, regarding two-phase flow pattern transitions, Int. Commun. Heat MassTransfer, 19: 29-39, 1992.

Breithaupt, J., New understanding physics for advanced level, Nelson Thornes, 2000.

Brown, J. S., Zilio, Claudio., Brignoli, R., Cavallini, A., Thermophysical properties and heat transfer and pressure drop performance potential of hydrofluoro-olefins, hydrochlorofluoro-olefins, and their blends, HVAC & Research, 20:2, 203-220, 2014.

Bruce, R. W., Handbook of lubrication and tribology: Theory and design, second edition, volume 2, CRC press, 2012.

Cavallini, A., Del Col, D., Matkovic, M., Rossetto, L., Frictional pressure drop during vapour-liquid flow in minichannels: Modelling and experimental evaluation, International Journal of Heat and Fluid flow 30:131-139, 2009.

Celata, G. P., Cumo, M., Dossevi, D., Jilisen, R. T. M., Saha, S. K., Zummo, S. G., Flow pattern analysis of flow boiling inside a 0.48 mm microtube, International journal of thermal sciences, 58:1-8, 2012.

Celata, G., Cumo, M., Dossevi, D., Jilisen, R., Saha, S., Zummo, G., Flow pattern analysis of flow boiling inside a 0.48 mm microtube. International Journal of Thermal Sciences, 58:1-8, 2012.

Chen, J. C., Correlation for boiling heat transfer to saturated fluids in convective flow. Industrial & Engineering Chemistry Process Design and Development, 5(3), 322-329, 1966.

Chen, L., Tian, Y. S. and Karayiannis, T. G., The effect of tube diameter on vertical two-phase flow regimes in small tubes, Int. J. of Heat and Mass Transfer. 49 (21-22): 4220-4230. 2006.

Cho, Y. I., Greene, G. A., Advances in heat transfer, Volume 43, Academic press, 2011.

Code of federal regulations, U. S. general services administration, office of federal register, 40: 81-84, 2008.

Coleman, J. W., Erause, J. E., Two phase pressure losses of R134a in microchannel tube headers with large free flow area ratios, Experimental Thermal and Fluid Science, 28:123-130, 2004.

Consolini, L. and Thome, J., Micro-channel flow boiling heat transfer of R-134a, R-236fa, and R-245fa, Microfluidics and Nanofluidics, Springer Berlin / Heidelberg, 6 (6): 731-746, 2009

Cooper, M.G., Saturation Nucleate Pool Boiling—A Simple Correlation", Inst. Chem. Eng.Symp. Ser., 86: 785–793, 1984.

Costa-Patry, E., Olivier, J., Nichita, B. A., Michel, B., Thome, J. R., Two-phase flow of refrigerants in 85 μm-wide multi-microchannels: Part I- Pressure drop, International Journal of Heat and Fluid Flow, 32: 451-463, 2011.

Croce, G.., D'Agaro, P., Numerical simulation of roughness effect on microchannel heat transfer and pressure drop in laminar flow, J. Phys. D: Appl. Phys. 38:1518–1530, 2005.

Davim, J. P., Surface integrity in machining, Springer, 2010.

Da-Wen Sun, Handbook of Frozen Food Processing and Packaging, Second edition. CRC Press. 2011

De Chiffre L, Lonardo PM, Trumpold H, Lucca DA, Goch G, Brown CA, Raja J, Hansen HN, Quantitative Characterisation of Surface Texture.Annals ofthe CIRP49(2):635–652, 2000

Del Col, D., Bisetto, A., Bortolato, M., Torresin, D., Rossetto, L., Experiments and updated model for two phase frictional pressure drop inside minichannels, International Journal of Heat and Mass Transfer, 67:326-337, 2013.

Del Col, D., Bisetto, A., Bortolato, M., Torresin, D., Rossetto, L., Experiments and updated model for two phase frictional pressure drop inside minichannels. International Journal of Heat and Mass Transfer, 67(0), 326-337, 2013.

Del Col, D., Bisetto, A., Bortolato, M., Torresin, D., Rossetto, L., Experiments and updated model for two phase fricitional pressure drop inside microchannels, International journal of heat and mass transfer, 67: 326-337, 2013.

Del Col, D., Bortolin, S., Torresin, D., Cavallini, A., Flow boiling of R1234yf in a 1 mm diameter channel, International journal of refrigeration, 36: 353-362, 2013a.

Dupont, V. and Thome, J. R., Evaporation in microchannels: influence of the channel diameter on heat transfer, Microfluid Nanofluid, 1: 119-127, 2005.

Ebadian, M. A., Lin, C. X., A review of high-heat-flux heat removal technologies, Journal of heat transfer, 133, 2011.

Evans, C. J., Bryan, J. B., "Structed", "Textured" or "Engineered" surfaces, Annals of the CIRP, 48:2, 1999.

Fabbri, M., Jiang, S., and Dhir, V. K., 2003, "Comparative Study of Spray and Multiple Micro Jets Cooling for High Power Density Electronic Applications," ASME Paper No. IMECE2003-42325.

Fatouh, M., El Kafafy, M., Assessment of propane/commercial butane mixtures as possible alternatives to R134a in domestic refrigerators, Energy conversion and management, 47: 2644-2658, 2006.

Fu, B-R., Lee, C-Y., Pan, C., The effect of aspect ratio on flow boiling heat transfer of HFE-7100 in a microchannel heat sink, International journal of heat and mass transfer, 58: 53-61, 2013.

Gamrat, G., Favre-Marinet, M., Le Person, S., Modelling of roughness effects on heat transfer in thermally fully-developed laminar flows through microchannels, International journal of thermal sciences, 48(12):2203-2214, 2009.

Gersey, C. O., Mudawar, I., Effects of heater length and orientation on the trigger mechanism for near-saturated flow boiling critical heat flux—I. photographic study and statistical characterization of the near-wall interfacial features. International Journal of Heat and Mass Transfer, 38(4), 629-641, 1995.

Gorenflo, D., Pool Boiling, VDI Heat Atlas, VDI Verlag, Dűsseldorf, 1993.

Griffiths, B., Manufacturing surface technology: Surface integrity and functional performance. Penton 1857180291. 2001.

Guo, Z., Li, Z., Size effect on microscale single-phase flow and heat transfer. International Journal of Heat and Mass Transfer, 46(1), 149-159, 2003.

Harirchian T, Garimella S. V. The critical role of channel cross-sectional area in Microchannel flow boiling heat transfer. International Journal of Multiphase Flow, 35:904-913, 2009.

Harirchian, T and Garimella, S. V., A comprehensive flow regime map for microchannel flow boiling with quantitative transition criteria, International Journal of Heat and Mass Transfer, 53: 2694-2702, 2010.

Harirchian, T., Garimella, S. V., Effects of channel dimension, heat flux, and mass flux on flow boiling regimes in microchannels. International Journal of Multiphase Flow, 35(4), 349-362, 2009a.

Harirchian, T., Garimella, S. V., Flow regime-based modeling of heat transfer and pressure drop in microchannel flow boiling. International Journal of Heat and Mass Transfer, 55(4), 1246-1260, 2012.

Hassan, I., Vaillancourt, M., Pehlivan, K, Two-phase flow regime transitions in microchannels: A comparative experimental study. Microscale Thermophysical Engineering, 9(2), 165-182, 2005.

Hirshfeld, H., Silverman, I., Arenshtam, A., Kijel, D., and Nagler, A.High Heat Flux Cooling of Accelerator Targets With Micro-Channels, Nucl.Instrum. Methods Phys. Res. A, 562(2): 903–905, 2006.

Huh, C., Kim, J., & Kim, M. H., Flow pattern transition instability during flow boiling in a single microchannel. International Journal of Heat and Mass Transfer, 50(5), 1049-1060, 2007.

Huo, X., Experimental study of boiling heat transfer in small diameter tubes, PhD thesis, London South Bank University, Lonond, UK, 2005.

Huo, X., Shiferaw, D., Karayiannis, T. G., Tian, Y. S., Kenning, D. B. R., Boiling two-phase pressure drop in small diameter tubes, Sixth International Conference on:

Enhanced, Compact and Ultra-Compact Heat Exchangers: Science, Engineering and Technology, Potsdam, Germany, September 16-21, 2007.

Hwang, Y. W., & Kim, M. S., The pressure drop in microtubes and the correlation development. International Journal of Heat and Mass Transfer, 49(11–12), 1804-1812, 2006.

ISO 25178 part 2 (2012) Geometrical product specification (GPS)—surface texture: areal—part 2: Terms, definitions and surface texture parameters. International Organization forStandardization

Jiang, X. J., Whitehouse, D. J., Technological shifts in surface metrology, CIRP Annals-Manufacturing technology, 61: 815-836, 2012.

Jones, B. J., McHale, J. P., Garimella, S. V., The influence of surface roughness on nucleate pool boiling heat transfer, Journal of heat transfer, 131 (12), 2009.

Joshi, Y., Kumar, P., Energy efficient thermal management of data centers, Springer, 2012.

Ju Lee, H., Yong Lee, S., Pressure drop correlations for two-phase flow within horizontal rectangular channels with small heights. International Journal of Multiphase Flow, 27(5), 783-796, 2001.

Kandasamy, R., Wang, X., Mujumdar, A. S., Application of phase change materials in thermal management of electronics, Applied thermal engineering, 27, 2822-2832, 2007.

Kandlikar, S. G, Schmitt, D., Characterization of surface roughness effects on pressure drop in single-phase flow in microchannels. Physics of fluids, 17. 100606. 2005

Kandlikar, S. G., Balasubramanian, P., An extension of the flow boiling correlation to transition, laminar, and deep laminar flows in minichannels and microchannels. Heat Transfer Engineering, 25(3), 86-93, 2004.

Kandlikar, S. G., Balasubramanian, P., Effect of gravitational orientation on flow boiling of water in 1054× 197 μm parallel minichannels. ASME 2004 2nd International Conference on Microchannels and Minichannels, 539-550, 2004a.

Kandlikar, S. G., Colin, S., Peles, Y, Garimella, S., Fabian Pease, R., Brandner, J. J., Tuckerman, D. B., Heat transfer in microchannels- 2012 status and research needs, Journal of heat transfer, 135(9), 2013.

Kandlikar, S. G., Grande, W. J., Evolution of microchannel flow passages- Thermohydraulic performance and fabrication technology, Heat Transfer Engineering, 24(1), 3-17, 2004.

Kandlikar, S. G., Heat Transfer Mechanisms During Flow Boiling in Microchannels, ASME J. Heat transfer,126(1): 8 –16, 2004.

Kandlikar, S. G., History, advances, and challenges in liquid flow and flow boiling heat transfer in microchannels: A critical review, Journal of heat transfer, 134, 2012.

Kandlikar, S. G., Kuan, W. K., Willistein, D. A., Borrelli, J., Stabilization of flow boiling in microchannels using pressure drop elements and fabricated nucleation sites, Journal of heat transfer, 124(8): 389-396, 2005.

Kandlikar, S. G., Nucleation characteristics and stability considerations during flow boiling in microchannels, Experimental thermal and fluid science, 30: 441-447, 2006.

Kandlikar, S. G., Scale effects on flow boiling heat transfer in microchannels: A fundamental perspective, International Journal of Thermal Sciences. 49: 1073-1085, 2010.

Kandlikar, S. G., Spiesman, P. H., Effect of surface characteristics on flow boiling heat transfer, Eng. Foundation Conference on Convective and Pool Boiling, Germany, 1997.

Kandlikar, S.G., Development of a Flow Boiling Map for Subcooled and Saturated Flow Boiling of Different Fluids in Circular Tubes, ASME Journal of Heat Transfer, 113:190-200, 1991.

Kandlikar, S.G., Spiesman, P. H., Effect of surface finish on flow boiling heat transfer, in: Proceedings of the 1998 ASME International Mechanical Engineering Congress and Exposition, pp. 157–163,1998.

Karayiannis, T. G., Mahmoud, M. M., Kenning, D. B. R., A study of discrepancies in flow boiling results in small to microdiameter metallic tubes, Experimental Thermal and Fluid Science, 36(0):126-142. 2012.

Karayiannis, T. G., Mahmoud, M. M., Kenning, D. B. R., A study of discrepanices in flow boiling results in small to microdiameter metallic tubes, Experimental thermal and fluid science, 36: 126-142, 2012.

Kawahara, A., Sadatomi, M., Nei, K. & Matsuo, H., Experimental study on bubble velocity, void fraction and pressure drop for gas-liquid two-phase flow in a circular microchannel, International Journal of Heat and Fluid Flow, 30 (5): 831-841, 2009

Kew, P.A., Cornwell, K., Correlations for the prediction of boiling heat transfer in small diameter channels, Applied Thermal Engineering, 17(8-10): 705-715. 1997.

Khan, M. G., Fartaj, A., A review on microchannel heat exchangers and potential applications, International journal of energy research, 35:553-582, 2011.

Khursheed, A., Scanning electron microscope optics and spectrometers, , World scientific, 2011.

Kirkwood, R.,Clean technology and the environment, Springer, 1994.

Kolb, G., Keller, S., O'Connell, M., Pecov, S., Schuerer, J., Spasova, B., Tiemann, D., Ziogas, A., Microchannel fuel processors as a hydrogen source for fuel cells in distributed energy supply systems, Energy fuels, 27: 4395-4402, 2013.

Koo, J., Jiang, L., Bari, A., Zhang, L., Wang, E., Kenny, T. W., Santiago, J. G., and Goodson, K. E., Convective Boiling in Microchannel Heat Sinks With Spatially-Varying Heat Generation, Proc. ITherm 2002, San Diego, CA, pp. 341–346, 2002.

Kubiak, K. J., Wilson, M. C. T., Mathia, T. G., Carval, Ph., Wettability versus roughness of engineering surfaces, Wear, 271: 523-528, 2011.

Kureta, M., Kobayashi, T., Mishima, K., Nishihara, H., Pressure drop and Heat Transfer for flow boiling of water in small diameter tubes, JSME International journal, series B, 41(43), 1998.

Lazarek, G.M. and Black, S. H., Evaporative heat transfer, pressure drop and critical heatflux in a small vertical tube with R-113, International Journal Heat Mass Transfer, 25(7):945-960, 1982.

Lee J, Mudawar I. Two-phase flow in high-heat-flux micro-channel heat sink for refrigeration cooling applications: part II-heat transfer characteristics.International Journal of Heat and Mass Transfer, 48:941-955, 2005.

Lee, D-H., Cho, N-G., Assessment of surface profile data acquired by a stylus profilometer, Measurement science and technology, 23, 2012.

Lee, H. J., Liu, D. Y., Alyousef, Y., Yao, S., Generalized two-phase pressure drop and heat transfer correlations in evaporative Micro/Minichannels. Journal of Heat Transfer, 132(4), 041004-041004, 2010.

Lee, J., Mudawar, I., Low-temperature two-phase microchannel cooling for high-heat-flux thermal management of defense electronics, IEEE transactions on components and packaging technologies, 32: 2, June 2009.

Lee, J., Mudawar, I., Two-phase flow in high-heat-flux micro-channel heat sink for refrigeration cooling applications: Part II—heat transfer characteristics. International Journal of Heat and Mass Transfer, 48(5), 941-955. 2005.

Lee, P. C., Tseng, F. G., Pan, C., Bubble dynamics in microchannels. part I: Single microchannel. International Journal of Heat and Mass Transfer, 47(25), 5575-5589, 2004.

Lerou, J. J., Tonkovich, A. L., Silva, L., Perry, S., McDaniel, J. M., Microchannel reactor architecture enables greener processes, Chemical Engineering Science, 65: 380-385, 2010.

Li, M., Dang, C., Fu, X., Ma, Y., Prediction for saturated flow boiling heat transfer in mini-channels. ASME 2013 Heat Transfer Summer Conference Collocated with the ASME 2013 7th International Conference on Energy Sustainability and the ASME 2013 11th International Conference on Fuel Cell Science, Engineering and Technology, 2013.

Li, M., Dang, C., Hihara, E., Flow boiling heat transfer of binary mixtures HFO1234yf/R32 in a smooth horizontal tube, International refrigeration and air conditioning conference, 2012.

Li, M., Dang, C., Hihara, E., Flow boiling heat transfer of HFO1234yf and HFC32 refrigerant mixtures in a smooth horizontal tube: Part II. prediction method. International Journal of Heat and Mass Transfer, 64(0), 591-608, 2013.

Li, W., and Wu, Z., A general criterion for evaporative heat transfer in micro/mini-channels, International Journal of Heat and Mass Transfer, 53, 1967-1976, 2010.

Li. M., Dang, C., Hihara, E., Flow boiling heat transfer of HFO1234yf and R32 refrigerant mixtures in a smooth horizontal tube: Part I. Experimental investigation. International Journal of Heat and Mass transfer, 55: 3437-3446, 2012.

Lin S, Kew PA, Cornwell K. Two-phase heat transfer to a refrigerant in a 1 mm diameter tube. In: 6th UK heat transfer conference in Edinburgh; September 1999.

Liu, Z., Winterton, R., A general correlation for saturated and subcooled flow boiling in tubes and annuli, based on a nucleate pool boiling equation. International Journal of Heat and Mass Transfer, 34(11), 2759-2766, 1991.

Lockhart, R.W. and Martinelli R.C., Proposed correlation of data for isothermal two-phase two-component flow in pipes. Chemical Engineering Progress, 45-39. 1949.

Lonardo P.M. , Lucca D.A., De Chiffre L.,Emerging Trends in Surface Metrology; ClRPAnnals, 51:701- 723, 2002.

Mahmoud, M., Karayiannis, T., A statistical correlation for flow boiling heat transfer in micro tubes. Proceedings of the 3rd European Conference on Microfluidics-Microfluidics, 3-5, 2012.

Mathia, T., Pawlus, P., Wieczorowski, M., Recent trends in surface metrology, Wear, 271: 494-508, 2011.

McGlen, R. J., Jachuck, R., Lin, S., Integrated thermal management techniques for high power electronic devices, Applied thermal engineering, 24, 1143-1156, 2004.

Mikielewicz, D. A., A new method for determination of flow boiling heat transfer coefficient in conventional-diameter channels and minichannels, Heat Transfer Engineering, 31 (4): 276-287. 2010.

Minjares, R., Refrigerants for light-duty passenger vechile air conditioning systems, The international council on clean transportation, 2011-3, 2011.

Minor, B., Spatz, M., HFO-1234yf low GWP refrigerant update, International refrigeration and air conditioning conference, Purdue, July 14-17, 2008.

Mishima, K., Hibiki, T., Some characteristics of air-water two-phase flow in small diameter vertical tubes, Int. J. Multiphase flow, 22(4): 703-712. 1996.

Moffat, R. J., Describing the uncertainities in experimental results, Experimental thermal and fluid science, 1: 3-17, 1988.

Mohammed Shah, M., Improved general correlation for critical heat flux during upflow in uniformly heated vertical tubes. International Journal of Heat and Fluid Flow, 8(4): 326-335, 1987.

Mohanraj, M., Jayaraj S., Muraleedharam, C., Comparative assessment of environmental-friendly alternatives to R134a in domestic refrigerators, Energy Efficiency, 1:189-198, 2008.

Morini, G. L., Lorenzini, M., Salvigni, S., Celata, G. P., Experimental analysis of microconvective heat transfer in the laminar and transitional regions, Experimental heat transfer, 23:73-93, 2010.

Mukherjee, A., Kandlikar, S. G., Numerical study of the effect of surface tension on vapour bubble growth during flow boiling in microchannels, Proceedings of ICNMM2006, Limerick, Ireland, ICNMM2006-96050, 2006.

Muralikrishnan, B., and Raja, J.,, Computational Surface and Roughness Metrology, Springer. 2008

Nielsen, H. S., Metrology Insight Vol. 3 No.1. Metrology Consulting, Inc. (April 2000).

Nino, V. G., Hrnjak, P., Newell, T., Characterization of Two-Phase Flow in Microchannels, University of Illinois at Urbana-Champaign, 2002.

Odabaee, M., Manchin, S., Hooman, K., Metal foam heat exchangers for thermal management of fuel cell systems- An experimental study, Experimental thermal and fluid science, 51: 214-219, 2013.

Ohadi, M., Choo, K., Dessiatoun, S., Cetegen, E., Emerging applications of microchannels, Next generation microchannel heat exchangers, Spirnger, 67-105, 2013.

Okazaki, Y., Effects of cold drawing and annealing on mechanical properties and microstructure of Co-Cr-Mo-Ni-Fe alloys for surgical implants, Materials Transactions, 49 (7): 1656-1660, 2008.

Oliphant, K., Webb, B. W., McQuay, M. Q., An experimental comparison of liquid jet array and spray impingement cooling in the non-boiling regime, Experimental thermal and fluid science, 18: 1-10, 1998.

Ong, C. L., & Thome, J. R., Flow boiling heat transfer of R134a, R236fa and R245fa in a horizontal 1.030 mm circular channel. Experimental Thermal and Fluid Science, 33(4), 651-663, 2009.

Owhaib, W., Experimental Heat Transfer, Pressure Drop and Flow Visualization of R134a in VerticalMini/Micro Tubes,Doctoral Thesis, Royal Institute of Technology, Stockholm, Sweden, 2007.

Oya, T., Upward liquid flow in small tube into which air streams (1st report, experimental apparatus and flow patterns). Bulletin of the JSME, 14(78):1320-1329, 1971.

Panão, M. R. O., Correia, A. M., Moreira, A. L. N., High-power electronics thermal management with intermittent multijet sprays, Applied thermal engineering, 37, 293-301, 2012.

Peng, X. F., Wang, B. X., Forced-convection and boiling characteristics in microchannels, Proceedings of heat transfer- 11th International heat transfer conference, 1:371-390, 1998.

Piasecka, M., Poniewski, M. E., Hysteresis phenomena at the onset of subcooled nucleate boiling in microchannels, Heat transfer engineering, 25(3):44-51, 2004.

Piasecka, M., Poniewski, M. E., Hysteresis phenomena at the onset of subcooled nucleate flow boiling in microchannels. Heat Transfer Engineering, 25(3), 44-51, 2004.

Poon, C.Y. and Bhushan, B., Comparison of surface roughness measurements by stylus profiler, AFM and non-contact optical profiler, Wear, 190: 76-88, 1995.

Qu, W., Mala, G. M., Li, D., Heat transfer for water flow in trapezoidal silicon microchannels, International journal of heat and mass transfer, 43(21):3925-3936, 2000.

Qu, W., Mudawar, I., Flow boiling heat transfer in two phase micro-channel heat sinks-I. Experimental investigation and assessment of correlation methods. Int. J. Heat MassTransfer, 46, 2755-2771, 2003.

R. Leech, Optical measurement or surface topography, Springer, 2011

Ravikumar, S. V., Jha, J. M., Tiara, A. M., Pal, S. K., Chakraborty, S., Experimental investigation of air-atomized spray with aqueous polymer additive for high heat flux applications, International journal of heat and mass transfer, 72: 362-377, 2014.

Revellin, R., Dupont, V., Ursenbacher, T., Thome, J. R., Zun, I., Characterization of diabatic two-phase flows in microchannels: Flow parameter results for R-134a in a 0.5 mm channel. International Journal of Multiphase Flow, 32(7), 755-774, 2006.

Revellin, R., Thome, J. R., A new type of diabatic flow pattern map for boiling heat transfer in microchannels, Journal of micromechanics and microengineering, 17(4): 788, 2007.

Saisorn, S. and Wongwises, S., A critical review of recent investigations on two-phase pressure drop in flow boiling micro-channels, Frontiers in Heat and Mass Transfer, 3, 013007, 2012.

Saisorn, S., Wongwises, S., The effect of channel diameter on flow pattern, void fraction and pressure drop of two-phase air-water flow in circular micro-channels, Experimental thermal and fluid science, 34(4): 454-462, 2010.

Saisorn, S., Wongwises, S., A critical review of recent investigations on two-phase pressure drop in flow boiling micro-channels, Frontiers in heat and mass transfer (FHMT), 3:013007, 2012.

Saitoh, S., Daiguji, H., Hihara, E., Effect of tube diameter on boiling heat transfer of R-134a in horizontal small-diameter tubes, Int. J. H and M Trans., 48:4973 -4984, 2005.

Saitoh, S., Daiguji, H., Hihara, E., Correlation for boiling heat transfer of R-134a in horizontal tubes including effect of tube diameter. International Journal of Heat and Mass Transfer, 50(25–26), 5215-5225, 2007.

Salek, E., The Handbook of Lubrication and Tribology: Theory and Design, CRC Press, 2012.

Schaeffer, R., Fundamentals of laser micromachining, CRC press, 2012.

Simmonds, W. H., Smith, R. J., Renton, R. E., Gregoriou, G., Tripp, J., Vlezel, C. H. F., Mattsson, L., Bjuggren, M., Tiziani, H. J., Jorndan, H. J., Optical non-contact techniques for engineering surface metrology, EUR 16161 EN, 1995.

Sitar, A., Sedmak, I., Golobic, I., Boiling of water and FC-72 in microchannels enhanced with novel features, International journal of heat and mass transfer, 55: 6446-6457, 2012.

small circular tubes. Int. J. Multiphase Flow 27, 1163–1177, 2001.

Sun, L., Mishima, K., An evaluation of prediction methods for saturated flow boiling heat transfer in mini-channels, International journal of heat and mass transfer, 52: 5323-5329, 2009.

Sun, L., Mishima, K., Evaluation analysis of prediction methods for two-phase flow pressure drop in mini-channels. International Journal of Multiphase Flow, 35(1), 47-54, 2009.

Szczukiewicz, S., Magnini, M., Thome, J. R., Proposed models, ongoing experiments and latest numerical simulations of microchannel two-phase flow boiling, International journal of multiphase flow, 59: 84-101, 2014.

Tabatabai, A., Faghri, A., A new two-phase flow map and transition boundary accounting for surface tension effects in horizontal miniature and micro tubes. Journal of Heat Transfer, 123(5), 958-968, 2001.

Tan, F. L., Tso, C. P., Cooling of mobile electronic devices using phase change materials, Applied thermal engineering, 24, 159-169, 2004.

Tan, Y. B., Xie, J. L., Duan, F., Wong, T. N., Toh, K. C., Choo, K. F., Chan, P. K., Chua, Y. S., Multi-nozzle spray cooling for high heat flux applications in a closed loop system, Applied thermal engineering, 54: 372- 379, 2013.

Taylor, J. B., Carrano, A. L., Kandlikar, S. G., Characterization of the effect of surface roughness and texture on fluid flow—past, present, and future. International Journal of Thermal Sciences, 45(10), 962-968, 2006.

Thome, J.R., Dupont, V., Jacobi, A.M., Heat transfer model for evaporation in microchannels. Part I: presentation of the model, Int. J. Heat Mass Transfer 47: 3375–3385, 2004.

Tie, P., Li, Q., Xuan, Y., Investigation on the submerged liquid jet arrays impingement cooling, Applied thermal engineering, 31, 2757-2763, 2011.

Tran, T. N., Chyu, M. -., Wambsganss, M. W., France, D. M., Two-phase pressure drop of refrigerants during flow boiling in small channels: An experimental investigation and correlation development. International Journal of Multiphase Flow, 26(11), 1739-1754, 2000.

Tran, T. N., Wambsganss, M. W., France, D. M., Small circular- and rectangular channel boiling with two refrigerants. International Journal Multiphase Flow, 22(3): 485-498. 1996.

Tran, T., Wambsganss, M., France, D., Small circular-and rectangular-channel boiling with two refrigerants. International Journal of Multiphase Flow, 22(3), 485-498, 1996.

Triplett, K. A., Ghiaasiaan, S. M., Abdel-Khalik, S. I., Sadowski, D. L., Gas–liquid two-phase flow in microchannels part I: Two-phase flow patterns. International Journal of Multiphase Flow, 25(3), 377-394, 1999.

Tuo, H., Hrnjak, P., Periodical reverse flow and boiling fluctuations in a microchannel evaporator of an air-conditioning system, International journal of refrigeration, 36: 1263-1275, 2013.

Vakili-Farahani, F., Agostini, B., Thome, J. R., Experimental study on flow boiling heat transfer of multiport tubes with R245fa and R1234ze(E), International journal of refrigeration, 36: 335-352, 2013.

Wambsganss, M., France, D., Jendrzejczyk, J., Tran, T., Boiling heat transfer in a horizontal small-diameter tube. Journal of Heat Transfer, 115(4), 963-972, 1993.

Wang, C., Chiang, C., Lu, D., Visual observation of two-phase flow pattern of R-22, R-134a, and R-407C in a 6.5-mm smooth tube. Experimental Thermal and Fluid Science, 15(4), 395-405, 1997.

Wang, Y., Sefiane, K., Effects of heat flux, vapour quality, channel hydraulic diameter on flow boiling heat transfer in variable aspect ratio micro-channels using transparent heating, International Journal of Heat and Mass Transfer, 55:2235-2243, 2012.

Wang, Y., Sefiane, K., Wang, Z., Harmand, S., Analysis of two-phase pressure drop fluctuations during micro-channel flow boiling, International Journal of Heat and Mass Transfer, 70:353- 362, 2014.

Wei, X., and Joshi, Y., Optimization Study of Stacked Micro-Channel Heat Sinks for Micro-Electronic Cooling, Proc. ITherm 2002, San Diego,CA, pp. 441–448, 2002.

Whitehouse, D. J., Handbook of surface and nanometerology, Taylor and Francis, 2nd ed., p 63. 2011.

Wu, H. Y., Cheng, P., An experimental study of convective heat transfer in silicon microchannels with different surface conditions, International journal of heat and mass transfer, 46(14):2547-2556, 2003.

Wu, H., & Cheng, P., An experimental study of convective heat transfer in silicon microchannels with different surface conditions. International Journal of Heat and Mass Transfer, 46(14), 2547-2556, 2003.

Xu, B., Shi, Y., Chen, D., Investigation on the heat transfer characteritics during flow boiling of liquefied natural gas in a vertical micro-fin tube, Cryogenics, 60: 65-78, 2014.

Xu, J., Li, D., Guo, J., Wu, Y., Investigations of phase inversion and frictional pressure gradients in upward and downward oil–water flow in vertical pipes. International Journal of Multiphase Flow, 36(11), 930-939, 2010.

Xu, Y., Fang, X., Su, X., Zhou, Z., Chen, W., Evaluation of frictional pressure drop correlations for two-phase flow in pipes, Nuclear Engineering and Design, 253:86-97, 2012.

Yang, C.-Y., Shieh, C.-C., Flow pattern of air–water and two-phase R-134a in

Yang, F., Dai, X., Peles, Y., Cheng, P., Khan, J., Li, C., Flow boiling phenomena in a single annular flow regime in microchannels (I): Characterization of flow boiling heat transfer, International journal of heat and mass transfer, 68: 703-715, 2014.

Yin, L., Jia, L., Guan, P., Liu, D., Experimental investigation on bubble confinement and elongation in microchannel flow boiling, Experimental thermal and fluid science, 54: 290-296, 2014.

Youguang, M., Xiyan, J., Dongji, W., Taotao, F., Chunying, Z., Measurement and Correlation of Pressure Drop for Gas-Liquid Two-phase Flow in Rectangular Microchannels, Fluid flow and transport phenomena, 18 (6), 940-947, 2010.

Yu, W., France, D. M., Wambsganss, M. W., Hull, J. R., Two-phase pressure drop, boiling heat transfer, and critical heat flux to water in a small-diameter horizontal tube. International Journal of Multiphase Flow, 28(6), 927-941, 2002.

Zhang, T., Cao, B., Fan, Y., Gonthier, Y., Luo, L., Wang, S., Gas-Liquid flow in circular microchannel. Part I: Influence of liquid physical properties and channel diameter on flow patterns, Chemical engineering science, 66 (23): 5791-5803, 2011.

Zhang, W., Hibiki, T., Mishima, K., Correlation for flow boiling heat transfer in mini-channels. International Journal of Heat and Mass Transfer, 47(26), 5749-5763, 2004.

Zhang, W., Hibiki, T., Mishima, K., Correlations of two-phase frictional pressure drop and void fraction in mini-channels, International Journal of Heat and Mass Transfer, 53:453-465, 2010.

Zhao, L., Rezkallah, K., Gas-liquid flow patterns at microgravity conditions. International Journal of Multiphase Flow, 19(5), 751-763, 1993.

Zhaun, R., Wang, W., Flow pattern of boiling in micro-channel by numerical simulation, International journal of heat and mass transfer, 55:1741-1753, 2012.

Zou, L., Jones, B. G., Heating surface material's effect on subcooled flow boiling heat transfer of R134a, Int. Journal of Heat and Mass Transfer,58(1–2): 168-174, 2013.

Zuckerman, N., Lior, N., Jet impingement heat transfer: Physics, correlations and numerical modelling, Advances in heat transfer, 39: 565-631, 2006.

Appendix A

Heat transfer correlations

	Correlation	Experimental conditions
Cooper (1984)	$h_{tp} = 55P_R^{0.12}(-\log_{10} P_R)^{-0.55}M^{-0.5}q^{0.67}$	6000 data points. Nucleate pool boiling.
Chen (1963)	$h_{tp} = Fh_{sp} + Sh_{nb}$ $h_{sp} = 0.023Re_f^{0.8}Pr_f^{0.4}\frac{k_f}{D}$ $h_{nb} = 0.00122\left(\frac{k_f^{0.79}Cp_f^{0.45}\rho_f^{0.49}}{\sigma^{0.5}\mu_f^{0.29}h_{fg}^{0.24}\rho_g^{0.24}}\right)$ $[T_w - T_{sat}(P_f)]^{0.24}[P_{sat}(T_w) - P_f]^{0.75}$ $S = \frac{1}{(1 + 2.53\ x\ 10^{-6}Re_{tp}^{1.17})}$ $Re_{tp} = Re_f F^{1.25}$ $F = \begin{cases} 1 & X_{tt}^{-1} \le 0.1 \\ 2.35(0.213 + X_{tt}^{-1})^{0.736} & X_{tt}^{-1} > 0.1 \end{cases}$ $X_{tt} = \left(\frac{\mu_f}{\mu_g}\right)^{0.1}\left(\frac{1-x}{x}\right)^{0.9}\left(\frac{\rho_g}{\rho_l}\right)^{0.5}$	x= 0.01-0.7
Gungor and Winterton (1986)	$h_{tp} = Eh_{sp} + Sh_{nb}$ $h_{sp} = 0.023Re_f^{0.8}Pr_f^{0.4}\frac{k_f}{D}$ $h_{nb} = 55P_R^{0.12}(-\log_{10} P_R)^{-0.55}M^{-0.5}q^{0.67}$ $E = 1 + 24000Bo^{1.16} + 1.37\left(\frac{1}{X_{tt}}\right)^{0.86}$ $S = \left(1 + 1.15x10^{-6}E^2Re_f^{1.17}\right)^{-1}$	4300 data points. D=2.95 – 32.0 mm. Water, R11, R12, R113, R114, R22, ethylene glycol.
Gungor and Winterton (1987)	$h_{tp} = (SS_2 + FF_2)h_{sp}$ $h_{sp} = \frac{0.023\ Re_l^{0.8}Pr_l^{0.4}\lambda_l}{D}$ $S = 1 + 3000Bo^{0.86}$ $F = 1.12\left(\frac{x}{1-x}\right)^{0.75}\left(\frac{\rho_l}{\rho_g}\right)^{0.41}$ $S_2 = Fr_l^{(0.1-2Fr_l)}$	R11, R12, R22, R113, R114, water

	$F_2 = Fr_l^{0.5}$ if horizontal and $Fr_l < 0.05$, otherwise S_2 and F_2 are equal to 1	
Liu and Winterton (1991)	$h_{tp}^2 = (Sh_{nb})^2 + \left(Fh_{sp}\right)^2$ $h_{sp} = \frac{0.023\ Re_l^{0.8} Pr_l^{0.4} \lambda_l}{D}$ $h_{nb} = 55 P_R^{0.12-0.087\ln\varepsilon}(-0.4343 \ln P_R)^{-0.55} M^{-0.5} q^{0.67}$ $F = \left[1 + xP_{R_l}\left(\frac{\rho_l}{\rho_g} - 1\right)\right]^{0.35}$ $S = \frac{1}{\left(1 + 0.055 F^{0.1} Re_l^{0.16}\right)}$	4300 data points. D=2.95 – 32.0 mm. Water, R11, R12, R113, R114, R22, ethylene glycol.
Lazarek and Black (1982)	$h_{tp} = 30\,Re_l^{0.857}\,Bo^{0.714}\left(\lambda_l / D_h\right)$	Based on 728 data points R113 D = 3.15 mm G = 125 – 750 kg/m^{2}s q = 14 – 380 kW/m^2 P = 1.3 – 4.1 bar R113
Tran et al. (1996)	$\alpha_{tp} = 840000\left(Bo^2 We_l\right)^{0.3}\left(\frac{\rho_l}{\rho_g}\right)^{-0.4}$ $We_l = \frac{G^2 D_h}{\rho_l \sigma}$	D = 2.4, 2.92 mm, G = 44 – 832 kg/m^{2}s q = 7.5 – 129 kW/m^2 P_R = 0.045 – 0.2 R12, R113
Kew and Cornwell (1997)	$h_{tp} = 30\,Re^{0.857}\,Bo^{0.714}\frac{k_f}{D}\left(1 - x\right)^{-0.143}$	R141b, D = 1.39 –

		3.69 mm
Warrier et al. (2002)	$h_{tp} = \left[1 + 6Bo^{1/16} - 5.3x^{0.65}(1 - 855Bo)\right]\frac{4.36k_L}{D}$	$0.00027 \le Bo \le 0.00089$ $0.03 \le x \le 0.55$ FC84, D_h = 0.75 mm
Thome et al. (2004)	$h(z) = \frac{t_{liquid}}{\tau} h_{liquid}(z) + \frac{t_{film}}{\tau} h_{film}(z) + \frac{t_{dry}}{\tau} h_{vapour}(z)$ $h_{film} = \frac{k_f}{\delta_0 - \delta_{end}} \ln\left(\frac{\delta_0}{\delta_{end}}\right)$ $\tau = \frac{1}{f_b}$ $f_b = \left(\frac{q}{q_{ref}}\right)^{1.74}$ $q_{ref} = 3328 \left(\frac{P_{sat}}{P_{crit}}\right)^{-0.5}$ $t_{liquid} = \frac{\tau}{1 + \frac{\rho_f}{\rho_g}\frac{x}{1-x}}$ $t_{vapour} = \frac{\tau}{1 + \frac{\rho_g}{\rho_f}\frac{1-x}{x}}$ $t_{dry\ film}(z) = \frac{\rho_f h_{fg}}{q}[\delta_0(z) - \delta_{min}]$ $\delta(z,t) = \delta_0(z) - \frac{q}{\rho_f h_{fg}} t$ $\frac{\delta_0(z)}{D} = C_{\delta_0}\left(3\sqrt{\frac{\upsilon_f}{U_p D}}\right)^{0.84}((0.07Bo^{0.41})^{-8} + 0.1^{-8})^{-1/8}$ $U_p = G_{tot}\left[\frac{x}{\rho_g} + \frac{1-x}{\rho_f}\right]$	
Zhang et al. (2004)	$h_{tp} = Fh_{sp} + Sh_{nb}$ $h_{nb} = 0.00122\left(\frac{k_f^{0.79} Cp_f^{0.45} \rho_f^{0.49}}{\sigma^{0.5} \mu_f^{0.29} h_{fg}^{0.24} \rho_g^{0.24}}\right)[T_w - T_{sat}(P_f)]^{0.24}[P_{sat}(T_w) - P_f]^{0.75}$ $S = \frac{1}{(1 + 2.53\ x\ 10^{-6} Re_f^{1.17})}$ For circular channels; $Nu._{lam} = 4.36$ $Nu._{turb} = 0.023 Re_f^{0.8} Pr_f^{0.4}$	1203 data points. Circular and rectangular channels. Vertical and horizontal orientation. P=0.101 – 1.21 MPa. G=23.4 – 2939 kg/m^{2}s. D_h=0.78 – 6 mm. Water, R11,

	$Nu_{.Collier}$ $= 0.17Re_f^{0.33}Pr_f^{0.43}\left(\frac{Pr_f}{Pr_w}\right)^{0.25}\left[\frac{g\beta\rho_f^2 D_h^3(T_w - T_f)}{\mu_f^2}\right]$ h_{sp} $= \begin{cases} \frac{k_f}{D_h} MAX(Nu_{.lam}, Nu_{.Collier}) if\ Re_f \geq 2000 \\ for\ vertical\ flow \\ \frac{k_f}{D_h} MAX(Nu_{.lam}, Nu_{.Collier}) if\ Re_f \leq 2300 fo \\ horizaontal\ flow \\ \frac{k_f}{D_h} Nu_{sp,turb,} if\ Re_f \geq \\ 2300\ for\ both \end{cases}$ $F = MAX(F', 1)$ $F' = 0.64\phi_f$ $\phi_f^2 = 1 + \frac{C}{X} + \frac{1}{X^2}$ $X = \left[\frac{\left(dP/dz\right)_f}{\left(dP/dz\right)_g}\right]^{0.5}$	R12, R113.
Lee and Mudawar (2005)	For x_e = 0.05; $h_{tp} = 3.856X^{0.267}h_{sp,f}$ $h_{sp,f} = \frac{Nu_{3-side\ heating}k_f}{D}$ $X = \left[\frac{\left(dP/dz\right)_f}{\left(dP/dz\right)_g}\right]^{0.5}$ For x_e = 0.05-0.55; $h_{tp} = 436.48Bo^{0.522}We_{lo}^{0.351}X^{0.665}h_{sp,f}$ For x_e = 0.55-1.0; $h_{tp} = max\{(108.6X^{1.665}h_{sp,g}), h_{sp,g}\}$ For laminar; $h_{sp,g} = \frac{Nu_{3-side\ heating}k_g}{D}$ For turbulent; $h_{sp,g} = 0.023Re_g^{0.8}Pr_g^{0.4}$	318 data points. R134a Water x_e=0.26-0.87 q=15.9-93.8 W/cm^2
Saitoh et al. (2007)	$h_{tp} = Fh_{sp} + Sh_{nb}$ $h_{nb} = 207\frac{k_f}{d_b}\left(\frac{qd_b}{k_f T_f}\right)^{0.745}\left(\frac{\rho_g}{\rho_f}\right)^{0.581} Pr_f^{0.533}$ For Re_f >1000, $h_{sp} = 0.023\frac{k_f}{D}\left(\frac{G_f D}{\mu_f}\right)^{0.8}\left(\frac{Cp_f\mu_f}{k_f}\right)^{1/3}$	2224 data points. R134a D= 0.5-11 mm

	For Re_f <1000, $h_{sp} = \frac{4.36k_f}{D}$ $d_b = 0.5\left[\frac{2\sigma}{g(\rho_f - \rho_g)}\right]^{0.5}$ $F = 1 + \frac{(1/X)^{1.05}}{1 + We_g^{-0.4}}$ $S = \frac{1}{1 + 0.4(Re_{tp}\, x\, 10^{-4})^{1.4}}$ $Re_{tp} = Re_f F^{1.25}$	
Bertsch et al. (2009)	$h_{tp} = (1 - x)h_{nb} + [1 + 80(x^2 - x^6)e^{-0.6Co}]h_{sp}$ $h_{nb} = 55P_R^{0.12-0.087\ln\varepsilon}(-0.4343\ln P_R)^{-0.55}M^{-0.5}q^{0.67}$ $h_{sp} = xh_{sp,go} + (1 - x)h_{sp,lo}$ $h_{sp,g\ or\ l\ o} = \left[3.66 + \frac{\frac{0.0668Re_{ko}Pr_{l\ or\ g}D}{L}}{1 + 0.04\left(\frac{Re_{ko}Pr_{l\ or\ g}D}{L}\right)}\right]\frac{\lambda_{l\ or\ g}}{D}$ $Re_{ko} = \frac{G_{tp}D}{\mu_{l\ or\ g}}$	3899 data points. D=0.16 – 2.92 mm. 12 different fluids including water, FC-77 and nitrogen.
Sun-Mishima (2009)	$h_{tp} = \frac{6Re_{lo}^{1.05}Bo^{0.54}}{We_l^{0.191}\left(\rho_l/\rho_g\right)^{0.142}}\frac{k_f}{D}$	2505 data points. 11 fluids D=0.21 – 6.05 mm
Li and Wu (2010)	$h_{tp} = 334Bo^{0.3}\left(Bd\,Re_L^{0.36}\right)^{0.4}\frac{k_L}{D}$ $Re_L = \frac{(1-x)GD}{\mu_L}$	769 data points D = 0.148 – 3.25 mm 12 different fluids including water, FC-77, ethanol, propane and CO_2.
Mikielewicz (2010)	$\frac{h_{tp}}{h_L} = \sqrt{\phi_{MS}^n + \frac{1}{1+P}\left(\frac{h_{nb}}{h_L}\right)^2}$	Applicable for conventional and small diameter

	$P = 0.00253\mathrm{Re}^{1.17} Bo^{0.6} (\phi_{MS} - 1)^{-0.65}$ $\phi_{MS} = \left[1 + 2\left(\frac{1}{f_1} - 1\right) xCo^{-1}\right](1-x)^{1/3} + \frac{x^3}{f_2}$ For laminar flow: $f_1 = \frac{\rho_g}{\rho_L}\frac{\mu_L}{\mu_g}, \qquad f_2 = \frac{\mu_g}{\mu_L}\frac{c_{pL}}{c_{pg}}\left(\frac{k_L}{k_g}\right)^{1.5}$ For turbulent flow: $f_1 = \frac{\rho_g}{\rho_L}\left(\frac{\mu_L}{\mu_g}\right)^{0.25}, \qquad f_2 = \left(\frac{k_g}{k_L}\right)$ $h_{np} = 55 P_r^{0.12 - 0.434 \ln R_p} (-\log P_r)^{-0.55} M^{-0.5} q^{0.67}$	channels.
Costa-Patry (2012)	$\mathrm{h_{film}} = \frac{\mathrm{k_f}}{\delta_0 - \delta_{\mathrm{end}} + 1\mathrm{x}10^{-9}} \ln\left(\frac{\delta_0}{\delta_{\mathrm{end}}}\right)$ $\mathrm{h_{annular}} = \frac{\mathrm{k_f}}{\delta_{\mathrm{avg}}}\left(0.0776\delta^{+0.9}\mathrm{Pr_f^{0.52}}\right)$ $\mathrm{h_{trans}} = (1 - \mathrm{r})\mathrm{h_{Thome}} + \frac{\mathrm{rh_{annular}}}{(1-\mathrm{r})\mathrm{h_{Thome}} + \mathrm{rh_{annular}}}(\mathrm{rh_{annular}} - (1 - \mathrm{r})\mathrm{h_{Thome}})$ $\mathrm{r} = \frac{\mathrm{x} - \mathrm{x_{trans}}}{0.4\,\mathrm{x_{exit}}} + 0.5$ $\mathrm{x_{trans}} \pm \frac{\mathrm{x_{exit}}}{5}$ $\mathrm{x_{transition}} = 425\left(\frac{\rho_g}{\rho_f}\right)^{0.1}\frac{\mathrm{Bo}^{1.1}}{\mathrm{Co}^{0.5}}$	
Mahmoud and Karayiannis (2012) (Correlation I)	$h_{tp} = 3414\frac{Bo^{0.625} We_L^{0.2}\,\mathrm{Re}_L^{0.1}}{Co^{0.6}}\frac{k_L}{D}$	8561 data points R134a D= 4.26 – 0.52 mm, G=100 – 500 kg/m^{2}s Pressure= 6 – 14 bar

Mahmoud and Karayiannis (2012) (Correlation II)	$h_{tp} = S_{new} h_{Cooper} + F_{new} h_L$ $h_{Cooper} = 55 P_r^{(0.12-0.4343\ln e)} \left(-\log P_r\right)^{-0.55} MW^{-0.5} q^{0.67}$ $h_L = \begin{cases} 4.36 \dfrac{k_L}{D} & \mathrm{Re}_L < 2000 \\ 0.023 \mathrm{Re}_L^{0.8} \mathrm{Pr}_L^{0.4} \dfrac{k_L}{D} & \mathrm{Re}_L > 3000 \end{cases}$ $\mathrm{Re}_L = \dfrac{(1-x)GD}{\mu_L}$ $F_{New} = \left(1 + \dfrac{A}{\mathrm{X}}\right)^{0.64}$ $A = 2.812 Co^{-0.408}$ $S_{New} = \dfrac{1}{1 + 2.56 \times 10^{-6} \left(\mathrm{Re}_L F_{New}^{1.25}\right)^{1.17}}$	8561 data points R134a D= 4.26 – 0.52 mm, G=100 – 500 kg/m^{2}s Pressure= 6 – 14 bar
Li et al. (2013)	$\mathrm{h_{tp}} = \mathrm{F h_{cv}} + \mathrm{S h_{nb}}$ $\mathrm{h_{nb}} = 55 \mathrm{P_R^{0.12}} (-\log_{10} \mathrm{P_R})^{-0.55} \mathrm{M}^{-0.5} \mathrm{q}^{0.67}$ $\mathrm{h_{cv}} = 0.023 \dfrac{k_f}{D} \left[\dfrac{G(1-x)D}{\mu_f}\right]^{0.8} Pr^{0.4}$ $\mathrm{X_{tt}} = \left(\dfrac{\mu_\mathrm{f}}{\mu_\mathrm{g}}\right)^{0.1} \left(\dfrac{1-\mathrm{x}}{\mathrm{x}}\right)^{0.9} \left(\dfrac{\rho_\mathrm{g}}{\rho_\mathrm{l}}\right)^{0.5}$ $\mathrm{F} = 1.0 + \dfrac{1.8 \left(0.3 + \dfrac{1}{\mathrm{X_{tt}}}\right)^{0.88}}{\left(1 + We_g^{-0.4}\right)}$ $\mathrm{S} = \dfrac{1}{0.5 + 0.5 \dfrac{\left(Re_{tp} x 10^{-3}\right)^{0.3}}{(Box 10^3)^{0.23}}}$	476 data points. HFO1234yf, HFC32. G=100 – 400 kg/m^{2}s.
Kim et al. (2013)	$\mathrm{h_{tp}} = \left(\mathrm{h_{nb}^2} + \mathrm{h_{cb}^2}\right)^{0.5}$ $\mathrm{h_{nb}} = \left[2345 \left(\mathrm{Bo} \dfrac{\mathrm{P_H}}{\mathrm{P_F}}\right)^{0.70} \mathrm{P_R^{0.38}} (1 - \mathrm{x})^{-0.51}\right] (0.023 \mathrm{Re_f^{0.8}} \mathrm{Pr_f^{0.4}} \dfrac{\mathrm{k_f}}{\mathrm{D}})$ $\mathrm{h_{cb}} = \left[5.2 \left(\mathrm{Bo} \dfrac{\mathrm{P_H}}{\mathrm{P_F}}\right)^{0.08} \mathrm{We_{lo}^{-0.54}} + 3.5 \left(\dfrac{1}{\mathrm{X_{tt}}}\right)^{0.94} \left(\dfrac{\rho_\mathrm{g}}{\rho_\mathrm{l}}\right)^{0.25}\right] \left(0.023 \mathrm{Re_f^{0.8}} \mathrm{Pr_f^{0.4}} \dfrac{\mathrm{k_f}}{\mathrm{D}}\right)$ $\mathrm{P_H}$ = heated perimeter	10,805 data points from 31 sources. 18 working fluids. D=0.19 – 6.5 mm. G=19 – 1608 kg/m^{2}s. x=0 – 1. $\mathrm{Re_{lo}}$=57 – 49,820.

	P_F = wetted perimeter $X_{tt} = \left(\frac{\mu_f}{\mu_g}\right)^{0.1} \left(\frac{1-x}{x}\right)^{0.9} \left(\frac{\rho_g}{\rho_l}\right)^{0.5}$	

Appendix B

Pressure drop correlations

	Correlation	Experimental conditions
Homogenous flow model	$\Delta P_f = \frac{2 f_{Lo} L_{tp} G^2}{D \rho_L}\left[1+\frac{x_e}{2}\left(\frac{\rho_L}{\rho_{Lv}}\right)\right]$ $\Delta P_{acc} = \frac{G^2}{\rho_L}\left(\frac{\rho_L}{\rho_{Lv}}\right)$ $\Delta P_g = \rho_{Lv} g \frac{L_{tp}}{x_e} \ln\left[1+x_e \frac{\rho_L}{\rho_{Lv}}\right]$	
Lockhart-Martinelli (1949)	$\Delta P_f = \frac{L_{tp}}{x_e}\int_0^{x_e} \frac{2 f_l G^2}{D \rho_f} \phi_f^2 \, dx$ $\phi_f^2 = 1 + \frac{C}{X} + \frac{1}{X^2}$ $X = \left(\frac{1-x}{x}\right)\left(\frac{\rho_g}{\rho_f}\right)^{0.5}\left(\frac{f_f}{f_g}\right)^{0.5}$ C = 5 for laminar liquid – laminar gas C = 12 for laminar liquid – turbulent gas C = 10 for turbulent liquid – laminar gas C = 20 for turbulent liquid – turbulent gas $\Delta P_g = g \frac{L_{tp}}{x_e}\int_0^{x_e} [\alpha \rho_g + (1-\alpha)\rho_f] \, dx$ $\Delta P_{acc} = \frac{G^2}{\rho_f}\left[\frac{x_e^2}{\alpha_e}\frac{\rho_f}{\rho_g} + \frac{(1-x_e)^2}{(1-\alpha_e)} - 1\right]$ $\alpha = \frac{1}{1+0.28 X_m}$	Water, benzene, kerosene, oil D = 1.49 – 25.83 mm.

	$$X_m = \left(\frac{1-x}{x}\right)^{0.64}\left(\frac{\rho_g}{\rho_f}\right)^{0.36}\left(\frac{\mu_f}{\mu_g}\right)^{0.07}$$	
Friedel (1979)	$$\Delta P_f = \frac{2f_{lo}G^2}{D\rho_f}\frac{L_{tp}}{x_e}\int_0^{x_e}\phi_{fo}^2\,dx$$ $$\phi_{fo}^2 = C_1 + \frac{3.24\,C_2}{Fr^{0.045}We^{0.035}}$$ $$C_1 = (1-x)^2 + x^2\left(\frac{\rho_f}{\rho_g}\right)\left(\frac{f_{go}}{f_{lo}}\right)$$ $$C_2 = x^{0.78}(1-x)^{0.24}\left(\frac{\rho_f}{\rho_g}\right)$$ $$\rho_{tp} = \left[\frac{x}{\rho_g} + \frac{1-x}{\rho_f}\right]^{-1}$$ $$We = \frac{G^2 D}{\rho_{tp}\sigma}$$ $$Fr = \frac{G^2}{\rho_{tp}Dg}$$ $$\Delta P_g = g\frac{L_{tp}}{x_e}\int_0^{x_e}\left[\alpha\rho_g + (1-\alpha)\rho_f\right]dx$$ $$\Delta P_{acc} = \frac{G^2}{\rho_f}\left[\frac{x_e^2}{\alpha_e}\frac{\rho_f}{\rho_g} + \frac{(1-x_e)^2}{(1-\alpha_e)} - 1\right]$$ $$\alpha = \frac{1}{1+0.28X_m}$$ $$X_m = \left(\frac{1-x}{x}\right)^{0.64}\left(\frac{\rho_g}{\rho_f}\right)^{0.36}\left(\frac{\mu_f}{\mu_g}\right)^{0.07}$$	25, 000 data points . $\frac{\mu_f}{\mu_g} < 1000$
Muller-Steinhagen and Heck (1986)	$$\Delta P_f = \frac{2f_{lo}G^2}{D\rho_f}\frac{L_{tp}}{x_e}\int_0^{x_e}\phi_{fo}^2\,dx$$ $$\phi_{fo}^2 = Y^2x^3 + (1-x)^{1/3}[1+2x(Y^2-1)]$$ $$Y = \sqrt{\frac{\left(\Delta P/\Delta L\right)_{go}}{\left(\Delta P/\Delta L\right)_{fo}}}$$ $$\Delta P_g = g\frac{L_{tp}}{x_e}\int_0^{x_e}\left[\alpha\rho_g + (1-\alpha)\rho_f\right]dx$$	9300 data points.

	$$\Delta P_{acc} = \frac{G^2}{\rho_f}\left[\frac{x_e^2}{\alpha_e}\frac{\rho_f}{\rho_g} + \frac{(1-x_e)^2}{(1-\alpha_e)} - 1\right]$$ $$\alpha = \frac{1}{1+0.28X_m}$$ $$X_m = \left(\frac{1-x}{x}\right)^{0.64}\left(\frac{\rho_g}{\rho_f}\right)^{0.36}\left(\frac{\mu_f}{\mu_g}\right)^{0.07}$$	
Wang et al. (1997)	$$\Delta P_f = \frac{L_{tp}}{x_e}\int_0^{x_e}\frac{2f_l G^2}{D\rho_f}\phi_f^2\, dx$$ $$\phi_f^2 = 1 + \frac{C}{X} + \frac{1}{X^2}$$ $$X = \left(\frac{1-x}{x}\right)\left(\frac{\rho_g}{\rho_f}\right)^{0.5}\left(\frac{f_f}{f_g}\right)^{0.5}$$ $$C = 0.000004566X^{0.128}Re_{lo}^{0.938}\left(\frac{\rho_f}{\rho_g}\right)^{-2.15}\left(\frac{\mu_f}{\mu_g}\right)^{5.1}$$ $$\Delta P_g = g\frac{L_{tp}}{x_e}\int_0^{x_e}\left[\alpha\rho_g + (1-\alpha)\rho_f\right]dx$$ $$\Delta P_{acc} = \frac{G^2}{\rho_f}\left[\frac{x_e^2}{\alpha_e}\frac{\rho_f}{\rho_g} + \frac{(1-x_e)^2}{(1-\alpha_e)} - 1\right]$$ $$\alpha = \frac{1}{1+0.28X_m}$$ $$X_m = \left(\frac{1-x}{x}\right)^{0.64}\left(\frac{\rho_g}{\rho_f}\right)^{0.36}\left(\frac{\mu_f}{\mu_g}\right)^{0.07}$$	R22, R134a, R407C D = 6.5 mm
Mishima and Hibiki (1996)	$$\Delta P_f = \frac{L_{tp}}{x_e}\int_0^{x_e}\frac{2f_l G^2}{D\rho_f}\phi_f^2\, dx$$ $$\phi_f^2 = 1 + \frac{C}{X} + \frac{1}{X^2}$$ $$X = \left(\frac{1-x}{x}\right)\left(\frac{\rho_g}{\rho_f}\right)^{0.5}\left(\frac{f_f}{f_g}\right)^{0.5}$$	D = 1.05 – 4 mm U_{gs} = 0.071- 49.4 m/s U_{ls} = 0.071-2.33

	$$C = 21\left(1 - e^{0.319D}\right)$$ $$\Delta P_g = g\frac{L_{tp}}{x_e}\int_0^{x_e}\left[\alpha\rho_g + (1-\alpha)\rho_f\right]dx$$ $$\Delta P_{acc} = \frac{G^2}{\rho_f}\left[\frac{x_e^2}{\alpha_e}\frac{\rho_f}{\rho_g} + \frac{(1-x_e)^2}{(1-\alpha_e)} - 1\right]$$ $$\alpha = \frac{1}{1+0.28X_m}$$ $$X_m = \left(\frac{1-x}{x}\right)^{0.64}\left(\frac{\rho_g}{\rho_f}\right)^{0.36}\left(\frac{\mu_f}{\mu_g}\right)^{0.07}$$	m/s
Tran et al. (2000)	$$\Delta P_f = \Delta P_{flo}\{1 + (4.3\Gamma^2 - 1)[N_{conf}x^{0.875}(1-x)^{0.875} + x^{1.75}]\}$$ $$N_{conf} = \frac{\sqrt{\frac{\sigma}{\left(g(\rho_f - \rho_g)\right)}}}{D}$$ $$\Delta P_g = g\frac{L_{tp}}{x_e}\int_0^{x_e}\left[\alpha\rho_g + (1-\alpha)\rho_f\right]dx$$ $$\Delta P_{acc} = \frac{G^2}{\rho_f}\left[\frac{x_e^2}{\alpha_e}\frac{\rho_f}{\rho_g} + \frac{(1-x_e)^2}{(1-\alpha_e)} - 1\right]$$ $$\alpha = \frac{1}{1+0.28X_m}$$ $$X_m = \left(\frac{1-x}{x}\right)^{0.64}\left(\frac{\rho_g}{\rho_f}\right)^{0.36}\left(\frac{\mu_f}{\mu_g}\right)^{0.07}$$	610 data points. R134a, R12, R113 D_h = 2.4 – 2.92 mm P=138 – 856 kPa G=33-832 kg/m^{2}s q=2.2-90.8 kW/m^2 0 < x < 0.95 For smooth tubes
Lee and Lee (2001)	$$\Delta P_f = \frac{L_{tp}}{x_e}\int_0^{x_e}\frac{2f_l G^2}{D\rho_f}\phi_f^2\,dx$$ $$\phi_f^2 = 1 + \frac{C}{X} + \frac{1}{X^2}$$ $$X = \left(\frac{1-x}{x}\right)\left(\frac{\rho_g}{\rho_f}\right)^{0.5}\left(\frac{f_f}{f_g}\right)^{0.5}$$	305 data points Rectangular channels Water D_h = 0.78 – 6.67 mm Re_{lo}=175-17700

$$C = A\lambda^q \psi^r Re_{lo}^s$$

For laminar liquid and vapour

A=6.8323x10^{-8}

q=-1.317

R=0.719

S=0.557

For laminar liquid and turbulent vapour

A=6.185x10^{-8}

q=0

R=0

S=0.726

For turbulent liquid and laminar vapour

A=3.627

q=0

R=0

S=0.174

For turbulent liquid and vapour

A=0.408

q=0

R=0

S=0.451

$$\Delta P_g = g\frac{L_{tp}}{x_e}\int_0^{x_e}\left[\alpha\rho_g + (1-\alpha)\rho_f\right]dx$$

$$\Delta P_{acc} = \frac{G^2}{\rho_f}\left[\frac{x_e^2}{\alpha_e}\frac{\rho_f}{\rho_g} + \frac{(1-x_e)^2}{(1-\alpha_e)} - 1\right]$$

$$\alpha = \frac{1}{1 + 0.28X_m}$$

	$X_m = \left(\frac{1-x}{x}\right)^{0.64}\left(\frac{\rho_g}{\rho_f}\right)^{0.36}\left(\frac{\mu_f}{\mu_g}\right)^{0.07}$	
Warrier et al. (2002)	$\Delta P_f = \frac{2 f_{lo} G^2}{D\rho_f}\frac{L_{tp}}{x_e}\int_0^{x_e}\phi_{fo}^2\, dx$ $\phi_L^2 = 1+\frac{C}{X}+\frac{1}{X^2}$ $X = \left(\frac{f_L}{f_g}\right)^{0.5}\left(\frac{\rho_g}{\rho_L}\right)^{0.5}\left(\frac{1-x}{x}\right)$ C = 38 for all flow regimes $\phi_{Lo}^2 = \phi_L^2\left(\frac{f_L}{f_{Lo}}\right)(1-x)^2$ $\Delta P_g = g\frac{L_{tp}}{x_e}\int_0^{x_e}\left[\alpha\rho_g + (1-\alpha)\rho_f\right] dx$ $\Delta P_{acc} = \frac{G^2}{\rho_f}\left[\frac{x_e^2}{\alpha_e}\frac{\rho_f}{\rho_g}+\frac{(1-x_e)^2}{(1-\alpha_e)}-1\right]$ $\alpha = \frac{1}{1+0.28X_m}$ $X_m = \left(\frac{1-x}{x}\right)^{0.64}\left(\frac{\rho_g}{\rho_f}\right)^{0.36}\left(\frac{\mu_f}{\mu_g}\right)^{0.07}$	FC84 D_h = 0.75 mm
Yu et al. (2002)	$\Delta P_f = \frac{L_{tp}}{x_e}\int_0^{x_e}\frac{2 f_l G^2}{D\rho_f}\phi_f^2\, dx$ $\phi_f^2 = \frac{1}{X^{1.9}}$ $X = \left(\frac{1-x}{x}\right)\left(\frac{\rho_g}{\rho_f}\right)^{0.5}\left(\frac{f_f}{f_g}\right)^{0.5}$ for laminar liquid – turbulent gas	Water D = 2.98 mm G = 50 – 200 kg/m^2 s P = 1.98 bar

	$\Delta P_g = g\frac{L_{tp}}{x_e}\int_0^{x_e}\left[\alpha\rho_g + (1-\alpha)\rho_f\right]dx$ $\Delta P_{acc} = \frac{G^2}{\rho_f}\left[\frac{x_e^2}{\alpha_e}\frac{\rho_f}{\rho_g} + \frac{(1-x_e)^2}{(1-\alpha_e)} - 1\right]$ $\alpha = \left(1 + \left[\frac{1-x}{x}\right]\left[\frac{\rho_g}{\rho_f}\right]^{0.67}\right)^{-1}$	
Qu and Mudawar (2003)	$\Delta P_f = \frac{L_{tp}}{x_e}\int_0^{x_e}\frac{2f_l G^2}{D\rho_f}\phi_f^2\,dx$ $\phi_f^2 = 1 + \frac{C}{X} + \frac{1}{X^2}$ $X = \left(\frac{1-x}{x}\right)\left(\frac{\rho_g}{\rho_f}\right)^{0.5}\left(\frac{f_f}{f_g}\right)^{0.5}$ for laminar liquid – laminar gas $C = 21\left(1-e^{-3190d_h}\right)(0.00418G + 0.0613)$ $\Delta P_g = g\frac{L_{tp}}{x_e}\int_0^{x_e}\left[\alpha\rho_g + (1-\alpha)\rho_f\right]dx$ $\Delta P_{acc} = \frac{G^2}{\rho_f}\left[\frac{x_e^2}{\alpha_e}\frac{\rho_f}{\rho_g} + \frac{(1-x_e)^2}{(1-\alpha_e)} - 1\right]$ $\alpha = \left(1 + \left[\frac{1-x}{x}\right]\left[\frac{\rho_g}{\rho_f}\right]^{0.67}\right)^{-1}$	D = 0.35 mm Water
Hwang and Kim (2006)	$\Delta P_f = \frac{L_{tp}}{x_e}\int_0^{x_e}\frac{2f_l G^2}{D\rho_f}\phi_f^2\,dx$ $\phi_f^2 = 1 + \frac{C}{X} + \frac{1}{X^2}$ $X = \left(\frac{1-x}{x}\right)\left(\frac{\rho_g}{\rho_f}\right)^{0.5}\left(\frac{f_f}{f_g}\right)^{0.5}$ $C = 0.227(Re_{lo})^{0.452}X^{-0.320}\left(N_{conf}\right)^{-0.820}$	R134a D = 0.244, 0.430, 0.792. Re_{fo}<2000

	$$N_{conf} = \frac{\sqrt{\frac{\sigma}{\left(g(\rho_f - \rho_g)\right)}}}{D}$$ $$\Delta P_g = g\frac{L_{tp}}{x_e}\int_0^{x_e}\left[\alpha\rho_g + (1-\alpha)\rho_f\right]dx$$ $$\Delta P_{acc} = \frac{G^2}{\rho_f}\left[\frac{x_e^2}{\alpha_e}\frac{\rho_f}{\rho_g} + \frac{(1-x_e)^2}{(1-\alpha_e)} - 1\right]$$ $$\alpha = \frac{1}{1+0.28X_m}$$ $$X_m = \left(\frac{1-x}{x}\right)^{0.64}\left(\frac{\rho_g}{\rho_f}\right)^{0.36}\left(\frac{\mu_f}{\mu_g}\right)^{0.07}$$	
Lee and Garimella (2007)	$$\Delta P_f = \frac{L_{tp}}{x_e}\int_0^{x_e}\frac{2f_l G^2}{D\rho_f}\phi_f^2\,dx$$ $$\phi_f^2 = 1 + \frac{C}{X} + \frac{1}{X^2}$$ $$X = \left(\frac{1-x}{x}\right)\left(\frac{\rho_g}{\rho_f}\right)^{0.5}\left(\frac{f_f}{f_g}\right)^{0.5}$$ for laminar liquid – laminar gas $$C = 2566G^{0.5466}D_h^{0.8819}(1-e^{-319D_h})$$ $$\Delta P_g = g\frac{L_{tp}}{x_e}\int_0^{x_e}\left[\alpha\rho_g + (1-\alpha)\rho_f\right]dx$$ $$\Delta P_{acc} = \frac{G^2}{\rho_f}\left[\frac{x_e^2}{\alpha_e}\frac{\rho_f}{\rho_g} + \frac{(1-x_e)^2}{(1-\alpha_e)} - 1\right]$$ $$\alpha = \left(1 + \left[\frac{1-x}{x}\right]\left[\frac{\rho_g}{\rho_f}\right]^{0.67}\right)^{-1}$$	Water D = 0.162 – 0.571 mm
Sun and Mishima (2009)	$$\Delta P_f = \frac{L_{tp}}{x_e}\int_0^{x_e}\frac{2f_l G^2}{D\rho_f}\phi_f^2\,dx$$ For the laminar flow region	2092 data points from 18 sources Water, refrigerants, CO_2.

	$$\phi_f^2 = 1 + \frac{C}{X} + \frac{1}{X^2}$$ $$C = 26\left(1 + \frac{Re_f}{1000}\right)\left[1 - exp\left(\frac{-0.153}{0.27La + 0.8}\right)\right]$$ For turbulent flow regime $$\phi_f^2 = 1 + \frac{C\left(\frac{Re_g}{Re_f}, \frac{1-x}{x}\right)}{X^{1.19}} + \frac{1}{X^2}$$ $$C = 1.79\left(\frac{Re_g}{Re_f}\right)^{0.4}\left(\frac{1-x}{x}\right)^{0.5}$$ $$\Delta P_g = g\frac{L_{tp}}{x_e}\int_0^{x_e}\left[\alpha\rho_g + (1-\alpha)\rho_f\right]dx$$ $$\Delta P_{acc} = \frac{G^2}{\rho_f}\left[\frac{x_e^2}{\alpha_e}\frac{\rho_f}{\rho_g} + \frac{(1-x_e)^2}{(1-\alpha_e)} - 1\right]$$ $$\alpha = \left(1 + \left[\frac{1-x}{x}\right]\left[\frac{\rho_g}{\rho_f}\right]^{0.67}\right)^{-1}$$	D = 0.506 – 12 mm $10 < Re_l < 37{,}000$ $3 < Re_g < 4 \times 10^5$
Lee et al. (2010)	$$\Delta P_f = \frac{L_{tp}}{x_e}\int_0^{x_e}\frac{2f_l G^2}{D\rho_f}\phi_f^2\,dx$$ $$\phi_f^2 = 1 + \frac{C}{X} + \frac{1}{X^2}$$ $$X = \left(\frac{1-x}{x}\right)\left(\frac{\rho_g}{\rho_f}\right)^{0.5}\left(\frac{f_f}{f_g}\right)^{0.5}$$ $$C = 121.6(1 - e^{-22.7Bd})x_e^{1.85}$$ $$\Delta P_g = g\frac{L_{tp}}{x_e}\int_0^{x_e}\left[\alpha\rho_g + (1-\alpha)\rho_f\right]dx$$ $$\Delta P_{acc} = \frac{G^2}{\rho_f}\left[\frac{x_e^2}{\alpha_e}\frac{\rho_f}{\rho_g} + \frac{(1-x_e)^2}{(1-\alpha_e)} - 1\right]$$ $$\alpha = \frac{1}{1 + 0.28X_m}$$	484 data points from 9 sources. Water and refrigerants. D < 3 mm

	$$X_m = \left(\frac{1-x}{x}\right)^{0.64}\left(\frac{\rho_g}{\rho_f}\right)^{0.36}\left(\frac{\mu_f}{\mu_g}\right)^{0.07}$$	
Li and Wu (2010)	$$\Delta P_f = \frac{L_{tp}}{x_e}\int_0^{x_e}\frac{2f_l G^2}{D\rho_f}\phi_f^2\,dx$$ $$\phi_f^2 = 1+\frac{C}{X}+\frac{1}{X^2}$$ $$X = \left(\frac{1-x}{x}\right)\left(\frac{\rho_g}{\rho_f}\right)^{0.5}\left(\frac{f_f}{f_g}\right)^{0.5}$$ $$C = \begin{cases} 11.9Bd^{0.45} & Bd \le 1.5 \\ 109.4\left(Bd\,\mathrm{Re}^{0.5}\right)^{-0.56} & 1.5 < Bd \le 11 \end{cases}$$ $$Bd = g\Delta\rho D^2/\sigma$$ $$\Delta P_g = g\frac{L_{tp}}{x_e}\int_0^{x_e}\left[\alpha\rho_g + (1-\alpha)\rho_f\right]dx$$ $$\Delta P_{acc} = \frac{G^2}{\rho_f}\left[\frac{x_e^2}{\alpha_e}\frac{\rho_f}{\rho_g}+\frac{(1-x_e)^2}{(1-\alpha_e)}-1\right]$$ $$\alpha = \frac{1}{1+0.28X_m}$$ $$X_m = \left(\frac{1-x}{x}\right)^{0.64}\left(\frac{\rho_g}{\rho_f}\right)^{0.36}\left(\frac{\mu_f}{\mu_g}\right)^{0.07}$$	769 data points D = 0.148 – 3.25 mm 12 different fluids
Zhang et al. (2010)	$$\Delta P_f = \frac{L_{tp}}{x_e}\int_0^{x_e}\frac{2f_l G^2}{D\rho_f}\phi_f^2\,dx$$ $$\phi_f^2 = 1+\frac{C}{X}+\frac{1}{X^2}$$ $$X = \left(\frac{1-x}{x}\right)\left(\frac{\rho_g}{\rho_f}\right)^{0.5}\left(\frac{f_f}{f_g}\right)^{0.5}$$ $$C = 21\left(1-\exp\left(-\frac{0.358}{La}\right)\right)$$ $$La = [\sigma/g\Delta\rho]^{0.5}/D$$	D = 0.07 – 6.25 mm. Adiabatic gas-liquid flow, adiabatic liquid-vapour flow and flow boiling

	$$\Delta P_g = g\frac{L_{tp}}{x_e}\int_0^{x_e}\left[\alpha\rho_g + (1-\alpha)\rho_f\right]dx$$ $$\Delta P_{acc} = \frac{G^2}{\rho_f}\left[\frac{x_e^2}{\alpha_e}\frac{\rho_f}{\rho_g} + \frac{(1-x_e)^2}{(1-\alpha_e)} - 1\right]$$ $$\alpha = \frac{1}{1+0.28X_m}$$ $$X_m = \left(\frac{1-x}{x}\right)^{0.64}\left(\frac{\rho_g}{\rho_f}\right)^{0.36}\left(\frac{\mu_f}{\mu_g}\right)^{0.07}$$	

Kim and Mudawar (2012)	$$\Delta P_f = \frac{L_{tp}}{x_e}\int_0^{x_e} \frac{2f_l G^2}{D\rho_f}\phi_f^2\, dx$$ $$\phi_f^2 = 1 + \frac{C}{X} + \frac{1}{X^2}$$ $$X^2 = \frac{(dP/dZ)_f}{(dP/dZ)_g}$$ $$(dP/dZ)_f = \frac{2f_f v_f G^2(1-x)^2}{D_h}$$ $$(dP/dZ)_g = \frac{2f_g v_g G^2 x^2}{D_h}$$ For circular channels; $f_k = 16Re_k^{-1}$ $\quad Re_k < 2000$ $f_k = 0.079Re_k^{-0.25}$ $\quad 2000 \leq Re_k < 20{,}000$ $f_k = 0.046Re_k^{-0.2}$ $\quad Re_k \geq 20{,}000$ Where subscript k denotes either f or g for the liquid or vapour phases, respectively. For turbulent liquid and vapour $$C = 0.39Re_{fo}^{0.03}Su_{go}^{0.10}\left(\frac{\rho_f}{\rho_g}\right)^{0.35}$$ For turbulent liquid and laminar vapour $$C = 8.7\ x\ 10^{-4}Re_{fo}^{0.17}Su_{go}^{0.50}\left(\frac{\rho_f}{\rho_g}\right)^{0.14}$$ For laminar liquid and turbulent vapour $$C = 0.0015Re_{fo}^{0.59}Su_{go}^{0.19}\left(\frac{\rho_f}{\rho_g}\right)^{0.36}$$ For laminar liquid and gas $$C = 3.25\ x\ 10^{-5}Re_{fo}^{0.44}Su_{go}^{0.50}\left(\frac{\rho_f}{\rho_g}\right)^{0.48}$$	7115 data points from 36 sources, 17 fluids. D = 0.0965 – 6.22 mm G= 4- 8528 kg/m^{2}s 0 < x <1 0.0052 < P_R < 0.91

	$$Su_{go} = \frac{\rho_g \sigma D_h}{\mu_g^2}$$ $$\Delta P_g = g \frac{L_{tp}}{x_e} \int_0^{x_e} \left[\alpha\rho_g + (1-\alpha)\rho_f\right] dx$$ $$\Delta P_{acc} = \frac{G^2}{\rho_f}\left[\frac{x_e^2}{\alpha_e}\frac{\rho_f}{\rho_g} + \frac{(1-x_e)^2}{(1-\alpha_e)} - 1\right]$$ $$\alpha = \frac{1}{1+0.28X_m}$$ $$X_m = \left(\frac{1-x}{x}\right)^{0.64}\left(\frac{\rho_g}{\rho_f}\right)^{0.36}\left(\frac{\mu_f}{\mu_g}\right)^{0.07}$$	
Del Col et al. (2013)	$$\Delta P_f = \frac{L_{tp}}{x_e}\int_0^{x_e} \frac{2 f_{lo} G^2}{D\rho_f}\phi_{fo}^2\, dx$$ $$f_{lo} = 0.046(Re_{lo})^{-0.2} + 0.7RR * X_{Del}$$ $$RR = \frac{2Ra}{D}$$ $$X_{Del} = \begin{cases} 0 & Re_{lo} \le Re_{lo}^+ \\ 1 & Re_{lo} \ge Re_{lo}^+ \\ 1 + \dfrac{A - 0.045Re_{lo}^{-0.2}}{0.7RR} & Re_{lo}^+ < Re_{lo} < 3500 \end{cases}$$ $$Re_{lo}^+ = \left(\frac{A+0.7RR}{0.046}\right)^{-5}$$ $$A = 8.9938 * 10^{-3}$$ $$\phi_{fo}^2 = Z + 3.595 * F * H * (1-E)^W$$ $$W = 1.398P_R$$ $$Z = (1-x)^2 + x^2\frac{\rho_f}{\rho_g}\left(\frac{\mu_g}{\mu_f}\right)^{3.542}$$ $$F = x^{0.9525}(1-x)^{0.414}$$ $$H = \left(\frac{\rho_f}{\rho_g}\right)^{1.132}\left(\frac{\mu_g}{\mu_f}\right)^{0.44}\left(1-\frac{\mu_g}{\mu_f}\right)^{3.542}$$ $$E = 0.015 + 0.44log\left[\left(\frac{\rho_{GC}}{\rho_f}\right)\left(\frac{\mu_f j_G}{\sigma}\right)^2 10^4\right]$$ $$if\ E \le 0, E = 0$$ $$if\ E > 0.95, E = 0.95$$	R134a, R245fa, R1234yf, R32 1.02 < Ra < 1.7 0.96 < D_h <2 mm 200 < G < 1000 kg/m^{2}s j_G >2.5